Ionic Liquid-Templated Synthesis of Mesoporous Carbons

by

Yaoguang Song, MSc, BSc

Being a thesis submitted for a degree of

Doctor of Philosophy

to the

School of Chemistry and Chemical Engineering

of

The Queen's University of Belfast

Based on research carried out under the direction of

Prof Peter Nockemann

School of Chemistry and Chemical Engineering

The Queen's University of Belfast

November 2022

DECLARATION

I declare that:

1) the thesis is not one for which a degree has been or will be conferred by any other university or institution;
2) the thesis is not one for which a degree has already been conferred by this University;
3) the work for the thesis is my own work and that, where materials are submitted by me for another degree or work undertaken by me as part of a research group has been incorporated into the thesis, the extent of the work thus incorporated has been clearly indicated;
4) the work described in this thesis is based on my own work carried out on a full-time basis between December 2018 and May 2022 in the QUILL Research Centre or School of Mechanical and Aerospace Engineering at the Queen's University of Belfast, or the Department of Chemical Process Engineering at the University of Strathclyde, or Diamond Light Source;
5) the composition of the thesis is my own work.

Signed Yaoguang Song

Date 14/11/2022

Dedicated to my parents.

PUBLICATIONS DURING PHD STUDY

(Chapter 3)

Song, Y., Norris, F., Hinchliffe, D., Xu, Y., Zhang, X., Nockemann, P., Ionic liquid-assisted synthesis of mesoporous polymers and carbon materials: the self-assembly mechanism. *Nanoscale*, **14**, 14212-14222 (2022)

(Chapter 4)

Song, Y., Zhang, X., Borucki, M., Klusener, P., Nockemann, P., Soft-templating synthesis of mesoporous carbons for supercapacitors: the role of cross-linking. To be submitted.

(Chapter 5)

Song, Y., Zhang, X., Klusener, P., Nockemann, P., Templating synthesis of mesoporous carbons for supercapacitors by recyclable ionic liquid templates. Currently in preparation.

(co-author)

Long, F., Zhang, X., Cao, X., Zhai, Q., Song, Y., Wang, F., Jiang, J., Xu, J., Mechanism investigation on the formation of olefins and paraffin from the thermochemical catalytic conversion of triglycerides catalyzed by alkali metal catalysts. *Fuel Processing Technology*, **200**, 106312 (2020).

ACKNOWLEDGEMENT

I want to give my biggest thanks to my supervisors, Prof Peter Nockemann and Dr Xiaolei Zhang who have continuously provided me with their full support, help, guidance, encouragement, and patience throughout my PhD. My PhD study witnessed the outbreak of the still ongoing COVID-19 pandemic that caused additional challenge to my work. Without them, I could hardly make any progress. I'd also like to thank my industrial mentor, Dr Peter Klusener (Shell) for inspiring me to review my work from an industrial perspective.

A big thank you also goes to the Bryden Centre for sponsoring my PhD research. Colleagues in the Bryden Centre, Prof David Rooney, Dr Neil Harrison, Miss Naomi Boyd, and Miss Karen Green, always offered their instant help whenever I needed them. Their warmth and kindness touched me greatly.

During my PhD, I've met many talented and helpful friends whilst working in the QUILL Research Centre, James Weir Building (Glasgow), and Ashby Building. The days we spent together, the chats, drinks, and foods we had, were lots of fun and shall be remembered.

Specially, I want to thank Prof Nathan Congdon and Dr Ana Sanchez. Thanks for having me to live with you guys and giving me a family life. Wherever I go in future, I remember I got a family in Northern Ireland.

Finally, I want to thank my parents and brother. Many thanks for believing in and supporting me all the time. I really appreciate it. Hope we can meet soon.

ABSTRACT

Mesoporous carbons (MCs) have been used for a wide range of applications including energy storage, catalysis, drug delivery, and pollutant removal due to their rich porosity and tuneable pore size. Meanwhile, lignin from biomass possesses a carbon content up to 60%, which has triggered increasing interest in employing lignin as precursor to prepare carbonaceous materials such as ordered MCs. Soft-templating synthesis proves to be the only feasible method so far to fabricate lignin-derived MCs with ordered mesopores. However, commonly used soft templates, block copolymers, are generally decomposed during the preparation thus barely recyclable, limiting the production of MCs at an industrial scale considering the relatively high price of block copolymers. Therefore, there is an imperative to seek more promising substitutes that feature excellent recyclability without sacrificing the templating effectiveness.

Long-chain ionic liquids (ILs) provide a good option due to their excellent amphiphilicity thus are increasingly used for the templating synthesis of various nanomaterials. The use of ILs as the template to fabricate MCs remains at the initial stage and ordered mesopores have not been achieved yet. This is mainly because of the lack of fundamental understanding on the self-assembly mechanism. Nevertheless, one notable advantage of ILs as the template is their excellent recyclability. This thesis explores the feasibility of employing amphiphilic ILs as recyclable template to fabricate ordered MCs for energy storage. The proposed templating synthesis is comprised of four major steps: 1) the self-assembly process, 2) the cross-linking of carbon precursors, 3) extraction of IL templates, and 4) calcination.

To fill up the gap on the self-assembly mechanism of IL-templated synthesis of MCs, a detailed study was first initiated over ternary mixtures containing IL templates, carbon precursor, and solvent by employing a combination of experimental and computational techniques such as small-angle X-ray scattering, polarised optical microscopy, coarse-grained molecular dynamics simulations, and density functional theory calculations. Special emphasis was put on the two crucial factors that eventually determine the topological structures of the resulting MCs, namely the morphology of IL templates and template-precursor spatial correlations. The morphologies of amphiphilic IL templates are not only tuneable through the adjustment of water concentration but also by the selection of the precursors. Carbon precursors with different hydroxyl moieties also lead to different precursor-template spatial correlations.

Upon understanding the self-assembly mechanism of IL-templated synthesis, the role of cross-linking reactions of carbon precursors was systematically studied in the pore architecture, surface functionality, and electrochemical performance of the resulting MCs as supercapacitor electrode materials. Three different cross-linkers, formaldehyde together with its two greener substitutes, glyoxal and glyoxylic acid, were compared during the cross-linking, aiming to guild the selection of suitable cross-linker when employing amphiphilic IL templates. Glyoxal as a greener cross-linker favours the preparation of ordered MCs with higher capacitance in both aqueous and IL electrolytes.

Based on the studies on the self-assembly mechanism and cross-linking reaction, the use of amphiphilic IL templates to prepare MCs for energy storage was explored by employing lignin model polymer, phloroglucinol-glyoxal polymer as carbon precursor, whilst assessing the recyclability of the chosen IL templates. The length of cationic alkyl chain, anion of IL templates, IL extraction process, and the percentage of IL template in IL/block copolymer co-templating mixtures were identified to influence the porosity, pore morphology, surface functionality, and electrochemical performance of the resulting MCs. Amphiphilic ILs played a bifunctional role in the templating synthesis, not only as soft template but also catalyst for the cross-linking. The catalytic ability of IL templates can overly cross-link the precursor and destabilise the ordered mesophase, thereby worsening the porosity of resulting MCs. Amphiphilic ILs with weaker catalytic ability can result in slightly richer pore architecture and higher capacitance for energy storage.

Moving forward from the templating mechanism to physical preparation, this work systematically explored the use of amphiphilic ILs as recyclable templates to fabricate ordered MCs. Each step in the proposed templating process played a significant role in the formation of highly ordered mesopores. Whilst the self-assembly mechanism study presented a theoretical basis on the feasibility of IL-templated synthesis, the cross-linking study pointed out the importance of choosing a suitable cross-linker. Although amphiphilic ILs showed great recyclability, other factors were also critical for the fabrication of ordered MCs, with the catalytic ability of IL templates themselves being the most prominent issue. The work provides a solid foundation on IL-templated synthesis of ordered MCs, which will direct future research effort into the customisation of IL templates to be employed solely for the templating synthesis, thereby further guiding the use of lignin as precursor to prepare MCs aiming for various applications.

ABBREVIATIONS

AA	All-atom
ACN	Acetonitrile
BET	Brunauer–Emmett–Teller
BJH	Barrett-Joyner-Halenda
CG	Coarse grained
CL&P	Canongia Lopes & Pauda
CMC	Critical micelllisation concentration
COM	Centre of mass
CTAB	Cetyltrimethylammonium bromide
C/P	Cross-linker/precursor
CV	Cyclic voltammetry
DFT	Density functional theory
DMSO	Dimethyl sulfoxide
EDLC	Electric double layer capacitor
EISA	Evaporation induced self-assembly
GG	Guaiacyl glycerol-b-guaiacyl ether
HAADF	High-angle annular dark-field
IL	Ionic liquid
IUPAC	International Union of Pure and Applied Chemistry
LLC	lyotropic liquid crystal
MC	Mesoporous carbon
MD	Molecular dynamics
NBO	Natural bond orbital
NMR	Nuclear magnetic resonance
NOESY	Nuclear overhauser effect spectroscopy
OPLS	Optimised potentials for liquid simulations
PPPM	Particle-particle particle-mesh
POM	Polarised optical microscopy
QM	Quantum mechanics
ReaxFF	Reactive force field
RDF	Radial distribution function
SAXS	Small-angle X-ray scattering

SEM	Scanning electron microscopy
SISA	Salt-induced self-assembly
STEM	Scanning transmission electron microscopy
TEM	Transmission electron microscopy
XPS	X-ray photoelectron spectroscopy
$[C_{10}C_{10}MIM]Cl$	1,3-didecyl-2-methylimidazolium chloride
$[C_{10}MIM]Br$	1-decyl-3-methylimidazolium bromide
$[C_2MIM][OAc]$	1-ethyl-3-methylimidazolium acetate
$[C_{10}MIM][OAc]$	1-decyl-3-methylimidazolium acetate
$[C_{12}MIM][OAc]$	1-dodecyl-3-methylimidazolium acetate
$[C_{18}MIM][MeSO_4]$	1-octadecyl-3-methylimidazolium methyl sulphate
$[C_{18}MIM][OAc]$	1-octadecyl-3-methylimidazolium acetate
$[N_{2220}][NTf_2]$	Triethylammonium bis(tetrafluoromethylsulfonyl)amide

CONTENTS

LIST OF FIGURES

LIST OF TABLES

Chapter 1

Prelude

Driven by the target of net zero, there is a global imperative to build sustainable energy systems by seeking for renewable energy sources whilst developing novel energy storage technologies. Biomass resource is an indispensable carbon negative feedstock thanks to its photosynthesis cycle that captures and converts carbon dioxide into hydrocarbons. Over 220 billion tons of lignocellulosic biomass residues from plants are generated globally per year.[1] Efficient utilisation of biomass feedstock can provide an alternative route to alleviate the environmental impact of the consumption of traditional fossil fuels. Therefore, it has drawn growing attention globally for the valorisation of biomass waste into high value-added products. Lignin is the second most abundant component from biomass possessing a high carbon content thus has been regarded as a promising precursor for carbonaceous materials. Meanwhile, mesoporous carbons (MCs) due to their high surface area, large pore volume, and particularly tuneable pore size are ubiquitously used in the field of energy storage by working as electrode materials. Therefore, this work is particularly interested in the conversion of lignin into MCs for energy storage.

This opening chapter firstly outlines a few of rudimentary concepts including lignin, mesoporous carbon, ionic liquid, and molecular dynamics simulations, then reviews recent research progress on related topics. In the end introduces the initiation of this work with overall aims and thesis structure depicted.

1.1. Overview

1.1.1. Lignin

Amongst all components of biomass, lignin is the second most abundant and nature's dominating aromatic polymer. Natural production of lignin on earth is estimated 0.5-3.6 billion tons per year whilst annual production for commercial lignin exceeds 70 million tons.[2,3] Notably, lignin has a carbon content up to 60%, accounting for 30% of terrestrial non-inorganic carbon,[4–6] which drives significant effort into the conversion of lignin into high value-added carbonaceous materials such as mesoporous carbons and carbon fibres.

So, what does lignin look like? From the aspect of chemical structure, lignin is comprised of three primary building units, namely syringyl (S), guaiacyl (G), and *p*-hydroxyphenyl (H) units (Figure 1.1).[7] Three monolignols are randomly linked together by C-C and ether bonds, yielding a highly branched three-dimensional structure. Therefore, both the structural and physicochemical properties of lignin are highly dependent on the chemical linkages and can vary significantly from different biomass resources and isolation methods. Figure 1.2

presents typical linkages between the monolignols of lignin, where β-O-4 linkage has been mostly studied, occupying the highest proportion amongst all linkages in both softwood and hardwood lignin.

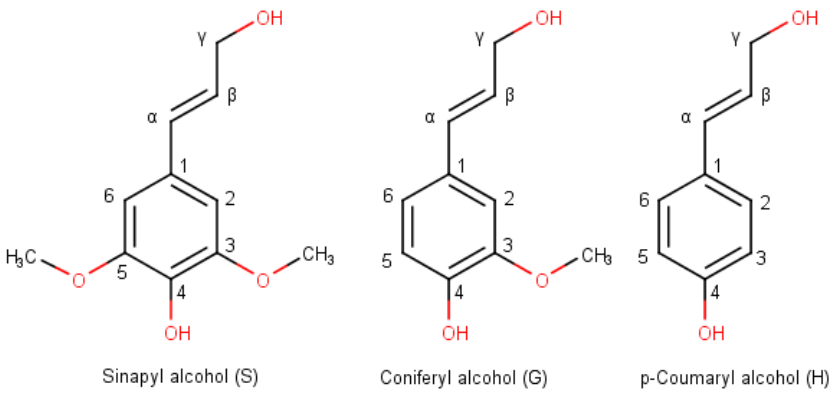

Figure 1.1. Three different monolignols of lignin.

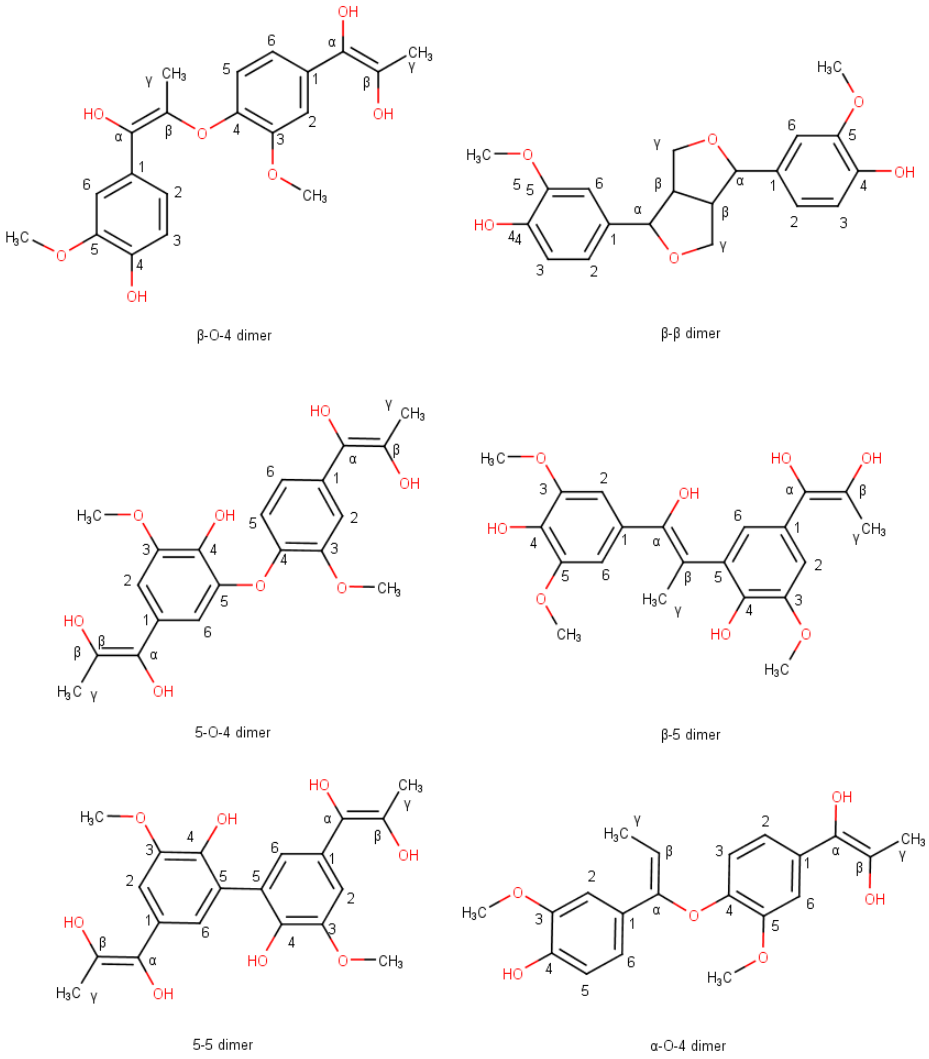

Figure 1.2. Typical linkages in lignin molecular structure.

So far, the only notable commercial approach for lignin valorisation is the successful production of vanillin from lignosulfonates, which can compete with petrochemical routes economically although the maximum yield is only about 7.5% by weight.[8] Currently, a major proportion of lignin is still consumed in industry to generate heat or electricity (by combustion), which are considered as low-energy resource due to the loss of chemical values existing in lignin. Thus, the full valorisation of lignin remains to be exploited by innovating more promising techniques other than combustion.

1.1.2. Lignin-derived mesoporous carbon

According to the definition of the International Union of Pure and Applied Chemistry (IUPAC), there are three categories of nanopores in terms of pore size: micropores (< 2nm), mesopores (2-50 nm), and macropores (> 50 nm). Mesoporous carbons (MCs) are carbonaceous materials with dominating pores in mesoporous range between 2 and 50 nm. They have many unique properties such as high surface area, large pore volume, and particularly tuneable pore size. Therefore, since their discovery, MCs have been widely used in numerous practical applications from catalysis and gas separation in industry to cutting-edge research fields such as energy storage and drug delivery.[9–12]

The first recorded successful preparation of highly ordered MC (CMK-1) applied a nano-casting technique by employing ordered mesoporous silica as hard template.[13] Later inspired by the fabrication of mesoporous molecular sieve MCM-41[14], amphiphilic surfactants started to be directly employed as soft template to fabricate MCs, rather than first synthesising mesoporous silica template then employing them for MC preparation. Ever since, templating method is regarded as the only effective method for the preparation of ordered MCs with tuneable pore size.

However, there are two problems that restrict the industrialisation of ordered MCs. The major concern is the high cost of sacrificial and expensive templating agents. Either hard template mesoporous silica or soft template organic surfactants are inevitably consumed during the template removal process by etching with strong acid/base or calcination. Seeking for template-free method or recyclable templates has drawn much attention to potentially achieve the production of ordered MCs at an industrial scale. Another issue is the high cost of traditional petroleum-derived carbon precursors, which drives research effort into seeking more sustainable precursors such as biomass waste for manufacturing cost reduction.

1.1.2.1. Applications of lignin-based mesoporous carbons

Lignin is a promising carbon precursor thanks to its high carbon content whilst MC materials represent one of the upper-class value-added products derived from lignin. Therefore, increasing research effort has been put into the preparation of MCs from lignin for various applications including, but not limited to, energy storage, catalysis, drug delivery, pollutant removal, and biosensor.

Energy storage

MC materials from lignin have a high potential for energy storage due to their excellent electrical conductivity and developed pore architectures. Supercapacitors including electric double layer capacitors (EDLCs) and pseudocapacitors are representative energy storage devices by employing MCs as active electrode materials.

The well-defined pore structures favour the ionic transport and charge accumulation, whilst surface functionalities could provide potential pseudocapacitance. Ruiz-Rosas *et al.*[15] reported lignin-based MCs with hierarchical structures for supercapacitors by employing zeolite Y and β as hard templates. Under the same preparation method, hierarchical porous carbons from lignin showed a better electrochemical performance than those from petroleum-pitch precursor. Lignin as the precursor gave rise to more oxygen-containing functionalities on the carbon surface, enhancing the pseudocapacitance. The gravimetric and volumetric capacitance of lignin-derived MCs reached 250 F/g and 140 F/cm^3 at a current density of 50 mA/g, with a capacitance maintenance over 70% at 20 A/g. Salinas-Torres *et al.*[16] also prepared lignin-based MCs *via* hard-template route. The resulting carbons showed capacitance around 140 F/g in 1 M H_2SO_4 aqueous electrolyte with a capacitance retention of 50 %. In a symmetric capacitor, energy density reached 4.2 Wh/kg at a power density of 1.3 kW/kg for carbon sample prepared by employing zeolite β template. Notably, the operating potential window could be further increased from 1.2 V to 1.4 V for asymmetric capacitor, resulting in a 50 % of increase in the energy density than that for symmetric capacitor. Compared with commercial activated carbon electrodes, MCs prepared by employing zeolite β template showed a better electrochemical performance with higher power densities despite templated MC exhibited a lower surface area and porosity. My earlier work[5] employed MgO as major template to prepare MCs from kraft lignin; resulting MCs were tested in three-electrode cells and showed a specific capacitance up to 186.3 F/g in 1 M H_2SO_4 electrolyte.

After 5000 cycles at 1 A/g, the capacitance retention remained 93.4%, presenting a great electrochemical stability.

With respect to the electrochemical performance of lignin-based MCs prepared by employing soft-template method, Saha *et al.*[17] reported a maximum gravimetric specific capacitance of 77.1 F/g for hardwood kraft lignin-derived MCs without activation in symmetric capacitor with a scan rate of 1 mV/s; the value is relatively lower than those achieved by hard-template methods. This might be because the carbon precursor was pre-cross-linked lignin and an imperfect self-assembly was produced during preparation. Consequently, the resulting carbon sample showed a lower mesoporosity thus a lower performance for ionic transport and charge storage than those prepared by small-fragment lignin with cross-linking agent. Ago *et al.*[18] fabricated lignin-based MC fibres *via* soft-template route, and resulting carbon fibrous network exhibited excellent capacitive behaviour in EDLCs with capacitance reaching 205 F/g in 0.5 M Na_2SO_4 electrolyte and electrical conductivity exceeding 386 S/m. Herou *et al.*[19] reported the preparation of highly-ordered MCs for supercapacitor by employing Pluronic F127 template with lignin/phloroglucinol (1:1) mixture as carbon precursor. Compared with MC solely from phloroglucinol precursor, mixing 50 wt% of lignin into phloroglucinol as carbon precursor showed an elevated volumetric capacitance of 90 F/cm^3 in 6 M KOH electrolyte with energy density of 3 Wh/L at 1 kW/L in symmetric two-electrode supercapacitors. Li *et al.*[20] reported a dual-templating synthesis of MC electrodes for supercapacitor from softwood lignin; resulting MC monolith exhibited an areal and volumetric capacitance of 3.0 F/cm^2 and 97.1 F/cm^3, respectively.

Doping heteroatoms can significantly improve the electrochemical performance of lignin-based MCs for energy storage. Jiang *et al.*[21] prepared N-doped MCs from lignin, which possessed a surface area of 870.2 m^2/g and a nitrogen content of 3.4%. The resulting N-doped MC was tested in a three-electrode cell and exhibited a large specific capacitance of 320.4 F/g with excellent cycle retention over 94.0% after 5000 times. Chen *et al.*[22] prepared NiO-doped MCs from sodium lignosulphonate *via* soft-template route, and the resulting MCs possessing NiO content between 49-79 wt% exhibited a large specific capacitance up to 880.2 F/g at 1.0 A/g with a maintenance of 90.9% at 10 A/g. The drastically improved capacitance mainly derived from the doping of NiO that provided pseudocapacitive behaviour. Rather than employing lignin as carbon precursor, Zhou *et al.*[23] used oxidised kraft lignin as doping agent of porous carbons for supercapacitors. In their work, N-doped porous carbons were first synthesised by employing silica microspheres as hard template and

dopamine as nitrogen precursor then the resulting carbons were doped with oxidised kraft lignin. The presence of hydroquinone group in lignin biomolecules and their derivatives can significantly enhance the pseudocapacitive behaviour of electrode materials. After doping with lignin, the capacitance was substantially increased to 412 F/g at a current density of 1 A/g, compared with the value of 154 F/g for the sample without loading oxidised kraft lignin. Recently, Liang *et al.*[24] employed Co^{2+} as metallic cross-linker to prepare Co-doped ordered MCs from lignin *via* soft-template route. Lignin was first extracted from walnut shell by ethanol and water. The resulting ordered MCs were washed with HCl acid to remove Co then further activated by $KHCO_3$ to achieve a hierarchical pore structure. The final hierarchical porous carbon showed a specific capacitance of 286 F/g with a specific energy density of 13.5 Wh/kg at power density of 44.3 kW/kg. The capacitance reached 249 F/g for Co-doped hierarchical porous carbon without washing out Co before activation, 219 F/g for ordered MC, 232 F/g for Co-doped ordered MC, and 96 F/g for MC prepared without using Co^{2+} cross-linker, respectively. The use of Co^{2+} metallic cross-linker greatly enhanced the capacitance whilst the doping of Co in the carbon materials without removing Co somehow decreased the electrochemical performance, especially at higher current densities.

Catalysis

Highly ordered mesopore channels could function as excellent nanoreactors therefore ordered MCs are also widely used for catalytic reaction. Qin *et al.*[25] reported the first successful fabrication of ordered MCs by solely employing lignin as carbon precursor. Softwood lignin were first pretreated to obtain different molecular weights then used as carbon precursor; the resulting MCs served as excellent catalyst support for Fischer-Tropsch synthesis with Fe_2O_3 nanoparticles incorporated as main catalyst. The catalytic ability was assessed by CO conversion; the highest conversion roughly reached up to 86.6% with a higher ratio between olefin to paraffin (O/P) of 3.78. The molecular weight of lignin played a crucial role in the preparation of highly ordered MCs and ensuing catalysis reaction.

Lignin-derived MCs have also been used for the conversion of fructose into 5-hydroxymethylfurfural.[26,27] Wang and Gan[26,27] reported the preparation of sulfonated MCs from kraft lignin by employing soft-template method. Resulting MCs were further modified with sulfonic acid to obtain solid acid catalyst, where the density of doped sulfonic acid was 0.65 mmol/g. A full conversion of fructose was achieved with an outcome yield over 98.0% at 140 °C for 2 h. The sulfonated lignin-derived MCs showed excellent reusability and stability; after 5-cycle experiment the product yield remained no less than 95.0%.

Sulfonated MCs from lignin were also used for the catalytic production of furfural from xylose.[28] Wang *et al.*[28] employed soft-template method to prepare ordered MC-SO_3H from a mixed carbon precursor of lignin and phloroglucinol with a mass ratio of 4:1. The as-synthesised MC-SO_3H exhibited an excellent catalytic performance by achieving full conversion of xylose into furfural with the highest yield reaching 76.7%.

Wang *et al.*[29] employed ferromagnetic lignin-based MCs for the catalytic hydrogenation of furfural to furfuryl alcohol. Organosolv lignin extracted from beechwood powder was used to replace up to 80% of phloroglucinol as carbon precursor. The prepared Ni-doped MC materials functioned as active and robust catalysts for the hydrogenation of furfural with a yield of furfuryl alcohol over 91.0% with the highest yield of 98.6%. Wang *et al.*[30] prepared metal-doped ordered MCs by employing Pluronic F127 template from organosolv lignin for the catalytic hydrogenation of furfural to furfuryl alcohol and tetrahydrofurfuryl alcohol. Various metallic cross-linkers were employed for the cross-linking of lignin precursor by coordination interaction including Ni^{2+}, Mg^{2+}, Fe^{3+}, Co^{2+}, Zn^{2+}, La^{2+}, and Ce^{3+}. Therefore, the resulting ordered MCs were single-metal doped or bimetal doped if bimetalic cross-linkers were used. A full conversion of furfural was achieved with maximum yields for furfuryl alcohol and tetrahydrofurfuryl alcohol of 64% and 100%, respectively.

Liu *et al.*[31] prepare lignin-based zero-valent Fe doped MCs for electrocatalytic reduction of nitrates to nitrogen by employing Pluronic F127 template and Fe^{3+} metallic cross-linker. The resulting Fe-doped MC exhibited a high nitrogen selectivity close to 100% whilst achieving a nitrate nitrogen removal capability up to 5373 mg N/g Fe. After 10 cycles, nitrate removal capacity remained at 1304 mg N/g Fe with a loss of 1.3% in nitrogen selectivity.

Drug delivery

MCs derived from lignin possess a rich porosity and ordered mesopore channels thus can be used as a controlled-release medium for drug delivery. Saha *et al.*[32] first reported the preparation of lignin-based MCs by employing soft-template method, where kraft-processed hardwood lignin was employed as carbon precursor. Captopril, an angiothensin-converting enzyme inhibitor, was selected as a representative drug to test the controlled-release properties of lignin-derived MCs. The release kinetics was studied with two regimes found within 48 h. In the fast release regime saw the rapid release of 60-70% of the drug at the beginning 3-4 h, followed by a slowly plateaued release profile. Lignin-based MCs showed high potential as alternate adsorbents for large-scale functional molecules from drug

adsorption and transport to controlled release. Saha *et al.*[33] further employed lignin-based MCs to investigate the loading and controlled release behaviour of three pharmaceuticals, namely captopril, furosemide, and ranitidine hydrochloride. A complete desorption in simulated aqueous solution was obtained over 30-40 h for the former two drugs, whilst the complete release time for ranitidine hydrochloride was no more than 10 h. Diffusivity was calculated based on release kinetics with values ranging from 10^{-22} to 10^{-24} m^2/s. Moreover, the pore texture property was found more important in the diffusion barrier of drugs than release environment.

Pollutants removal

MCs from lignin can be used to pretreat water by acting as adsorbents to pollutants such as antibiotics, metal, and humic acid.

Xie *et al.*[34] reported the removal of two harmful antibiotics in water with templated carbons derived from renewable sodium lignin sulfonate by employing halloysite nanotubes as template followed by KOH activation. Resulting carbon samples showed promising performance in a wide pH range for adsorption of antibiotics, with ultrahigh adsorption capacities for tetracycline of 1297.0 mg/g and chloramphenicol of 1067.2 mg/g. Particularly, after 5 cycles, regeneration capacity decreased by 28.8% and 26.7% for tetracycline and chloramphenicol respectively compared with values of the initial cycle. Nevertheless, the remaining adsorption capacity of the recycled carbon samples still outperformed other previously reported adsorbents, indicating that lignin-derived MCs as adsorbents are regenerative and recyclable. Ge *et al.*[35] prepared hierarchical porous carbons from sodium lignosulphonate for ciprofloxacin removal by employing graphene oxide as template coupled with KOH activation. The maximum monolayer adsorption for ciprofloxacin after activation by KOH reached as high as 980.4 mg/g at 318 K, higher than values at room temperature and 318 K without activation (675.7 and 925.9 mg/g, respectively). However, adsorption performance for templated carbons before KOH activation was not provided. Zhao *et al.*[36] reported soft-templating synthesis of MC spheres from sodium lignosulphonate for the treatment of a highly toxic radioactive element, uranium (VI). A maximum adsorption capacity of 109.46 mg/g and 195.6 mg/g were achieved in simulated radioactive solution and actual wastewater, respectively. Jedrzejczyk *et al.*[37] prepared lignin-based MCs for the removal of humic acid from water by employing various block copolymers as templates; the highest adsorption capacity for humic acid reached up to 175 mg/g.

Biosensor

Ordered MCs are believed to promote direct electron transfer by immobilisation of the enzyme or the "wiring" of the flavin adenine dinucleotide to the electron surface due to the large surface area and high conductivity.[38] Beaucamp *et al.*[38] prepared lignin-based MC nanofibers for the immobilisation of glucose oxidase, where carbon precursor was a blend of 50 wt% of alcell lignin and 50 wt% of polylactic acid. Resulting MC fibres exhibited a mesopore volume over 50% with smaller mesopores around 2.2 nm, which influenced the immobilisation of glucose oxidase mostly. Glucose oxidase was casted dropwise on the gold/carbon substrate to prepare biosensor. At a maximum condition, a linear response to the addition of glucose ranging from 0.15-2.7 mM was achieved with the prepared biosensor whilst showing an excellent selectivity to glucose and limit of detection of 50 μA/(mM·cm^2) and 89 μmol/L, respectively.

1.1.2.2. Templating preparation of lignin-based MCs

Hard-template synthesis

Hard-template synthesis method is also known as inorganic-template method, which means inorganic nanomaterials including zeolites, molecular sieves, metal oxides and some salts are employed as sacrificial moulds to fabricate MCs. Resulting materials reversely replicate the topology of moulds thus show opposite topologies with the templating materials. This replication approach is comprised of three major steps: a) preparation of template/precursor composite, b) calcination under inert atmosphere, and c) template removal. The porosity and pore structures of MCs can be tailored by selecting different hard templates or adjusting preparation conditions.[39] Commonly used inorganic hard templates can be categorised into two types, nanoporous and non-porous.

When the chosen hard templates have nanoporous structures, such as mesoporous molecular sieves and zeolites, resulting MCs possess pore architectures opposite with templates. To be specific, carbon precursors impregnated in the template pore channels will become the new pore wall after calcination whilst the pore walls of templates will generate new pores after being removed by etching. Therefore, the pore architecture and porosity of resulting carbon materials are highly dependent on the chosen template. As mesoporous molecular sieves get more diverse, it turns to be feasible to customise the mesopore structures of lignin-derived MCs for a specific application by carefully choosing templates. Figure 1.3 depicts the templating mechanisms of hard-templating synthesis and soft-templating synthesis.

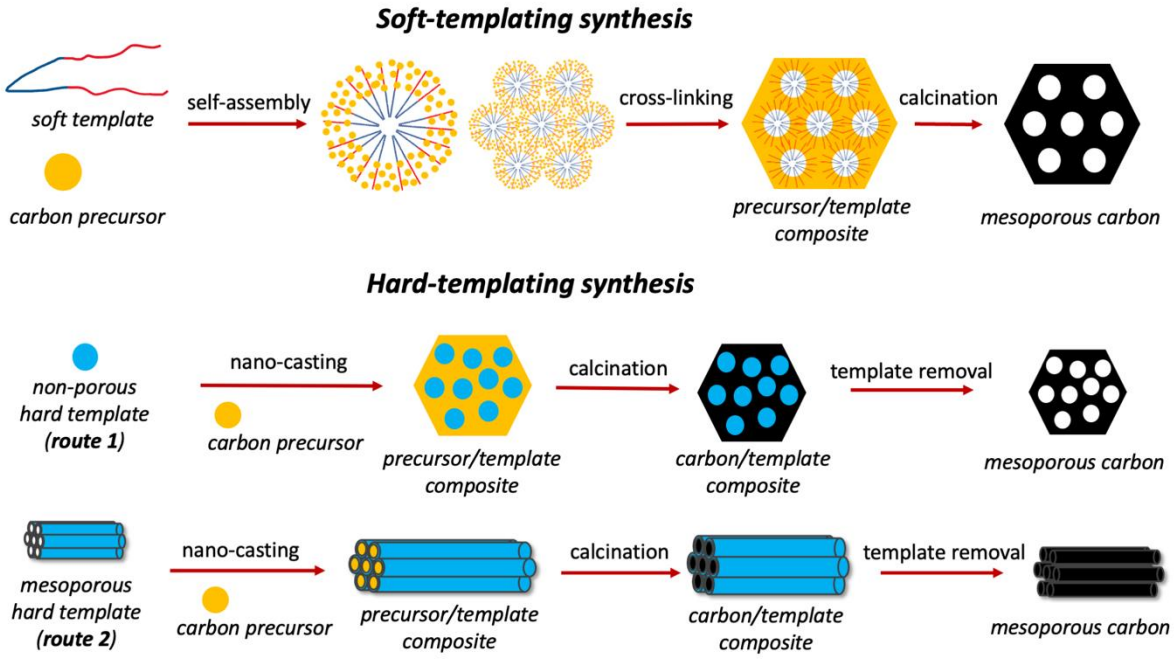

Figure 1.3. Comparison of different templating mechanisms.

Ruiz-Rosas *et al.*[15] synthesised MCs with hierarchical pore structures for supercapacitors from Alcell lignin by employing two different zeolites as templates (Alcell lignin refers those derived from solvolysis process by ethanol as opposed to those by kraft pulping to delignify biomass resource[40]). In a typical procedure, Alcell lignin was first dissolved in ethanol in the presence of β and Y zeolites. Lignin/template mixed composites were sequentially prepared by using liquid-phase impregnation technique at room temperature to ensure lignin filled with template channels, followed by drying in oven. After carbonisation under nitrogen and template removal by NaOH solution, lignin-based porous carbons were obtained. The surface area of resulting carbons ranged from 650 to 950 m^2/g, with a maximum mesopore volume of 0.85 cm^3/g. The mesopore volume and size increased when changing templates from Y to β zeolites. Regarding to mesopore size of templated carbons, Y and β zeolites under 700 °C resulted in mesopores around 2.7 and 9.3 nm, respectively. Compared with the carbon samples from petroleum pitch precursor, both surface area and mesopore volumes of lignin-based carbons were much higher; this could be associated with the higher content of phenolic and carbonyl surface groups in lignin, leading to a higher structural shrinkage with increasing temperature than for pitch-based carbons.[15]

Beside of templates themselves, there are other factors that also influence the eventual nanostructures of lignin-derived carbons such as carbonisation temperature and mixing ratio of lignin/template composites. Valero-Romero *et al.*[41] systematically investigated the

synthesis condition on structural and chemical properties of the resulting carbons. Four zeolites with different frameworks were chosen as inorganic templates, namely zeolite Y, zeolite β, ZSM-5, and mordenite, whilst Alcell lignin was employed as carbon precursor to fabricate MC materials by liquid-phase impregnation technique. There was a decrease in carbon yield with the increasing lignin percentage in lignin/zeolite mixture, and with the rising calcination temperature from 500 °C to 900 °C. For carbon samples derived from employing different zeolite templates, the yield of carbon products was basically in the order of zeolite Y > Mordenite > zeolite β > ZSM-5, with a maximum yield of 62.9%.[41] The pore size distribution of resulting carbon products is mainly determined by the template and highly independent with carbon precursor. Consequently, the resulting carbons from lignin showed similar pore architectures with those from other precursors such as petroleum pitch. This is because of the same pore formation mechanism by the replication of template pore channel. With respect to the pore morphologies, templated carbons synthesised with zeolite Y, ZSM-5, and mordenite showed similar topologies with dominating micropores, whilst mesopores around 10 nm were obtained in carbon material prepared by employing zeolite β template. The higher mesoporosity in β zeolite-based carbon was mainly attributed to the hierarchical character of β zeolite nanocrystal aggregation, which showed a dominating particle size about 17 nm. By a space-occupying effect of each single aggregation, resulting mesopores were disordered rather than highly ordered.

Salinas-Torres *et al.*[16] also used Alcell lignin precursor to fabricate hierarchical porous carbons for supercapacitors by hard-template method, where zeolite β and Y were selected as structure-directing templates. The mixing mass ratio between lignin precursor and zeolite template was constrained as 1:1 with a carbonisation temperature of 900 °C. Surface area and mesopore volume for Y zeolite-resultant carbon reached 670 m^2/g and 0.10 cm^3/g, whilst those were 930 m^2/g and 1.19 cm^3/g for β zeolite-resultant carbon. With respect to the pore architecture, a bi-modal pore size distribution was obtained where micropores were dominating regardless of the template whilst mesopores showed different diameters. β zeolite as the template generated more mesopores in resulting carbon than Y zeolite. The dominating micropores were mainly duplicated from the framework of zeolites as the thicknesses of pore walls for zeolite β and Y are both 1.0 nm. Moreover, zeolite β template also resulted in mesopores of 3.5 nm and 7-24 nm (with a largest proportion at 13 nm). Compared with templated lignin-based MCs, commercial activated carbon possesses a surface area of 2180 m^2/g, but over 95% of pores are micropores. Overall, when preparing templated porous

carbons, carbon precursors can not only be impregnated into the pore channel of hard templates, but also deposit on the external surface of template nanocrystals to serve as moulds by a space occupying effect.

Commonly seen non-porous hard templates include colloidal silica, silica nanospheres, metal oxides, natural minerals. When employing these non-porous hard templates to prepare MC materials, resulting mesoporosity and pore structures are tuned mainly by total quantity and particle size of the chosen template.

Fierro *et al.*[42] synthesised microporous-mesoporous carbons from Kraft lignin precursor by employing colloidal silica particles with two different sizes of 13 and 20 nm as templates. Kraft lignin was first pretreated with $NaHCO_3$, ethylene diamine or NaOH aqueous solutions to remove inorganic matter, resulting lignin precursor in different particle sizes ranging from 23 to 4640 nm. With respect to the preparation, lignin/template composites were first prepared by dispersing kraft lignin and silica colloids into $NaHCO_3$ aqueous solution, neutralisation with diluted HCl, slow solvent evaporation, and aging in vacuum oven. After a programmed heating and template removal, lignin-based MCs were obtained. The resulting MCs exhibited surface area and pore volume of 200-660 m^2/g and 0.4-0.76 cm^3/g respectively. The colloidal silica particle template led to different mesopores; dominating uniform spherical mesopores of 14 and 25 nm for carbons were obtained by employing silica colloid template with particle size of 13 and 20 nm, respectively.

Controlling the particle size of non-porous template is critical for the formation of mesopores in the resulting lignin-based MCs. Chang *et al.*[43] prepared porous carbons from sodium lignin sulfonate by employing silica nanospheres as templates. Resulting porous carbons possessed dominating micropores and a small proportion of mesopores with diameter of 2-4 nm. After etching silica template, the obtained carbon presented a three-dimensional continuous cellular-like structure with an average pore diameter about 200 nm, which belongs to macropore range. Therefore, silica spheres in Chang's work seem not suitable for mesopore formations.

Graphene oxide was also reported as hard template to prepared lignin-based MCs. Ge *et al.*[35] prepared MCs from sodium lignosulphonate by employing graphene oxide as template. The resulting carbon product was sequentially activated by KOH to enrich the porosity. However, pore texture properties of templated carbon before KOH activation were not provided. Eventual lignin-based MCs after KOH activation showed dominating mesopores of 2.8 nm

with large surface area and total pore volume of 3223 m^2/g and 2.28 cm^3/g, respectively. Due to the lack of pore texture property of carbon product before KOH activation, the feasibility of employing graphene oxide as the template remained unclear as most pores could derive from the KOH activation process.

So far, the hard templates mentioned above are generally pre-synthesised before being used to produce lignin-derived MCs. Natural minerals and metal oxides with certain particle size or structures were also reported feasible for inorganic templating synthesis.

Xie *et al.*[34] synthesised MCs from sodium lignin sulfonate for the adsorption of antibiotics where a class of natural silicate mineral, halloysite nanotubes were employed as templates. Resulting MC showed a surface area and pore volume of 389.8 m^2/g and 0.770 cm^3/g, which was 8 times larger than that without using template. However, the pore size distribution was disordered ranging from 2.0 to 100 nm with an average mesopore size of 7.0 nm. Pore structures were closely packed long tubular channels, which was stemmed from the direct replication of regular nano-tubular structures of halloysite nanotubes. After further activation by KOH at 850 °C for 1 h, the proportion of micropores was largely enhanced, where surface area and pore volume were 2320 m^2/g and 1.342 cm^3/g, respectively.

My previous work[5] reported the preparation of MCs from alkaline lignin by employing nano-sized MgO particles template, which functioned as main template by a space occupying effect. Compared with other hard templates such as silica, MgO nanoparticles appeared much easier to be removed by diluted acid thus possess high recyclable potential. Hard template MgO nanoparticles were formed *in situ* from the pyrolysis of Mg acetate. Resulting MC featured a large mesopore rate over 83% with dominating mesopores around 10 nm. The specific surface area and total pore volume reached 712 m^2/g and 0.9 cm^3/g, respectively. Mesoporosity of MC can be controlled by the amount of MgO particles, mixing ratio of MgO/lignin. Different drying techniques were investigated; vacuum-drying and freeze-drying techniques were carried out to lower drying temperature thereby preventing template aggregation. Vacuum drying produced more regular mesopore structures compared with the normal procedure under room temperature.

Xie *et al.*[44] reported the use of NaCl template assisted KOH activation to produce MC nanosheets from sodium lignosulphonate. Compared with sample without NaCl template, nanosheet structures in the resulting carbon sample were arbitrary because of the irregular accumulation of NaCl crystal cube. Moreover, the porosity of resulting MC was significantly

improved when using NaCl template. By solely employing NaCl template without KOH activation, resulting carbon showed a surface area and pore volume of 438 m^2/g and 0.85 cm^3/g, with an average mesopore of 8.83 nm, as opposed to the value of 3.1 nm for the control experiment without using NaCl template. After activation, surface area and pore volume were increased to 3505 m^2/g and 2.00 cm^3/g with a reduced mesopore of 2.3 nm on average.

The role of K_2CO_3 and KOH as template has been reported in the preparation of lignin-based MCs.[45,46] In fact, K_2CO_3 and KOH are widely-used porogens by functioning as activation reagents. Therefore, these practices are supposed to be categorised as conventional chemical activation methods.

Beside of being employed as carbon precursor, lignin can also be used as doping agent for porous carbons. Zhou *et al.*[23] first synthesised N-doped porous carbons by employing silica microspheres as hard template and dopamine as nitrogen precursor. Oxidised kraft lignin was loaded onto the N-doped porous carbons for supercapacitors. There was a declined porosity after loading lignin where surface area and pore volume decreased from 640.2 m^2/g and 1.33 cm^3/g before to 422.3 m^2/g and 0.90 cm^3/g after loading lignin.

Different from the porogens used in conventional carbonisation-activation methods, hard-templates generally do not react with lignin carbon precursor thus only function as sacrificial substrates by a space occupying effect. Mesopore structures of resulting MCs are highly tuneable by direct replication of the framework of nanoporous templates or by adjusting the particle size of non-porous templates. However, there are a few concerns regarding the scaling-up production of MCs from lignin by employing hard-template method. When using non-porous nanoparticles as the hard template, the mesopores in the resulting lignin-based MCs are comparatively disordered and lack of mesopore channels. Employing ordered porous silica/zeolites templates can produce highly ordered pore channels, but most ordered pore channels are microporous with mesopores being disordered. This is mainly associated with the multi-branched molecular structures of lignin, which made it challenging to sufficiently impregnate the highly branched lignin fragments into pore channels of silica-based hard templates. Consequently, almost all hard-templating synthesised lignin-based MCs exhibit a broad mesopore size distribution or hierarchical pore structures rather than highly ordered mesoporous structures. On the other hand, the removal of silica-based templates requires the use of corrosive chemicals such HF and NaOH; this could expose another limitation to the scaling-up production at an industrial level for a long run.

Soft-template synthesis

Soft-template synthesis (also known as organic-template synthesis) normally refers to the preparation of MCs by using organic compounds as templates such as amphiphilic surfactants. Figure 1.4 shows typical phenolic monomers and cross-linkers that are used to prepare polymers as carbon precursor. The preparation steps is comprised of two major steps: the preparation of template/precursor composite by evaporation induced self-assembly (EISA) and carbonisation of template/precursor composite[47]. As shown in Figure 1.3, during the EISA process to prepare ordered MCs, amphiphilic surfactants are expected to form cylindrical micelles then attach carbon precursors with the hydrophilic part of templates *via* hydrogen bonding or electrostatic interactions.[48] The ordered meso-structured topologies of resulting MCs can be customised by controlling the morphology of micelles. Amphiphilic block copolymers are one of the most extensively employed soft templates.

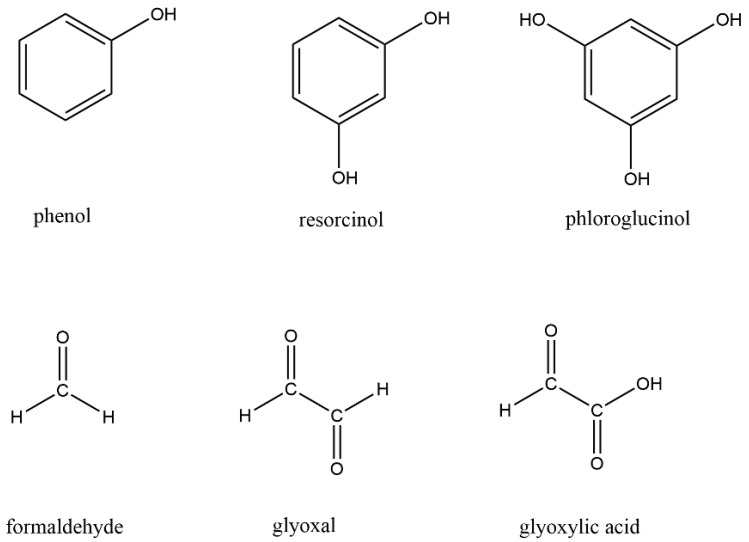

Figure 1.4. Representative phenolic polymer precursor monomers and cross-linkers.

Soft-template synthesis of MCs was inspired by the fabrication of mesoporous molecular sieves MCM-41.[14] Li *et al.*[49] reported for the first time the use of organic surfactant to prepare MCs, where cetyltrimethylammonium bromide (CTAB) acted as the soft template and the resulting carbons exhibited wormlike vesicular morphologies with mesopores of 2-4 nm and shell of 5-30 nm. Later Liang *et al.*[50] reported the first successful preparation of highly ordered MCs *via* soft-template strategy, where amphiphilic PS-P4VP and resorcinol-formaldehyde-polymer were employed as soft template and carbon precursor. Carbon precursor monomer resorcinol interacted with PS-P4VP template through H-bonding self-assembly. Uniform hexagonal mesopore channels were obtained with diameter of 33.7±2.5 nm. Recently, inspired by using cross-linked phenolic polymer as carbon precursor, research

effort has been directed into the use of natural lignin, an already cross-linked aromatic polymer, to prepare MCs by employing soft-template methods.

Saha *et al.*[32] first reported soft-template synthesis of lignin-derived MCs for drug storage and controlled delivery where the soft template was a commercial amphiphilic surfactant Pluronic F127, a tri-block copolymer with average molecular weight of 12600 and molecular formula of $(PEO)_{106}(PPO)_{70}(PEO)_{106}$ (where PEO and PPO stand for polyethylene oxide and polypropylene oxide, respectively). Ever since, block copolymers are extensively employed template for the preparation of lignin-based MCs because their decomposition takes place around 350 °C with almost no char yields after carbonisation.[51] For a preparation procedure, kraft-processed hardwood lignin and Pluronic F127 were first dissolved in tetrahydrofuran (THF), followed by adding cross-linking agent formaldehyde. After forming of template/lignin composite in the self-assembly process, cross-linking reaction took place to form a continuous polymer matrix. Finally, programmed calcination was carried out for carbonisation and simultaneous template removal. Resulting lignin-based MCs exhibited a specific surface area and total pore volume of 418 m^2/g and 0.50 cm^3/g, respectively. The mesopore volume of 0.34 cm^3/g was twice the micropore volume, indicating the dominating mesopores. However, in line with hard-template synthesis, pore size distribution of resulting soft-templated MCs were still relatively broad ranging between 2.5-12.0 nm. Compared with pre-cross-linked lignin as carbon precursor, lower-molecular-weight fraction of lignin seemingly favoured the soft-template synthesis of MCs, therefore the porosity of resulting MCs was much richer than that directly employing pre-cross-linked lignin as carbon precursor.

Later, Saha *et al.*[17] further studied the use of pre-cross-linked kraft lignin to synthesise MCs *via* soft-template route without adding any cross-linking agent. Resulting MC showed a dominating mesopore content over 82%. However, considerable decreases were measured in both surface area and total pore volume of 185 m^2/g and 0.28 cm^3/g, respectively. With phloroglucinol-formaldehyde polymer as carbon precursor, the resulting MC showed much richer porosity with larger surface area of 400 m^2/g and bigger pore volume of 0.57 cm^3/g; mesopore rate increased to 91% with a narrower pore size distribution between 4-6 nm.[33] From phloroglucinol-formaldehyde polymer to pre-cross-linked lignin, the decreased porosity may be related to the structural complexity of carbon precursors. The molecular weight of carbon precursors exerts a critical effect on the pore structure of resulting MCs. In fact, when

producing MCs from biomass lignin, the higher cross-linking degree the lignin molecular structure is, the less likely to attain developed porosity and cramped pore size distribution.[5]

Considering the structural similarity between lignin and phenolic polymer, lignin is increasingly used as carbon precursor to replace phenolic polymers, which are generated by the cross-linking reaction of phenolic monomers and cross-linking reagents. Herou *et al.*[19] reported a greener synthesis route for preparing ordered MCs from a mixed carbon precursor comprised of organosolv lignin and phloroglucinol crosslinked by glyoxal. As a less toxic cross-linker than formaldehyde, glyoxal provided an alternative substitute to make the production of MCs from lignin more sustainable. The organosolv lignin used in their work had a relatively low molecular weight (M_w/M_n/PD = 2286/3834 g/mol) with a narrow distribution (PD = 1.67). By replacing 50 wt% of phloroglucinol with lignin, the resulting MC showed a mesoporous volume and pore size of 0.5 cm^3/g and 3.9 nm, which were smaller than those of sample from solely employing phloroglucinol-glyoxal as the carbon precursor (0.82 cm^3/g and 7.3 nm). However, no noticeable chemical crosslinking interactions were found between lignin and glyoxal. Therefore, lignin could be regarded as "impurity" of phloroglucinol-glyoxal-polymer and acted as additive carbon precursor. Gan and Wang[26,27] prepared sulfonated MCs by employing kraft lignin and phenol-formaldehyde-polymer mixture as carbon precursor. By replacing 66.7% of phenol with kraft lignin, the resulting sulfonated MC exhibited well-ordered mesopores of 3.42 nm with a surface area and pore volume of 261.7 m^2/g and 0.067 cm^3/g. Wang *et al.*[29] employed a mixed lignin/phloroglucinol carbon precursor to prepare ordered MCs by using Pluronic F127 template. Organosolv lignin could replace phloroglucinol up to 80%. Resulting MC materials showed a specific surface area and pore volume of 674 m^2/g and 0.62 cm^3/g with ordered mesopores of 5.0 nm, although the porosity of resulting MC decreased slightly due to the doping of Ni. Wang *et al.*[52] prepared ordered MCs from lignin-phenol-formaldehyde precursor by employing Pluronic F127 template. Alkali lignin was isolated and purified from the black liquor of Masson pine pulp. Two preparation procedures for the self-assembly were investigated namely evaporation induced self-assembly (EISA) in organic solution and salt-induced self-assembly (SISA) in aqueous solution. Both procedures generated two-dimensional *p6mm* hexagonal mesopores, but MCs from SISA process exhibited a less ordered mesopore structures. SISA process resulted in a higher porosity in the resulting MCs than EISA process; a specific surface area and mesopore volume of 598 m^2/g and 0.14 cm^3/g were obtained for SISA process whist the values for MC *via* EISA process were 345 m^2/g and

0.03 cm^3/g, respectively. This SISA process could provide a more environmentally friendly process for the synthesis of lignin-based MCs at an industrial scale by avoiding volatile organic solvent. Wang *et al.*[28] employed a mixed carbon precursor to prepare ordered MC-SO_3H *via* soft-template method, where 75 wt% of organosolv lignin and 25 wt% of phloroglucinol cross-linked with glyoxal were employed as carbon precursor. The as-synthesised MC-SO_3H exhibited a high surface area and total pore volume of 607 m^2/g and 0.47 cm^3/g with a dominating mesopore size of 5.0 nm.

To gain more insight into the influence of molecular weight of lignin precursor on the mesopore structures, Qin *et al.*[25] synthesised MCs from lignin with different molecular weights by using Pluronic F127 as soft template. This is the first report that successfully produced MCs from lignin precursor with highly ordered mesoporous channels. Softwood lignin enriched with G and S units was selected as carbon resource, where the G units exceed S units in number. After pretreatment, lignin precursors had different molecular weights: 1055, 1476, and 2996 g/mol, respectively. In preparation, cross-linking agent formaldehyde (formalin solution) was added for the cross-linking reaction. All experimental parameters remain unchanged except the molecular weight of lignin precursor. Both the surface area and pore volume of resulting MCs increased with the declining molecular weight of lignin carbon precursor. The maximum values reached 466.1 m^2/g and 0.62 cm^3/g, respectively. Moreover, MCs showed well-ordered mesopores channels with long range with a dominating mesopore diameter of 3.9 nm. As lignin molecular weight increased, disruption in the order of mesoporous structures became more evident.

Indeed, when using phenolic polymer as the carbon precursor to prepare ordered MCs, molecular weight of carbon precursor also played an important in the formation of mesopores. Meng *et al.*[53] employed low-molecular-weight phenol-formaldehyde-polymer as carbon precursor to prepare a family of ordered MCs with different morphologies; polymer precursors with molecular weights ranging between 200-5000 favoured the formation of the ordered mesostructures.

Moving forward from phenolic polymer to lignin, lower-molecular-weight and less-branched lignin fragments have higher mobility thus generate a more favourable interaction with soft templates.[5,25,32] The highly branched lignin carbon precursor can lead to an imperfect self-assembly of surfactant micelles in the randomly cross-linked matrix, thereby destroying the well-organised mesophase formed by the soft-templates.[33] Therefore, a conclusion can be drawn that small-molecular-fragments and low-molecular-weights of lignin as the carbon

precursor can make it feasible to prepare MCs with highly ordered mesopore channels; this also guides the pretreatment of lignin towards improving the feasibility of producing high value-added MCs from lignin at an industrial level.

Soft-template method can also be used to prepared heteroatom-doped MCs from lignin. Doping heteroatoms could decrease the porosity and pore diameter of lignin-based MCs. Chen *et al.*[22] prepared NiO-doped MCs from commercial sodium lignosulphonate for supercapacitors. During preparation, both Pluronic F127 and KOH were added sequentially to play roles of porogens. The resulting NiO-doped MCs, in which NiO accounted for 49-79 wt%, showed high surface areas (503-802 m^2/g), large pore volumes (0.46-0.68 cm^3/g), and dominant mesopores (3.7 nm). However, mesopore structures were random and disordered. As mentioned previously, sulfonated MCs were prepared by Gan and Wang[26,27] from kraft lignin and phenol-formaldehyde-polymer mixture to convert fructose into 5-hydroxymethylfurfural. The resulting MCs were modified with sulfonic acid to obtain the solid acid catalytic ability, where -SO_3H density reached 0.65 mmol/g. A surface area and pore volume of 261.7 m^2/g and 0.067 cm^3/g were obtained with well-ordered mesopores of 3.42 nm. Jiang *et al.*[21] employed Pluronic F127 as soft template to fabricate nitrogen-doped MCs from lignin with tetrasodium salt of ethylenediamine tetraacetic acid as nitrogen-donator. Resulting N-doped MC possessed a high surface area of 870.2 m^2/g with a nitrogen content of 3.39%, whilst mesopores were about 30 nm. In fact, the nitrogen-containing organic salt contained sodium which could function as activation agent to enrich the pore structures. Therefore, this practice belongs to a combinational approach of soft-template synthesis and chemical activation. Wang *et al.*[29] reported the use of Pluronic F127 template to fabricate Ni-doped lignin-based MCs by employing organosolv lignin mixed with phloroglucinol as the carbon precursor. Ni-doping decreased the porosity and the mesopore diameter of lignin-derived MCs. The prepared Ni-doped MC materials showed a specific surface area and pore volume of 595 m^2/g and 0.47 cm^3/g with mesopores of 4.5 nm, whilst values for MC without Ni doping were 674 m^2/g, 0.62 cm^3/g, and 5.0 nm, respectively. Wang *et al.*[28] prepare ordered MC-SO_3H *via* soft-template method from a mixed carbon precursor comprised of 75 wt% of organosolv lignin and 25 wt% of phloroglucinol cross-linked with glyoxal. Resulting MC-SO_3H exhibited a surface area and pore volume of 607 m^2/g and 0.47 cm^3/g. Doped S atoms in the resulting MC reached 2.2 wt%, equivalent to a load density of -SO_3H group of 0.61 mmol/g. The sulfonate process did not significantly destroy the ordered two-dimensional hexagonal mesopore structures thus mesopores remained around 5.0 nm.

When employing soft-template method to prepare lignin-based MCs, metallic cross-linkers can be used to replace organic aldehyde cross-linkers by coordination interactions with lignin. Wang *et al.*[30] proposed one-pot synthesis of ordered MCs by employing Pluronic F127 template from organosolv lignin which was cross-linked by metallic cross-linkers rather than aldehydes such as formaldehyde, glyoxal, and glyoxylic acid. Various metallic cross-linkers proved to be effective for the cross-linking of lignin precursor by coordination interaction including Ni^{2+}, Mg^{2+}, Fe^{3+}, Co^{2+}, Zn^{2+}, La^{2+}, and Ce^{3+}. Organosolv lignin was first extracted by ethanol from lignocellulosic biomass waste such as walnut shell, macadamia nutshell, and tobacco stem; the extracted lignin exhibited rich hydroxyl groups, a moderate molecular weight (weight-average of 4732 g/mol, number-average of 4083 g/mol), and less branched structure due to the presence of H unit offering linear chains. As discussed above, lower molecular weight and less branched structure of lignin favour the self-assembly of soft template thus the formation of ordered mesopores.[25,30] The resulting metal-doped ordered MCs possessed highly ordered mesopore channels with pore diameter tuneable between 4.2-6.9 nm, whilst the surface area and pore volume ranged from 481-826 m^2/g and 0.30-0.48 cm^3/g. This method can be extended to the preparation of dual-metal-doped ordered MCs by using bimetallic cross-linkers.

Liang *et al.*[24] employed Pluronic F127 template to prepare Co-doped ordered MCs from lignin by using Co^{2+} as metallic cross-linker instead of aldehyde. Lignin was first extracted from walnut shell by ethanol and water. The resulting ordered MCs were washed with HCl acid to remove Co then further activated by $KHCO_3$ to achieve a hierarchical pore structure. Resulting ordered MC exhibited dominating mesopores of 4.5 nm with a surface area and pore volume of 716 m^2/g and 0.62 cm^3/g, as opposed to the values of 567 m^2/g and 0.48 cm^3/g for MC prepared without employing Co^{2+} crosslinker with disordered mesopores of 3.9 nm. Without washing out Co, the Co-doped MC showed a surface area and pore volume of 566 m^2/g and 0.50 cm^3/g with a dominating mesopore of 4.2 nm. After further activation with $KHCO_3$, the porosity was increased significantly whilst the mesopore rate declined substantially, regardless of with/without washing Co out.

Liu *et al.*[31] reported the use of Fe^{3+} metallic cross-linker to prepare lignin-based zero-valent Fe doped MCs by employing Pluronic F127 template. The resulting Fe-doped MC showed a surface area from 384 to 666 m^2/g as calcination temperature increased from 400 to 800 °C, conversly the ordered mesopores delined from 5.2 to 4.0 nm at the same amount of Fe^{3+} cross-linker. The total volume of MCs ranging between 0.43-0.55 cm^3/g. By adjusting the

amount of Fe^{3+} cross-linker, mesopores could be further decreased to 3.7 nm, with a Fe content of 8.4-25.8%.

Jedrzejczyk *et al.*[37] employed various block copolymers as templates to prepare lignin-based MCs for the removal of humic acid from water. Propargylated lignin was employed as carbon precursor, which self-crosslinked before carbonisation to form a continuous polymer matrix by Claisen arrangement. Resulting MCs showed surface area and pore volume of 95-367 m^2/g and 0.05-0.33 cm^3/g respectively, however the mesopores were disordered with pore diameters ranging from 3.3 to 36.6 nm.

Beside of block copolymers, some other organic amphiphiles were also employed as the soft template, such as poly(methyl methacrylate), CTAB, and polyvinyl alcohol. Seo *et al.*[54] prepared porous carbon foams by using colloidal poly(methyl methacrylate) particles as the template. Kraft lignin mixed with resorcinol-formaldehyde-resin were used as carbon precursor. Resulting carbon foam showed open cell structures with an average pore opening close to 6.0 μm; the size of pores lay in the range of macroporous beyond the scope of mesoporous materials. Zhao *et al.*[36] prepared MCs from sodium lignosulfonate by hydrothermal and template method, using CTAB as a template. Spherical and cotton-like shaped MCs were obtained with a pore size of 4.6 nm, whilst MCs without employing template appeared single spherical shape. Compared with MCs without using CTAB template, the BET surface area of carbon samples increased substantially from 66.7 m^2/g to 633.1 m^2/g by adding CTAB template, whilst the pore volume remained about 0.4 cm^3/g with doubled MC particle diameters. Normally, hydrothermal carbonisation process produces spherical carbon materials, therefore spherical shaped MCs were obtained with the use of CTAB template. Ago *et al.*[18] fabricated lignin-based MC fibres *via* soft-template route, where polyvinyl alcohol was employed as electrospinning facilitator and sacrificial soft template. Resulting freestanding lignin nanofiber network possessed a mesopore rate more than 70%, with a large surface area over 2005 m^2/g and pore volume of 0.7 cm^3/g.

In comparison with hard-template synthesis, one notable advantage of soft-template method is the skipping of additional template removal process because of the simultaneous thermodegradation of soft templates during calcination. Therefore, soft-template route does not involve the use of corrosive chemicals such as HF and NaOH. Concomitantly, this exposes additional challenge to soft-template method because of the inevitable consumption of soft template, lacking recyclability. Lignin-based MCs prepared through soft-template approach have dominating highly ordered mesopores especially when employing small-

molecular-fragments or low-molecular-weight lignin as carbon precursor. By controlling the initial structures of lignin, soft-template method can be used to customise the mesostructures of MCs. Considering that lignin from different isolation methods normally features different properties, effective pretreatment of lignin can be crucial for soft-templated ordered MCs.

Dual-template synthesis

Dual-template synthesis of MCs is a combination approach by employing two templates simultaneously, where there is a main and an assisting template regardless of organic templates or inorganic templates.

Li *et al.*[20] reported the preparation of lignin-derived MC monoliths by employing block copolymer Pluronic P123 [$(PEO)_{20}(PPO)_{70}(PEO)_{20}$] and mesoporous molecular sieve KIT-6 as templates. The resulting MC sample through dual-template route showed different pore architectures from those prepared by single-template route. MC prepared by solely employing Pluronic P123 template exhibited a broad pore size distribution between 10-50 nm, with a BET surface area and pore volume of 350 m^2/g and 0.35 cm^3/g, respectively. Whilst MC prepared through dual-template route showed much richer porosity with a BET surface area and pore volume of 803 m^2/g and 0.86 cm^3/g, respectively. Notably, pore size of MC/KIT-6 composite dominated at 6.3 nm, but mesopores of 3.4 and 50 nm, and even macropores of 100 nm appeared after etching KIT-6 template out from carbons. Due to the presence of KIT-6 template in MC/KIT-6 composite, the dominating mesopores of 6.3 nm mainly stemmed from the hard template, where there was imperfect impregnation of lignin into the pore channels of KIT-6 (with mesopore width of 8.4 nm).

Some research used two templates but one of them was not acting as template. For example, my previous work[5] prepared lignin-derived MCs by employing MgO and Pluronic F127 as templates, with resulting mesopores around 10 nm. Pluronic F127 functioned mostly as the dispersant to prevent the agglomeration of main template MgO nanoparticles, therefore that practice was classified into hard-template synthesis rather than dual-template synthesis.

So far, lignin-based MCs prepared *via* dual-template route feature hierarchical and random mesopore structures. If two soft templates such block copolymers are simultaneously employed as templates, it will be still feasible to prepare MCs with highly uniform mesopore channels from lignin when using small-molecular-fragments or low-molecular-weight lignin as carbon precursor.

In summary, three template-synthesis routes to fabricate ordered MCs from lignin were reviewed including hard-template, soft-template, and dual-template methods. Hard-template route that employs inorganic materials as templates normally do not interact with carbon precursor lignin by functioning as sacrificial substrates only by a space occupying effect. However, it can be challenging to impregnate carbon precursor lignin into template pore channels, resulting in a collapse and shrinkage of mesopores thus a disordered mesopore topology. Moreover, the use of corrosive chemicals such as NaOH and HF to etch the hard template, may cause damage to the facilities for a long run. Soft-template route by the self-assembly of amphiphilic surfactants proved to be an effective approach to fabricate MCs with highly ordered mesoporous topologies. Soft templates are simultaneously degraded during carbonisation to generate mesopores. Such inevitable consumption of soft template restricts the feasibility to produce MCs on an industrial level. Particularly, the commonly used soft template block copolymers are expensive. The non-recyclability of soft templates can increase economic cost substantially. Dual-template route combines the advantages of both hard-template and soft-template methods, but simultaneously features the disadvantages of both. Overall, soft-template method has the highest potential to produce ordered MCs to gain high values from lignin if more promising soft templates can be found that have both excellent amphiphilicity and recyclability.

1.1.3. Ionic liquid

Ionic liquids (ILs) normally refer to liquid or molten salts that are composed entirely of ions and remain fluid at a temperature below 100 °C.[55] Figure 1.5 shows the typical structures of most commonly seen ILs, including protic and aprotic ILs. The structural diversity of ILs enable themselves excellent physicochemical properties such as negligible volatility, good thermal stabilities and conductivity. Therefore, ILs have been ubiquitous in various applications including but not limited to energy storage, nanomaterial fabrication, catalysis, and biorefinery.[56–70] In this section, the use of ILs in the dissolution and degradation of lignin, and the preparation of carbon materials will be summarised.

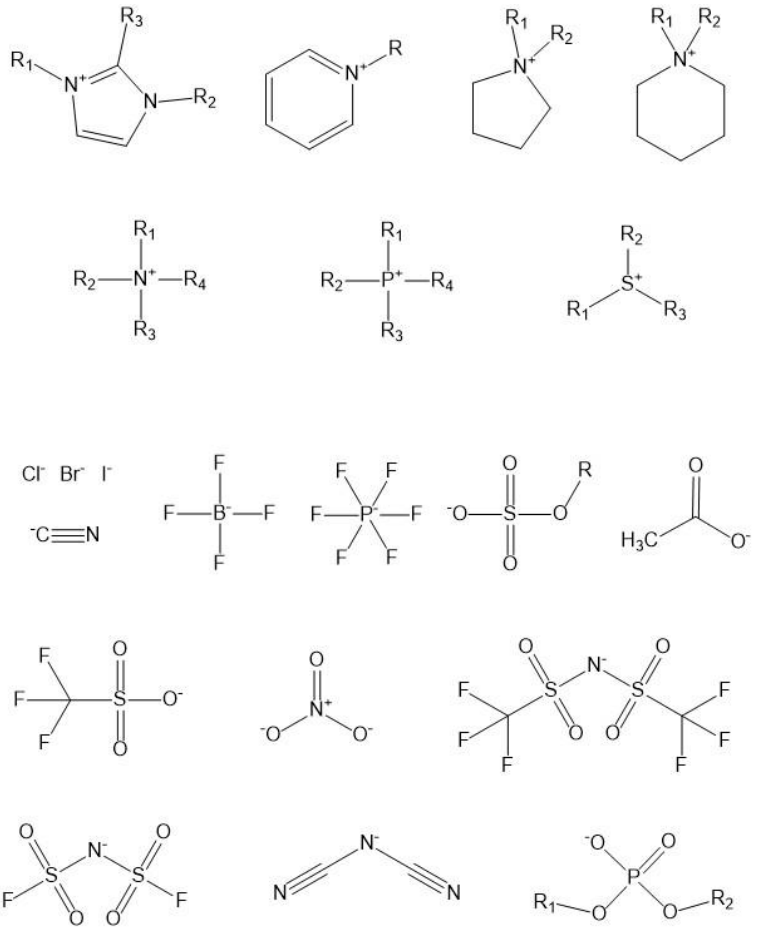

Figure 1.5. Representative ionic liquid cation and anion structures.

1.1.3.1. Ionic liquids for lignin pretreatment

ILs have a negligible volatility thus have been regarded as "green" solvents in synthetic process and reaction media. Much effort has been directed into the use of ILs in the valorisation of lignocellulosic biomass. ILs initially were found effective to dissolve cellulose through hydrogen-bonding between the hydroxyl group and anions.[71] Mäki-Arvela *et al.*[72] reviewed the dissolution of lignocellulosic materials using ILs where the dissolution of lignin was summarised briefly. Szalaty *et al.*[73] provided a comprehensive review on recent development in the dissolution and activation (or modification) of lignin using ILs.

Kilpeläinen *et al.*[74] achieved full dissolution of raw biomass including Norway spruce and sawdust, and Southern pine thermomechanical pulp fibres by using imidazolium based ILs such as 1-butyl-3-methylimidazolium chloride and 1-allyl-3-methylimidazolium chloride. However, the solutions after dissolution were not fully transparent except the practice using 1-benzyl-3-methylimidazolium chloride. The presence of benzyl group in IL cation boosted their interaction with aromatic lignin therefore a fully clear solution was obtained. Most ILs

only exhibited a partial dissolution of wood chips due to the compact structure of the wood cell wall which prevented ILs diffusing into the interior of wood cells.

Brandt *et al.*[75] studied lignin isolation from *Miscanthus giganteus* by employing IL 1-butylimidazolium hydrogen sulphate ([HC_4IM][HSO_4]) as extraction solvent. Through the cleavage of lignin-hemicellulose linkages, lignin could be isolated in the chosen ILs, which further broke the glycosidic, ester, and β-O-4 ether bonds to depolymerise lignin. The resulting lignin was carbohydrate-free, low-sulphur-content, and low-molecular-weight. However, longer pretreatment times in ILs induced repolymerisation of isolated lignin fragments, which modified the composition of later-stage lignin by enriching the guaiacyl (G) and *p*-hydroxyphenyl (H) units and phenolic hydroxyl groups.

It was shown that anions of ILs influence the solubility of lignin significantly. Pu *et al.*[76] dissolved up to 20 wt% lignin from pine kraft pulp by employing aprotic ILs as green solvents. With the same cation $[C_4MIM]^+$, ILs containing varying anions showed a different lignin solubility in the order: $[MeSO_4]^-$ > Cl^-, Br^- >> $[PF_6]^-$. Large and non-coordinative anions such as $[BF_4]^-$ and $[PF_6]^-$ are not ideally capable of dissolving lignin. Merino *et al.*[77] investigated lignin solubility in ILs containing multiple aromatic substitutes on imidazolium cations under microwave irradiation. 18 ILs with different cations and anions were synthesised for the dissolution of kraft lignin. ILs with multi-aromatic cations and methane sulfonate anions showed excellent lignin dissolving capacities, with the best performance achieving 42 % of lignin solubility after 5 min of microwave irradiation at 90 °C. Density functional theory (DFT) study was further performed to model the dissolution phenomena by calculating Gibbs free energy with β-O-4 models as lignin model compounds. The strongest interaction was observed between H atoms in the hydroxyl groups of lignin model and O atoms in anions of ILs; anions rather than cations exert more important effect on the dissolution of lignin.

Non-imidazolium based ILs are also suitable to dissolve lignin. Considering the cost of IL preparation, non-imidazolium based ILs are usually less expensive and easier to synthesis than imidazolium based ILs. Glas *et al.*[78] employed a series of ammonium, phosphonium, pyrrolidinium based ILs for the dissolution of lignin, where tributylmethylphosphonium methyl sulphate and *N*-butyl-*N*-methylpyrrolidinium dicyanamide showed comparatively higher dissolution ability for kraft lignin of 460 and 390 g/kg, respectively. After dissolving, ILs could be easily recycled with a recovery of 98±1% each time whist the molecular structures of lignin remained unchanged.

Gschwend *et al.*[79] proposed a protocol to delignify biomass then purify lignin by employing low-cost protic ILs where acidic IL triethylammonium hydrogen sulphate was used for the pretreatment of biomass. The pretreatment took place at 120 °C for 8 h or 150 °C for 1 h. A water/IL mixing ratio of 2:8 resulted in an optimum pretreatment. Different biomass feedstocks showed different outcome with respect to lignin yields; recovered lignin accounted for 20% and 5% of initial biomass weight for *Miscanthus* (grass) and pine (softwood), respectively. The lower recovery of lignin for pine (softwood) was associated with the presence of the G type lignin in softwood, which are more recalcitrant to dissolve than those in grass. Beside of yielding odour-free lignin, the proposed method not only led to slightly lower saccharides yields such as glucose but also exhibited high moisture tolerance which can further reduce solvent cost or decrease the viscosity.

Compared with lignin pretreatment technology by wet ball milling with phosphoric acid, the use of ILs, particularly [C_2MIM][OAc], can significantly reduce the average molecular weight, polydispersity, and particle size of the resulting lignin, whilst preserving the amount of phenolic hydroxyl and carboxyl groups and reducing the methoxy group.[80]

Computational modelling can provide insights into experimental phenomenon on an atomistic/molecular level. Some theoretical works were also reported to investigate the dissolution of lignin and biomass in ILs. Janesko[81] employed dispersion-corrected DFT to model the interaction between lignocellulose and imidazolium chloride ILs, where 1-(4-methoxyphenyl)-2-methoxyethanol and (1,4)-dimethoxy-β-D-glucopyranose were selected as model compounds for lignin and cellulose, respectively. Lignin model compounds were able to form a complex with 1-methyl-3-methylimidazolium cation of IL strongly bonded by π-stacking interaction and H-bonds and showed a comparable interaction strength with inion of ILs. Besides, the solubility of lignin and cellulose could be enhanced by the introduction of π-conjugated substituents in the cations of ILs, although they interacted with other phenyl group in lignin structure by π-stacking instead of the phenyl group of lignin model compounds.

Casas *et al.*[82] pointed out the major roles of IL anions rather than cations in the dissolution of lignin and cellulose; H-bonding interactions between anions and lignocellulosic materials are the main interaction force, with acetate, chloride and formate anions being the most promising anions. Electrostatic force and Van der Waals interactions could also enhance the solubility of lignin and cellulose but were secondary driven forces and less significant than H-bonding interactions.

Zhang *et al.*[83] performed a DFT study which confirmed the key role of anions in forming H-bonds for lignin dissolution, with acetate, chloride, and $MeSO_4$ exhibiting much stronger H bonding interactions than PF_6^-. Notably, anions had strongest interactions with lignin at the position α-OH of guaiacyl glycerol-b-guaiacyl ether (GG), one type of β-O-4 linked dimer compounds, whilst cations had strongest interaction with lignin at the γ-OH position. With respect to the cations of ILs, the length of cationic alkyl chain in imidazolium based cations did not significantly influence the H-bonding interaction between cations and GG, but π-stacking interaction was found a major way in dissolving lignin for cations.

Zubeltzu *et al.*[84] investigated the role of cations in the dissolution of lignin. Imidazolium based cation $[C_4MIM]^+$ and protic $[Et_3NH]^+$ interacted with lignin by dispersion only whilst choline cation, also established H-bonding interactions in addition to the dispersion interaction, with lignin model compound thereby providing an enhanced stabilisation of the hydroxyl group of lignin. Given that anions establish sufficiently strong H-bonding interactions to dissolve lignin as well as cellulose, cations may ultimately determine the affinity of ILs towards lignin.

As suggested by the study of Brandt and coworkers, ILs can not only dissolve lignin but also depolymerise lignin.[75] Wen *et al.*[76] reported for the first time the chemical transformation of lignin apart from the biomass matrix during pretreatment by imidazolium based ILs. The pretreatment of lignin using IL 1-ethyl-3-methylimidazolium acetate ($[C_2MIM][OAc]$) resulted in a decreased aliphatic hydroxyl group content possibly originated from the dehydration reaction and an increased phenolic hydroxyl group content due to the cleavage of β-O-4' linkages. De Gregorio *et al.*[85] investigated the delignification of two raw biomass resources, pine and willow, and subsequent oxidative degradation of lignin in protic IL 1-butylimidazolium hydrogen sulphate ($[HC_4IM][HSO_4]$) coupled with a vanadium-based polyoxometalate as oxidative catalyst. The oxidative depolymerisation of lignin mainly generated phenols, aromatic vanillin, and syringaldehyde products. Shorter pretreatment time for lignin obtained from pine resulted in an overall higher yield of aldehyde products with vanillin being the exclusive product. With molecular oxygen as the oxidant, a 5 wt% of loading of polyoxometalate catalyst in $[HC_4IM][HSO_4]$ gave rise to an optimal amount of both vanillin and syringaldehyde product. Prado *et al.*[70] studied lignin depolymerisation directly in black liquors, where two ILs, $[HC_4IM][HSO_4]$ and triethylammonium hydrogen sulphate ($[Et_3NH][HSO_4]$), were employed as delignification agents to extract lignin from raw biomass *Miscanthus Giganteus*. The initial mixing ratio of biomass *Miscanthus*, water and IL was 1:2:8 with H_2O_2 as oxidation agent added directly into the black liquors that

contained ILs as degradation media. Lignin extracted *via* $[HC_4IM][HSO_4]$ exhibited higher reactivity for the degradation with aromatic acids such as vanillic acid being the major product components of lignin depolymerisation.

1.1.3.2. Ionic liquids for MCs

Ionic liquids as material precursors

ILs have negligible volatility thus are suitable as carbon precursor for carbonisation process to make functional carbon materials. The structural diversity of ILs makes it feasible to design carbon materials doped with specific heteroatoms.

Table 1.1 lists the representative work that prepared carbon materials, particularly MCs, by employing ILs as the precursor for carbon matrix and heteroatoms. Some claimed that ILs also played the role of template or structure directing agent, where such templating role indeed was quite limited. Overall, ILs are relatively costly so using ILs as the sacrificial carbon precursors will inevitably increase the barrier to produce MCs on an industrial scale.

Table 1.1. Summary of the preparation of porous carbons by employing ILs as precursor.

Source	Ionic liquids	The role of ILs	porogens	Carbon products
Chen *et al.*[86], 2022	Poly ILs	C, N precursor	KOH	N-doped porous carbon
Zhou *et al.*[87], *2021*	Phosphoric acid protic ILs	C & heteroatoms precursor, porogen	$(NH_4)_2HPO_4$	N, P-doped porous carbons
Luo *et al.*[88], 2021	$[C_4MIM][NTf_2]$	C, N, S precursor	n/a	Heteroatoms-doped carbons
Karimi *et al.*[89], *2020*	MPIHS	C, N, S precursor	SBA-15	N, S-doped MCs
Zdolšek *et al.*[90], 2019	$[C_4MIM][MeSO_3]$	N, S precursor	n/a	N, S-doped porous carbon
Zhou *et al.*[91], 2019	Amino acid protic ILs	C, N, O, S precursor	n/a	N, S-doped porous carbon
Liu *et al.*[92], review paper, 2019	ILs, poly ILs	precursors	n/a	Heteroatom-doped porous carbons
Shao *et al.*[93], 2018	Poly ILs	precursors	porous membrane	Porous carbon membrane
Zhao *et al.*[94], 2018	[BVIM]Br, and poly-ILs PBVImBr, PBVIMBrA	C & N precursor, template	n/a	Disordered mesoporous carbon nitride
Rafiee *et al.*[95], 2018	MPIHS	C, N precursor	SBA-15	Ordered MCs
Zhao *et al.*[96], 2018	$[C_2MIM][DCA]$	N, C precursor	Pluronic F127	Ordered MCs
Su *et al.*[97], 2018	Cyano-based ILs	precursor	n/a	Disordered porous carbon
Chen *et al.*[98], 2017	$[C_nMIM]Br$ (n = 4, 8, 12, and 16)	C & N precursor, soft template	TEOS and ILs	N-doped hollow MC spheres
Gong *et al.*[99], 2016	Poly-IL ($PCMVImTf_2N$)	N, C precursor	carbon nitride nanosheets	N-doped porous carbon nanosheets

Haghighi *et al.*[100], 2015	MPIHS	C precursor	SBA-15	IL-derived fibrillated MCs
She *et al.*[101], 2015	$[C_4MIM][NTf_2]$	C, N, S precursor	n/a	N, S-doped porous carbon
Wilson *et al.*[102], 2015	$[C_2MIM][DCA]$	N, C precursor	silica nanospheres	N-doped porous carbon
Zhang *et al.*[103], 2014	Protic ILs	C, N precursor	n/a	N-doped porous carbons
Kazemi *et al.*[104], 2014	MPIHS	C precursor	SBA-15	IL-derived fibrillated MCs
Sahraie *et al.*[61], 2014	$[C_2MIM][DCA]$, [THIA][DCA], [TEP]Br, and $[C_2MIM][TCB]$	Heteroatom precursor	$FeCl_3$	Heteroatom-doped porous carbons
Karimi *et al.*[105], 2014	MPIHS	C precursor	SBA-15	IL-derived fibrillated MCs
Zhang *et al.*[106], 2014	Protic ILs	C, N precursor	n/a	N-doped porous carbons
Fechler *et al.*[107], 2013	$[C_2MIM][DCA]$, [BMP][DCA], and $[C_2MIM][TCB]$	N, B, C precursor	salts	Heteroatom-doped MCs
Qiu *et al.*[108], 2013	$[C_4MIM][DCA]$	C, N precursor	SBA-15	N-doped MCs
Chen *et al.*[109], 2013	$[C_nMIM]Br$ (n = 4, 8, 12, and 16)	N, C precursor	silica nanospheres	N-doped hollow MC spheres
Karimi *et al.*[110], 2012	MPIHS	C precursor	SBA-15	IL-derived fibrillated MCs
Hasché *et al.*[111], 2011	[BMP][DCA]	N, C precursor	Silica nanoparticles	N-doped MC supported platinum nanoparticles
Yang *et al.*[112], 2010	$[C_2MIM][DCA]$	N, C precursor	silica nanoparticles	N-doped porous carbons
Paraknowitsch *et al.*[113], 2010	$[C_2MIM][DCA]$, [3-BMP][DCA]	N, C precursor	SBA-15	N-doped MCs
Wang *et al.*[114], 2010	$[C_4MIM][NTf_2]$	N, S, C precursor	TEOS	N, S-doped porous carbon
Lee *et al.*[93], 2009	Nitrile-functionalised ILs	N, C precursor	n/a	N-doped porous carbons

ILs as the template

Long-chain ionic liquids (ILs) have excellent amphiphilicity, which is one key criteria during the selection of appropriate soft templates for the preparation of MCs. Lyotropic liquid crystals (LLCs), micelles, and (micro) emulsions formed by ILs have already drawn much attention in templating synthesis of nanomaterials. Hejazifar *et al.*[115] reviewed three types of IL-based microemulsions that are widely used for polymerisation and material preparations. Kang *et al.*[59] summarised recent explorations on employing ILs as templates, as well as synthetic media and precursors, to fabricate various dimensional nanomaterials, including zero-dimensional nanoparticles, one-dimensional nanowires/nanotubes/nanorods, two-dimensional nanosheets, and three-dimensional porous materials. The utilisation of ILs as templates (or structure-directing agents) for material preparation is still continuously growing.[59,64,116–122] In general, the rationale for achieving diverse structures lies in confining

IL templates during self-assembly into various morphologies, mainly: spherical, columnar, and lamellar.

The use of ILs as templates to prepare porous polymer and carbon materials still remains at an initial stage, despite their growing popularity in the fabrication of carbon materials and other nanomaterials. Nevertheless, one notable advantage of employing ILs as the template is that they can be recycled.[117,123–126] After polymerisation/cross-linking reaction, ILs can be easily extracted out from the polymer/IL composites by Soxhlet extraction with solvents typically acetone and methanol. This makes ILs more promising as the preparation cost of MCs will be potentially reduced in large scale production.

So far, no highly ordered pore structures have been reported as of yet. Xie *et al.*[126] employed a reusable IL 1-butyl-3-methylimidazolium tetrachloroferrate (iii) to prepare hierarchical porous carbons *via* ionothermal carbonisation of carbohydrates. The IL played a triple role: soft template, solvent, and catalyst, but no obvious ordered mesoporosity was obtained. Yang *et al.*[127] prepared porous resorcinol-formaldehyde-resultant polymer gels and carbon aerogels employing ILs with various cation chain lengths (2-8 carbon atoms) as templates. As the length of alkyl chains increased, resulting porous aerogels showed increased specific surface area. However, IL templates were decomposed during pyrolysis and the resulting pore structures were disordered. Nagy *et al.*[117] reported the use of ILs as recyclable templates and metal-free catalyst for polymerisation to synthesise porous polymer gels from phenolic compounds. The ILs were extracted out from polymer/ILs composites using water and acetone in sequence. The influence of different cations and anions on the porosity of the polymers was studied. The ILs employed in their work were less amphiphilic as the longest chain length of cation only reached 4 carbon atoms. Generally, ILs show noticeable amphiphilicity when the alkyl side chain has over 6 carbon atoms[128–131], though microphase separation could occur with shorter alkyl chains[132].

The absence of ordered pore structures in aforementioned explorations can be associated with: 1) the use of less amphiphilic ILs as soft templates which are unable to form long range ordered mesostructures, and 2) the lack of fundamental understanding on how to effectively manipulate the morphologies of templates in systems containing both IL templates and carbon precursors. Once understanding the self-assembly mechanism of IL-templated synthesis, it could be possible to prepare MCs by employing ILs as the recyclable soft template.

1.1.4. Molecular dynamics simulation

Computational modelling becomes a more flexible, cheaper, and sometimes safer option to do research than the traditional practical experiments in laboratory. Molecular dynamics (MD) simulation plays an important part in multiscale modelling providing insights into experimental phenomena at an atomistic/molecular level. As shown in Figure 1.6, MD simulation can be classified into reactive MD, classic all-atom MD, and coarse-grained (CG) MD simulations based on the simulation scale from nanometre and nanosecond to micrometre and microsecond. There have been numerous publications introducing MD simulations and their applications. Here in this section, the use of MD simulation in the study of lignin properties and the self-assembly of amphiphilic ILs are described briefly, thereby focusing on the main aim of this work that proposes a new method to prepare MCs from lignin by employing ILs as the soft template.

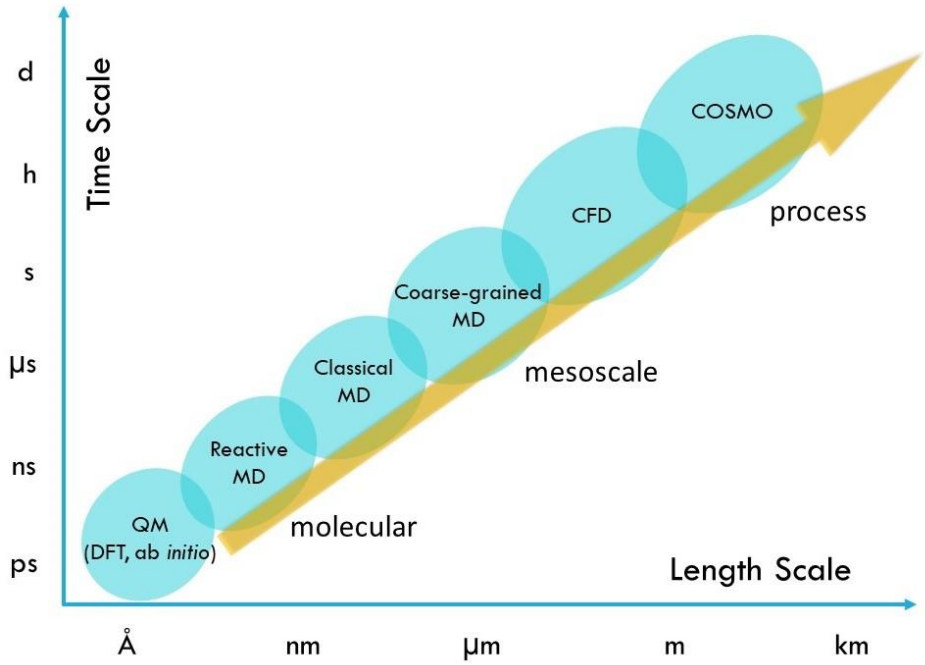

Figure 1.6. Molecular dynamics simulations in length scale and time scale.[133]

1.1.4.1. MD simulations for lignin

For the valorisation of lignin, much effort has been directed into understanding its structural and physicochemical properties. However, the molecular structures of lignin are too complicated, resulting in high challenge to clarify its properties solely by performing practical laboratory experiments. Computational modelling especially MD simulations as an assisstant powerful tool can be used to investigate the dynamic properties of complicated

large-scale systems. In this section, a brief description on MD simulations will be first introduced, then typical MD simulations for lignin are covered where possible.

As described earlier, although ab *initio* and DFT represent the most accurate calculation methods, quantum mechanics (QM) are too computationally intensive, which significantly limits their performance in modelling large system for longer time especially for lignin molecules. MD simulations offer an alternative choice to balance the dilemma between computational cost and accuracy level by training empirical models.

The core component underpinning MD simulations is the empirical potential function or so-called molecular mechanics force field. A MD force field is usually trained by QM calculation for performing large simulation systems for longer time whilst remaining desired accuracy to deliver reliable atomistic/molecular interactions and thermodynamic properties. Typically, the potential energy function has the following form:

$$E_{total} = E_{bonds} + E_{angles} + E_{dihedrals} + E_{impropers} + E_{nonbonded} \qquad \text{(Equation 1.1)}$$

The total energy of stytem is comprised of energy terms for bonds, angles, dihedrals/torsions, improper dihedrals, and nonbonded interactions, respectively. To be explicit, the nonbonded pairoff energy term also consists of two contributions, namely van der Waals and Coulomb interactions.

There are three types of force fields, namely all-atom force fields, reactive force fields (ReaxFF), and coarse-grained (CG) force fields. Typical all-atom force fields include CHARMM (Chemistry at HARvard Macromolecular Mechanics)[134], OPLS (Optimized Potential for Liquid Simulations)[135], AMBER (Assisted Model Building with Energy Refinement), and so forth. ReaxFF is particularly designed for reactive systems *via* a general bond-order-dependent potential, which is mainly based on the relationship between bond order and bond distance on one hand and between bond order and bond energy on the other hand.[136] CG force-fields trade more accuracy for calculation speed by maping a few heavy atoms together with the hydrogen atoms attached into one single bead to significantly reduce the total interaction sites. Therefore, CG MD simulations are widely used to model large system for longer time scale.

One of the most representative all-atom potential functions for lignin is the CHARMM force field[134,137] that is approximately represented by (Equation 1.2:

$$E_{total} = \sum_{bonds} K_b(b - b_0)^2 + \sum_{angles} K_\theta(\theta - \theta_0)^2 + \sum_{U-B} K_{UB}(s - s_0)^2 + \sum_{dihedrals} K_\phi[1 + \cos(n\phi - \delta)] + \sum_{impropers} K_\psi(\psi - \psi_0)^2 + \sum_{nonbonded} \left\{ \epsilon_{ij} \left[\left(\frac{\sigma}{r_{ij}} \right)^{12} - \left(\frac{\sigma}{r_{ij}} \right)^{6} \right] + \frac{q_i q_j}{4\pi D r_{ij}} \right\} \quad \text{(Equation 1.2)}$$

where K_b, K_θ, K_{UB}, K_φ, K_ψ represent bond, angle, Urey-Bradley, dihedral/torsion, and improper dihedral force constants, respectively; b, θ, s, φ, ψ are bond distance, bond angle, Urey-Bradley 1, 3-distance, dihedral/torsion angle, and improper dihedral angle with the subscript zero denoting the equilibrium values; n and δ involved in dihedral term represent its periodicity and phase. With respect to nonbonded interaction between one pair of atoms, i and j at a distance of r_{ij}, van der Waals interaction is described with the Lennard-Jones 6-12 potential with parameters ϵ and σ for the well depth and distance at minimum potential value whilst the rest part of (Equation 1.2 is associated with the Coulomb electrostatic interaction with parameter q and D referring to atomic partial charges and effective dielectric constant.

To investigate the structural and dynamic properties of lignin even for lignocellulose at molecular level by performing MD simulation, Petridis *et al.*[137] reported a parameterisation of lignin based on the empirical CHARMM potential function. The optimisation of parameterisation was trained against QM calculation results, thereby assessing the feasibility of the trained force field to reproduce reliable properties of lignin with special focus on β-O-4 linkage of lignin and the compatibility with already-existing CHARMM potential parameters. All QM calculations were carried out with NWChem 5.0 package. The new set of parameterisation was further verified by simulating a crystal of a lignin fragment molecule and comparing structural features from MD simulation with experimental results. The simulation system was comprised of 128 dimers with periodic boundary condition in isobaric-isothermal ensemble (NPT). Simulation results appeared overall good agreement with experimental data, confirming the favourable capability of newly trained lignin CHARMM parameters to study lignin composition and structural effects on degradation of lignocellulosic biomass.

Schulz *et al.*[138] outlined a strategy to handle large biomolecular systems with multimillion-atom both fastly and accurately with a special focus on the precipitation of lignin onto cellulose. To achieve this, Reaction Field method was used to calculate long-range Coulomb eletrostatic interaction, with simulation accuracy assessed in comparion with results calculated by Particle Mesh Ewald method. Cellulose and lignocellulosic biomass models with neutral charge group in aqueous solution were selected to perform benchmark simulations with GROMACS package, where the models were chosen respectively from cellulose[139] and lignin[137] CHARMM force fields. Results indicated that Reation Field method could reproduce properties as consistent with those calculated by Particle Mesh Ewald method whilst extending the simulation time scale to microsecond. By using Reation Field method instead, the performance was significantly improved with a calculation efficiency of 30 ns/day in scaling benchmark simulations of celloluse and lignocellulose aqueous system.

Petridis *et al.*[140] later investigated the temperature-dependent structural and dynamic properties of softwood lignin polymer in aqueous solution by employing all-atom MD simulations with an extensive simulation time of 17.5 μs. CHARMM force field for lignin and TIP3P water model were selected for the simulation. All MD simulations were carried out in GROMACS package with charge groups for water but neutral group for lignin under four temperatures: 300, 360, 420, and 480 K. For softwood lignin model, nine different lignin models were built in consistence with softwood lignin average compositions; the structural units for lignin were G type monomers and connected by various interunit-linkages with various branch point numbers and locations along the chain to ensure models of dissimilarities. The interunit linkages were comprised of 50% β-O-4', 30% 5-5', 10% α-O-4', and 10% β-5'. With the decreasing temperature, lignin models were observed to transit from extended and mobile comformations with enhanced dynamics to lower-temperature compact states with glassy dynamics. The distinguishing lignin collapse from extended to collapsed state derived from the release of water molecules in the hydration shell, which exhibited relatively lower compressibility of at low temperature.

Lindner *et al.*[141] studied preferential association behaviour of lignin with cellulose and itself *via* MD simulations, where CHARMM lignin force field was used to perform simulations with GROMACS software. Lignin model was comprised of 61 G unit monomers whilst cellulose fibre had 36 chains with each chain consisting of 160 monomers. Results indicated lignin strongly tended to aggregate with itself and cellulose. Notably, cellulose in crystalline regions exhibited higher tendency to associate with lignin than those in non-crystalline

regions. This could be associated to the stronger hydration of cellulose in non-crystalline regions, although the average direct interaction energy between lignin and cellulose seemed independent with cellulose crystallinity.

Zhang *et al.*[142] performed DFT calculations combined with MD simulation to investigate the cleavage mechanism of β-O-4 linkage of lignin model compound guaiacylglycerol-β-guaiacyl ether (GG) by using -SO_3H functionalised IL [C_3SO_3Hmim][HSO_4]. For the MD simulation, CHARMM force field parameters were used for both lignin model compound and IL. Three possible pathways were identified to convert GG to guaiacol by IL [C_3SO_3Hmim][HSO_4], where the -SO_3H group in IL cation played a substantial role in the solvation of lignin.

Wang *et al.*[143] employed CHARMM force filed to study the dissolution and aggregation of enzymatic hydrolysis lignin in organic-water binary mixtures including acetone-water, THF-water, and ethanol-water mixtures. Compared witih pure organic solvents, the solubilities of lignin are significantly improved with 30% of water added. An optimal dissolution performance was achieved in acetone-water mixture (with a volume ratio of 70%:30%) with a maximum saturated solubility of 35.6%.

Beside of CHARMM force field, other force fields were also employed in MD studies of lignin. Zhang *et al.*[144] studied thermodynamic properties of both softwood and hardwood lignin *via* the employment of COMPASS, DREIDING, and UNIVERSAL force fields. Glass transition temperature, density, and solubility of both types of lignin were investigated with DL_POLY package. Larger simulation cells delivered relatively improved thermodynamic properties than smaller cells. The glass transition temperature, density, and solubility of softwood lignin obtained from MD simulation showed good consistence with experimental results whilst the model for hardwood lignin showed a poor alignment with experimental results evidenced by the low solubility parameter. This could be associated with the model themselves in this work which sacrificed accuracy to reduce computational requirement by excluding the calculation of molecular electron density.

Vermaas *et al.*[145] proposed a comprehensive lignin force field following the standard CHARMM force field parameterisation method that incorporated all lignin linkages and lignin modifications within a self-consistent framework and can be used to describe both lignin-lignin interlinkages and lignin-carbohydrate interlinkages. The newly trained set of parameters for lignin reproduced the experimental result more accurately whilst lowering down the error compared with QM calculations. Later, Vermaas *et al.*[146] investigated the

solubility of lignin in various organic solvents by employing the newly proposed lignin models, with a special focus on the structural changes of lignin polymers in varying solvent environments. Amongst varying solvents including ethanol, methanol, acetone, DMSO, THF, dioxane, hexane, and water, the performance in solubilising lignin polymers was comparable, with each solvent mixture having their own optimal or near-optimal performance.

More recently, Mohan *et al.*[147] investigated the dissolution mechanism of lignin in ILs and deep eutectic solvents by performing multi-resolution MD simulations, where all models were based on CHARMM36 force field. IL cholinium lysinate [Ch][Lys] was a better solvent for lignin dissolution thus can be used to remove lignin from biomass such as hardwood and grassy-type biomass.

ReaxFF force field was first put forward by van Duin and coworkers[136] particularly designed for reactive systems. The potential is shown as (Equation 1.3, where van der Waals interaction was described by Morse potential instead of Lennard-Jones potential. It presents a general bond-order-dependent potential by employing bond order and bond energy to decribe chemical bonds rather than employing explicit bonds with a fixed bond length, which means ReaxFF force field is capable of being used to model both the cleavage and the formation of chemical bonds. Detailed description is available in their publications[136,148].

$$E_{system} = E_{bonds} + E_{over} + E_{under} + E_{val} + E_{pen} + E_{tors} + E_{conj} + E_{vdWaals} + E_{Coulomb} \quad \text{(Equation 1.3)}$$

Salmon *et al.*[149] studied the thermal decomposition process of lignite Morwell coal that is enriched in aromatic chemcial structures and has similar structure with lignin. C/H/O ReaxFF set of parameters for hydrocarbon oxidation[148] was employed to investigate the defunctionalisation, depolymerisation, and rearrangement behaviours during pyrolysis. Simulation results confirmed that phenolic structures formed during the defunctionalisation of methoxy functions, and double bonds conjugated with aromatic rings during decarboxylation and dehydroxylation of lignin side chain, whilst the C-C bonds in lignin side chain were observed to generate gaseous hydrocarbons after cleavage.

Beste[150] studied the oxidative thermal conversion of softwood lignin in LAMMPS package using C/H/O ReaxFF parameters designed for hydrocarbon oxidation[148]. Seven dilignol model systems with seven most common linkages were employed to represent lignin structures with initial simulation box containing over 3000 atoms. Reactive MD simulations

were performed in NVT ensemble after energy minimisation to calculate activation energy for model compounds conversion. Initial formation mechanisms of formaldehyde as one of the major conversion products were revealed. Notably, during the production of carbon fibre from softwood lignin, the stablising reactions were identified to cause rigid and cyclic connections between phenolic units. With similar simulation conditions, Beste[151] further investigate the oxidative thermal conversion behaviour of softwood lignin in the production of carbon fibre by using different large lignin fragments as precursor. The lignin precursor was composed of G and S units randomly that were linked by various linkages instead of simple dilignol lignin model compounds. This work mainly focused on the oxidative stabilising transformation steps that converted flexible linkages within lignin to rigid and cyclic connections, especially the chemical transformation involving oxygen and conjugated sp^2 carbon atoms.

Zhang *et al.*[152] performed large-scale ReaxFF MD simulations with a GPU-enabled GMD-Reax code and analysis tool VARxMD to study the overall pyrolysis behaviour of softwood lignin. The initial lignin models were derived from Adler softwood lignin model[153] with atoms number of 15920. NVT ensemble was employed for the simulation of lignin pyrolysis process with ReaxFF parameters designed for shocked polymers[154]. A three-stage pyrolysis mechanism was proposed, namely the cleavage of α-O-4 and β-O-4 linkages at low temperatures, the cracking of all linkages and conversion of propyl chains and methoxy substituents, and the formation of heavy pyrolysates at high temperatures. Their work presented an overall description of lignin pyrolysis pathways with the resulting pyrolysate species of small molecules. The initial conversion pathways of lignin were investigated in detail with respect to linkages and linked monomer rings.[155] C_α/C_β ether bond cleavage at the first stage contributed to the major evolution pathway for α-O-4, β-O-4 and α-O-4/β-5 linkages and their connected monomer aryl rings. Moreover, the reactivity of ring opening was closely associated with their connected and neighbouring linkages.

López-Albarrán *et al.*[156] performed ReaxFF MD simulations to reveal the influence of the type and content of mono- and oligolignol lignin precursors on the mechanical properties of resulting adhesive, with a special focus on Young's modulus on cellulose I-β crystalline surface. C/H/O ReaxFF parameters and LAMMPS package were employed for all reactive MD simulations. Results confirmed that coupling energies of lignin oligolignol and cellulose complex calculated from MD simulation were highly correlating with the Young's modulus

measured by experiments; trilignol G-(β-O-4)-S-(β-β)-S and dilignol G-(β-β)-G contributed mostly to lignin-derived adhesives.

Li *et al.*[157] investigated the gasification of lignin in supercritical water by performing reactive MD simulations. Three main gasification products of lignin were identified as CO_2, H_2, and CH_4. As the temperature increased, there was an increasing effect on the yields of the three gasification products, especially on the proportion of H_2. With the increased density of supercritical water, the yields of three gas products also showed significant improvement due to the higher participation of water in the gasification process.

Recently, Wang *et al.*[158] studied the gasification of softwood lignin in supercritical carbon dioxide in the presence of platinum nanoparticles as catalysts by employing reactive MD simulations. The main gasification products were identified as CO and H_2. Compared with the gasification without Pt catalysts, the addition of Pt nanoparticles considerably improved the gasification process with respect to the amount of CO_2 cracking, the yield of gas products, and the gasification rate.

Overall, due to its complicated molecular structures of lignin, MD simulations are mainly applied to lignin model compounds. Classic all-atom MD simulations were used to study the structural and physical properties of lignin such as the precipitation and dissolution, whilst reactive MD simulations were used to investigate the conversion of lignin into small chemicals through chemical processes such as pyrolysis, gasification, and degradation.

1.1.4.2. MD simulations for the self-assembly of ILs

The use of MD simulations to study the dynamic and interfacial properties, or the applications, of ILs has been extensively reported and there are also some comprehensive review papers available.[133,159,160] Many empirical and sophisticated force fields have been developed for ILs including ReaxFF force fields, classic all-atom force fields, and coarse-grained force fields. Focusing on the main aim of this thesis on employing amphiphilic ILs as the recyclable template to prepare MCs, this section briefly describes some work on the self-assembly of ILs, which is the determining step of the templating process of MCs fabrication.

For liquid simulations, it is inevitable to mention the OPLS-AA force field developed by Jorgensen *et al.*[135]. This is one of the most broadly applicable force field which yields highly accurate description for organic liquids. Based on the OPLS-AA functional form, Canongia Lopes & Pauda (CL&P) force field is developed as one of the most representative all-atom force fields particularly designed for ILs; this is a non-polarisable force field with high

transferability and compatibility within various IL families.[161] First designed for 1-alkyl-3-methylimidazolium based ILs[162], CL&P force field later extended the framework to a total of twelve IL families incorporating four cation families and eight anion families/individual ions; the cations include alkylimidazolium, alkylpyridinium, alkylphosphonium, and alkylammonium based ILs with their polyalkylated, cyclic, and functionalised derivatives whist anions include halogens, nitrate, dicyanamide, triflate, bis(sulfonyl)imide, alkylsulfates, alkylsulfonates, phosphates and their derivatives.[161]

However, CL&P force field does not consider the explicit polarisation of electron clouds, yielding reliable accuracy on estimating the equilibrium or structural properties of ILs but slowing down the microscopic dynamics.[161] Based on the widely used CL&P force field, a new polarisable CL&Pol force field was proposed by incorporating Drude-induced dipoles and scaling the empirical parameters used in Lennard-Jones potential for non-bonded interactions.[163,164] This newer force field has been extended to a wider range including protic ILs, deep eutectic solvents, alkali metal electrolytes, and glycols.[165,166]

Other representative all-atom force fields include the APPLE&P force field, a pioneering polarisable force field proposed by Borodin[167] that can be used to describe a wide range of IL families, and OPLS-VSIL force field proposed by Doherty *et al.*[168] for imidazolium based ILs to provide more accurate dynamical and thermochemical properties and correct intermolecular interactions between ions.

In spite of various empirical all-atom models developed, atomistic simulations are mostly limited within the study of initial aggregation of ILs-solvent mixtures.[159,160,169,170] Multiple factors were identified as being able to influence the formation of IL micelle clusters, including: the water concentration, the length of cationic side chain, solvation ability of the anion, and the influence of temperature.[122,128–131,171–174] For example, Bhargava *et al.*[175–177] employed CL&P all-atom force field to investigate the initial cation aggregations of [C_nMIM][Br] both in bulk solution and vapor-liquid interface. The cation aggregated forming micelle clusters with aggregation number between 15 and 24, whilst bromide anion exhibited a salvation shell of around seven water molecules.[175] Cationic alkyl chains formed the core of the micelle cluster leaving the polar imidazolium rings exposed to aqueous phase. The aggregation number of IL cations showed a steady increase trend with the increasing length of cationic alkyl chain.[176] Besides, ILs possessing a cationic alkyl chain length over 6 carbon atoms showed apparent amphiphilicity thus formed aggregates.[177] Vicent-Luna *et al.*[128] employed CL&P force field to investigate the micellization behaviour of 1-alkyl-3-

methylimidazolium chloride ILs. Structural changes and dynamic properties were investigated in detail for ILs with varying cationic alkyl chain length from 4 to 12. CL&P force field proved to be feasible in predicting the formation of micelle clusters of ILs in aqueous solution whilst producing reliable critical micellization concentrations (CMCs) in line with experimental data. Otero-Mato *et al.*[178] reported the use of CL&P force field to study the solvation behaviour of IL [C_2MIM][OAc] in aqueous solution. The addition of water does not destabilise the structure of the IL around the solute sphere and the orientation of ions in neighbouring solute particles but can significantly improve the mobility of solute particles in comparison with that in pure ILs. Freitas *et al.*[179] investigated the structural and dynamic properties of alkylpyridinium based IL [$C_{10}C_1$Pyrr][NTf_2] at interface and in confinement by employing CL&P force field. The calculated structure factor and pair distribution functions showed a well agreement with experimental data, whilst revealing the experimentally inaccessible properties such as in-plane structures and relaxation rates.

However, considering that the morphology reorganisation usually occurs in microsecond to millisecond, coarse-grained MD (CG MD) simulations are more fittingly poised, in terms of time scale and system size, to probe the mesoscopic self-assembly behaviour.[169]

CG models describe a group of heavy atoms with their linking hydrogen atoms into one single bead (one interaction site) using different mapping strategies whilst anticipating simulation results consistent with that from all-atom MD simulations.

For the imidazolium based ILs, there are mainly two types of mapping scheme with respect to the imidazolium ring. Bhargava *et al.*[180,181] constructed CG models by representing cationic imidazolium ring with three beads to maintain its planarity whilst the cationic alkyl chains and water were mapped in accordance with "the 3-to-1 principle"[182]. Quasi-spherical and hexagonal columnar phases were successfully predicted. Li *et al.*[183] proposed a fused CG model for IL [C_nMIM][BF_4]; the imidazolium ring was reconstructed by using five beads with four outer beads individually fused with one central bead, whilst each carbon atom together with its linking hydrogen atoms was solely mapped into a single bead like those used in united-atom models. This model was used to study the capacitance of IL electrolyte with porous carbon electrodes. Another common mapping method saw the coarse-graining of whole imidazolium ring into one single large bead.[184–193] Different atom mapping schemes for the same molecule could induce discrepant results in the structural and dynamic properties of ILs. Keeping the planarity of imidazolium ring gives better interfacial properties in line with experimental data whereas mapping the whole ring into one bead produces better

dynamic properties.[194] However, these CG models are not compatible and transferable with each other, therefore reparameterization was essential if new chemical structures are involved in the system.[181]

Yoo *et al.*[195] employed the IL CG model proposed by Bhargava *et al.*[180,181] to investigated the cytotoxicity of ILs on unicellular organisms, where the microbial cell membrane was represented by using 1-palmiltoyl-2-oleoyl-phosphatidylcholine (POPC) lipid bilayer, the most abundant lipid in L-α-phosphatidylcholine bilayer. The cytotoxicity of imidazolium based ILs [C_nMIM]Cl exhibited an increasing trend with increasing cationic alkyl chain length thereby showing stronger ability to disrupt the cell membrane by embedding in.

To improve the transferability and compatibility of CG models, Crespo *et al.*[172] recently proposed a new IL model based on MARTINI force field[196] to study the phase behaviour of ILs in aqueous solution. This new CG model is applicable to study multi-component systems. The phase behaviour of IL [C_nMIM]Cl was investigated with respect to the length of cationic alkyl chain, IL concentration in aqueous solution, and temperature. Morphological evolution process of ILs were investigated within various morphologies including spherical, columnar hexagonal, and lamellar bilayer structures. However, this CG model muddled different anions being indistinguishable. For example, bromide and chloride are described with the same type of beads with molecular weight being the only difference. The hydrogen bonding ability of these two anions are indeed different but such difference is not manifested in Martini force field. On the other hand, the performance of such CG models based on MARTINI force field are likely to be further boosted by applying a shifted Lennard-Jones potential with a shorter cut-off and replacing the Coulomb cut-off with reaction-field whilst performing MD on GPUs rather than CPUs to allow a significant speedup.[197]

Similar to the all-atom force field, Zeman *et al.*[198] proposed a dipole-polarisable CG model for IL [C_4MIM][PF_6], where the Drude oscillators were employed to describe the electronic polarizability. The explicitly polarised model was expected to be an improved CG model, reproducing more reliable results including density, enthalpy of valorisation, diffusion coefficient, and electrical conductivity than implicitly polarised model.

For protic ILs, Yang *et al.*[199] parameterised a CG model for alkylammonium based IL electrolyte tetraethylammonium tetrafluoroborate [TEA][BF_4] trained against the OPLS-AA force field. The electrolyte was mixed with acetonitrile solvent with activated carbon-based electrodes for supercapacitors. The proposed CG model provided atomistic perspective on the

ion exchange mechanism between IL electrolyte region and the porous carbon electrode, thereby revealing the pore size - electrolyte ions relationship during designing porous carbon-based supercapacitors. Schaeffer *et al.*[200] developed a transferrable CG model based on MARTINI force field for alkylphosphonium based IL tributyltetradecylphosphonium chloride $[P_{44414}]Cl$ to the study the mechanism of its phase separation in aqueous biphasic system containing either HCl or NaCl. The phase separation behaviour of $[P_{44414}]Cl$ was significantly different in biphasic systems containing either HCl or NaCl. The presence of hydronium cation promoted a stronger interaction between hydronium cation and micelle surface, the positively charged head group, as well as the interaction between each micelle cluster. Moreover, larger aliphatic moieties attached to the central phosphorous atom can weaken the electrostatic repulsion interaction of cationic moieties, making $[P_{44414}]^+$ cation less ionic.

To meet the increasing popularity of ILs in various applications, MD simulations of ILs developed fast by providing atomic/molecular perspective to experimental phenomenon especially in the study of the self-assembly behaviour of amphiphilic ILs. With respect to the computational cost, classic all-atom MD simulations were mainly limited in the study of initial aggregation or micellization behaviour of amphiphilic ILs whilst CG MD simulations were more fittingly poised by further trading acceptable accuracy for speed thus widely employed to study the morphological evolution process of amphiphilic ILs.

1.2. Aim of this work

Aromatic lignin has been regarded as a promising precursor for carbonaceous materials due to its high carbon content. One of the high value-added products from lignin are ordered mesoporous carbons (MCs), which have been used in a wide range of applications including energy storage, catalysis, drug delivery, and pollutant removal. The preparation of ordered MCs from lignin for energy storage provides a potential approach to generate high economic benefit from low-value lignin, whilst contributing to the development of high-performance energy storage technologies.

However, there remains a huge challenge in the current templating synthesis techniques for ordered MCs, which requires seeking more promising soft templates. Templating synthesis, especially soft-templating, proves to be an effective as well as the only method so far to fabricate highly ordered MCs from lignin with tuneable pore diameters. In most practices, the prevailing block copolymer templates (such as Pluronic F127 and P123) were decomposed to generate pore channels during calcination thus they were barely recyclable; this has increased

the barrier to produce MCs from lignin at large scale as block copolymers are relatively expensive. Therefore, it is critical to seek more promising soft templates that possess excellent recyclability without sacrificing the templating effectiveness.

During soft-templating synthesis of MCs, phenolic polymers have been regarded as a preliminary model polymer for lignin to some extent. Soft-templating synthesis was first applied to phenolic polymers as carbon precursors then extended to lignin. Moving forward from phenolic polymers to lignin, phenolic polymers show great similarity with lignin for both being complicated aromatic polymers but with less complicated structures, thus they are less recalcitrant than lignin. Therefore, when seeking new soft templates, it could be a practical strategy to first start with the cross-linked phenolic polymers as carbon precursor (and lignin model polymer). Once viable, the successful implementation can be transferred to lignin precursors and eventually achieve the exploitation of added value from lignin.

Long-chain ionic liquids (ILs) due to their excellent amphiphilicity have been widely used for templating synthesis of various nanomaterials. The use of amphiphilic ILs to fabricate MCs remains at an initial stage. So far, no highly ordered MCs were reported yet by employing IL templates mostly because of the lack of fundamental understanding of the mechanism of IL-templated synthesis. Nevertheless, one notable advantage of ILs is that they can be easily extracted out from IL/polymer composites before calcination, thereby achieving the recycling and reuse of templating agents. Thus, long-chain ILs become the candidate template in this work to fabricate ordered MCs.

The overall aim of this work is to systematically explore the feasibility of employing amphiphilic ILs as the recyclable template to fabricate ordered MCs for supercapacitors. With the new IL templates, there will be four major steps in the proposed templating process including 1) the self-assembly of IL template and carbon precursor in solvent, 2) cross-linking of carbon precursor to obtain mesoporous polymer framework, 3) recycling of IL templates by extraction, and 4) carbonisation. Considering the lack of fundamental understanding on the mechanism of IL-templated synthesis of MCs, this thesis aims to first reveal the templating mechanism with the assistance of multi-scale investigation, involving CG MD simulations, DFT exploration, and experimental validation. Based on the theoretical knowledge on the templating mechanism, practical explorations on the preparation of ordered MCs for supercapacitors will be carried out, with a special purpose to identify key factors in major steps of the templating process that can influence the fabrication of highly ordered MCs and their electrochemical performance. Specifically, the role of cross-linking in the

formation of highly ordered mesopores will be studied, aiming to point out how to choose a suitable cross-linker for the templating synthesis. Then the influence of IL templates themselves and the recycling of IL templates on the pore architecture, surface functionality, and electrochemical performance of resulting MCs will be highlighted to provide insight into how to fabricate ordered MCs by employing ILs as the recyclable templates.

1.3. Outline of the thesis

To achieve the overall aim and based on the major steps of the proposed templating synthesis process, this thesis is comprised of six chapters.

Chapter 1 first summarises recent progress on the templating synthesis and typical applications of ordered MCs, especially from lignin, proving that soft-templating synthesis is the only effective route so far to prepare lignin-derived ordered MCs and that cross-linked phenolic polymers can be regarded as lignin model polymer during templating synthesis. Then, an overview of the use of ILs in the pretreatment of lignin and the preparation of MCs is provided, pointing out the high potential of amphiphilic ILs as the recyclable template for templating synthesis of MCs. Finally, the use of MD simulations in the study of lignin properties and the self-assembly of amphiphilic ILs is described briefly, which indicates that MD simulations can serve as an assisting tool to understand the mechanism of IL-templated synthesis of MCs.

Figure 1.7 depicts a simplified scheme of the proposed method to prepare MCs by employing amphiphilic ILs as the recyclable template. The self-assembly of IL template and carbon precursor in solution is the first process. This thesis will first introduce the investigations of the self-assembly mechanism by a combination of computational and experimental techniques. *Chapter 2* explores the selection of a suitable type of force fields for simulation and their reliability for studying the self-assembly mechanism, which can be regarded as a benchmark for the ensuing chapter. In *Chapter 3*, the self-assembly mechanism of the IL template in the presence of carbon precursors will be investigated in detail, where the morphological evolution process and the spatial correlation between IL template and carbon precursor will be studied by performing CG MD simulations, DFT calculations, and experimental validation. The results from *Chapter 3* point out the direction towards the manipulation of IL morphologies and the selection of carbon precursor. *Chapter 4* systematically studies the role of cross-linking reactions of phenolic precursors, especially different cross-linkers, in pore architectures, surface functionality, and electrochemical

performance of the resulting MCs, thereby guiding the selection of a suitable cross-linker for IL-templated synthesis of MCs. Based on the results from earlier chapters, *Chapter 5* systematically explores the use of amphiphilic IL templates to prepare MCs for energy storage from lignin model polymer, phloroglucinol-glyoxal-polymer, identifies the most crucial factors that influence the templating synthesis, and assesses the recyclability of the selected IL templates. In the end, *Chapter 6* mainly summarises this thesis with suggestions on the future work provided.

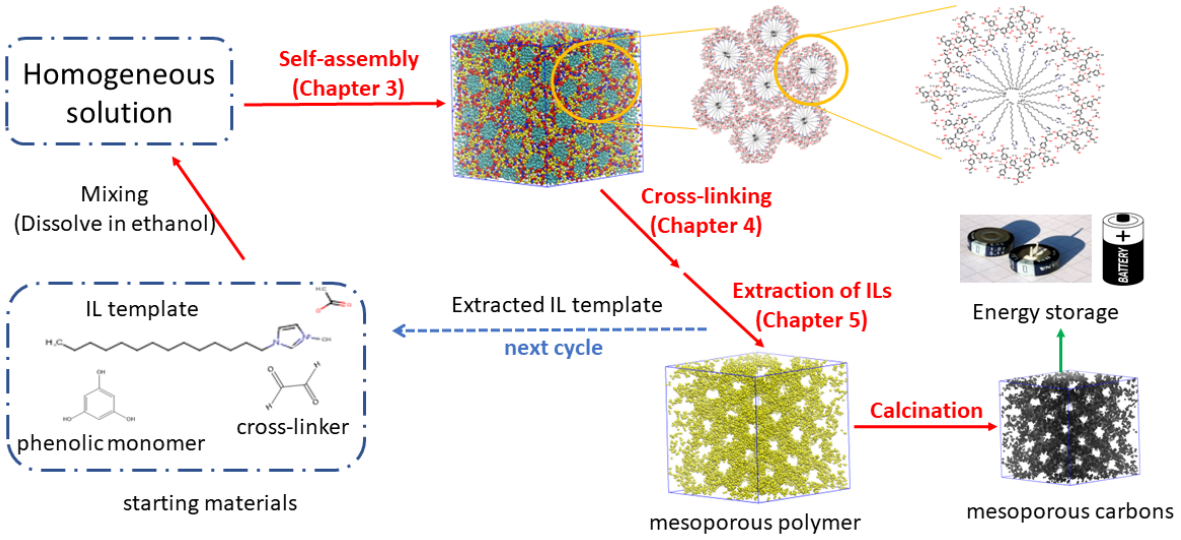

Figure 1.7. Scheme of the proposed method using amphiphilic ILs to fabricate MCs for energy storage.

1.4. References

1 M. L. Zhang, Y. T. Fan, Y. Xing, C. M. Pan, G. S. Zhang and J. J. Lay, *Biomass and Bioenergy*, 2007, **31**, 250–254.

2 T. Saito, R. H. Brown, M. A. Hunt, D. L. Pickel, J. M. Pickel, J. M. Messman, F. S. Baker, M. Keller and A. K. Naskar, *Green Chem.*, 2012, **14**, 3295–3303.

3 S. Chatterjee and T. Saito, *ChemSusChem*, 2015, 8, 3941–3958.

4 D. Montané, V. Torné-Fernández and V. Fierro, *Chem. Eng. J.*, 2005, **106**, 1–12.

5 Y. Song, J. Liu, K. Sun and W. Xu, *RSC Adv.*, 2017, **7**, 48324–48332.

6 J. M. Rosas, R. Berenguer, M. J. Valero-Romero, J. Rodríguez-Mirasol and T. Cordero, *Front. Mater.*, 2014, **1**, 1–17.

7 E. Dorrestijn, L. J. J. Laarhoven, I. W. C. E. Arends and P. Mulder, *J. Anal. Appl. Pyrolysis*, 2000, **54**, 153–192.

8 H.-R. Bjørsvik and F. Minisci, *Org. Process Res. Dev.*, 1999, **3**, 330–340.

9 M. R. Benzigar, S. N. Talapaneni, S. Joseph, K. Ramadass, G. Singh, J. Scaranto, U. Ravon, K. Al-Bahily and A. Vinu, *Chem. Soc. Rev.*, 2018, **47**, 2680–2721.

10 A. Eftekhari and Z. Fan, *Mater. Chem. Front.*, 2017, 1, 1001–1027.

11 M. S. Attia, M. Y. Hassaballah, M. A. Abdelqawy, M. Emad-Eldin, A. K. Farag, A. Negida, H. Ghaith and S. E. Emam, *Drug Dev. Ind. Pharm.*, 2021, **47**, 1029–1037.

12 W. Li, J. Liu and D. Zhao, *Nat. Rev. Mater.*, 2016, **1**, 16023.

13 R. Ryoo, S. H. Joo, M. Kruk and M. Jaroniec, Ordered mesoporous carbons.

14 J. S. Beck, J. C. Vartuli, W. J. Roth, M. E. Leonowicz, C. T. Kresge, K. D. Schmitt, C. T. W. Chu, D. H. Olson, E. W. Sheppard, S. B. McCullen, J. B. Higgins and J. L. Schlenker, *J. Am. Chem. Soc.*, 1992, **114**, 10834–10843.

15 R. Ruiz-Rosas, M. J. Valero-Romero, D. Salinas-Torres, J. Rodríguez-Mirasol, T. Cordero, E. Morallón and D. Cazorla-Amorós, *ChemSusChem*, 2014, **7**, 1458–1467.

16 D. Salinas-Torres, R. Ruiz-Rosas, M. J. Valero-Romero, J. Rodríguez-Mirasol, T. Cordero, E. Morallón and D. Cazorla-Amorós, *J. Power Sources*, 2016, **326**, 641–651.

17 D. Saha, Y. Li, Z. Bi, J. Chen, J. K. Keum, D. K. Hensley, H. A. Grappe, H. M. Meyer, S. Dai, M. P. Paranthaman and A. K. Naskar, *Langmuir*, 2014, **30**, 900–910.

18 M. Ago, M. Borghei, J. S. Haataja and O. J. Rojas, *RSC Adv.*, 2016, **6**, 85802–85810.

19 S. Herou, M. C. Ribadeneyra, R. Madhu, V. Araullo-Peters, A. Jensen, P. Schlee and M. Titirici, *Green Chem.*, 2019, **21**, 550–559.

20 H. Li, D. Yuan, C. Tang, S. Wang, J. Sun, Z. Li, T. Tang, F. Wang, H. Gong and C. He,

Carbon N. Y., 2016, **100**, 151–157.

21 T. Jiang, Q. Sun, W. Xu, G. Zhao and J. Shi, *Int. J. Electrochem. Sci.*, 2018, **13**, 11480–11490.

22 F. Chen, W. Zhou, H. Yao, P. Fan, J. Yang, Z. Fei and M. Zhong, *Green Chem.*, 2013, **15**, 3057–3063.

23 B. Zhou, Z. Li, W. Liu, Y. Shao, X. Ren, C. Lv and Q. Liu, *Electrochim. Acta*, 2021, **398**, 139307.

24 Y. Liang, X. Liu and X. Qi, *Int. J. Biol. Macromol.*, 2022, **213**, 610–620.

25 H. Qin, R. Jian, J. Bai, J. Tang, Y. Zhou, B. Zhu, D. Zhao, Z. Ni, L. Wang, W. Liu, Q. Zhou and X. Li, *ACS Omega*, 2018, **3**, 1350–1356.

26 L. Gan, L. Lyu, T. Shen and S. Wang, *Appl. Catal. A Gen.*, 2019, **574**, 132–143.

27 S. Wang, L. Lyu, G. Sima, Y. Cui, B. Li, X. Zhang and L. Gan, *Korean J. Chem. Eng.*, 2019, **36**, 1042–1050.

28 X. Wang, M. Qiu, Y. Tang, J. Yang, F. Shen, X. Qi and Y. Yu, *Int. J. Biol. Macromol.*, 2021, **187**, 232–239.

29 X. Wang, M. Qiu, R. L. Smith, J. Yang, F. Shen and X. Qi, *ACS Sustain. Chem. Eng.*, 2020, **8**, 18157–18166.

30 X. Wang, X. Liu, R. L. Smith, Y. Liang and X. Qi, *Green Chem.*, 2021, **23**, 8632–8642.

31 X. Liu, Y. Wang, R. L. Smith, L. Liu and X. Qi, *Sci. Total Environ.*, 2022, **836**, 155640.

32 D. Saha, E. A. Payzant, A. S. Kumbhar and A. K. Naskar, *ACS Appl. Mater. Interfaces*, 2013, **5**, 5868–5874.

33 D. Saha, K. E. Warren and A. K. Naskar, *Carbon N. Y.*, 2014, **71**, 47–57.

34 A. Xie, J. Dai, X. Chen, P. Ma, J. He, C. Li, Z. Zhou and Y. Yan, *Chem. Eng. J.*, 2016, **304**, 609–620.

35 W. Ge, Z. Zhou, P. Zhang, Q. Zhang, Z. Cao, R. Zhang, Y. Yan and J. Dai, *J. Ind. Eng. Chem.*, 2018, **66**, 456–467.

36 W. Zhao, X. Lin, H. Cai, T. Mu and X. Luo, *Ind. Eng. Chem. Res.*, 2017, **56**, 12745–12754.

37 M. A. Jedrzejczyk, J. Engelhardt, M. R. Djokic, V. Bliznuk, K. M. Van Geem, A. Verberckmoes, J. De Clercq and K. V. Bernaerts, *ACS Omega*, 2021, **6**, 15222–15235.

38 A. Beaucamp, M. Culebras and M. N. Collins, *Green Chem.*, 2021, **23**, 5696–5705.

39 A. M. Puziy, O. I. Poddubnaya and O. Sevastyanova, *Top. Curr. Chem.*, 2018, 95–128.

40 E. K. Pye and J. H. Lora, *Tappi J.*, 1991, 74, 113–118.

41 M. J. Valero-Romero, E. M. Márquez-Franco, J. Bedia, J. Rodríguez-Mirasol and T. Cordero, *Microporous Mesoporous Mater.*, 2014, **196**, 68–78.

42 C. M. Fierro, J. Górka, J. A. Zazo, J. J. Rodriguez, J. Ludwinowicz and M. Jaroniec, *Carbon N. Y.*, 2013, **62**, 233–239.

43 Z. Chang, J. Dai, A. Xie, J. He, R. Zhang, S. Tian, Y. Yan, C. Li, W. Xu and R. Shao, *Ind. Eng. Chem. Res.*, 2017, **56**, 9367–9375.

44 A. Xie, J. Dai, Y. Chen, N. Liu, W. Ge, P. Ma, R. Zhang, Z. Zhou, S. Tian, C. Li and Y. Yan, *Adv. Powder Technol.*, 2019, 30, 170–179.

45 J. Dai, A. Xie, R. Zhang, W. Ge, Z. Chang, S. Tian, C. Li and Y. Yan, *J. Mol. Liq.*, 2018, **256**, 203–212.

46 Yang Zhang, Baojun Yu, Jie Zhang, Xiaohui Ding, Jingxuan Zeng, Mingming Chen, Chengyang Wang, *CHEMELECTROCHEM*, 2018, **5**, 2142–2149.

47 D. Saha, R. Zacharia and A. K. Naskar, in *Polymer Precursor-Derived Carbon*, 2014, vol. 1173, pp. 61–83.

48 C. Liang and S. Dai, *J. Am. Chem. Soc.*, 2006, **128**, 5316–5317.

49 Z. Li, W. Yan and S. Dai, *Carbon N. Y.*, 2004, **42**, 767–770.

50 C. Liang, K. Hong, G. A. Guiochon, J. W. Mays and S. Dai, *Angew. Chemie - Int. Ed.*, 2004, **43**, 5785–5789.

51 D. Saha, R. Zacharia and A. K. Naskar, in *Polymer Precursor-Derived Carbon*, 2014, vol. 1173, pp. 61–83.

52 S. Wang, G. Sima, Y. Cui, L. Chang and L. Gan, *Mater. Lett.*, 2020, **264**, 127318.

53 Y. Meng, D. Gu, F. Zhang, Y. Shi, L. Cheng, D. Feng, Z. Wu, Z. Chen, Y. Wan, A. Stein and D. Zhao, *Chem. Mater.*, 2006, **18**, 4447–4464.

54 J. Seo, H. Park, K. Shin, S. H. Baeck, Y. Rhym and S. E. Shim, *Carbon N. Y.*, 2014, **76**, 357–367.

55 R. D. Rogers and K. R. Seddon, *Science (80-.).*, 2003, **302**, 792–793.

56 S. Shahzad, A. Shah, E. Kowsari, F. J. Iftikhar, A. Nawab, B. Piro, M. S. Akhter, U. A. Rana and Y. Zou, *Glob. Challenges*, 2019, **3**, 1800023.

57 L. Yu and G. Z. Chen, *Front. Chem.*, 2019, **7**, 272.

58 K. Goossens, K. Lava, C. W. Bielawski and K. Binnemans, *Chem. Rev.*, 2016, **116**, 4643–4807.

59 X. Kang, X. Sun and B. Han, *Adv. Mater.*, 2016, **28**, 1011–1030.

60 A. Jordan and N. Gathergood, *Chem. Soc. Rev.*, 2015, **44**, 8200–8237.

61 N. Ranjbar Sahraie, J. P. Paraknowitsch, C. Göbel, A. Thomas and P. Strasser, *J. Am.*

Chem. Soc., 2014, **136**, 14486–14497.

62 V. I. Pârvulescu and C. Hardacre, *Chem. Rev.*, 2007, **107**, 2615–2665.

63 M. Kar, O. Tutusaus, D. R. MacFarlane and R. Mohtadi, *Energy Environ. Sci.*, 2019, **12**, 566–571.

64 Q. Yang, Z. Zhang, X. G. Sun, Y. S. Hu, H. Xing and S. Dai, *Chem. Soc. Rev.*, 2018, **47**, 2020–2064.

65 X. Zhu, C. Peng, H. Chen, Q. Chen, Z. K. Zhao, Q. Zheng and H. Xie, *ChemistrySelect*, 2018, **3**, 7945–7962.

66 Y. Qiao, W. Ma, N. Theyssen, C. Chen and Z. Hou, *Chem. Rev.*, 2017, 117, 6881–6928.

67 M. Watanabe, M. L. Thomas, S. Zhang, K. Ueno, T. Yasuda and K. Dokko, *Chem. Rev.*, 2017, 117, 7190–7239.

68 C. Dai, J. Zhang, C. Huang and Z. Lei, *Chem. Rev.*, 2017, 117, 6929–6983.

69 D. R. MacFarlane, M. Forsyth, P. C. Howlett, M. Kar, S. Passerini, J. M. Pringle, H. Ohno, M. Watanabe, F. Yan, W. Zheng, S. Zhang and J. Zhang, *Nat. Rev. Mater.*, 2016, 1.

70 R. Prado, A. Brandt, X. Erdocia, J. Hallet, T. Welton and J. Labidi, *Green Chem.*, 2016, **18**, 834–841.

71 R. P. Swatloski, S. K. Spear, J. D. Holbrey and R. D. Rogers, *J. Am. Chem. Soc.*, 2002, **124**, 4974–4975.

72 P. Mäki-Arvela, I. Anugwom, P. Virtanen, R. Sjöholm and J. P. Mikkola, *Ind. Crops Prod.*, 2010, 32, 175–201.

73 T. J. Szalaty, Ł. Klapiszewski and T. Jesionowski, *J. Mol. Liq.*, 2020, **301**, 1–30.

74 I. Kilpeläinen, H. Xie, A. King, M. Granstrom, S. Heikkinen and D. S. Argyropoulos, *J. Agric. Food Chem.*, 2007, **55**, 9142–9148.

75 A. Brandt, L. Chen, B. E. Van Dongen, T. Welton and J. P. Hallett, *Green Chem.*, 2015, **17**, 5019–5034.

76 Y. Pu, N. Jiang and A. J. Ragauskas, *J. Wood Chem. Technol.*, 2007, **27**, 23–33.

77 O. Merino, G. Fundora-Galano, R. Luque and R. Martínez-Palou, *ACS Sustain. Chem. Eng.*, 2018, **6**, 4122–4129.

78 D. Glas, C. Van Doorslaer, D. Depuydt, F. Liebner, T. Rosenau, K. Binnemans and D. E. De Vos, *J. Chem. Technol. Biotechnol.*, 2015, **90**, 1821–1826.

79 F. J. V. Gschwend, A. Brandt, C. L. Chambon, W.-C. Tu, L. Weigand and J. P. Hallett, *J. Vis. Exp.*, 2016, 54246.

80 Y. Qu, H. Luo, H. Li and J. Xu, *Biotechnol. Reports*, 2015, **6**, 1–7.

81 B. G. Janesko, *Phys. Chem. Chem. Phys.*, 2011, **13**, 11393–11401.

82 A. Casas, J. Palomar, M. V. Alonso, M. Oliet, S. Omar and F. Rodriguez, *Ind. Crops Prod.*, 2012, **37**, 155–163.

83 Y. Zhang, H. He, K. Dong, M. Fan and S. Zhang, *RSC Adv.*, 2017, **7**, 12670–12681.

84 J. Zubeltzu, E. Formoso and E. Rezabal, *J. Mol. Liq.*, 2020, **303**, 112588.

85 G. F. De Gregorio, R. Prado, C. Vriamont, X. Erdocia, J. Labidi, J. P. Hallett and T. Welton, *ACS Sustain. Chem. Eng.*, 2016, **4**, 6031–6036.

86 C. Chen, H. Wang, N. Feng, Y. Wang, H. Wan, J. Ma and G. Guan, *Colloids Surfaces A Physicochem. Eng. Asp.*, 2022, **644**, 128906.

87 H. Zhou, S. Wu, H. Wang, Y. Li, X. Liu and Y. Zhou, *J. Hazard. Mater.*, 2021, **402**, 124023.

88 S. Luo, J. Hu, S. Guo, D. Yu, P. Dong, M. Xu, L. Han, M. Li, Y. Lin, F. Liu, C. Zhang and Y. Zhang, *Nanotechnology*, 2021, **32**, 395701.

89 B. Karimi, F. Mansouri and H. Vali, *ACS Appl. Nano Mater.*, 2020, **3**, 10612–10627.

90 N. Zdolšek, R. P. Rocha, J. Krstić, T. Trtić-Petrović, B. Šljukić, J. L. Figueiredo and M. J. Vujković, *Electrochim. Acta*, 2019, **298**, 541–551.

91 H. Zhou, Y. Zhou, L. Li, Y. Li, X. Liu, P. Zhao and B. Gao, *ACS Sustain. Chem. Eng.*, 2019, **7**, 9281–9290.

92 D. Liu, L. Dai, X. Lin, J. F. Chen, J. Zhang, X. Feng, K. Müllen, X. Zhu and S. Dai, *Adv. Mater.*, 2019, **31**, 1804863.

93 J. S. Lee, X. Wang, H. Luo, G. A. Baker and S. Dai, *J. Am. Chem. Soc.*, 2009, **131**, 4596–4597.

94 S. Zhao, Y. Zhang, J. Fang, H. Zhang, Y. Wang, Y. Zhou, W. Chen and C. Zhang, *ACS Sustain. Chem. Eng.*, 2018, **6**, 8291–8299.

95 M. Rafiee, B. Karimi and H. Shirmohammadi, *Electrocatalysis*, 2018, **9**, 632–639.

96 X. Zhao, S. Li, H. Cheng, J. Schmidt and A. Thomas, *ACS Appl. Mater. Interfaces*, 2018, **10**, 3912–3920.

97 Y. Su, H. Wang, J. Zhao, M. H. Rummeli, Y. Gao, Y. B. Jiang, L. Zhang and G. Zou, *Electrochim. Acta*, 2018, **280**, 258–265.

98 A. Chen, Y. Li, L. Liu, Y. Yu, K. Xia, Y. Wang and S. Li, *Appl. Surf. Sci.*, 2017, **393**, 151–158.

99 J. Gong, H. Lin, M. Antonietti and J. Yuan, *J. Mater. Chem. A*, 2016, **4**, 7313–7321.

100 B. Haghighi, B. Karimi, M. Tavahodi and H. Behzadneia, *Mater. Sci. Eng. C*, 2015, **52**,

219–224.

101 Y. She, Z. Lu, M. Ni, L. Li and M. K. H. Leung, *ACS Appl. Mater. Interfaces*, 2015, **7**, 7214–7221.

102 B. E. Wilson, S. He, K. Buffington, S. Rudisill, W. H. Smyrl and A. Stein, *J. Power Sources*, 2015, **298**, 193–202.

103 S. Zhang, K. Dokko and M. Watanabe, *Chem. Mater.*, 2014, **26**, 2915–2926.

104 S. H. Kazemi, B. Karimi, A. Fashi, H. Behzadnia and H. Vali, *J. Solid State Electrochem.*, 2014, **18**, 2419–2424.

105 B. Karimi, H. Behzadnia and H. Vali, *ChemCatChem*, 2014, **6**, 745–748.

106 S. Zhang, M. S. Miran, A. Ikoma, K. Dokko and M. Watanabe, *J. Am. Chem. Soc.*, 2014, **136**, 1690–1693.

107 N. Fechler, T. P. Fellinger and M. Antonietti, *Adv. Mater.*, 2013, **25**, 75–79.

108 B. Qiu, C. Pan, W. Qian, Y. Peng, L. Qiu and F. Yan, *J. Mater. Chem. A*, 2013, **1**, 6373–6378.

109 A. Chen, Y. Yu, H. Lv, Y. Wang, S. Shen, Y. Hu, B. Li, Y. Zhang and J. Zhang, *J. Mater. Chem. A*, 2013, **1**, 1045–1047.

110 B. Karimi, H. Behzadnia, M. Rafiee and H. Vali, *Chem. Commun.*, 2012, **48**, 2776–2778.

111 F. Hasché, T. P. Fellinger, M. Oezaslan, J. P. Paraknowitsch, M. Antonietti and P. Strasser, *ChemCatChem*, 2012, **4**, 479–483.

112 W. Yang, T. P. Fellinger and M. Antonietti, *J. Am. Chem. Soc.*, 2011, **133**, 206–209.

113 B. J. P. Paraknowitsch, J. Zhang, D. Su, A. Thomas and M. Antonietti, *Adv. Mater.*, 2010, **22**, 87–92.

114 X. Wang and S. Dai, *Angew. Chemie*, 2010, **122**, 6814–6818.

115 M. Hejazifar, O. Lanaridi and K. Bica-Schröder, *J. Mol. Liq.*, 2020, **303**, 112264.

116 J. Xia, J. Di, H. Li, H. Xu, H. Li and S. Guo, *Appl. Catal. B Environ.*, 2016, **181**, 260–269.

117 B. Nagy, E. Geissler and K. László, *Microporous Mesoporous Mater.*, 2020, **294**, 109888.

118 Z. L. Xie and D. S. Su, *Eur. J. Inorg. Chem.*, 2015, **2015**, 1137–1147.

119 M. Zhen, J. Yu and S. Dai, *Adv. Mater.*, 2010, 22, 261–285.

120 B. G. Trewyn, C. M. Whitman and V. S. Y. Lin, *Nano Lett.*, 2004, **4**, 2139–2143.

121 Z. Chen, T. L. Greaves, R. A. Caruso and C. J. Drummond, *J. Mater. Chem.*, 2012, **22**, 10069–10076.

122 H. Kaper and B. Smarsly, in *Zeitschrift fur Physikalische Chemie*, De Gruyter, 2006, vol. 220, pp. 1455–1471.

123 M. aki Murakami, Y. Kaneko and J. ichi Kadokawa, *Carbohydr. Polym.*, 2007, **69**, 378–381.

124 P. Snedden, A. I. Cooper, K. Scott and N. Winterton, *Macromolecules*, 2003, **36**, 4549–4556.

125 K. Matsumoto and T. Endo, *Macromolecules*, 2008, **41**, 6981–6986.

126 Z. L. Xie, R. J. White, J. Weber, A. Taubert and M. M. Titirici, *J. Mater. Chem.*, 2011, **21**, 7434–7442.

127 H. Yang, X. Cui, Y. Deng and F. Shi, *J. Mater. Chem.*, 2012, **22**, 21852–21856.

128 J. M. Vicent-Luna, J. M. Romero-Enrique, S. Calero and J. A. Anta, *J. Phys. Chem. B*, 2017, **121**, 8348–8358.

129 Y. Zhao, S. Gao, J. Wang and J. Tang, *J. Phys. Chem. B*, 2008, **112**, 2031–2039.

130 J. N. A. Canongia Lopes and A. A. H. Pádua, *J. Phys. Chem. B*, 2006, **110**, 3330–3335.

131 I. Goodchild, L. Collier, S. L. Millar, I. Prokeš, J. C. D. Lord, C. P. Butts, J. Bowers, J. R. P. Webster and R. K. Heenan, *J. Colloid Interface Sci.*, 2007, **307**, 455–468.

132 S. S. Sarangi, B. L. Bhargava and S. Balasubramanian, *Phys. Chem. Chem. Phys.*, 2009, **11**, 8745–8751.

133 K. Dong, X. Liu, H. Dong, X. Zhang and S. Zhang, *Chem. Rev.*, 2017, **117**, 6636–6695.

134 B. R. Brooks, R. E. Bruccoleri, B. D. Olafson, D. J. States, S. Swaminathan and M. Karplus, *J. Comput. Chem.*, 1983, **4**, 187–217.

135 W. L. Jorgensen, D. S. Maxwell and J. Tirado-Rives, *J. Am. Chem. Soc.*, 1996, **118**, 11225–11236.

136 A. C. T. Van Duin, S. Dasgupta, F. Lorant and W. A. Goddard, *J. Phys. Chem. A*, 2001, **105**, 9396–9409.

137 L. Petridis and J. C. Smith, *J. Comput. Chem.*, 2009, **30**, 457–467.

138 R. Schulz, B. Lindner, L. Petridis and J. C. Smith, *J. Chem. Theory Comput.*, 2009, **5**, 2798–2808.

139 M. Kuttel, J. W. Brady and K. J. Naidoo, *J. Comput. Chem.*, 2002, **23**, 1236–1243.

140 L. Petridis, R. Schulz and J. C. Smith, *J. Am. Chem. Soc.*, 2011, **133**, 20277–20287.

141 B. Lindner, L. Petridis, R. Schulz and J. C. Smith, *Biomacromolecules*, 2013, **14**, 3390–3398.

142 Y. Zhang, F. Huo, Y. Wang, Y. Xia, X. Tan, S. Zhang and H. He, *Front. Chem.*, 2019, **7**, 1–11.

143 J. Wang, Y. Qian, L. Li and X. Qiu, *ChemSusChem*, 2020, **13**, 4420–4427.

144 L. Zhang and E. J. LeBoeuf, *Org. Geochem.*, 2009, **40**, 1132–1142.

145 J. V. Vermaas, L. Petridis, J. Ralph, M. F. Crowley and G. T. Beckham, *Green Chem.*, 2019, **21**, 109–122.

146 J. V. Vermaas, M. F. Crowley and G. T. Beckham, *ACS Sustain. Chem. Eng.*, 2020, **8**, 17839–17850.

147 M. Mohan, K. Huang, V. R. Pidatala, B. A. Simmons, S. Singh, K. L. Sale and J. M. Gladden, *Green Chem.*, 2022, **24**, 1165–1176.

148 K. Chenoweth, A. C. T. Van Duin and W. A. Goddard, *J. Phys. Chem. A*, 2008, **112**, 1040–1053.

149 E. Salmon, A. C. T. van Duin, F. Lorant, P. M. Marquaire and W. A. Goddard, *Org. Geochem.*, 2009, **40**, 1195–1209.

150 A. Beste, *J. Phys. Chem. A*, 2014, **118**, 803–814.

151 A. Beste, *Energy and Fuels*, 2014, **28**, 7007–7013.

152 T. Zhang, X. Li, X. Qiao, M. Zheng, L. Guo, W. Song and W. Lin, *Energy and Fuels*, 2016, **30**, 3140–3150.

153 E. Adler, *Wood Sci. Technol.*, 1977, **11**, 169–218.

154 T. R. Mattsson, J. M. D. Lane, K. R. Cochrane, M. P. Desjarlais, A. P. Thompson, F. Pierce and G. S. Grest, *Phys. Rev. B*, 2010, **81**, 1–9.

155 T. Zhang, X. Li and L. Guo, *Langmuir*, 2017, **33**, 11646–11657.

156 P. López-Albarrán, A. Pizzi, P. Navarro-Santos, R. Hernández-Esparza and J. Garza, *Int. J. Adhes. Adhes.*, 2017, **78**, 227–233.

157 H. Li, B. Xu, H. Jin, K. Luo and J. Fan, *Fuel Process. Technol.*, 2019, **192**, 203–209.

158 T. Wang, X. Liu, J. Xu, W. Afzal and M. He, *J. CO2 Util.*, 2022, **59**, 101959.

159 Y. L. Wang, B. Li, S. Sarman, F. Mocci, Z. Y. Lu, J. Yuan, A. Laaksonen and M. D. Fayer, *Chem. Rev.*, 2020, 120, 5798–5877.

160 D. Bedrov, J. P. Piquemal, O. Borodin, A. D. Mackerell, B. Roux and C. Schröder, *Chem. Rev.*, 2019, 7940–7995.

161 J. N. Canongia Lopes and A. A. H. Pádua, *Theor. Chem. Acc.*, 2012, 131, 1–11.

162 J. N. C. Lopes, J. Deschamps and A. A. H. Pádua, *J. Phys. Chem. B*, 2004, **108**, 2038–2047.

163 K. Goloviznina, Z. Gong and A. A. H. Padua, *Wiley Interdiscip. Rev. Comput. Mol. Sci.*, 2022, **12**, 1–16.

164 K. Goloviznina, J. N. Canongia Lopes, M. Costa Gomes and A. A. H. Pádua, *J. Chem.*

Theory Comput., 2019, **15**, 5858–5871.

165 K. Goloviznina, Z. Gong, M. F. Costa Gomes and A. A. H. Pádua, *J. Chem. Theory Comput.*, 2021, **17**, 1606–1617.

166 K. Goloviznina, Z. Gong and A. A. H. Padua, *Wiley Interdiscip. Rev. Comput. Mol. Sci.*, 2022, **12**, 1–16.

167 O. Borodin, *J. Phys. Chem. B*, 2009, **113**, 11463–11478.

168 B. Doherty, X. Zhong and O. Acevedo, *J. Phys. Chem. B*, 2018, **122**, 2962–2974.

169 B. L. Bhargava, Y. Yasaka and M. L. Klein, *Chem. Commun.*, 2011, **47**, 6228–6241.

170 M. Salanne, *Phys. Chem. Chem. Phys.*, 2015, **17**, 14270–14279.

171 R. Vanyúr, L. Biczók and Z. Miskolczy, *Colloids Surfaces A Physicochem. Eng. Asp.*, 2007, **299**, 256–261.

172 E. A. Crespo, N. Schaeffer, J. A. P. Coutinho and G. Perez-Sanchez, *J. Colloid Interface Sci.*, 2020, **574**, 324–336.

173 K. Dong, X. Liu, H. Dong, X. Zhang and S. Zhang, *Chem. Rev.*, 2017, 117, 6636–6695.

174 M. A. Firestone, P. G. Rickert, S. Seifert and M. L. Dietz, *Inorganica Chim. Acta*, 2004, **357**, 3991–3998.

175 B. L. Bhargava and M. L. Klein, *J. Phys. Chem. A*, 2009, **113**, 1898–1904.

176 B. L. Bhargava and M. L. Klein, *J. Phys. Chem. B*, 2009, **113**, 9499–9505.

177 B. L. Bhargava and M. L. Klein, *Soft Matter*, 2009, **5**, 3475–3480.

178 J. M. Otero-Mato, V. Lesch, H. Montes-Campos, J. Smiatek, D. Diddens, O. Cabeza, L. J. Gallego and L. M. Varela, *J. Mol. Liq.*, 2019, **292**, 1–10.

179 A. A. De Freitas, K. Shimizu, A. M. Smith, S. Perkin and J. N. Canongia Lopes, *J. Chem. Phys.*, 2018, **148**, 1–12.

180 B. L. Bhargava, R. Devane, M. L. Klein and S. Balasubramanian, *Soft Matter*, 2007, **3**, 1395–1400.

181 B. L. Bhargava and M. L. Klein, *Mol. Phys.*, 2009, **107**, 393–401.

182 W. Shinoda, R. Devane and M. L. Klein, *Mol. Simul.*, 2007, **33**, 27–36.

183 B. Li, K. Ma, Y. L. Wang, M. Turesson, C. E. Woodward and J. Forsman, *Phys. Chem. Chem. Phys.*, 2016, **18**, 8165–8173.

184 Y. Wang, S. Feng and G. A. Voth, *J. Chem. Theory Comput.*, 2009, **5**, 1091–1098.

185 Y. Wang, S. Izvekov, T. Yan and G. A. Voth, *J. Phys. Chem. B*, 2006, **110**, 3564–3575.

186 Y. Wang, W. Jiang, T. Yan and G. A. Voth, *Acc. Chem. Res.*, 2007, **40**, 1193–1199.

187 Y. Wang and G. A. Voth, *J. Am. Chem. Soc.*, 2005, **127**, 12192–12193.

188 D. Roy and M. Maroncelli, *J. Phys. Chem. B*, 2010, **114**, 12629–12631.

189 D. Roy, N. Patel, S. Conte and M. Maroncelli, *J. Phys. Chem. B*, 2010, **114**, 8410–8424.

190 C. Merlet, M. Salanne, B. Rotenberg and P. A. Madden, *J. Phys. Chem. C*, 2011, **115**, 16613–16618.

191 C. Merlet, M. Salanne and B. Rotenberg, *J. Phys. Chem. C*, 2012, **116**, 7687–7693.

192 D. Sun and J. Zhou, *AIChE J.*, 2013, **59**, 2630–2639.

193 A. Moradzadeh, M. H. Motevaselian, S. Y. Mashayak and N. R. Aluru, *J. Chem. Theory Comput.*, 2018, **14**, 3252–3261.

194 H. A. Karimi-Varzaneh, F. Müller-Plathe, S. Balasubramanian and P. Carbone, *Phys. Chem. Chem. Phys.*, 2010, **12**, 4714–4724.

195 B. Yoo, B. Jing, S. E. Jones, G. A. Lamberti, Y. Zhu, J. K. Shah and E. J. Maginn, *Sci. Rep.*, 2016, **6**, 1–7.

196 S. J. Marrink, H. J. Risselada, S. Yefimov, D. P. Tieleman and A. H. De Vries, *J. Phys. Chem. B*, 2007, **111**, 7812–7824.

197 D. H. De Jong, S. Baoukina, H. I. Ingólfsson and S. J. Marrink, *Comput. Phys. Commun.*, 2016, **199**, 1–7.

198 J. Zeman, F. Uhlig, J. Smiatek and C. Holm, *J. Phys. Condens. Matter*, 2017, **29**, 1–12.

199 P. Y. Yang, S. P. Ju, H. S. Hsieh, J. Sen Lin and J. Y. Hsieh, *Comput. Mater. Sci.*, 2019, **166**, 293–302.

200 N. Schaeffer, G. Pérez-Sánchez, H. Passos, J. R. B. Gomes, N. Papaiconomou and J. A. P. Coutinho, *Phys. Chem. Chem. Phys.*, 2019, **21**, 7462–7473.

Chapter 2

Molecular dynamics simulation of binary ionic liquid systems: a benchmark study

2.1. Introduction

When employing amphiphilic ionic liquids (ILs) as the recyclable template to prepare mesoporous carbons (MCs), the first step, as described in *Chapter 1*, will be the investigation of the self-assembly process of IL templates in the presence of carbon precursors. The aim is to gain insights into the self-assembly mechanism and identify effective ways to manipulate the morphologies of IL templates. Molecular dynamics (MD) simulation combined with experimental techniques can be powerful tools to achieve this goal as MD simulation provides perspectives for experimental phenomena on an atomistic/molecular level. Therefore, the use of MD simulations has increasingly gained popularity in studying the dynamic and interfacial properties of IL systems, with a range of force fields developed concomitantly such as reactive force fields, classic atomistic force fields, and coarse-grained force fields.

Before carrying out MD simulations to study the self-assembly mechanism of IL templates in the presence of carbon precursors, the first task is to select an appropriate type of force field and to assess its capability to study the self-assembly of IL binary systems in the absence of carbon precursors as a benchmark. This aims to ensure that the chosen type of force field will produce reliable results when to investigate a more complicated system comprising the carbon precursor. Given that this thesis initially anticipates to combine computational design and experimental preparation of MCs as much as is achievable, an ideal force field is expected to be consistently capable for computational simulations throughout all steps of the templating synthesis including the self-assembly, cross-linking, and carbonisation process; reactive force fields are seemingly suitable for this type of task. However, such expectation is impossible to achieve so far due to the limitation of computing capability of supercomputers, even by performing simulations on the state-of-art supercomputers. Therefore, in this thesis, MD simulations focuses on individual steps, especially the self-assembly process which is the first step that directly influences the topology of the resulting MCs. Nevertheless, a range of force fields were still evaluated including reactive, classic atomistic, and coarse-grained force fields, providing guidance for future work once the computing capability of supercomputers is substantially improved to allow the modelling of all steps using a single consistent force field. In this chapter, the benchmark work will stress on two aspects: 1) the feasibility of the chosen force field to predict the morphologies of IL templates in binary systems, and 2) the reliability of the predicted morphological evolution process compared with experimental results with a special focus on the critical micelle concentrations (CMCs) where morphology

transition occurs. Therefore, *Chapter 2* explores the selection of force fields and their reliability for studying the self-assembly mechanism.

2.2. Methodology

2.2.1. Selection of force fields

Reactive force field (ReaxFF). Alongside of the self-assembly process, chemical reactions such as the cross-linking reaction and carbonisation are also involved in the whole proposed preparation method. Reactive force field (ReaxFF) becomes one of the options as it was particularly developed to deal with the breaking and forming of chemical bonds in reactive systems by eschewing explicitly defined chemical bonds whilst using bond order instead.[1,2] Moreover, it has excellent transferability, therefore the same set of parameters are also applicable to study the other processes in the proposed method. In this chapter, two sets of ReaxFF parameters were tested for the benchmark work, one trained particularly for IL tetrabutylphosphonium glycinate[3], labelled as ReaxFF A, and another set of parameters describing well imidazolium compounds[4], labelled as ReaxFF B.

Classic all-atom (AA) force field. This type of force fields defines explicit atoms, bonds, angles, dihedrals, and improper dihedral parameters. One of the typical all-atom force fields particularly developed for ILs is the CL&P force field, which derived from the OPLS-AA/AMBER framework.[5,6] The CL&P force field has been extended to a broad range of IL families including imidazolium, N-alkylpyridinium, ammonium, and tetraalkylphosphonium based ILs with various anion models available.[6] The CL&P force field was chosen as the representative atomistic force field for the benchmark. Note that the current CL&P force field does not incorporate polarisation effect by adding Drude or using a scaled charge, which proves to be more reliable to predict the properties of ILs.

Coarse-grained (CG) force field. By trading acceptable accuracy for speed, CG force field describes a group of atoms into one single bead (one interaction site) by using different mapping strategies whilst anticipating the satisfactory reproduction of all-atom MD results. For imidazolium based ILs, two typical mapping schemes were reported by Bhargava *et al.*[7,8] and Wang *et al.*[9] with the major difference lying in the representation of the imidazolium ring. Bhargava remained its planarity by using three beads thereby producing ideal interfacial properties, whilst Wang described the imidazolium ring with one single bead thereby yielding a better dynamic properties.[10] Since the formation of IL micelles separates the system into

two phases, hydrophobic and hydrophilic phase, Bhargava *et al.*'s mapping scheme highlighting the interfacial properties was employed as the representative CG force field.

2.2.2. Simulation details

The initial configurations were built with packages including Avogadro, VMD TopoTools, and PACKMOL[11]. MD simulations were performed with LAMMPS package[12] on two supercomputing platforms, namely Kelvin at Queen's University Belfast and ARCHIE-WeSt at University of Strathclyde. All MD trajectory files were visualised by VMD.

Reactive MD simulation. Density is one of the rudimentary parameters of liquid system, thus this can assess the accuracy of the chosen force field as the preliminary screening criterion. Therefore, prior to studying the self-assembly of IL aqueous solution, the two sets of chosen ReaxFFs were first examined on pure IL 1-ethyl-3-methylimidazolium acetate, [C_2MIM][OAc], to assess their accuracy in producing density values. For this purpose, 125 pairs of [C_2MIM][OAc] were put randomly into a cubic simulation box with a size of 65 Å. Real units and periodic boundary condition were used. Energy minimisation was first performed by using the steepest descent algorithm with a stopping tolerance of 10^{-6} for both energy and force. Then the NPT ensemble (constant atom numbers, pressure, temperature) with a time step of 0.25 fs was used for the equilibrium run at 298.15 K, 1 atm, where pressure and temperature were constrained by the Martyna-Tuckerman-Tobias-Klein (MTTK) barostat[13,14] and the Nosé-Hoover thermostat[15,16], respectively.

For the investigation of IL morphology in aqueous solution, IL 1-dodecyl-3-methylimidazolium acetate, [C_{12}MIM][OAc], was used for its longer cationic alkyl chain hence superior amphiphilicity. 15 pairs of [C_{12}MIM][OAc] with 480 H_2O molecules were put randomly into a cubic simulation. After energy minimisation, 1 ns of simulation in NPT ensemble was performed to reach equilibrium at 298.15 K, 1 atm, followed by 8.5 ns of simulation in a NVT ensemble (constant atom numbers, volume, temperature) for a production run. Time steps were 0.25 fs and 0.5 fs for NPT and NVT ensemble.

Classic AA-MD simulation. In order to facilitate the observation of the aggregation behaviour of the IL in AA-MD simulation, the IL 1,3-didecyl-2-methylimidazolium chloride, [$C_{10}C_{10}$MIM]Cl, with double alkyl chains was used due to its stronger amphiphilicity with significantly lower CMC than it is found for an IL with a single alkyl chain.[17–20] To avoid the error caused by finite-size effect[21], 5555 water molecules were put randomly into a cubic simulation box of 100 Å in size with 50 and 100 pairs of ILs, respectively. A CL&P force

filed[6] was employed with real units and periodic boundary condition. Energy minimisation was first performed by using the steepest descent algorithm with a stopping tolerance of 10^{-6} for both energy and force. Then the NPT ensemble was used for the equilibrium run at 298.15 K, 1 atm. Pressure and temperature were constrained by the same barostat and thermostat as those in Reactive MD simulation. NVT ensemble was used for the production run with a time step of 1 fs and trajectory was recorded every 1 ps. Long-range Coulomb electrostatic interactions were calculated by Particle-Particle Particle-Mesh (pppm) solver. Cut-off distances for Van Der Waals and Coulomb interactions were 12 Å.

CG MD simulation. Limited by the availability of CG models for ILs, 1-decyl-3-methylimidazolium bromide [C_{10}MIM]Br with a single cationic alkyl chain was used for CG MD simulation. Compared with the double-chain IL used in AA MD simulation, single-chain IL also has an excellent amphiphilicity, but its preparation is overall easier in favour of experimental validation. The coarse-graining scheme for cation followed a "3 to 1" principle, where three heavy atoms with accompanying hydrogen atoms are represented by one single bead. Detailed parameters for non-bonded interactions are shown in Table 2.1 with mapping scheme for IL models depicted in Figure 2.1, which directly follow Bhargava *et al.*'s work[22]. Water bead was a "3 to 1" mapped model developed by Shinoda.[23] Note that scaled-charge beads with a scaling factor of 0.25 was used for IL cation and anion to compensate the missing polarisation effect, thereby providing better predictions of both dynamic and interfacial properties of ILs.[22]

Table 2.1. Lennard-Jones interaction parameters[22].

Bead pair	ε (kJ/mol)	σ (Å)	Bead pair	ε (kJ/mol)	σ (Å)
A-A	0.4422	5.1000	C-F	2.1757	3.9000
A-B	1.5079	5.1000	C-G	0.6276	4.2000
A-C	1.1464	5.0000	C-H	2.0920	3.6500
A-D	0.8715	4.5000	D-D	1.7573	4.5060
A-E	0.6623	4.3000	D-E	1.7573	4.5060
A-F	2.3070	4.1000	D-F	1.8577	4.5455
A-G	0.4184	4.7000	D-G	0.4184	5.0000
A-H	2.0920	3.8500	D-H	1.4226	4.4385
B-B	0.6276	5.4000	E-E	1.7573	4.5060
B-C	0.6811	5.3000	E-F	1.8577	4.5455
B-D	0.7531	5.1000	E-G	0.8368	5.2000
B-E	1.1887	4.3000	E-H	1.4226	4.4385
B-F	1.1522	4.7000	F-F	1.9623	4.5850
B-G	0.5021	4.2500	F-G	0.4184	5.1000
B-H	2.0920	3.8500	F-H	1.5062	4.4780
C-C	0.4184	4.6000	G-G	7.5103	4.0000
C-D	0.8535	3.7600	G-H	3.7447	3.9000
C-E	1.0627	3.7600	H-H	3.7447	4.3710

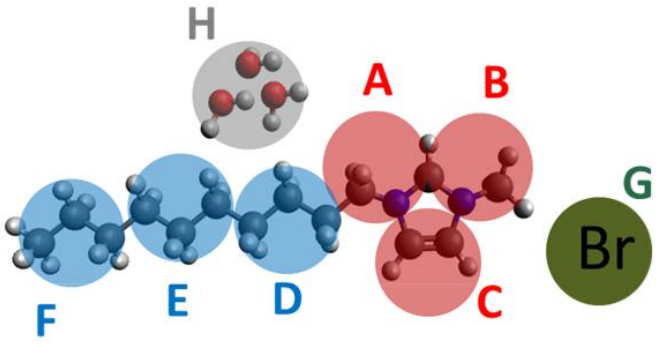

Figure 2.1. CG models for [C_{10}MIM]Br and water[22].

For the simulation procedure, the conjugate gradient algorithm was used for energy minimisation. The rest of procedures were the same with AA-MD simulation, except that pressure was constrained by the Nosé-Hoover barostat. Trajectory was recorded every 5 ps with a time step of 4 fs. Cut-off distances for Van Der Waals and Coulomb interactions were 15 Å. Surface tension (γ) was calculated to get the CMC values by the most common manner which doubled the simulation box in z-direction and measure the difference between the average of the pressure-tensor elements ($\gamma = - L_z/4 (P_{xx} + P_{yy} - 2 P_{zz})$[10,24] as an indicator to predict micelle morphology transitions.[25] The self-diffusion coefficient was obtained by calculating the mean-square displacement from position data.

2.2.3. Experiment

[C_{10}MIM]Br was purchased from Sigma-Aldrich and used as received. Figure 2.2 shows IL solutions with increasing IL concentration. Surface tension of [C_{10}MIM]Br/water aqueous solution was test by using Wilhelmy Plate Method. Each measurement was averaged from three parallel tests. A binary [C_{10}MIM]Br/H_2O system formed a lyotropic liquid crystalline phase at high IL contents; therefore, the experimental measurement of surface tension was limited below 60 wt%.

Figure 2.2. Mixing IL/water solutions at different IL wt% (from left to right): 0 %, 1.08%, 4.07%, 8.04%, 29.80%, 35.73%, 40.32%, 46.00%, and 56.07%.

2.3. Results and discussion

2.3.1. The feasibility of Reactive MD simulation

2.3.1.1. Density

As shown in Figure 2.3, after reaching equilibrium, pure [C_2MIM][OAc] bulk system showed a same equilibrium density fluctuating at 1.12 cm^3/g, regardless of which ReaxFF was used. Compared with the experimental value of 1.10 cm^3/g[26], both sets of reactive force fields showed an error of only 1.8%. This suggest that ReaxFF may have a high accuracy and reliability to study the self-assembly of ILs.

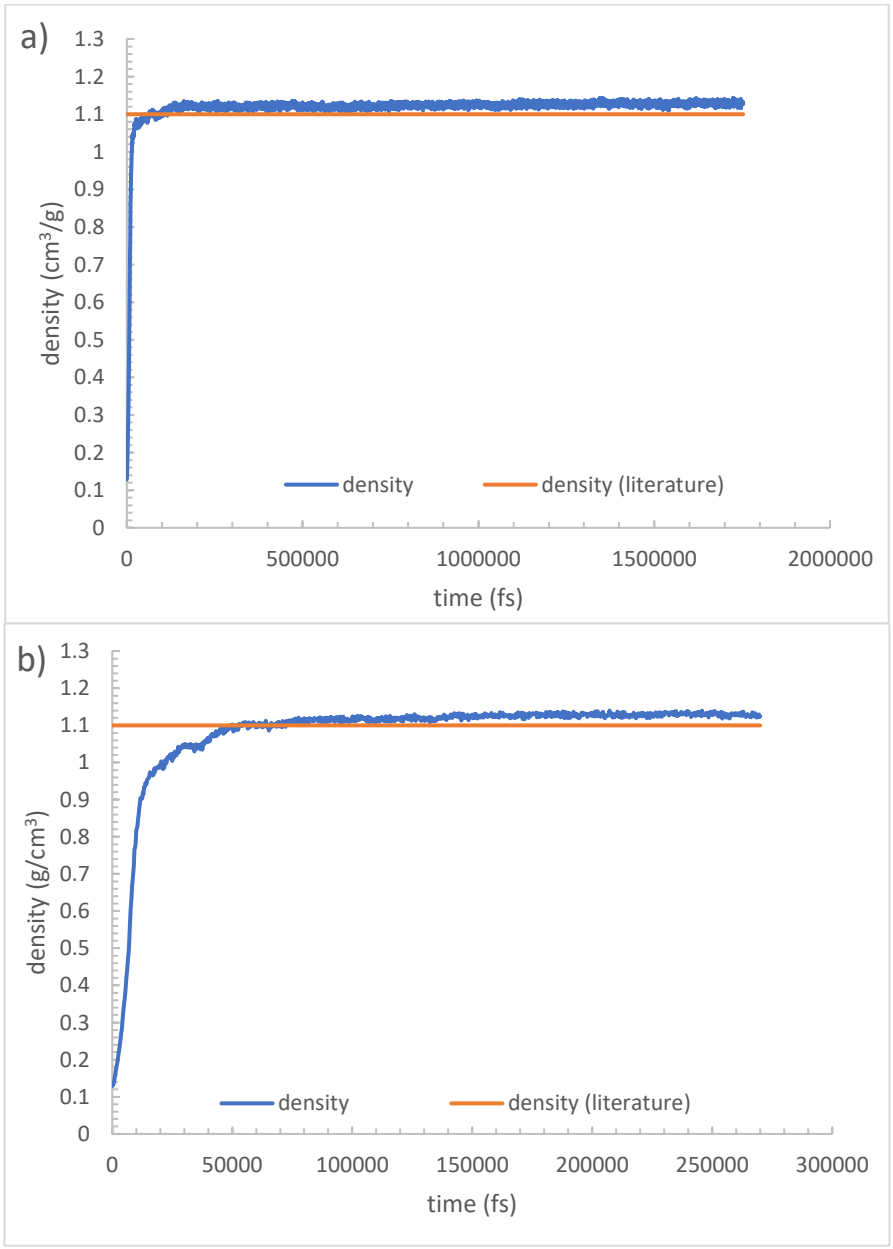

Figure 2.3. Density changes of pure [C_2MIM][OAc] during the equilibrium run of reactive MD simulation with different sets of force fields: a) ReaxFF A and b) ReaxFF B.

2.3.1.2. Investigation of the self-assembly of ILs

The micellization of ILs was test with [C_{12}MIM][OAc] binary system. After 1 ns of simulation in NPT ensemble, the system reached an equilibrium state with a concentration of 0.1 M (Figure 2.4b), followed by 8.5 ns of production run in NVT ensemble. There was no micelle aggregation observed after 8.5 ns, though 5 ns of production run were reported to form micelle clusters by employing OPLS-AA force field[27]. Normally, the micellization of ILs usually occurs spontaneously, longer simulation time is needed until the aggregation forms. However, this poses a big problem for the reactive MD simulation in terms of the computational cost. With 36 CPUs, it took over one week for HPC Kelvin to record 8.5 ns of trajectory during production run. Therefore, it is hardly feasible to employ reactive MD simulation to investigate the self-assembly of ILs due to the huge wall-time consumption, though reactive force field seems applicable for the later process of the proposed preparation method such as the cross-linking and carbonisation process.

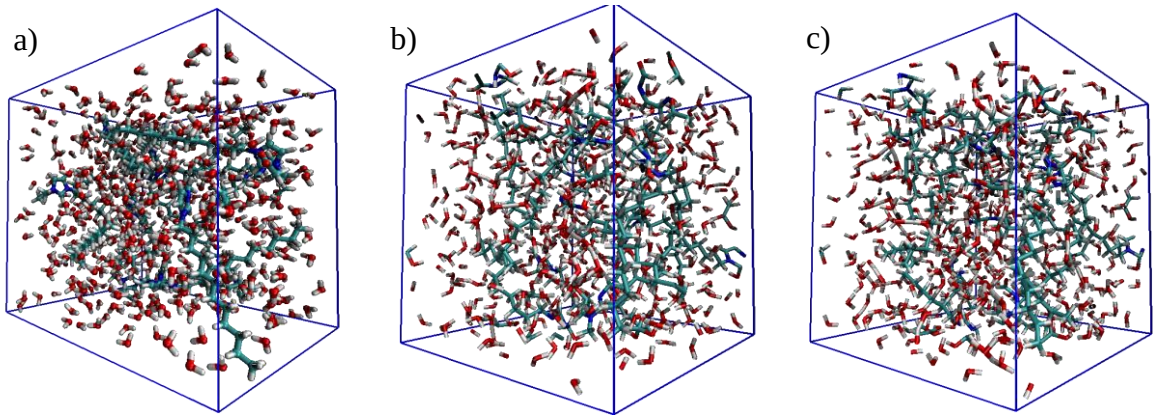

Figure 2.4. Snapshots of 15 pairs of [C_{12}MIM][OAc] in aqueous solution: a) initial configuration (equivalent concentration 0.034 M), b) equilibrium state (IL concentration 0.104 M), and c) after 8.5 ns of production run (0.104 M) (colour code: nitrogen in blue, carbon in cyan, oxygen in red, hydrogen in white).

2.3.2. The aggregation study of ILs with AA MD simulation

Figure 2.5 compares the initial state of [$C_{10}C_{10}$MIM]Cl in mixture before equilibrium and the configuration with IL aggregation after 20 ns of production run. As shown in Figure 2.5b, when the aggregation formed in bulk aqueous solution, the hydrophobic alkyl chains aggregated together forming the micelle cores whilst the imidazolium head groups faced outwards in water phase forming the outer layer of micelle clusters. Due to its unique structure with double alkyl chains, some [$C_{10}C_{10}$MIM]Cl molecules bridged two separate clusters together with each alkyl chain linking with a different cluster and imidazolium ring exposed in the aqueous phase between the two clusters.

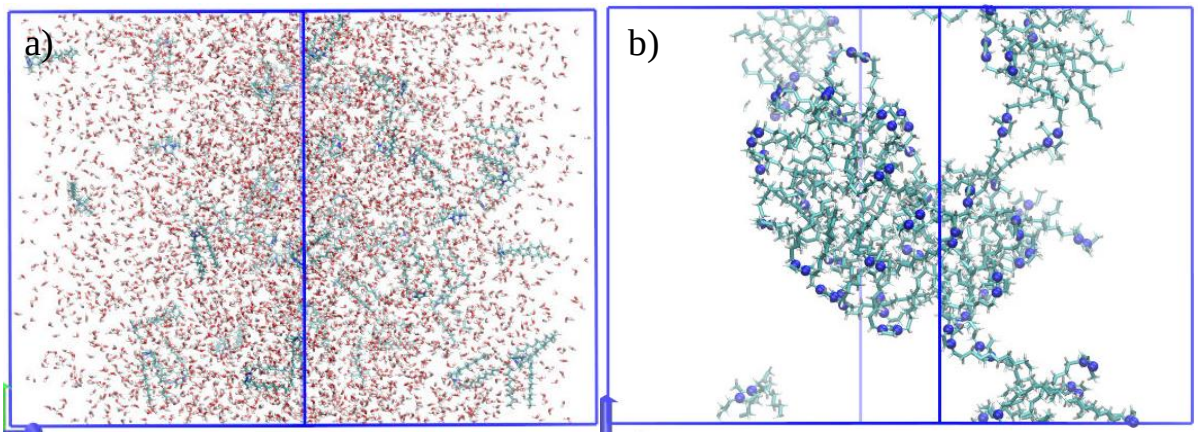

Figure 2.5. a) Initial configuration of 50 pairs of [$C_{10}C_{10}$MIM]Cl in aqueous solution, and b) configuration after 20 ns production run (colour code: nitrogen in blue sphere, carbon in cyan, hydrogen in white. Water and anion are not shown for the ease of visualisation).

Besides, the equilibrated system volume was $2.01 \cdot 10^5$ Å^3 corresponding to a molar concentration of 0.41 M, which is far over the estimated CMC value of 0.40 mM[25]. Figueira-Gonzalez *et al.*[25] studied the self-aggregation and morphological evolution of [$C_{10}C_{10}$MIM]Cl by experimental techniques; a lamellar bilayer phase is expected to form at a molar concentration of 0.41 M. However, the AA-MD simulation only presented the aggregation behaviour after 20 ns production run rather than the formation of lamellar bilayer phase. This suggests that the morphological evolution might remain on-going after 20 ns as the morphology reorganisation usually occurs in microsecond to millisecond.[28] Consequently, longer simulation time is needed to produce the eventual authentic morphology. However, similar with the reactive MD simulation, AA-MD simulation is also computationally intensive and time-consuming despite being much faster than the reactive MD. It still took nearly a week of wall-time to record 20 ns of trajectories with 36 CPUs. Therefore, AA-MD simulations are typically employed in the aggregation study of ILs around the CMC or in the calculation of interfacial and dynamic properties. To study the morphological evolutions of the IL templates, AA-MD simulations will probably also exhibit a limited competency.

2.3.3. CG MD simulation

CG MD simulations were performed for binary systems with an IL content between 1.05% and 83.60% to ensure a full demonstration of all potential morphologies. The simulation details are summarised in Table 2.2.

Table 2.2. Summary of CG MD simulations for [C_{10}MIM]Br/water binary systems.

ILs wt%	Number of water beads	Number of ILs	Morphology	
			298.15 K	343.15 K
1.1%	52840	100	Spherical	Spherical
4.1%	13210	100	Spherical	Spherical
7.8%	6605	100	Spherical	Spherical
30.0%	6605	500	Spherical	Spherical
35.6%	6605	650	Spherical	Spherical
40.5%	6605	800	Spherical	Spherical
45.9%	6605	1000	Spherical/rod-like	Spherical/rod-like
56.0%	6605	1500	Rod-like/cylindrical	Hexagonal cylindrical
63.0%	6605	2000	Partly hexagonal	Hexagonal cylindrical
65.2%	6605	2200	Partly hexagonal	Hexagonal cylindrical
68.0%	6605	2500	Hexagonal cylindrical	Hexagonal cylindrical
71.8%	6605	3000	Hexagonal cylindrical	Transition
74.8%	6605	3500	Transition	Transition
77.3%	6605	4000	Transition	Lamellar bilayer
79.3%	6605	4500	Lamellar bilayer	Lamellar bilayer
81.0%	6605	5000	Lamellar bilayer	Transition
82.0%	6605	5370	Transition	Transition
83.6%	3303	3000	Transition	Transition

2.3.3.1. Morphological evolution

The morphology of IL micelles was first studied at 298.15 K with increasing IL concentration in the binary systems. At a low IL content of 1.1 wt%, the corresponding molar concentration was 0.035 M, higher than the reported CMC values of 0.02 M[29], and spherical micelle clusters formed. Figure 2.6a shows the spherical micelles formed at IL content of 4.1 wt%, where the imidazolium ring head groups were exposed to the aqueous phase whilst the hydrophobic alkyl chains formed the micelle cores. As the IL content increased to 40.5 wt%, the micelle clusters remained spherical, but the total number of micelle clusters showed a steady growth, yielding a much denser solution (Figure 2.6d).

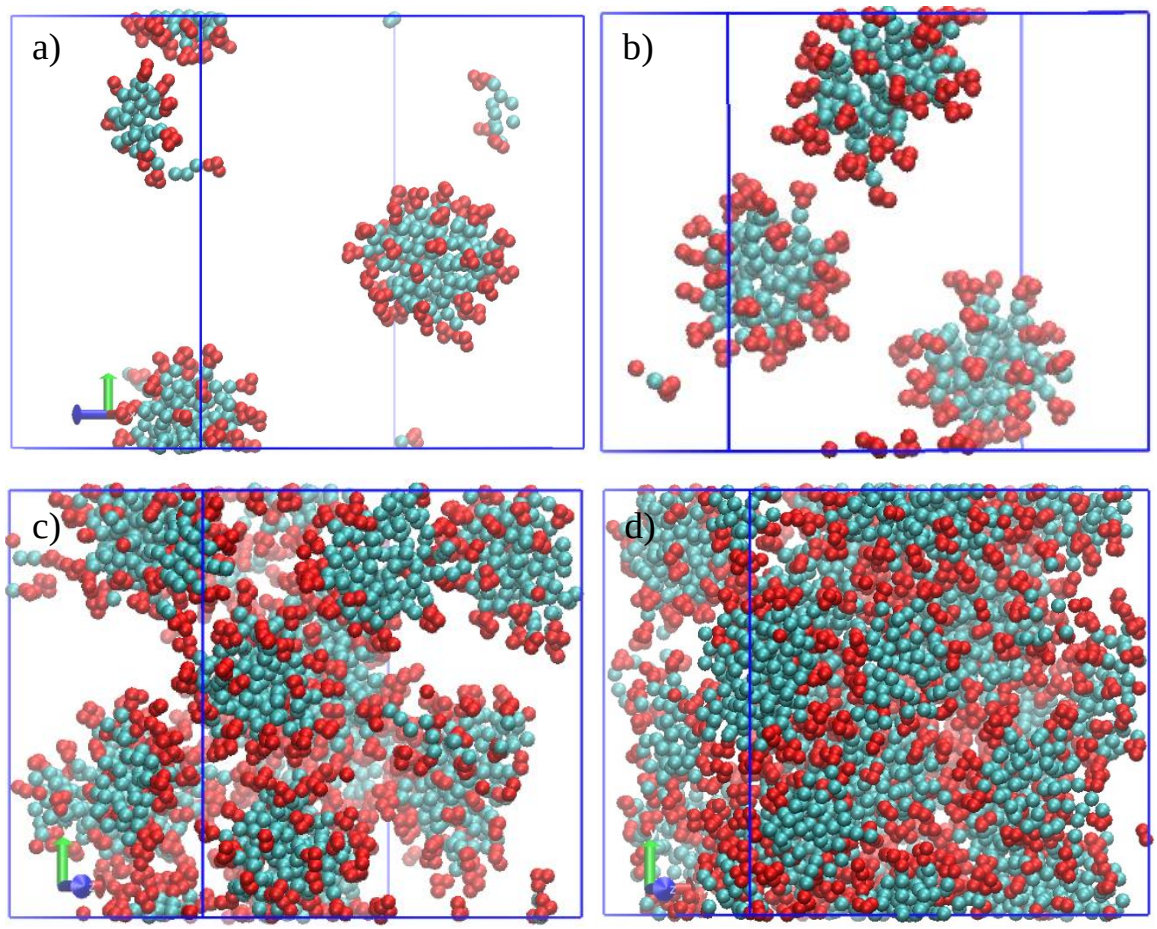

Figure 2.6. Snapshots of micelle morphologies with increasing IL content: a) 4.1 wt%, b) 7.8 wt%, c) 30.0 wt%, and d) 40.5 wt% (Head group: red, alkyl chain: cyan. Water and anion are not shown for the ease of visualisation).

As the IL content further increased to 45.9 wt%, the density of spherical clusters seemed to have reached a maximum and the spherical clusters started to grow longer or merged into short rod-like/cylindrical micelles (Figure 2.7a). As the IL content continued increasing, the cylindrical micelles grew longer and evolved into worm-like cylindrical (Figure 2.7b), partly ordered hexagonal cylindrical structures (Figure 2.7c) at 63.0 wt% and 65.2 wt%, respectively. This range of IL contents can be defined as a transition stage from spherical clusters into hexagonal micelles.

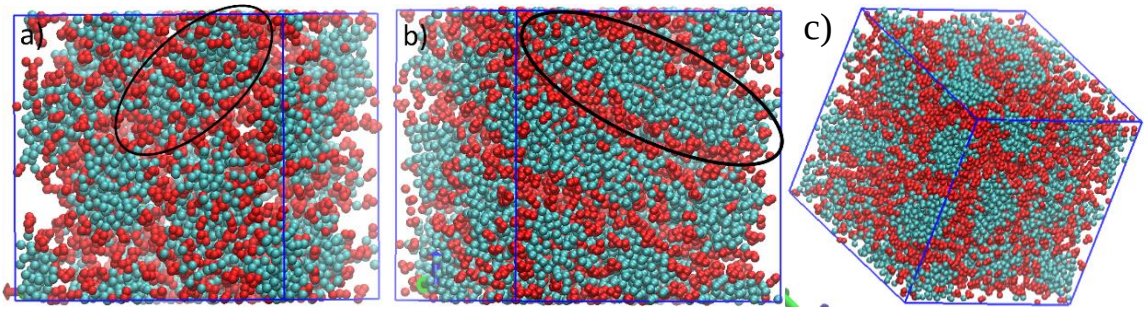

Figure 2.7. Snapshots of micelle morphologies with increasing IL content: a) 45.9 wt%, b) 56.0 wt%, and c) 65.2 wt% (colour code keeps the same).

As shown in Figure 2.8a, highly ordered hexagonal cylindrical micelles formed at IL contents between 68.0 wt% and 71.8 wt%. After a short transition phase, lamellar bilayer structures formed at IL contents between 79.3 wt% and 81.0 wt% (Figure 2.8b), followed by another transition phase at IL content over 82.0 wt%.

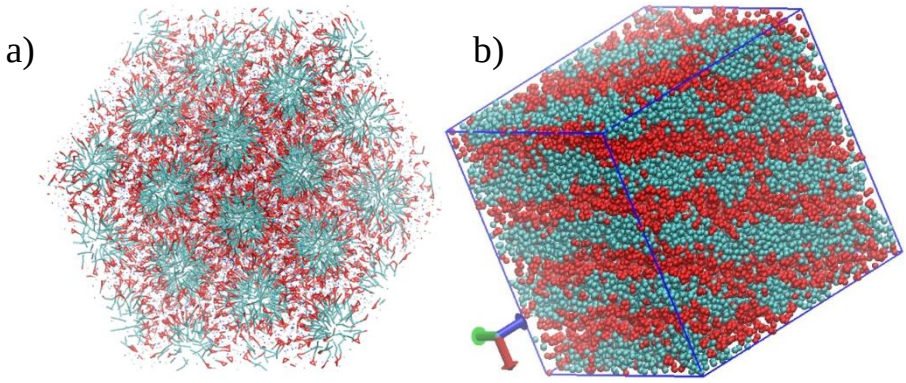

Figure 2.8. a) Hexagonal cylindrical structures at an IL content of 68.0 wt% and b) lamellar bilayer structures at an IL content of 79.3 wt% (colour code keeps the same).

Overall, CG MD simulation is capable to be used on investigating the self-assembly of ILs in mixtures. Three distinct morphologies were successfully identified for [C_{10}MIM]Br/water systems; the corresponding IL contents (IL wt%) for each morphology were predicted as spherical at a range from CMC to 45.9 wt%, hexagonal cylindrical at 68.0 - 71.8 wt%, and lamellar bilayers at 79.3 - 81.0 wt%. In some cases, lamellar-hexagonal dual-phase regions can be observed near surface region of binary IL/water mixtures[30], but such a dual-phase region was not observed in the CG MD simulations for [C_{10}MIM]Br/water binary systems. This is because the CG MD simulation in this work only focused on the bulk system rather than the surface.

2.3.3.2. Density and molar concentration

Figure 2.9 shows the density and molar concentration at different IL contents in the mixture. The predicted molar concentration presented a nearly linear relationship with the IL content

especially at lower contents. The predicted density first increased linearly then dropped to around 1.0 g/cm^3 after hitting a peak value of 1.08 g/cm^3 at 63.0 wt%. The decline in density at higher IL contents could be associated with the formation of lyotropic liquid crystalline phase. Normally, because of the coarse-graining of a group of atoms into a single bead, the dynamic diameter for the ring structures could be slightly exaggerated when developing the models, therefore the CG simulation may produce an underestimated stacking distance resulting in lower densities than realistic values.[31–34] Upon noticing this limitation, it could be more practical to focus on the interfacial properties only rather than the numerical calculations or performing atomistic interaction analysis.

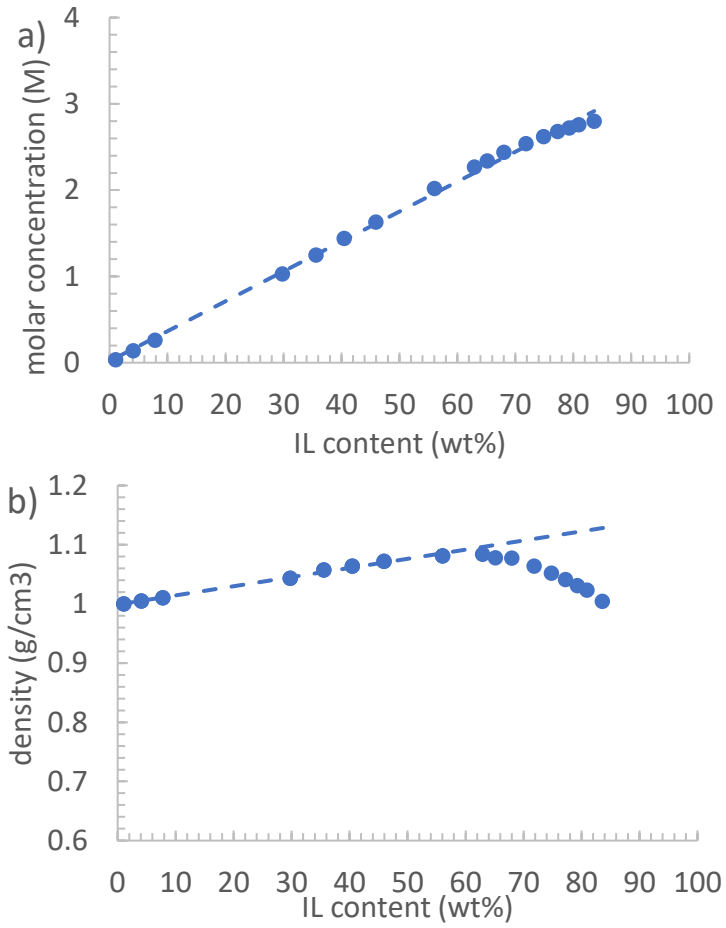

Figure 2.9. Equilibrated molar concentration a) and density b) as functions of IL content in the binary mixture.

2.3.3.3. Surface tension

Due to the formation of lyotropic liquid-crystalline at higher IL contents, experimental measurements were limited for binary systems comprised of IL contents below 60 wt%. Figure 2.10 compares the experimental and simulated surface tensions. As the IL content in aqueous solution increased to 1.1 wt%, experimental value first dropped sharply then

rebounded to 39.44 mN/m at an IL content of 4.1 wt%. This value is close to the reported CMC of 39 mN/m for [C_{10}MIM]Br/water mixture[29], indicating the formation of spherical clusters. As the IL content continued increasing, the measured surface tension by experiments declined steadily before the IL content reached 46.0 wt%. A slight increase was observed at 56.1 wt%, after which the IL binary mixture became highly viscous and lyotropic gels started to form, indicating the formation of cylindrical micelles. According to the simulation (Figure 2.6, Figure 2.7), there was an increase in the total number of spherical clusters before IL content reached 56.0 wt% then spherical micelles evolved into rod-like/cylindrical aggregations. Figure 2.11 shows the snapshots of simulated surface tension calculations at varying concentrations. Amphiphilic IL molecules are expected to preferentially cover the liquid-vapour interface first then form micelles once the concentration reached CMCs. As shown in Figure 2.11a, at IL content of 1.1 wt%, small spherical micelle clusters have already formed in the bulk phase with a single layer of IL molecules covered on each artificial liquid-vapour interface due to the concentration having exceeded CMC. The hydrophobic cationic alkyl chains were exposed to the artificial vapour phase with hydrophilic imidazolium ring being immersed in the bulk aqueous phase. As the IL content increased, the surface coverage of ILs remained similar but the micelle cluster grew larger. At higher contents, hexagonal and lamellar bilayers were observed with one layer of ILs still covering the interface (Figure 2.11g and h). The observation of morphological evolutions from CG MD simulations and experimental studies by measuring surface tension measurement and optical observation of the formation of lyotropic gels over 56.0 wt% indicate that CG MD simulations are capable to reasonably predict the evolution from spherical to cylindrical micelles.

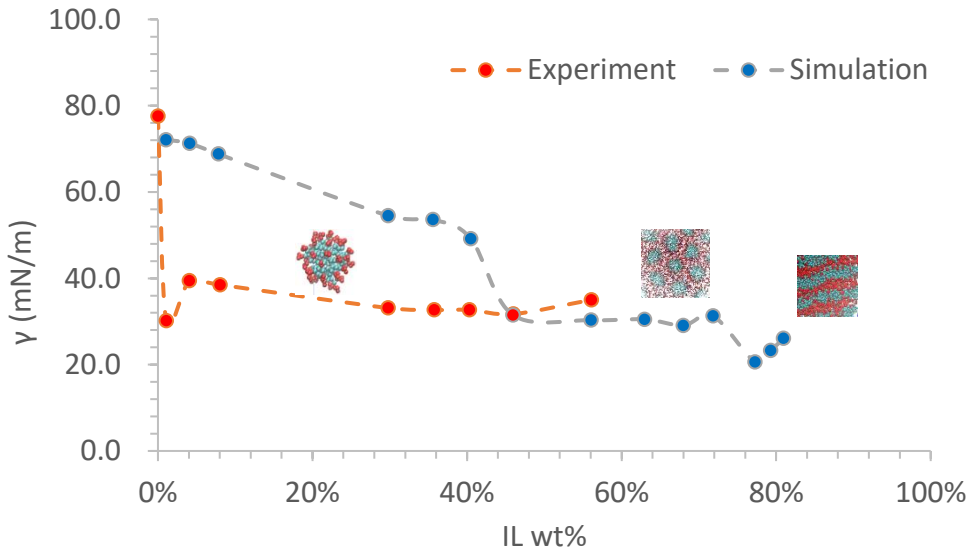

Figure 2.10. Surface tension of IL binary mixtures.

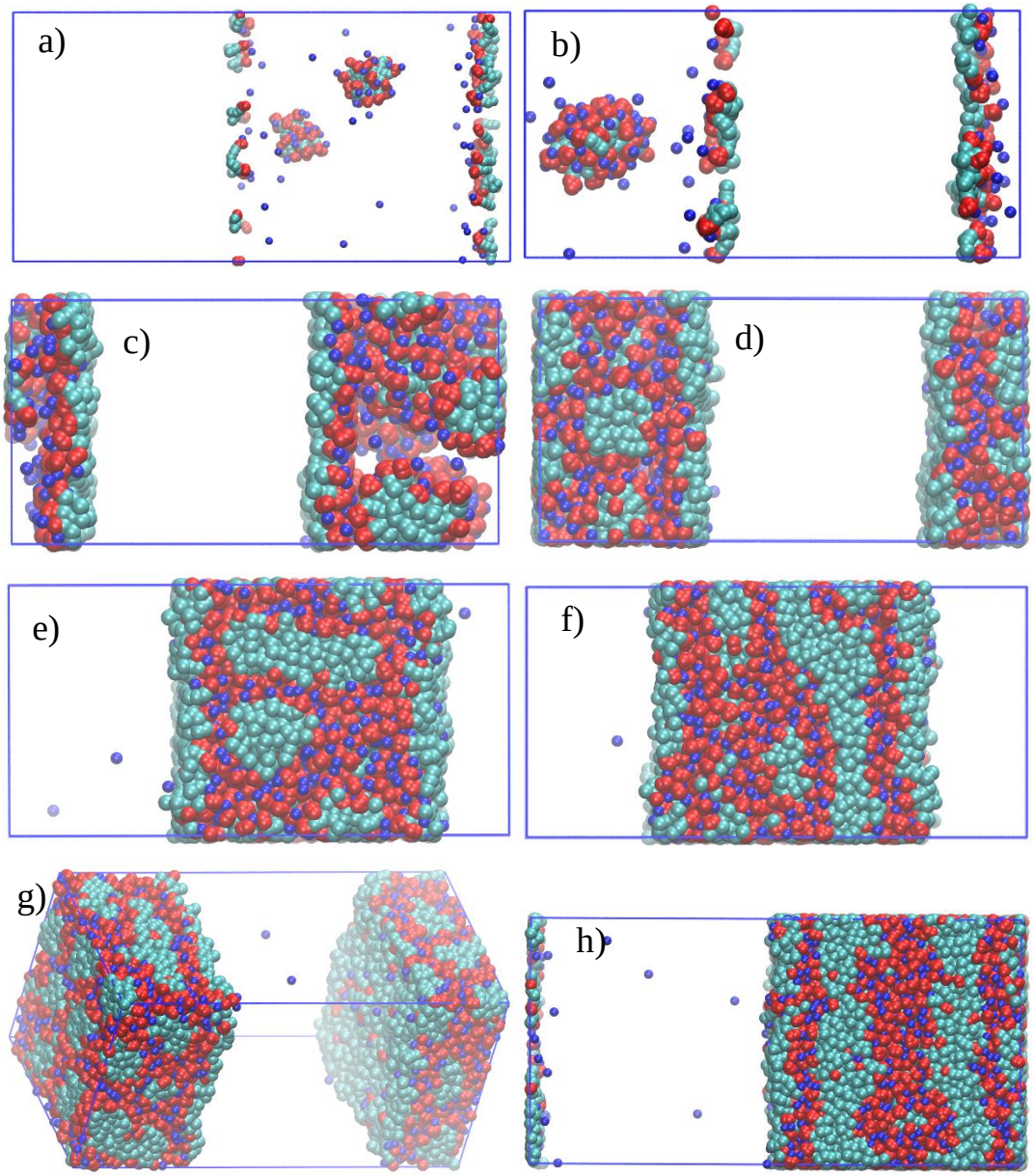

Figure 2.11. Snapshots of simulated surface tension calculations at increasing IL contents: a - h) 1.1, 4.1, 30.0, 45.9, 56.0, 65.2, 68.0, and 79.3 wt%, respectively. (Head group: red, alkyl chain: cyan, anion: blue. Water beads are not shown for the ease of visualisation)

Although the morphology predicted by CG MD simulation were reasonable, surface tension calculated from simulation violates with experimental values. As shown in Figure 2.10, the profile of surface tension obtained from simulation is comprised of three sections corresponding to the three morphologies, namely: a linear declining section for spherical morphology at IL contents below 40.5 wt%, a plateau section for cylindrical morphology between 45.9 - 71.8 wt%, and another drop for lamellar bilayer phase over 77.3 wt%. There is a discrepancy in the surface tension values between simulation and experiment at IL contents below 40.5 wt%. This might be caused by the CG models themselves under unbalanced mixing ratios and by the missing of long-range corrections to surface tension.[35]

During simulation, three water molecules were represented by one single bead thus the detailed interaction was sacrificed. Moreover, the total number of ILs at lower IL contents was very small leaving the simulation box filled dominatingly with water beads. Consequently, such unbalanced mixing ratio between ILs and water beads may have influenced the performance of CG MD simulation and yielded interfacial properties close to water by taking ILs as "impurity", hence the linear decline in the predicted value at low IL contents. A reparameterization or choosing an improved CG model may be needed to produce more reasonable surface tension values by CG MD simulations. Once the appropriate long-range corrections are added to thermodynamic property, especially surface tension, a more rigorous comparison is expected to achieve in the simulated and experimental surface tension values at low IL contents.

2.3.3.4. Self-diffusion coefficient

Self-diffusion coefficient is also an experimental criterion that can be used to indicate morphology transitions.[25] Figure 2.12 shows the calculated self-diffusion coefficient from CG MD simulation with the data labelled in orange, grey, and yellow for expected spherical, hexagonal cylindrical, and lamellar bilayer morphologies, respectively. Based on the profile only, it is highly challenging to identify the morphologies of ILs by using the self-diffusion coefficient from simulation. This might also be stemmed from the CG models themselves as explained in last section. Reliable statistic values may require the use of more sophisticated CG models by adding long-range corrections.

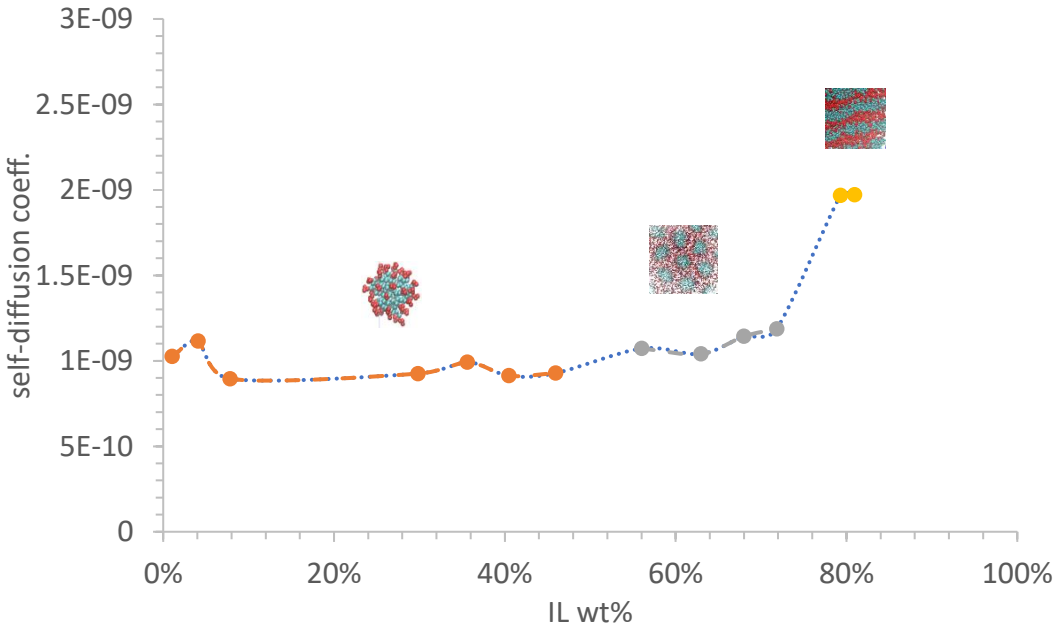

Figure 2.12. Self-diffusion coefficient of IL binary systems obtained from CG MD simulation.

2.3.3.5. The influence of temperature on the morphological evolution

As proposed in the preparation method to use ILs as the recyclable template for the fabrication of MCs, the second step involves the cross-linking reaction of carbon precursor monomers at temperature typical over 70 °C. However, the role of temperature in the morphological evolution of IL templates remains unclear. Therefore, CG MD simulation was also performed under an elevated temperature of 343.15 K. As shown in Figure 2.13 and Table 2.2, with the temperature rising from 298.15 K to 343.15 K, the CMC values, where the morphological transition occurred, shifted to a lower IL content. Particularly, the hexagonal cylindrical and lamellar bilayer phases occurred earlier as the IL content increased in the binary systems. This is likely because higher temperature brings an increased kinetic energy and an accelerated molecule motion, which assists the system to cross energy barrier required by morphology evolution.

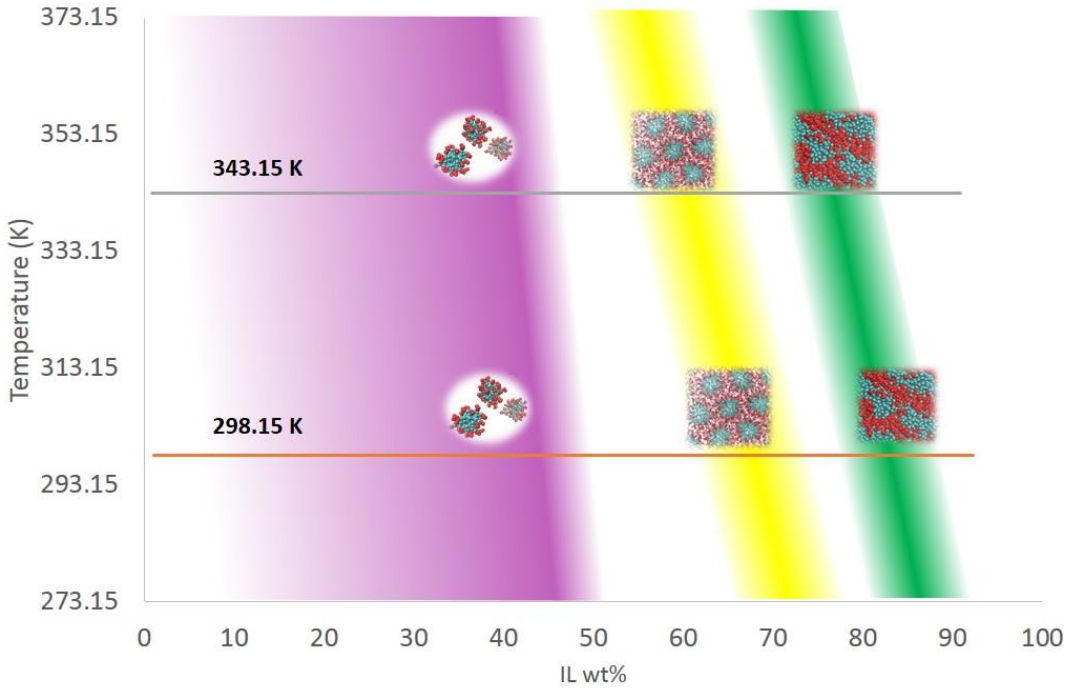

Figure 2.13. Influence of temperature on the morphological evolution of IL templates.

2.4. Conclusions

Three different types of force fields were investigated with respect to their feasibility to study the self-assembly of IL templates in binary system as a benchmark for the study of a more complicated system in the following chapter. Reactive force field yielded reasonably reliable data in density calculation, whilst classic all-atom force field predicted the micellization of

imidazolium based ILs as potential templates. However, both reactive and all-atom force field were too computationally expensive and time-consuming for the study of morphological evolutions. For this purpose, CG force field outperformed both reactive and classic all-atom force fields by successfully predicting the morphologies of IL templates with the predicted morphological evolution in line with experimental results. Moreover, CG force field also showed capability in studying the role of temperature in the morphological evolution of IL templates. An improved or more sophisticated CG models will be needed to generate more reliable statistic values such as surface tension. Overall, this benchmark work suggests that CG force field is a suitable type of force field to systematically investigate the self-assembly mechanism of IL templates for the preparation of MCs in ternary systems comprising of IL templates, carbon precursors, and solvent.

2.5. References

1 A. C. T. Van Duin, S. Dasgupta, F. Lorant and W. A. Goddard, *J. Phys. Chem. A*, 2001, **105**, 9396–9409.

2 T. P. Senftle, S. Hong, M. M. Islam, S. B. Kylasa, Y. Zheng, Y. K. Shin, C. Junkermeier, R. Engel-Herbert, M. J. Janik, H. M. Aktulga, T. Verstraelen, A. Grama and A. C. T. Van Duin, *npj Comput. Mater.*, 2016, **15011**, 1–14.

3 J. Medina-Ramos, W. Zhang, K. Yoon, P. Bai, A. Chemburkar, W. Tang, A. Atifi, S. S. Lee, T. T. Fister, B. J. Ingram, J. Rosenthal, M. Neurock, A. C. T. Van Duin and P. Fenter, *Chem. Mater.*, 2018, **30**, 2362–2373.

4 Y. Yang, Y. K. Shin, S. Li, T. D. Bennett, A. C. T. Van Duin and J. C. Mauro, *J. Phys. Chem. B*, 2018, **122**, 9616–9624.

5 J. N. C. Lopes, J. Deschamps and A. A. H. Pádua, *J. Phys. Chem. B*, 2004, **108**, 2038–2047.

6 J. N. Canongia Lopes and A. A. H. Pádua, *Theor. Chem. Acc.*, 2012, 131, 1–11.

7 B. L. Bhargava, R. Devane, M. L. Klein and S. Balasubramanian, *Soft Matter*, 2007, **3**, 1395–1400.

8 B. L. Bhargava and M. L. Klein, *Soft Matter*, 2009, **5**, 3475–3480.

9 Y. Wang, S. Feng and G. A. Voth, *J. Chem. Theory Comput.*, 2009, **5**, 1091–1098.

10 H. A. Karimi-Varzaneh, F. Müller-Plathe, S. Balasubramanian and P. Carbone, *Phys. Chem. Chem. Phys.*, 2010, **12**, 4714–4724.

11 L. Martinez, R. Andrade, E. G. Birgin and J. M. Martínez, *J. Comput. Chem.*, 2009, **30**, 2157–2164.

12 S. Plimpton, *J. Comput. Phys.*, 1995, **117**, 1–19.

13 G. J. Martyna, D. J. Tobias and M. L. Klein, *J. Chem. Phys.*, 1994, **101**, 4177–4189.

14 M. E. Tuckerman, J. Alejandre, R. López-Rendón, A. L. Jochim and G. J. Martyna, *J. Phys. A. Math. Gen.*, 2006, **39**, 5629–5651.

15 S. Nose, *Mol. Phys.*, 2002, **100**, 191–198.

16 W. G. Hoover, *Canonical dynamics: Equilibrium phase-space distributions*, 1985, vol. 31.

17 F. M. Menger, J. S. Keiper and V. Azov, *Langmuir*, 2000, **16**, 2062–2067.

18 K. Roy and H. Kabir, *Chem. Eng. Sci.*, 2012, **81**, 169–178.

19 M. Jalali-Heravi and E. Konouz, *J. Surfactants Deterg.*, 2003, **6**, 25–30.

20 M. Cepeda, R. Daviña, L. García-Río, M. Parajó, P. Rodríguez-Dafonte and M.

Pessêgo, *Org. Biomol. Chem.*, 2013, **11**, 1093–1102.

21 S. Gabl, C. Schröder and O. Steinhauser, *J. Chem. Phys.*, 2012, **137**, 94501.

22 B. L. Bhargava and M. L. Klein, *Mol. Phys.*, 2009, **107**, 393–401.

23 W. Shinoda, R. DeVane and M. L. Klein, *Mol. Simul.*, 2007, **33**, 27–36.

24 M. Salanne, C. Simon, P. Turq and P. A. Madden, *Comptes Rendus Chim.*, 2007, **10**, 1131–1136.

25 M. Figueira-González, V. Francisco, L. García-Río, E. F. Marques, M. Parajó and P. Rodríguez-Dafonte, *J. Phys. Chem. B*, 2013, **117**, 2926–2937.

26 E. Quijada-Maldonado, S. Van Der Boogaart, J. H. Lijbers, G. W. Meindersma and A. B. De Haan, *J. Chem. Thermodyn.*, 2012, **51**, 51–58.

27 J. M. Vicent-Luna, J. M. Romero-Enrique, S. Calero and J. A. Anta, *J. Phys. Chem. B*, 2017, **121**, 8348–8358.

28 B. L. Bhargava, Y. Yasaka and M. L. Klein, *Chem. Commun.*, 2011, **47**, 6228–6241.

29 Q. Q. Baltazar, J. Chandawalla, K. Sawyer and J. L. Anderson, *Colloids Surfaces A Physicochem. Eng. Asp.*, 2007, **302**, 150–156.

30 H. Kaper and B. Smarsly, *Zeitschrift fur Phys. Chemie*, 2006, **220**, 1455–1471.

31 X. Periole and S.-J. Marrink, in *Biomolecular Simulations*, Humana Press, Totowa, NJ, 2013, pp. 533–565.

32 S. J. Marrink, H. J. Risselada, S. Yefimov, D. P. Tieleman and A. H. De Vries, *J. Phys. Chem. B*, 2007, **111**, 7812–7824.

33 C. A. López, A. J. Rzepiela, A. H. de Vries, L. Dijkhuizen, P. H. Hünenberger and S. J. Marrink, *J. Chem. Theory Comput.*, 2009, **5**, 3195–3210.

34 R. Alessandri, J. J. Uusitalo, A. H. de Vries, R. W. A. Havenith and S. J. Marrink, *J. Am. Chem. Soc.*, 2017, **139**, 3697–3705.

35 A. Ghoufi, P. Malfreyt and D. J. Tildesley, *Chem. Soc. Rev.*, 2016, **45**, 1387–1409.

Chapter 3

Ionic liquid-assisted synthesis of mesoporous carbons: the self-assembly mechanism

3.1. Introduction

Typically, during a soft-templating synthesis of mesoporous polymers and mesoporous carbons (MCs) (*via* one additional step of calcination), the self-assembly of soft templates separates the mixture into two phases, a hydrophobic core of the micelles and a hydrophilic corona part. The two key factors determining the topological structures of mesoporous polymer- and carbon-based materials are the morphologies of soft templates and the spatial correlation between precursor and the hydrophilic part of the template.[1,2] Employing amphiphilic ionic liquids (ILs) as the soft template is expected to follow the same mechanism. As shown in Figure 3.1, the successful implement also requires the thorough understanding of both the morphological evolutions of IL templates in mixture and the spatial distributions of precursors and IL templates.

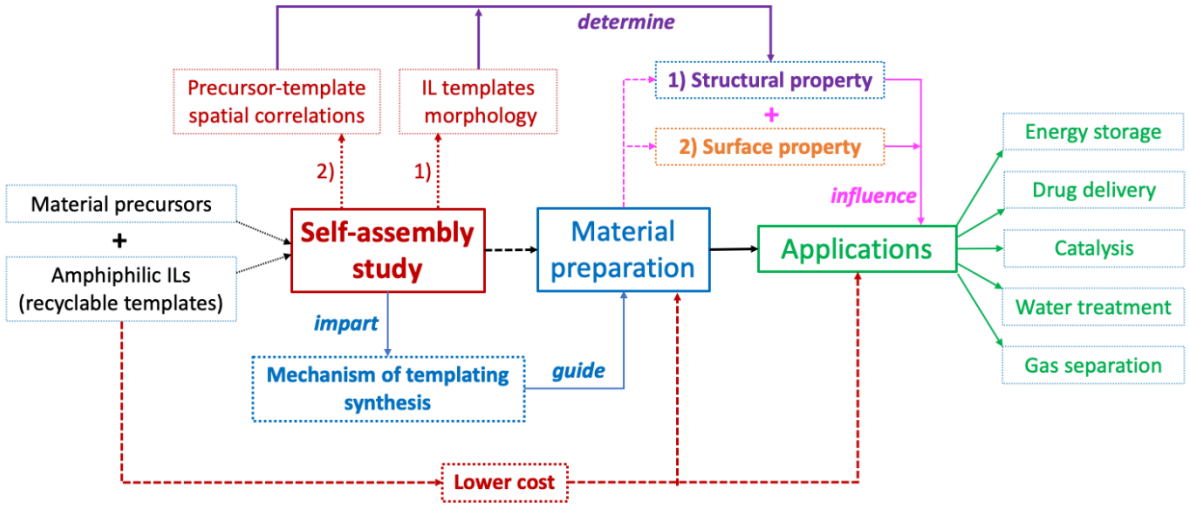

Figure 3.1. The importance of self-assembly study in templating synthesis of MCs using IL templates.

Although there has been extensive research, both computational and experimental, which investigated the phase behaviour of amphiphilic ILs, most of the published work focused on the micellization/aggregation of ILs in the presence of another single component, especially IL aqueous binary mixtures. Multiple factors were identified as being able to facilitate the formation of IL micelle clusters, such as the water concentration, the length of the cationic side chain, the solvation ability of the anion, the charge density of cationic head group, and the influence of temperature.[3–11] However, in practical templating fabrication, three or more chemical species would inevitably be encompassed in total, including but not limited to: IL templates, material precursors, and solvents. In such scenarios, there is a lack of detailed theory whether the presence of material precursors will influence the self-assembly of IL templates, particularly their morphologies, and the precursor-template spatial correlations.

Consequently, it adds to the challenge to effectively design polymer and carbon materials with coveted structures aiming for specific applications.

This chapter investigates the self-assembly behaviour of ternary mixtures comprised of IL templates, material precursors, and solvent through a combination of computational and experimental techniques. The overall aim is to shed light on the templating mechanism of long-chain IL templates in the presence of material precursors and give insight into the effective design of coveted carbon nanomaterials for various applications. To achieve this, two crucial factors to soft-templating synthesis were explored, 1) the morphology of the IL templates and 2) the spatial correlation between carbon precursor and IL template. The morphological evolution process was studied under varying water contents, different precursors, as well as various temperatures, to understand how IL templates assemble into certain morphologies. The influence of different material precursors on the template-precursor spatial correlation was investigated, providing key information on precursors selection towards desired nanostructured materials. Interestingly, the precursors were found to play a crucial role in both the morphologies of IL templates and template-precursor spatial correlations. This, to the best of our knowledge, has not been reported before. More importantly, this study provides a fundamental understanding on the mechanism of soft-templating synthesis of nano-structured polymer and carbon materials by employing amphiphilic ILs as recyclable templates. By gaining insights into how the structures of the resulting materials could be potentially customised aiming for various applications, this chapter also guides the preparation of MCs for energy storage in the later chapters.

3.2. Methodology

Multi-scale modelling, from the most accurate quantum mechanics (QM) to molecular dynamics (MD) simulations, has been regarded as a powerful assistant tool to gain insight at an atomistic/molecular level. To study the self-assembly behaviour of ILs, various empirical models have been developed including atomistic[12–14] and coarse-grained (CG) models[9,15–27]. However, atomistic models are limited within the study of structural/dynamic properties or initial micellization of ILs.[28–31] CG models that trade explicit atomistic interactions for computational speed, are more fittingly poised to probe the mesoscopic organisation or self-assembly behaviour considering the intrinsic slow nature of these spontaneous processes.[30]

In this chapter, CG MD simulations were employed to study the self-assembly behaviour of ternary mixtures containing IL templates, polymer precursor, and solvent. Moreover, CG

force fields proved high feasibility and reliability in the investigation of morphological evolutions of amphiphilic ILs in *Chapter 2*. Detailed atomistic interactions were investigated by performing density functional theory (DFT) calculations. Experimental techniques were also carried out wherever possible to provide solid *in situ* evidence.

3.2.1. CG MD simulations

An improved compatible CG models for IL cation and anion were based on MARTINI version 2.2 force field[32], and derived from the works of Crespo *et al.*[9] and Huet *et al.*[33] respectively. As shown in Figure 3.2, the IL cation was comprised of 6 beads, labelled cation n (n = 1-6), where beads cation 1-3 and cation 4-6 represented imidazolium ring and the alkyl chain, respectively. The carbon atoms on the cationic alkyl chain were labelled C1-C10 (from the first carbon bonding with the imidazolium ring to the terminal carbon atom). All phenolic compounds were coarse-grained into three beads to maintain the planarity of aromatic rings; their models were tailored based on benzene model[34] and chlorobenzene model[35]. Beads containing hydroxyl groups were represented by SP1 particles whilst the rest by SC5 particles. "Bond length" of SC5-SP1 and SP1-SP1 were refined into 0.30 and 0.31 nm, slightly larger than original value of 0.27 nm for SC5-SC5 in benzene model thereby matching with the alterations of both geometric centre and mass centre of phenolic compounds.

As shown in Table 3.1, the IL content in the aqueous solutions ranged from 10 wt% to 82 wt%, whilst the polymer precursors, phenolic monomers, were added individually at constant molar ratio of IL:phenolic compound 1:1 for the ease of investigating the interactions. Initial configurations of the three-component systems were built randomly by PACKMOL[36] to ensure all the simulations started from a heterogeneous state. Non-bonded interactions were described by a shifted Lennard-Jones 12-6 and Coulomb potentials with a cut-off of 11 Å. Long-range Coulombic interactions were calculated by particle-particle particle-mesh (pppm) method with a tolerance of 10^{-5}. Energy minimisation was first performed using conjugate gradient algorithm with a stopping tolerance of 10^{-8} and 10^{-10} for energy and force respectively, followed by a simulation in NPT ensemble at 358.15 K then quenched to 298.15 K to reach equilibrium. Starting from higher temperature can provide a higher kinetic energy to avoid systems from being trapped in local energy minimum rather than overall minimum. Pressure and temperature were constrained at 1 atm by the Martyna-Tobias-Klein (MTK) barostat[37], and Nosé-Hoover thermostat[38,39]. All CG MD simulations were performed on LAMMPS[40] and trajectory files from the simulation were visualised on VMD package[41]. The timestep for simulation was 10 fs and production runs were recorded for 2 μs.

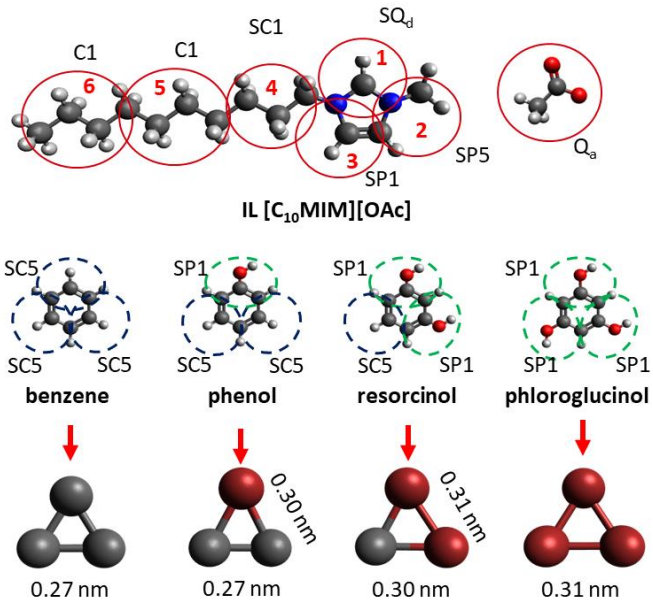

Figure 3.2. CG models employed in this work.

Table 3.1. Summary of ternary systems with final morphologies from CG MD simulations.

Mixtures	$\frac{water}{IL+water} wt\%$	Precursor	Morphologies from simulation	
ILs + water + phenolics			298.15 K	358.15 K
1000 + 140000 + 1000	89.9 wt%	phenol	spherical	spherical
2000 + 125400 + 2000	80.0 wt%	phenol	spherical	spherical
3000 + 72000 + 3000	60.5 wt%	phenol	spherical	spherical
3000 + 48000 + 3000	50.5 wt%	phenol	spherical	spherical
3250 + 40000 + 3250	44.0 wt%	phenol	hexagonal columnar	spherical
3500 + 36000 + 3500	39.6 wt%	phenol	hexagonal columnar	hexagonal columnar
4000 + 32000 + 4000	33.8 wt%	phenol	hexagonal columnar	hexagonal columnar
4300 + 28000 + 4300	29.3 wt%	phenol	hexagonal columnar	lamellar bilayer
4600 + 24000 + 4600	25.0 wt%	phenol	lamellar bilayer	lamellar bilayer
4600 + 16000 + 4600	18.2 wt%	phenol	lamellar bilayer	lamellar bilayer
3250 + 40000 + 3250	44.0 wt%	resorcinol	spherical	spherical
4000 + 32000 + 4000	33.8 wt%	resorcinol	spherical	spherical
4600 + 24000 + 4600	25.0 wt%	resorcinol	hexagonal columnar	hexagonal columnar
4600 + 16000 + 4600	18.2 wt%	resorcinol	hexagonal columnar	hexagonal columnar
4600 + 24000 + 4600	25.0 wt%	phloroglucinol	spherical/rod-like	spherical/rod-like
4600 + 16000 + 4600	18.2 wt%	phloroglucinol	hexagonal columnar	hexagonal columnar
4600 + 16000 + 4600	18.2 wt%	benzene	lamellar bilayer	lamellar bilayer
3000 + 48000 + 0	50.5 wt%	n/a	hexagonal columnar	hexagonal columnar
4600 + 16000 + 0	18.2 wt%	n/a	hexagonal columnar	hexagonal columnar

3.2.2. DFT calculations

DFT calculations were carried out with Gaussian 16 program[42]. M06-2X method was employed at the def2-TZVP level with an additional D3 dispersion correction. No symmetry constraints were imposed during the calculations. Natural bond orbital (NBO) analysis was performed to study the H-bonding interactions within all ternary systems, atomic charges, and the stabilization energy of the electron delocalization ($E^{(2)}_{n\rightarrow\sigma^*}$). In comparison with NBO analysis, quantum theory of atoms in molecules (QTAIM) analysis was also performed with Multiwfn program[43] to analyse the H-bonding interactions by finding values at the bond critical point (BCP), namely the electron density at the BCP (ρ_{BCP}), the Laplacian of the electron density at the BCP ($\nabla^2\rho_{BCP}$), and electron energy density at the BCP (H_{BCP}). The ρ_{BCP} values were used to estimate H-bond energies in kJ/mol using the correlation for a charged IL system proposed by Emamian and coworkers[44].

$$E_{H-bond} = -1390.5 \times \rho_{BCP}/\text{a.u.} - 4.4606 \qquad \text{(Equation 3.1)}$$

3.2.3. Experiments

3.2.3.1. Synthesis of 1-decyl-3-methylimidazolium acetate, [C_{10}MIM][OAc]

[C_{10}MIM][OAc] was prepared through a typical two-step method: the alkylation of 1-methylimidazole with 1-bromodecane and a metathesis reaction for anion exchange from a bromide to acetate.

In a typical procedure, 1-methylimidazole (0.40 mol, 99%, Sigma-Aldrich) was mixed in toluene (400 mL, ≥99.7%, Sigma-Aldrich) with a slight excess of 1-bromodecane (0.44 mol, 98%, Sigma-Aldrich). The flask was equipped with a stir bar and refluxed at 110 °C using an oil bath for 24 h. Toluene was carefully removed using a rotavapor then the product was further washed with diethyl ether (200 mL, ≥99.5%, Sigma-Aldrich) for 3 times. [C_{10}MIM]Br was obtained as yellowish viscous oil (yield: 88%).

For the metathesis reaction, [C_{10}MIM]Br was first dissolved in absolute ethanol (≥99.8%, Fisher Scientific) with KOAc (≥99%, Sigma-Aldrich), then above mixture was stirred at ambient temperature for at least 2 h. Slight excess of KOAc was necessary to guarantee the displacement of Br^-. A white precipitate was filtered to separate the insoluble KBr out of solution, where the solvent was evaporated by rotavapor to remove ethanol. Cold acetone (≥99.8%, Fisher Scientific) was then added, and the flask was left in refrigerator for 12 h to totally precipitate KBr and excessive KOAc. After filtering again, potassium salts were

totally removed, the remaining acetone was removed by rotavapor. The product was further purified under high vacuum at 50 °C overnight. [C_{10}MIM][OAc] was finally obtained as yellowish oil, less viscous than [C_{10}MIM]Br (yield: 94%).

3.2.3.2. Characterisation

Nuclear magnetic resonance (NMR) spectroscopy. The synthesised ILs were characterised by NMR spectroscopy to ensure no detectable impurity with chloroform-d as solvent. Proton spectra were recorded on Bruker Avance III 400 MHz NMR spectrometer. 2D ^{1}H-^{1}H NOESY is a very sensitive spectroscopic technique to examine the spatial microenvironment of protons by measuring spin-lattice relaxation. All IL/water/phenolic compound ternary mixtures were studied by 2D NOESY NMR experiments where dimethyl sulfoxide-d6 (DMSO-d6) was used as external standard. NEOSY spectra were recorded on Bruker 600 MHz NMR spectrometer.

1-decyl-3-methylimidazolium bromide

^{1}H NMR (chloroform-d, 400 MHz): δ 10.11 (s, 1 H), 7.58 (s, 1 H), 7.38 (s, 1 H), 4.15 (t, 2 H), 3.96 (s, 3 H), 1.73 (m, 2 H), 1.00-1.20 (m, 14 H), 0.68 (t, 3 H). ^{13}C NMR (chloroform-d, 100 MHz): δ 137.0, 123.8, 122.1, 50.0, 36.6, 31.7, 30.2, 29.3, 29.2, 29.1, 28.8, 26.1, 22.5, 13.9.

1-decyl-3-methylimidazolium acetate

^{1}H NMR (chloroform-d, 400 MHz): δ 10.80 (s, 1 H), 7.39 (s, 1 H), 7.35 (s, 1 H), 4.06 (t, 2 H), 3.87 (s, 3 H), 1.72 (m, 2 H), 1.72 (m, 3 H), 0.80-1.30 (m, 14 H), 0.64 (t, 3 H). ^{13}C NMR (chloroform-d, 100 MHz): δ 177.1, 139.2, 123.2, 121.5, 49.6, 35.9, 31.5, 30.1, 29.1, 29.0, 28.9, 28.7, 26.0, 25.4, 22.4, 13.9.

Small-angle X-ray Scattering (SAXS). SAXS data were recorded by the Offline DL-SAXS instrument Xeuss 3.0 (Excillium Ga MetalJet source, 9.2 keV, λ = 0.71 Å) in Diamond Light Source, Harwell Campus, Oxfordshire. The sample was transferred into a capillary (1.5 mm of outer diameter) and sealed tightly. Measurements were carried out under vacuum at variable temperatures with a detector to sample distance of 275 mm to ensure all possible characteristic peaks detected (q range 0.05-1.13 Å^{-1}). An acquisition time of 300 s was used for all the samples. Data was corrected by subtraction of transmission and background scattering. The intensity was plotted versus scattering vector, $q = (4\pi \sin\theta)/\lambda$.

Polarised optical microscopy (POM). Phase examinations were performed under an Olympus BX50 microscope. All samples' textures were determined at 298.15 K with a Linkam TH600 hot stage and TP 92 temperature controller.

3.3. Results and discussion

1-alkyl-3-methylimidazolium based ILs are the most studied family for templating synthesis.[8,46–53,23] 1-decyl-3-methylimidazolium acetate ([C_{10}MIM][OAc]) was chosen due to the following reasons: 1) [C_{10}MIM]$^+$ as cation has desired amphiphilicity, and 2) the acetate anion not only has a strong dissolution ability[54–58] and is slightly basic, but also makes the process greener by being halogen-free. Phenolic compounds such as phenol, resorcinol, and phloroglucinol that have been used extensively to prepare porous polymer/carbon materials were selected as precursor monomers and were added equimolarly as IL templates.

The morphological evolution process of amphiphilic IL templates in ternary mixtures is first emphasised under varying water content, precursors, and temperature. The template-precursor spatial correlation is subsequentially highlighted, which together with template morphology determine the resulting topological structures of nanomaterials. Finally, potential consequences of this chapter are briefly discussed with possible promising syntheses routes proposed for some nanomaterials targeting applications.

3.3.1. Validation of CG MD models

Due to the change of CG models, it is essential to carry out study on binary IL systems as a benchmark as done in *Chapter 2*, before investigating the morphological study of ternary IL systems, although the reliability of Martini CG model has been tested in the original work for a different anion.[9] Small-angle X-ray scattering (SAXS) measurements were first carried out to seek for experimental evidence of the morphologies of binary mixtures, acting as model validation, then applied to ternary mixtures. Table 3.2 summarises the scattering peak locations of binary systems with interpreted morphologies. As shown in Figure 3.3a, the SAXS profiles of [C_{10}MIM][OAc]/water binary mixtures containing 18-50 wt% of water indicate the dominating hexagonal phase, evidenced by the characteristic scattering vector ratio q_1:q_2:q_3 = 1:√3:√4.[59,60] CG MD simulation also pointed out an ordered hexagonal structure with water contents between 18.2-50.5 wt% (Figure 3.3b), which suggests the great reliability of CG model for [C_{10}MIM][OAc]. Therefore, we can expect such model can be used to predict the morphological evolutions of ternary mixtures containing phenolic compounds. This results for IL/water binary mixtures show similar trend with the reports for

other anions based ILs. With the same cation, the liquid crystalline phase for [C_{10}MIM][Br] ionogels, as well as nitrate-based ionogels, undergoes: lamellar, hexagonal perforated layers and hexagonal phases when the weighted concentration of water in the system ranges from 11-16%, 17% and 40% respectively.[11] Goodchild *et al.*[61] studied the phase behaviour of [C_{10}MIM][Cl]/water mixture through ^{1}H NMR technique. Hexagonal columnar morphology was found to be the major mesophase at the water concentrations from 6-44% by weight.

With the rise of temperature, these sharp characteristic scattering peaks become less intense even unobservable due to higher kinetic energy. Only a single broad q_1 peak was detected for [C_{10}MIM][OAc]/water binary mixtures containing 34 wt% of water when temperature reached to 358.15 K (Figure 3.3c). This is likely because higher temperature brings increased kinetic energy, so the fixed liquid crystalline lattice was disrupted, leaving a dynamic short-range structural ordering. At this point, the lyotropic mesophase reversibly melted into an isotropic liquid phase and the long-range liquid crystallinity was disturbed, resulting in a dynamic short-range structural ordering of IL cations.

Beside of the validation of [C_{10}MIM][OAc] model, the reliability of models for phenolic compounds were also investigated, especially phenol, since CG models for resorcinol and phloroglucinol are derivates of phenol model. The simulated density for phenol was 0.81 g/cm^3 at 298.15 K, compared with experimental value of 1.07 g/cm^3. Note that Martini 2.2 models typically underestimated the stacking distance in the ring structures. Therefore, the same is true for models of benzene and chlorobenzene, yielding underestimated densities.[34,35]

Table 3.2. Summary of scattering peaks of binary IL systems at varying water contents

q values for scattering peaks of binary IL systems with varying water contents	q_1 (Å^{-1})	q_2 (Å^{-1})	q_3 (Å^{-1})	Morphology of IL templates
18 wt%	0.23	0.40	0.45	Hexagonal columnar
25 wt%	0.22	0.39	-	Hexagonal columnar
34 wt%	0.22	0.38	-	Hexagonal columnar
50 wt%	0.22	0.37	-	Hexagonal columnar
60 wt%	0.20	-	-	spherical
70 wt%	0.18	-	-	spherical
80 wt%	0.17	-	-	spherical
90 wt%	0.16	-	-	spherical

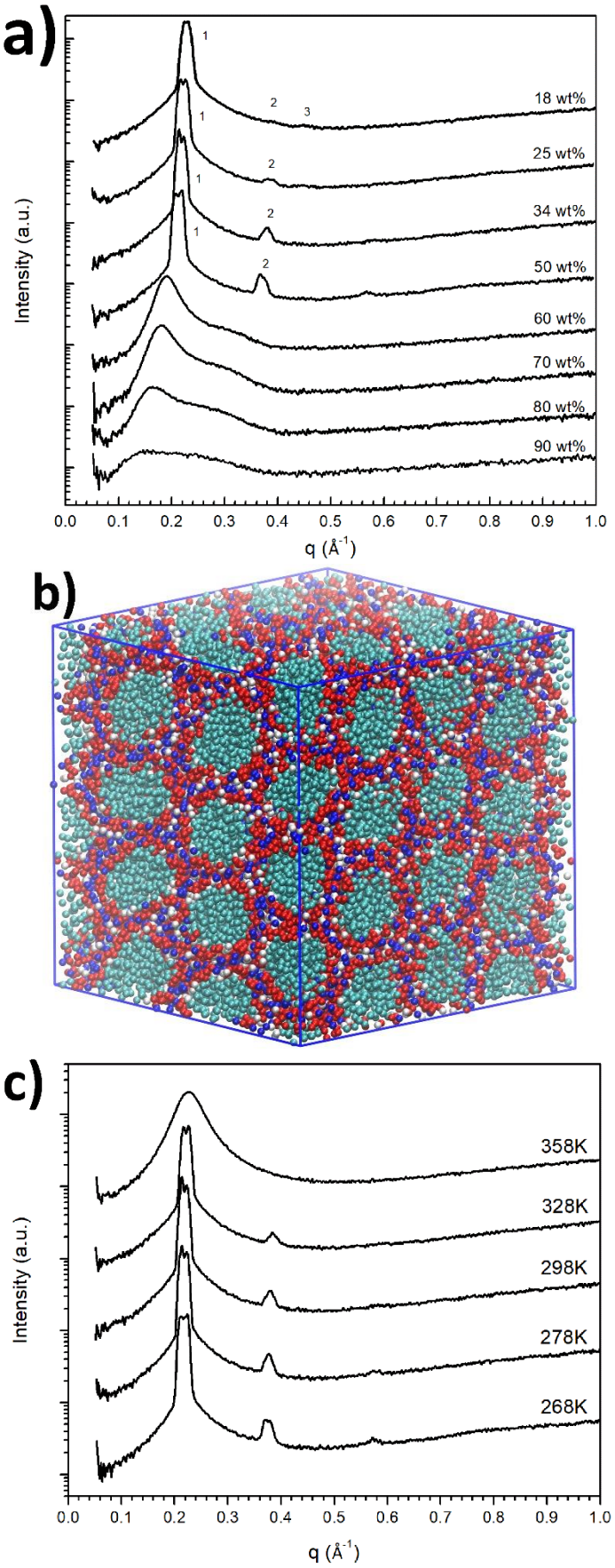

Figure 3.3. a) SAXS diffractogram of [C_{10}MIM][OAc]/water binary mixtures with varying water contents at 25 °C; b) snapshot from MD simulation of [C_{10}MIM][OAc]/water binary mixtures with 18.2 wt% of water; and c) SAXS diffractogram of [C_{10}MIM][OAc]/water binary mixture containing 34 wt% of water at various temperatures.

3.3.2. Influence of water content on the morphology of IL templates

The self-assembly process of $[C_{10}MIM][OAc]$/water/phenol ternary systems with varying water contents at 298.15 K was first studied *via* CG MD simulations coupled with experimental techniques. All ternary systems with corresponding morphologies are summarised in Table 3.1. Figure 3.4 shows three typical morphologies formed by $[C_{10}MIM]^+$ cations in the presence of phenol as the precursor. With the decreasing water content (H_2O wt% = $m(H_2O)/(m(H_2O)+m(ILs))$, excluding phenolic precursor) in the mixture, spherical, columnar, and lamellar phases formed sequentially once the IL concentration exceeded the critical micelle concentration (CMC). Figure 3.4a presents a disordered configuration of spherical micelle clusters formed when the relative water content is 50.5 wt%. As the water content decreased, a spherical-to-rod transition was expected at water content between 44.0-50.5 wt%, where dense spherical clusters were expected to slowly grow longer and transit into rod-like or cylindrical clusters due to having exceeded the critical packing parameter for spherical micelle clusters. Eventually long rod-like clusters reorganised and evolved into honeycomb-like hexagonal columnar phase with long-range order (Figure 3.4b); corresponding water content ranged from 29.3-44.0 wt%. After a short transition stage, lamellar sheet-like arrays as shown in Figure 3.4c were formed as the water content was smaller than 25.0 wt%.

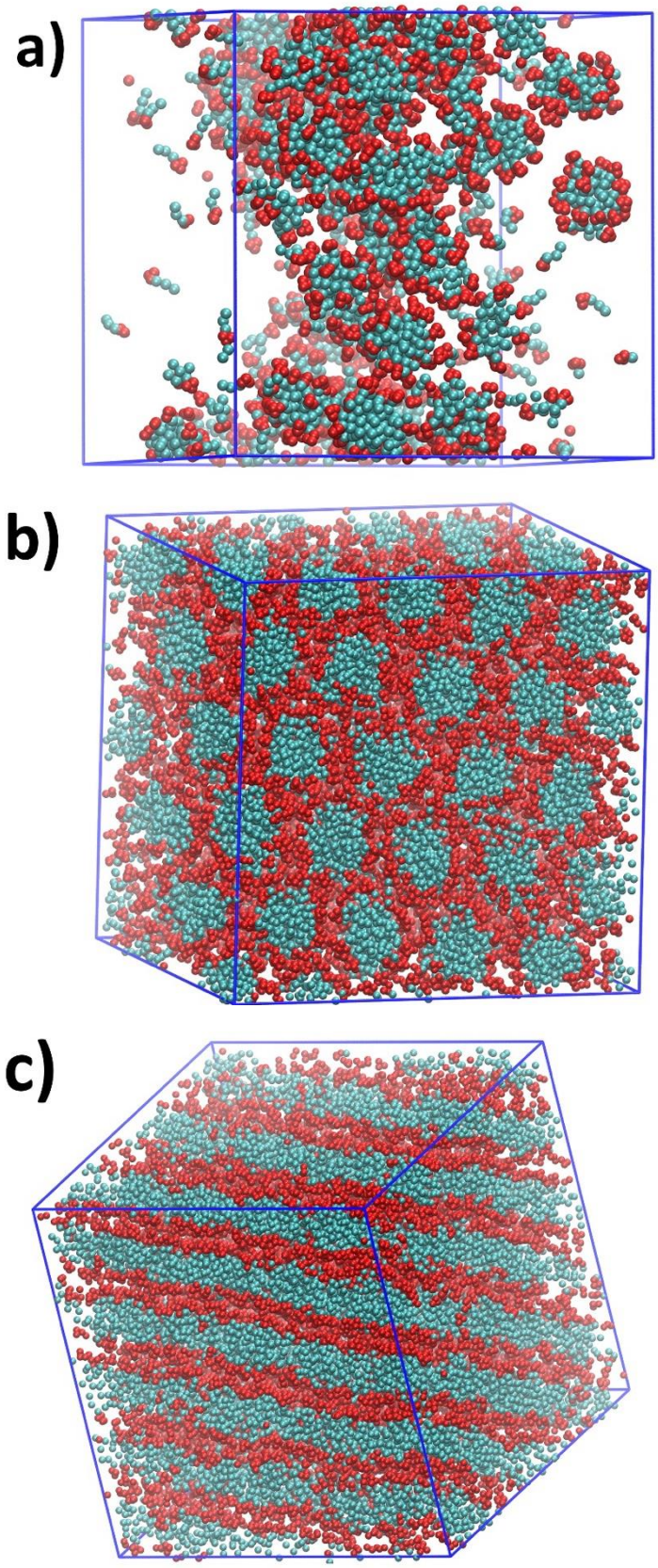

Figure 3.4. Snapshots of [C_{10}MIM][OAc]/water/phenol ternary systems at water contents around: a) 50 wt%, b) 34 wt%, and c) 25 wt% (Red and cyan beads represent imidazolium rings and alkyl chains of IL cations, respectively. Phenol, water, and anions are not shown for clarity).

During a typical morphology evolution process in IL/water binary mixtures, the formation of lyotropic liquid crystals (LLCs) or lyotropic gels indicates that the mixture is in a lyotropic phase. Different texture patterns from POM can be linked to certain morphologies, such as a hexagonal columnar or smectic phase.[59,60,62–66] POM was also performed to observe [C_{10}MIM][OAc]/water/phenol ternary mixtures. Figure 3.5a shows a characteristic fan-like pattern of [C_{10}MIM][OAc]/water binary lyotropic gels with a water content around 18 wt%, indicating the presence of dominating hexagonal liquid crystalline structures. However, ternary mixture containing phenol exhibited a clear liquid phase (Figure 3.5b), although hexagonal columnar and smectic lamellar morphologies are observable in CG MD simulations.

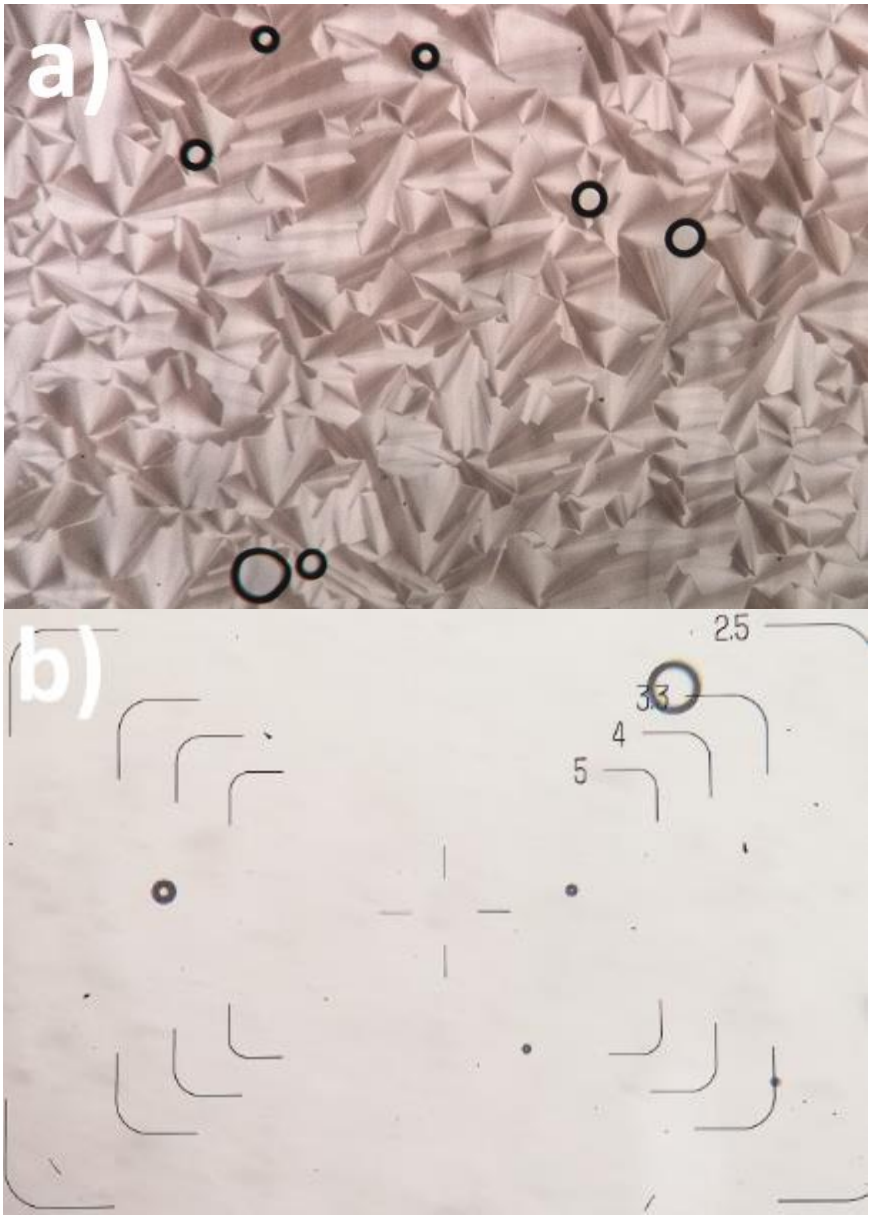

Figure 3.5.POM images at 18 wt% of water: a) [C_{10}MIM][OAc]/water binary mixture; b) [C_{10}MIM][OAc]/water/phenol ternary mixture.

The absence of LLCs or lyotropic gels on a macroscopic aspect does not necessarily indicate that IL templates in ternary mixtures are not confined in hexagonal or lamellar arrays. In neat long-chain 1-alkyl-3-methylimidazolium salts, the crystalline phase exhibited highly ordered lamellar arrays at lower temperatures but could directly turn into isotropic liquids after melting.[67] Analogous temperature-dependent mesophase behaviours were also seen in IL/water binary mixtures.[60,65] Heating could cause an increased kinetic energy and faster molecule motion, which destabilises the periodic three-dimensional H-bonding lattices. Although the liquid crystalline phases disappeared after melting, the array of long-chain cations still maintained a dynamic short-range structural ordering.[67] The disappear of LLCs or gels in ternary mixture is likely due to the addition of phenol precursor.

Figure 3.6 shows SAXS pattern for ternary mixtures containing phenol where only broad peaks were observed rather than sharp intense peaks. The SAXS pattern for ternary mixture containing 18 wt% of water showed a single broad peak centred at 0.24 $Å^{-1}$, which could be associated with the relative structural ordering in short-range. With the increase in water content from 30 wt%, the q_1 peak got lower and shifted to lower *q* range, while a second broad peak q_2 got higher and centred around 0.38 $Å^{-1}$. When the water content exceeded 50 wt%, both peaks became weaker then merged into a much broader peak for mixture containing 90 wt% of water. Owing to the less intense nature of these scattering peaks, it is challenging to interpret morphological information for IL templates in ternary mixture. However, when the mixtures were quenched down to 263.15 K, more recognisable scattering peaks were manifested, which is probably because lower temperature resulted in slower molecule motion due to lower kinetic energy. As shown in Figure 3.7, two scattering peaks at 0.22 and 0.44 $Å^{-1}$ were observed for a ternary mixture containing 18 wt% of water; the ratio $q_1:q_2 = 1:2$ indicates the formation of lamellar bilayer array with a repeating distance $d = 2\pi/q$ = 28.5 Å. At 44 wt% of water, a hexagonal phase was detected with a scattering vector ratio of $q_1:q_2 = 1:\sqrt{3}$. The broad peak observed from ternary mixture containing 90 wt% of water indicates that IL cations were dominatingly assembled into spherical clusters.

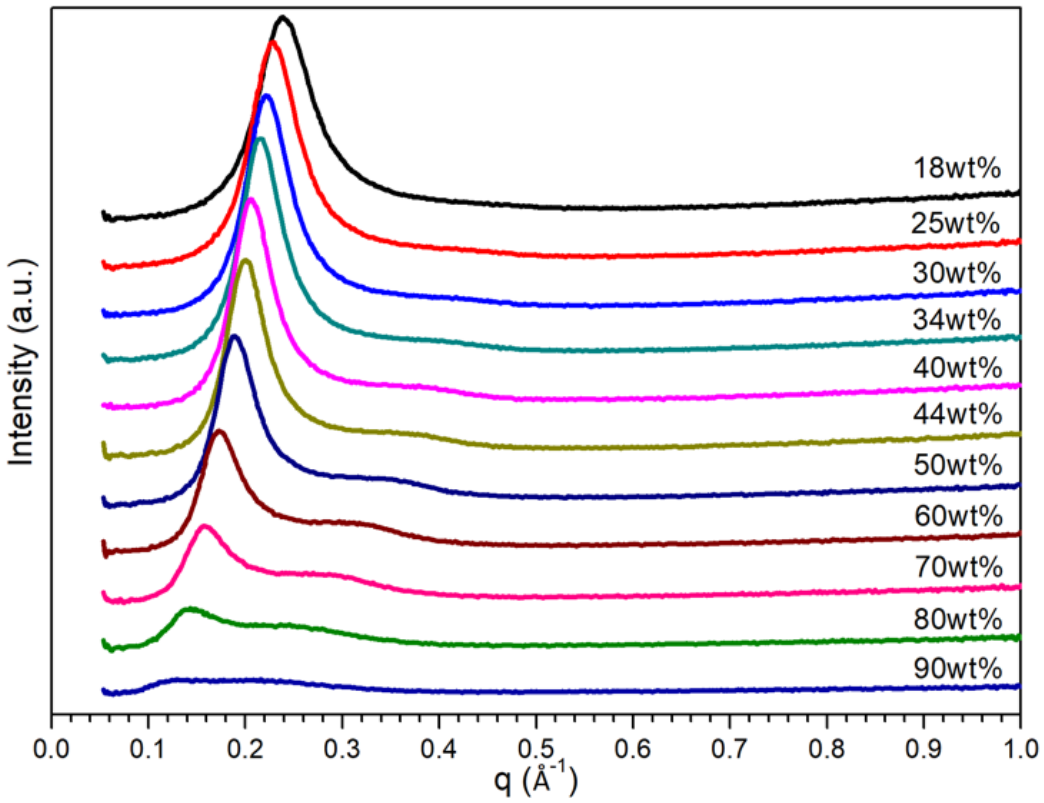

Figure 3.6. SAXS patterns of [C_{10}MIM][OAc]/water/phenol ternary mixtures with varying water contents at 298.15 K.

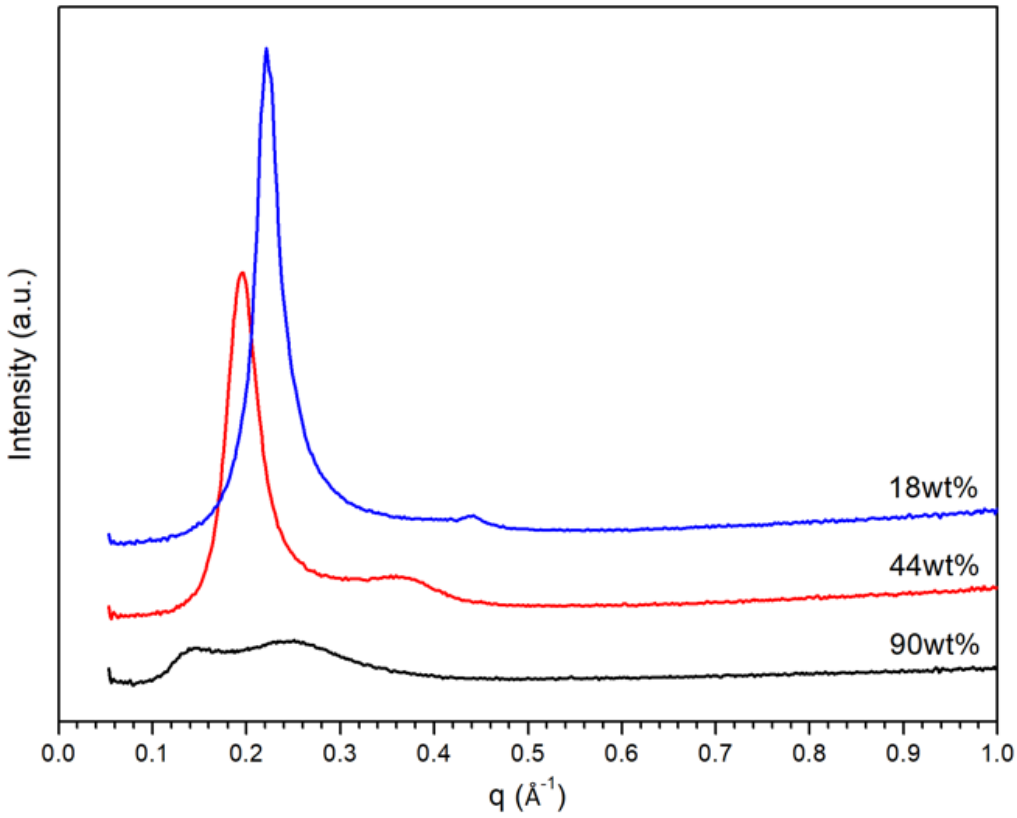

Figure 3.7. SAXS patterns of [C_{10}MIM][OAc]/phenol/water ternary mixtures at 263.15 K.

The SAXS result implies that the introduction of phenol can destabilise the H-bonding lattice between IL and water leading to a weakened scattering intensity of characteristic peaks for ternary mixtures. This is likely attributed to the hydroxyl group in phenol that enables phenol to interact with ILs and water *via* H-bonding.

The detailed interaction energies for ternary systems are also obtained from DFT calculations with a single ion pair and varying water numbers (Figure 3.8). The overall system interaction energy showed a steady growth from 619.2 to 1439.8 kJ/mol when the number of water molecules increased in the system. This growth is mostly contributed by the interactions of water-IL pair (from 78.2 to 425.8 kJ/mol) and water-water pair (from 0 to 566.2 kJ/mol). Noticeably, the interaction within [C_{10}MIM][OAc] molecules became weaker, evidenced by the declining interaction energy from 430.9 to 315.4 kJ/mol. Since H-bonding is the predominating interaction pathway between [C_{10}MIM][OAc] and water, adding more water into the ternary system essentially enlarges the H-bonding probability of IL with water and initiates the morphological evolution of micelles during self-assembly. In the presence of a precursor, phenol showed a significantly strong H-bonding interaction with [C_{10}MIM][OAc], especially *via* acetate···H-phenol bond. Consequently, the H-bonding lattices between ILs and water were destabilised by the competitional interaction between IL with phenol, hence the disappear of the liquid crystalline mesophase.

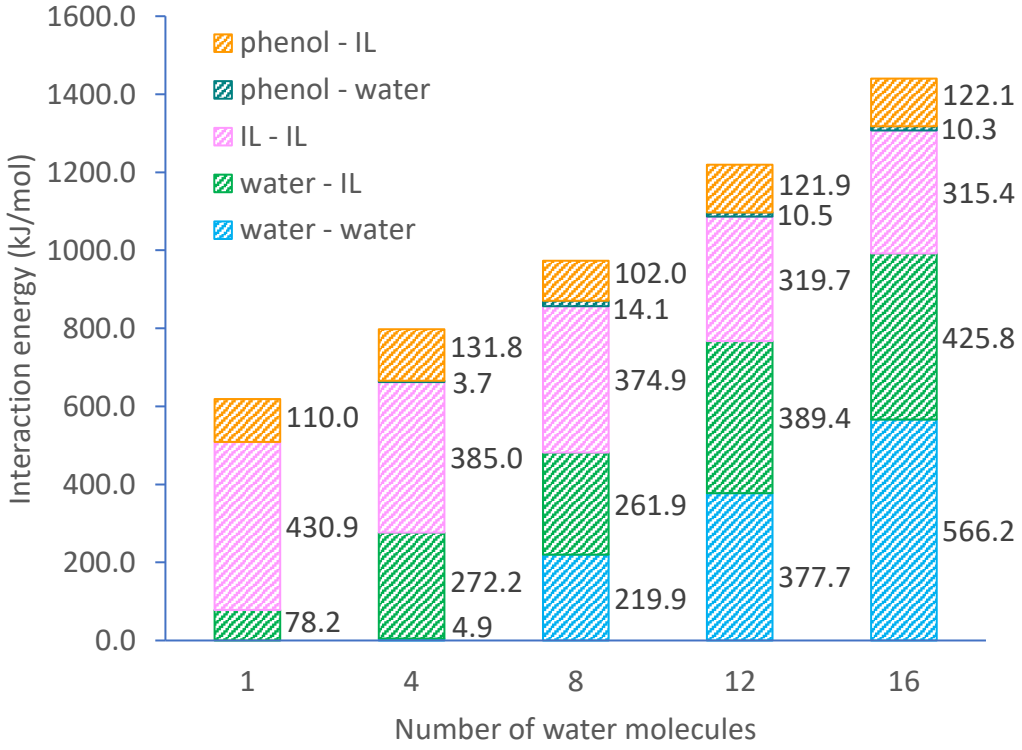

Figure 3.8. Energy changes with increasing water concentration in ternary systems.

3.3.3. Influence of different precursors on the morphology of IL templates

Beside of phenol, resorcinol and phloroglucinol are also extensively used precursors for porous polymer and carbon materials. CG-MD simulations were performed for ternary mixtures containing resorcinol and phloroglucinol individually to reveal whether different precursor could influence the self-assembly of ILs during templating synthesis. A benzene based ternary mixture was studied for comparison. Due to their accumulative hydroxyl groups from 0 to 3, these four aromatic compounds possess increasing hydrophilicity and hydrogen bonding ability in the order of benzene < phenol < resorcinol < phloroglucinol. The mixing ratio in ternary systems remained equal, so the only variable was the increasing hydroxyl functionality and consequent H-bonding ability.

The eventual configurations of ternary mixtures at 18 wt% of water are shown in Figure 3.9. The benzene based ternary mixture also presented a planar lamellar phase like their phenol counterpart. In comparison with [C_{10}MIM][OAc]/water binary mixture where dominating hexagonal columnar phase was observable, the addition of equimolar of phenol or benzene has changed the morphology of [C_{10}MIM]$^+$ micelles. Most noticeably, when using resorcinol and phloroglucinol as precursors, the morphology of the [C_{10}MIM][OAc] became hexagonal columnar, which is expected to appear at higher water contents for phenol-based cases. This indicates that the introduction of more hydroxyl functionalities also plays an analogous role as increasing water ratio in mixture. One hydroxyl functionality on a phenolic compound can act as one H-bond donor and acceptor while per water molecule has double the H-bonding capacity of phenol; phloroglucinol is able to form H-bonds quantitively equal that of phenol "plus" water at maximum. Indeed, the self-assembly of ternary IL systems and such morphological evolution derive from the competition between the hydrophobic attraction interactions at the cationic alkyl chain-water interface and the hydrophilic, ionic repulsion interactions of the headgroups, which together determine the bending or curvature energy and the preferred packing geometry to satisfy the critical packing parameters.[68] Increasing the number of hydroxyl groups in the phenolic compounds from phenol to phloroglucinol can change the competition of these two interactions by increasing the hydrophilic, ionic repulsion interactions and decreasing hydrophobic attractions, thus the morphology changed from lamellar bilayer to hexagonal columnar structures.

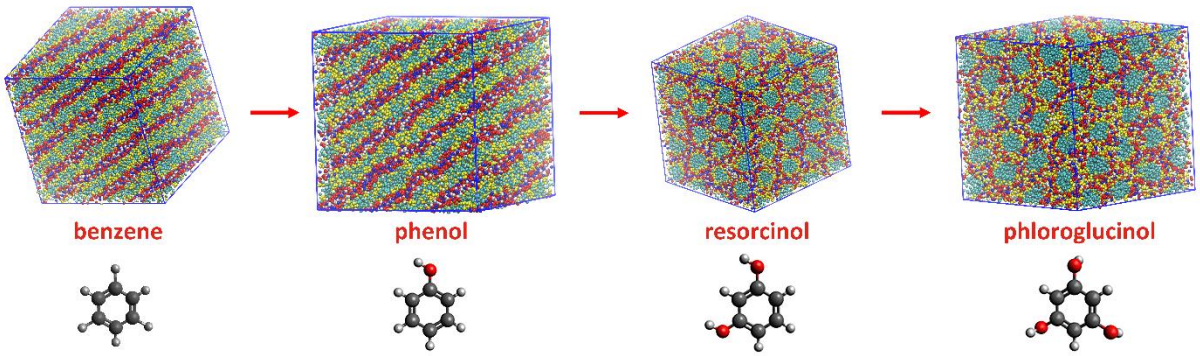

Figure 3.9. Morphology evolution under increasing hydroxyl groups in precursors at the same mixing ratio (Red: imidazolium ring, cyan: alkyl chain, blue: acetate, yellow: phenolic compounds, white: water).

The SAXS profiles of the ternary mixtures with the four different precursors are shown in Figure 3.10. Only broad peaks were observed for ternary mixtures, except that containing benzene where its scattering vector ratio q1: q2 = 1:2 signifies the presence of smectic lamellar phase. With the increase in hydroxyl groups, the broad scattering q1 peak got stronger from ternary mixture containing phenol. The absence of the second scattering peak q2 makes it more challenging to interpret the morphological structures of $[C_{10}MIM]^+$ cations in a ternary mixture containing resorcinol or phloroglucinol.

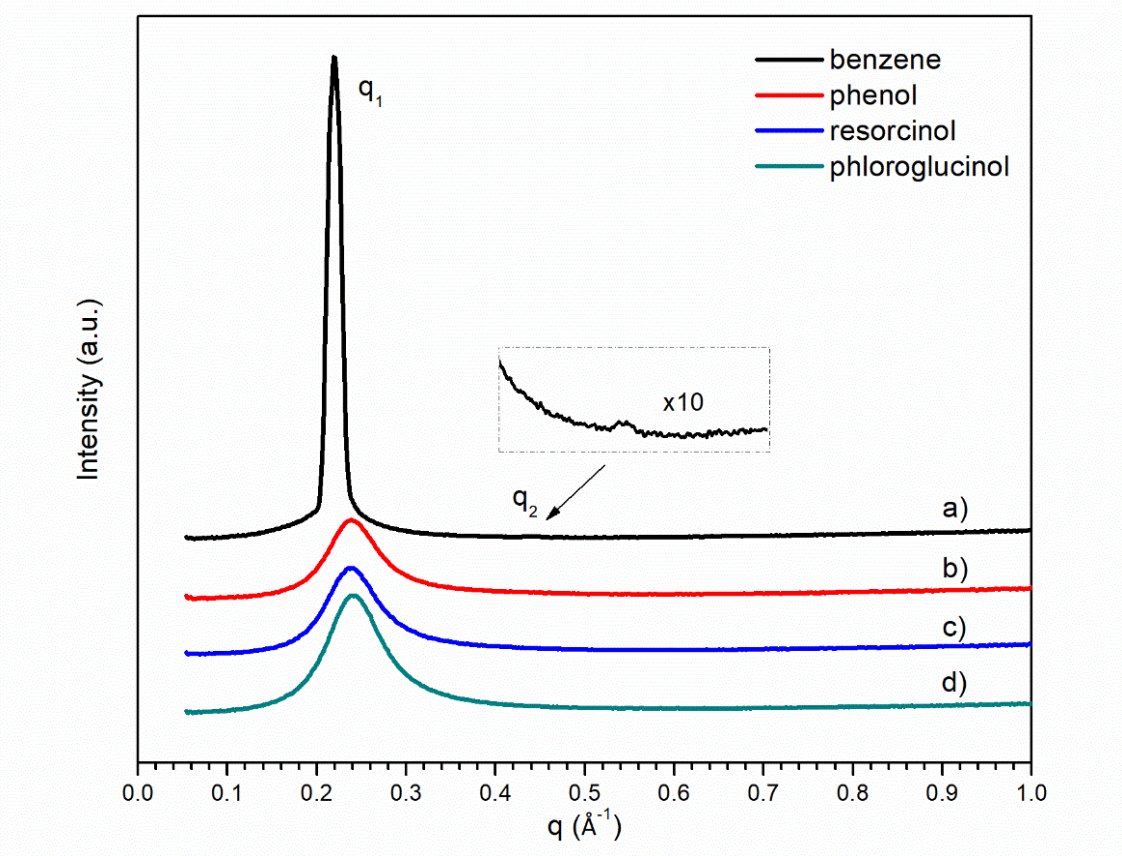

Figure 3.10. SAXS pattern of ternary mixtures containing 18 wt% of water with different precursors: a-d) benzene, phenol, resorcinol, and phloroglucinol, respectively.

The SAXS profiles of ternary mixtures at varying temperatures are shown in Figure 3.11. All scattering peaks became higher with the decreasing temperature. As shown in Figure 3.11a and b, ternary mixture containing phenol at lower temperatures showed more recognisable scattering peaks, especially at 263 K. At 34 wt% of water, the scattering ratio of q1:q2 = 1:√3 indicates the dominating hexagonal columnar phase. At 18 wt% of water, the scattering ratio of q1:q2 = 1:2 confirms the formation of lamellar bilayer structures. However, for ternary mixtures containing resorcinol or phloroglucinol, lower temperature did not manifest other scattering peaks such as q2 peak (Figure 3.11c and d). Unlike their phenol counterpart, lower temperatures did not make the interpretation of SAXS profiles more straightforward as there was still only one broad scattering peak observable.

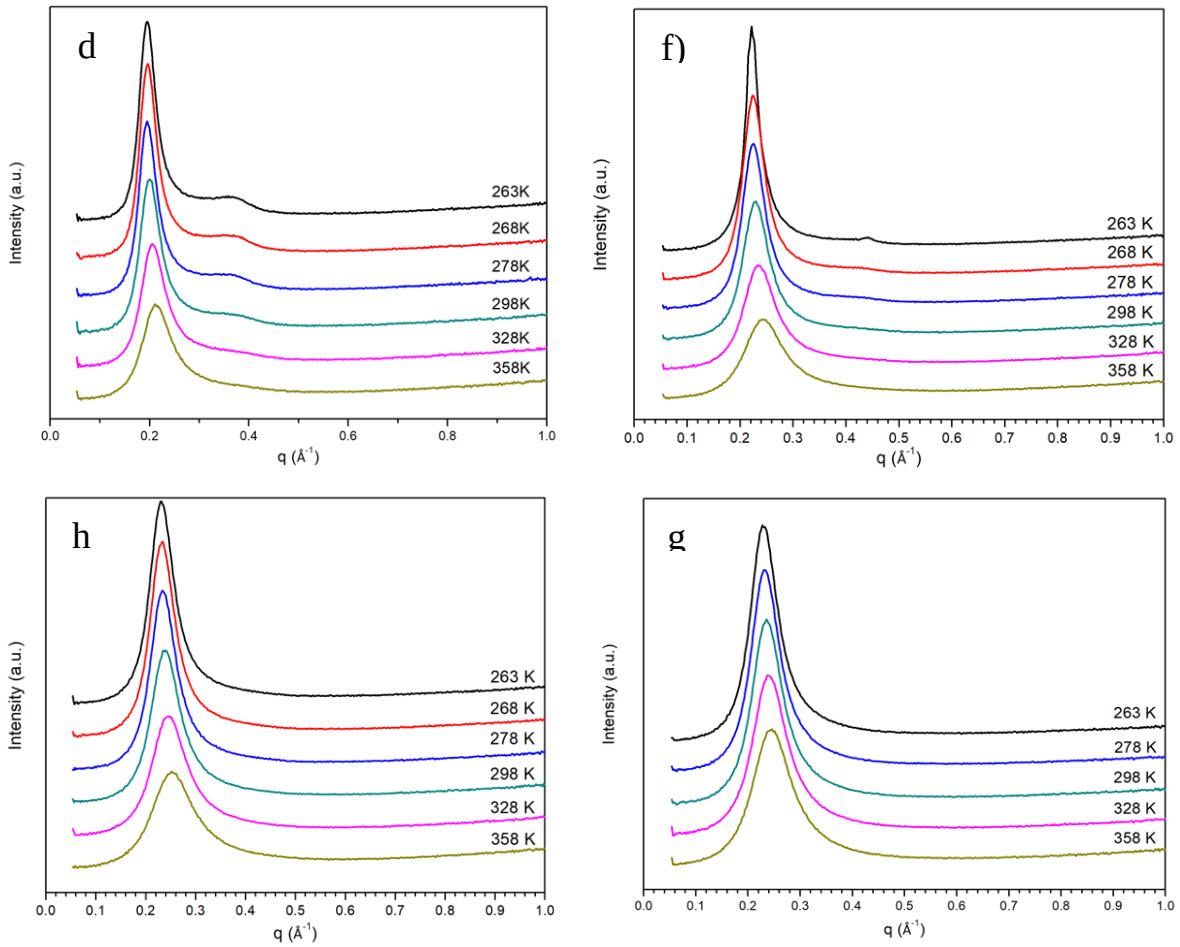

Figure 3.11. SAXS profiles for ternary mixtures at various temperatures for different precursors: a) phenol at 34 wt% of water, b) phenol at 18wt% of water, c) resorcinol at 18wt% of water, and d) phloroglucinol at 18wt% of water.

POM was performed for ternary mixtures containing resorcinol and phloroglucinol. No lyotropic gels or LLCs were observed, although a hexagonal array was predicted by the CG MD simulation. The absence of a lyotropic gel phase did not apply to the [C_{10}MIM][OAc]/water/benzene system, the cross pattern of which could be associated with

the formation of a lamellar phase (Figure 3.12a).[59,65,66] Liquid crystalline phases were also reported observable in [C_{16}MIM][Br]/water/p-xylene ternary mixtures.[59] This is because neither benzene nor p-xylene has functional moieties containing hetero-atoms to serve as H-bond donors and acceptors, therefore benzene and p-xylene are chemically stable in mixtures and unlikely to destabilise the H-bonding interactions between IL and water. However, when resorcinol or phloroglucinol were added in molar quantities lower than the concentration of [C_{10}MIM][OAc], lyotropic gels were observed for ternary mixtures; the representative fan-like pattern exhibits the characteristics of hexagonal liquid crystalline lattice[59,65,66] (Figure 3.12b). This phenomenon confirmed that phenolic compounds compete with water to form H-bonds with ILs, particularly acetate anion. When the molar concentration of the ILs is higher than that of the precursors, phenolic compounds are likely confined in dynamic hexagonal arrays *via* H-bonds with [C_{10}MIM][OAc] and water, and excessive concentrations of [C_{10}MIM][OAc] form liquid-crystalline by H-bonding interactions with water generating lyotropic gels on a macroscopic aspect. When resorcinol or phloroglucinol was added equimolarly with [C_{10}MIM][OAc], the strong scattering q_1 peak in their SAXS profiles could be resulted from the formation of hexagonal columnar arrays.

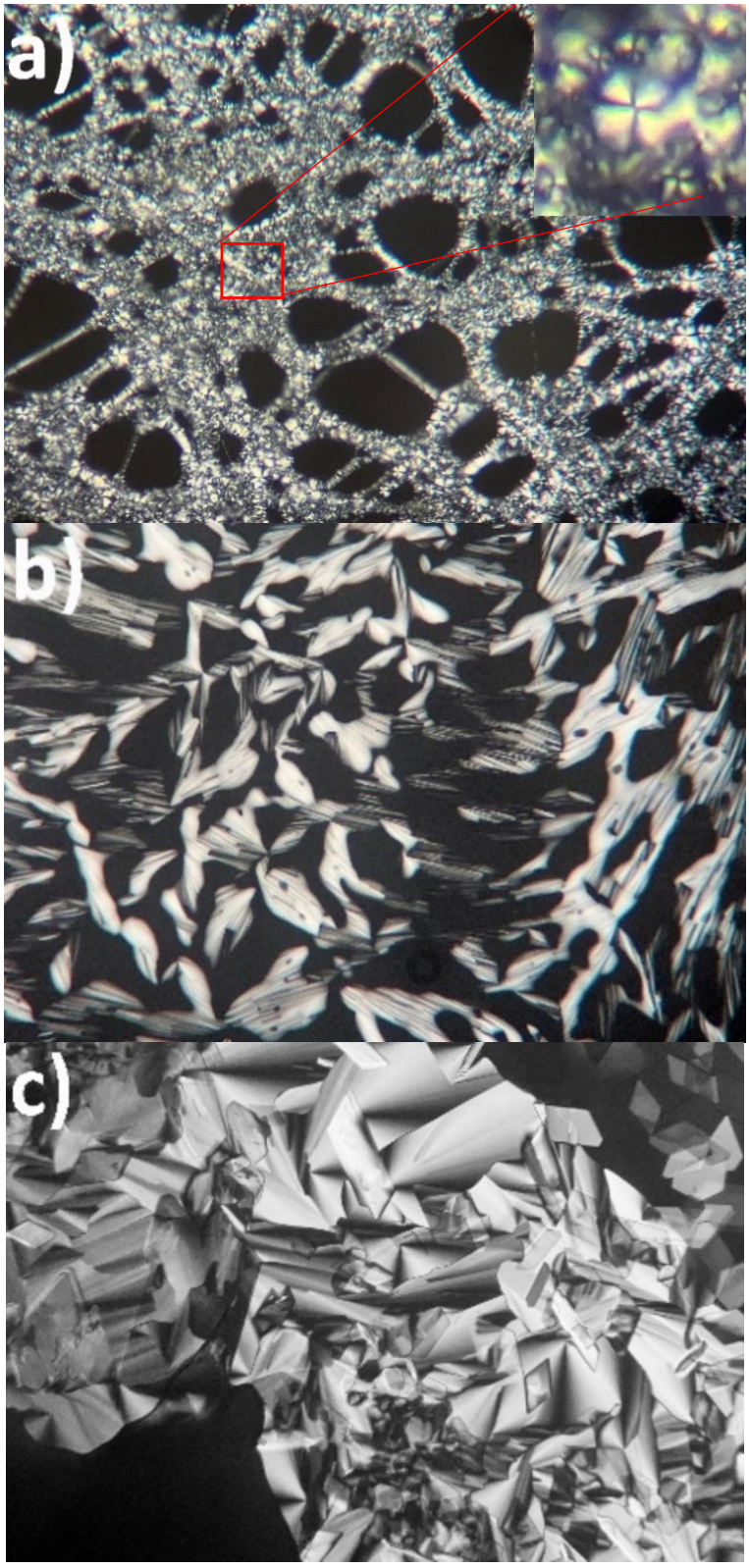

Figure 3.12. Representative POM images of lyotropic phase for ternary mixtures at around 18 wt% of water: a) ternary mixture containing benzene at [C_{10}MIM][OAc]/benzene ratio of 1:1; b) [C_{10}MIM][OAc]/water/resorcinol at [C_{10}MIM][OAc]/precursor ratio of 1:0.5; c) [C_{10}MIM][OAc]/water/phloroglucinol at [C_{10}MIM][OAc]/precursor ratio of 1:0.5.

To reveal how hydroxyl moieties on polymer precursors influence the morphology of IL templates, DFT calculations were performed for ternary systems containing different

precursors at the same mixing ratio ([C_{10}MIM][OAc]:water:phenolic compound = 1:1:4, at which the weighted content of water is approximately 18 wt%). Figure 3.13a shows the overall interaction energies of four ternary mixtures. It was found that non-hydrogen bonding was the major interaction for the benzene-based ternary system, within which the Van der Waal forces and hydrophobic interactions likely dominated the self-assembly. Upon the addition of phenolic compounds containing hydroxyl groups, H-bonding interactions became the major driving force for self-assembly. The increase in the number of hydroxyl groups led to a steady growth in H-bonding energies from 329.2 to 539.5 kJ/mol. Conversely, the non-hydrogen bonding interaction energy declined gradually from 383.9 to 252.8 kJ/mol. This trend became more evident in a ternary system containing phloroglucinol, within which the H-bonding energy was more than twice that of non-H-bonding interactions.

To further investigate the role of increasing numbers of hydroxyl groups, H-bonds were classified in two types: the H-bonds associated with phenolic compounds (*i.e.* phenolic···H-acetate, phenolic···H-water, phenolic···H-cation, water···H-phenolic, and acetate···H-phenolic), the H-bonds involving the $[C_{10}MIM]^+$ cation, acetate anion, and water. As shown in Figure 3.13b, benzene barely forms H-bonds with the other two species and the only H-bonds exist between ILs and water, mainly acetate···H-water. In the presence of a growing number of hydroxyl groups, the H-bonding energy associated with phenolic compound sees a steady rise from 145.7 kJ/mol in ternary mixture containing phenol to 241.0 kJ/mol in that with phloroglucinol. An obvious diminishing effect in acetate···H-water interactions is shown as the hydroxyl group triples. This is because the acetate···H-phenolic bond and water···H-phenolic bond are two dominating H-bonds, contributing to over 92% of total H-bonding energy involving phenolic precursors, especially the former. When phenolic compounds compete in their interactions with water, the number of H-bonds formed between acetate and water became less. Consequently, more water molecules tended to form H-bonds with themselves *via* O···H-O bond, whose energy value climbed from 39.5 (in phenol case) to 72.2 kJ/mol (in phloroglucinol case) with an increment around 16.3 kJ/mol per hydroxyl group. This also elucidates how phenolic compounds could destabilise the periodic H-bonds lattice between ILs and water, hence the disappear of lyotropic gels.

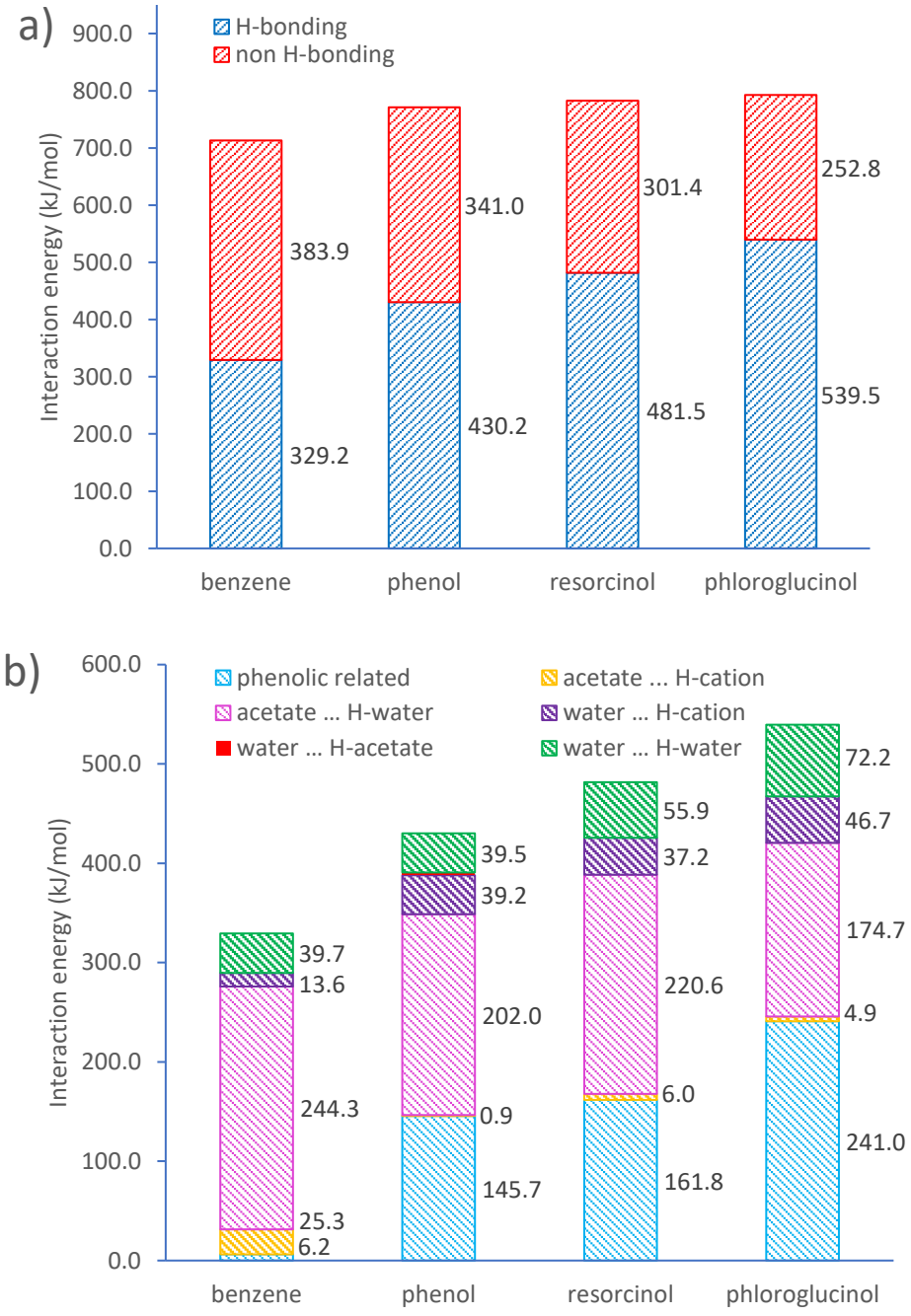

Figure 3.13. a) Total interaction energy and b) H-bonding interaction energy changes with increasing hydroxyl group numbers obtained by natural bond orbital (NBO) analysis.

Detailed H-bonding interaction energy and individual significant H-bond within four different ternary systems can be found in Table 3.3, Table 3.4, and Figure 3.14. Table 3.3 summarises all the H-bonding interaction energies measured by NBO analysis for ternary systems containing phloroglucinol, resorcinol, phenol, and benzene, respectively. The parameters found by the NBO and QTAIM analysis for each single significant H-bond found for the different phenolic systems are listed in Table 3.4, with the percentage in total interaction energy these H-bonds contribute shown in Figure 3.14.

In general, the different parameters found by QTAIM and NBO analysis agree well with the relative strength of the H-bonds. The strengths of H-bonds were approximately the same for the different phenolic compounds, with the main difference being an increase in the number of significant H-bonds and in the percentage of the total interaction contributed by H-bonds for the phenolics with more hydroxyl groups. Only three significant H-bonds were found for the benzene ternary system whereas nine were found for the phloroglucinol system. Three water-H…acetate bonds were found for every system, with a single phenolic-H…acetate involving the hydrogen of the hydroxyl group, except for benzene as without the presence of the hydroxyl group was not able to form this type of H-bond. Above these four H-bonds, the acetate/anion displayed a saturation(-like) effect and did not form any further significant H-bonds. According to most of the metrics given in Table 3.4, these H-bonds where acetate is the hydrogen acceptor were the strongest formed, with acetate-H…water strongest for the benzene and resorcinol systems and acetate-H…phenolic strongest for the phenol and resorcinol. The resorcinol and phloroglucinol systems also displayed a strong H-bond of type phenolic-H…water, with the phloroglucinol system also showing a weaker bond of type water-H…phenolic. Interestingly, the addition of significant H-bonds with increasing hydroxyl groups can only partially be explained by bonds where the phenolic is directly involved. Indeed, the resorcinol and phloroglucinol also displayed a significant water-cation H-bond and an increase in the number of significant water-water H-bonds can also be seen from only one for phenol to two for resorcinol and phloroglucinol. This indicates that the different phenolic compounds influence the H-bonding ability of other molecules in the system by competing. The lack of a dramatic increase in the number of H-bonds directly involving the hydroxyl group of resorcinol and phloroglucinol can be observed. This could be further evidence that the smaller system size of the DFT calculations may cause the missing of some possible H-bonds of the hydroxyl group due to the lack of neighbouring IL systems; the differences in H-bonding between phenol and resorcinol/phloroglucinol as calculated by DFT might be smaller than real values. For instance, only one oxygen of a phenolic is a H-acceptor for only the phloroglucinol situation displaying that this type of bonding is possible yet does not occur frequently in the DFT modelling due to the additional hydroxyl groups of the resorcinol and phloroglucinol molecules being in a position where they do not form bonds with molecules from neighbouring IL systems which would be there in reality. This could be attributed to the low water content in mixtures, around 18 wt% and there is strong competition to form H-bonds between $[C_{10}MIM][OAc]$, water, and phenolic compounds.

Table 3.3. H-bonding interaction energy within ternary systems.

Hydrogen bonds	**Ternary mixtures**			
	phloroglucinol	**resorcinol**	**phenol**	**benzene**
acetate ... H-cation	4.85	6.02	0.88	25.31
acetate … H-water	174.72	220.62	202.00	244.35
acetate … H-phenolic	134.14	74.48	133.93	0.00
water … H-cation	46.74	37.24	39.16	13.64
water … H-acetate	0.00	0.00	2.93	0.00
water … H-water	72.22	55.90	39.54	39.71
water … H-phenolic	88.28	84.52	0.00	6.23
phenolic … H-cation	0.00	0.00	0.84	0.00
phenolic … H-acetate	0.00	0.00	1.30	0.00
phenolic … H-water	18.58	2.76	9.62	0.00
Total energy (kJ/mol)	539.53	481.54	430.20	329.24

Table 3.4. Parameters found by QTAIM and NBO analysis for each significant H-bond in ternary mixtures.

benzene						
molecules involved	bond length (A)	ρ_{BCP} (a.u.)	$\nabla^2\rho_{BCP}$ (a.u.)	H_{BCP}	H-bond energy from ρ_{BCP} (kJ/mol)	E2 kJ/mol
water-H…acetate	1.677	0.04752	0.12699	-0.00904	-70.54	124.60
water-H…acetate	1.767	0.03892	0.12009	-0.00401	-58.57	84.10
water-H…acetate	1.929	0.02443	0.10520	0.00239	-38.43	22.22
phenol						
molecules involved	bond length (A)	ρ_{BCP} (a.u.)	$\nabla^2\rho_{BCP}$ (a.u.)	H_{BCP}	H-bond energy from ρ_{BCP} (kJ/mol)	E2 kJ/mol
phenolic-H…acetate	1.642	0.04954	0.1362	-0.00980	-73.35	128.74
water-H…acetate	1.714	0.04317	0.1254	-0.00648	-64.49	88.32
water-H…acetate	1.796	0.03322	0.1200	-0.00087	-50.66	55.77
water-H…acetate	1.803	0.03429	0.1178	-0.00162	-52.14	57.91
water-H...water	1.909	0.02690	0.1003	0.00095	-41.87	40.04
resorcinol						
molecules involved	bond length (A)	ρ_{BCP} (a.u.)	$\nabla^2\rho_{BCP}$ (a.u.)	H_{BCP}	H-bond energy from ρ_{BCP} (kJ/mol)	E2 kJ/mol
phenolic-H…acetate	1.795	0.03490	0.1152	-0.00221	-52.99	74.48
water-H…acetate	1.634	0.04992	0.1378	-0.00994	-73.88	113.47
water-H…acetate	1.798	0.03318	0.1162	-0.00121	-50.59	57.82
water-H…acetate	1.861	0.03077	0.1084	-0.00033	-47.24	49.33
cation-H...water	2.072	0.02036	0.0774	0.00251	-32.78	33.60
phenolic-H…water	1.761	0.03852	0.1182	-0.00413	-58.03	84.52
water-H...water	1.967	0.02375	0.0912	0.00176	-37.49	30.92
water-H...water	1.988	0.02285	0.0913	0.00211	-36.23	24.98
phloroglucinol						
molecules involved	bond length (A)	ρ_{BCP} (a.u.)	$\nabla^2\rho_{BCP}$ (a.u.)	H_{BCP}	H-bond energy from ρ_{BCP} (kJ/mol)	E2 kJ/mol
phenolic-H…acetate	1.650	0.04845	0.1360	-0.00911	-71.83	131.46
water-H…acetate	1.691	0.04047	0.1421	-0.00364	-60.74	84.18
water-H…acetate	1.811	0.03394	0.1139	-0.00175	-51.65	56.36
water-H…acetate	1.920	0.02567	0.1005	0.00152	-40.15	30.84
cation-H...water	1.999	0.02420	0.0902	0.00196	-38.12	45.02
phenolic-H…water	1.736	0.03987	0.1236	-0.00451	-59.90	88.28
water-H…phenolic	1.977	0.02125	0.0895	0.00267	-34.01	18.58
water-H...water	1.929	0.02687	0.0979	0.00083	-41.83	38.66
water-H...water	1.942	0.02542	0.0977	0.00148	-39.81	32.05

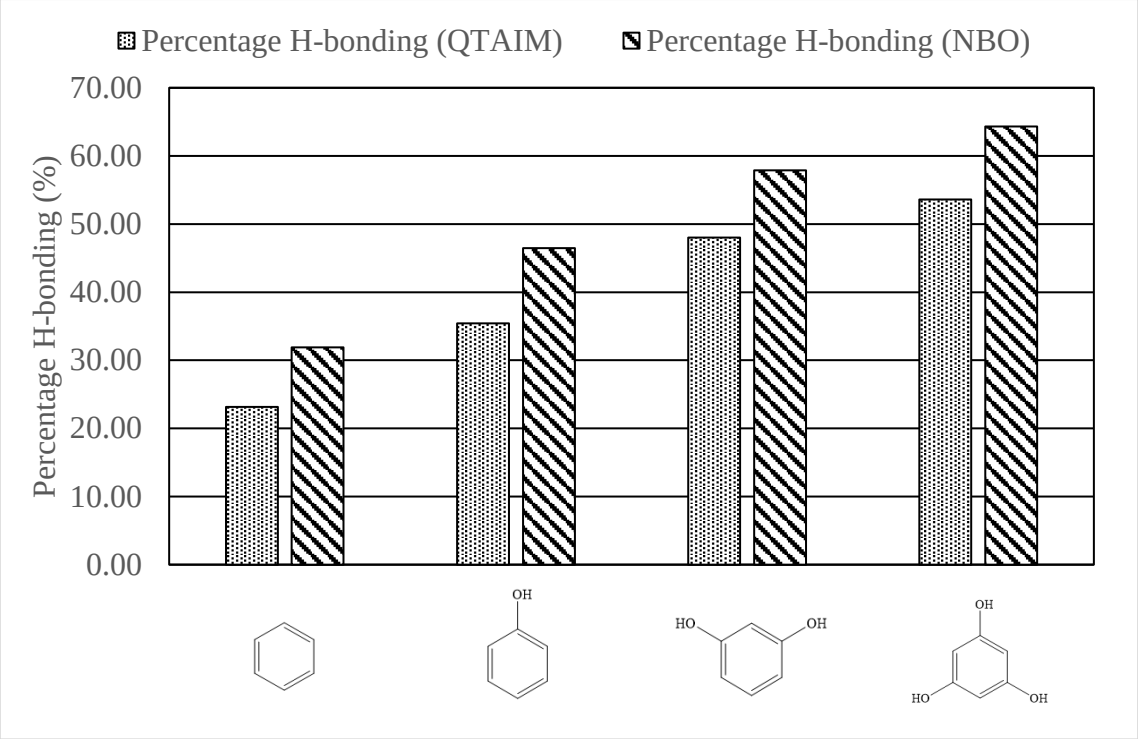

Figure 3.14. Comparison of QTAIM and NBO analysis in measuring the percentage of H-bonding contribution to total interaction energy.

H-bonding in systems incorporating ions is likely to correlate with charge transfer between ion pairs; this brings difficulties in estimating the H-bond energy.[69] We studied the charge transfer from acetate to $[C_{10}MIM]^+$ cation within ternary systems with a single isolated ion-pair; corresponding values were 0.228e, 0.229e, 0.257e, and 0.230e for mixtures containing benzene, phenol, resorcinol, and phloroglucinol, respectively. Considering that the values for individual per anion in bulk systems are expected to be slightly smaller[69], the charge transfer values within ternary systems with different phenolic precursors are quite comparable. Therefore, the increase in H-bonding interaction energy values is attributed primarily to the growing hydroxyl group number.

During revealing the atomistic interactions within the ternary systems by performing DFT calculation, there are some inherent limitations. DFT calculations neglected the factor of temperature and the statistical sampling of relevant degrees of freedom at operating temperatures. It stresses on the global minimum energy and the realistic interactions at 298.15 K may slightly differ from those result by DFT calculation. Moreover, DFT calculations were performed for single-unit ternary systems containing only one IL molecule for the ease of analysing the interactions. This inevitably ignored other assemble possibilities and the effect of cooperative solvent due to lack of solvent molecules near neighbouring IL molecules. Atomistic MD simulations may be more suitable to manifest the realistic

interactions, but this requires the parameterisation of reliable compatible atomistic models for all chemical species especially for phenolic compounds.

3.3.4. Influence of temperature on the morphology of IL templates

Temperature is also a typical factor that influences the phase behaviour of amphiphiles in binary mixture.[9] During templating synthesis, the cross-linking of phenolic precursors is normally carried out above 343.15 K, where morphology evolution might be different with that at lower temperatures.

As shown in Table 3.1 and Figure 3.15, CG MD simulation results indicate that the morphology evolution at 358.15K, a typical temperature for cross-linking, follows the same trend with that at lower temperature, but the phase transition points (or CMCs) varies slightly. For IL/water/phenol ternary mixture with 44 wt% of water, IL templates present spherical structures at higher temperature which then evolve into ordered hexagonal columnar phases after temperature quenching. Morphological evolution has not taken place at higher temperature yet. Similarly, the third CMC with morphology transiting from hexagonal columnar to smectic lamellar happens at a higher water content at 358.15 K than that at 298.15 K. This is possibly because the larger kinetic energy at a higher temperature is accelerating the molecule motions, which makes it easier to cross the energy barrier for morphology transition.

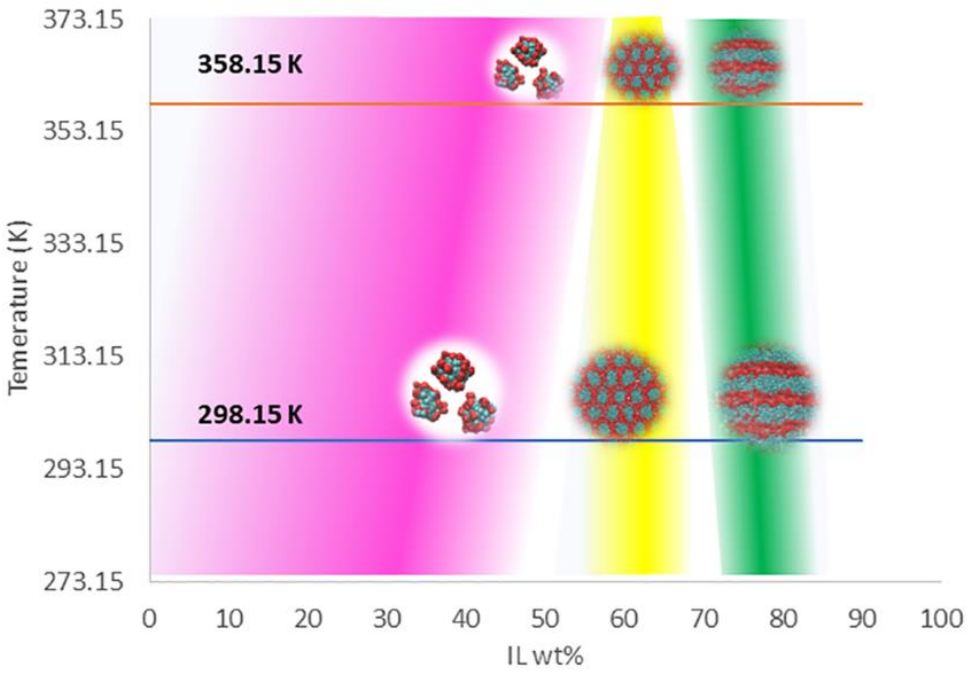

Figure 3.15. Influence of temperature on the morphology evolution of [C_{10}MIM][OAc]/water/phenol ternary mixtures.

Note that current Martini 2.2 models have several potential limitations to be used in this work, especially with respect to the applicability and availability of CG models. For example, CG models for ILs were initially trained to fit experimental results at room temperature, their performance at higher temperature remains to be rigorously studied although they can lead to predictions on the morphological changes at higher temperatures. Moreover, sophisticated CG models for typical cross-linkers (such as formaldehyde, glyoxal, and glyoxylic acid) need to be trained at varying temperatures to enable the study of the influence of cross-linkers on the morphologies of IL templates in a quaternary system including ILs, phenolic compounds, solvent, and cross-linkers. With the increasing numbers of chemical species in the system, it will also add up the challenge for experimental validation of such models regarding the measurement of morphology by scattering technique. Beside of this, other limitations also exist such as the underestimated packing distance, which typically leads to a smaller density value than experimental value and this has already been discussed earlier in this chapter.

3.3.5. Polymer precursor – IL template spatial correlation analysis

In a practical templating synthesis of mesoporous polymer and carbon materials, precursors are expected to be first attached and subsequently being cross-linked in the amphiphilic part of the templates.[1,70,71] Therefore, it is important to understand the spatial correlations between precursors and IL templates.

In Figure 3.9, the distribution difference of various phenolic precursors in mixtures can be observed. For ternary mixtures containing 18 wt% of water, phenol (yellow particles), as well as benzene, mostly resides in the hydrophobic cores formed by the aggregation of alkyl chain of $[C_{10}MIM]^+$ cations (cyan particles); resorcinol and phloroglucinol are dispersed toward the outer layer, the aqueous phase. The increasing number of hydroxyl groups in phenolic precursors are likely to not only influence the morphology of IL templates, also the distribution of phenolic precursors within the multiple-species systems.

To acquire a more detailed distributional preference, centre of mass (COM) radial distribution functions (RDFs) were extracted from the simulation. The anion-water pair is the most prominent correlation throughout four ternary systems (Figure 3.16). This might be attributed to the strong H-bonding ability between acetate and water, where $RCOO^-$ is expected to form 6 H-bonds with water molecules on average.[72] For ternary mixtures containing benzene or phenol, the subsequent strongest correlations are cation-anion and cation-water pairs while the weakest correlation is found between the precursor with the ILs

and water (Figure 3.16a, b). As the number of hydroxyl groups increases in the precursor, the peaks for the resorcinol-anion correlation and resorcinol-water correlation grow higher, leaving the cation-resorcinol correlation as the weakest (Figure 3.16c). The correlation of the phloroglucinol-acetate pair becomes the second strongest, followed by the phloroglucinol-water pair. The presence of more hydroxyl groups to polymer precursors seemingly favours the interaction between precursor and aqueous phase.

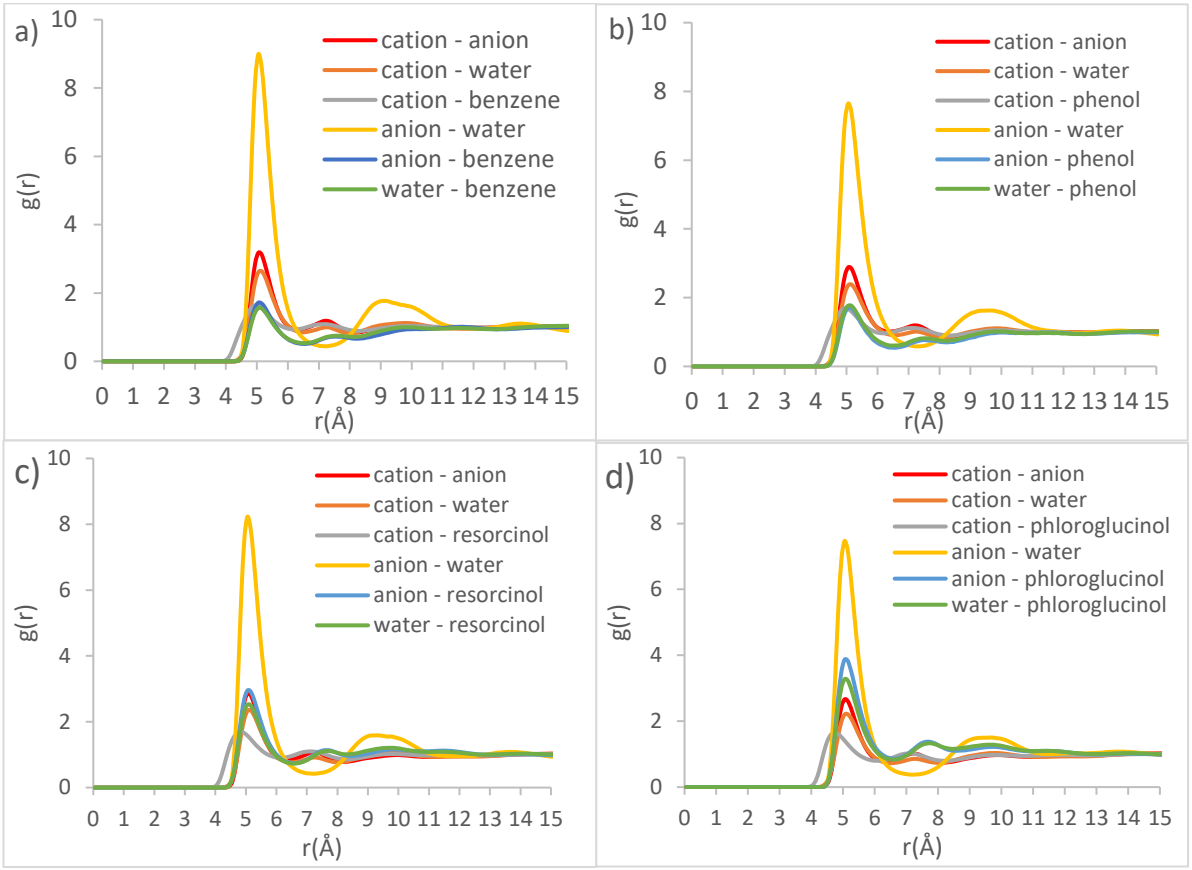

Figure 3.16. COM RDFs for ternary systems containing a) benzene, b) phenol, c) resorcinol, and d) phloroglucinol, respectively.

Figure 3.17 shows the detailed site-site RDFs between phenolic precursors and $[C_{10}MIM]^+$ cation, which plays the role of a template (beads cation 1-3 and 4-6 represent the imidazolium ring and alkyl chain, respectively; see Figure 3.2). Phenol, as well as benzene, has the strongest correlation with bead cation 4, followed by cation 5 and 6 (Figure 3.17b). This indicates phenol has a distributional preference towards the area where the alkyl chain attaches to the imidazolium ring. The interactions between resorcinol and the imidazolium ring of the cation become stronger, whereas the correlation for cation 4-resorcinol pair remains the strongest (Figure 3.17c). Compared with phenol, the two hydroxyl groups in resorcinol double its H-bonding ability. Consequently, resorcinol is dispersed towards the imidazolium ring where there is a higher possibility to interact with acetate and water *via* H-

bonds. In ternary mixture containing phloroglucinol (Figure 3.17d), the strongest site-site correlations are found in phloroglucinol with cation 1 and cation 2, as opposed to cation 4 as witnessed previously. Since phloroglucinol has mostly dispersed into the hydrophilic phase, the outer layer of template clusters, its correlations with alkyl chain become the weakest.

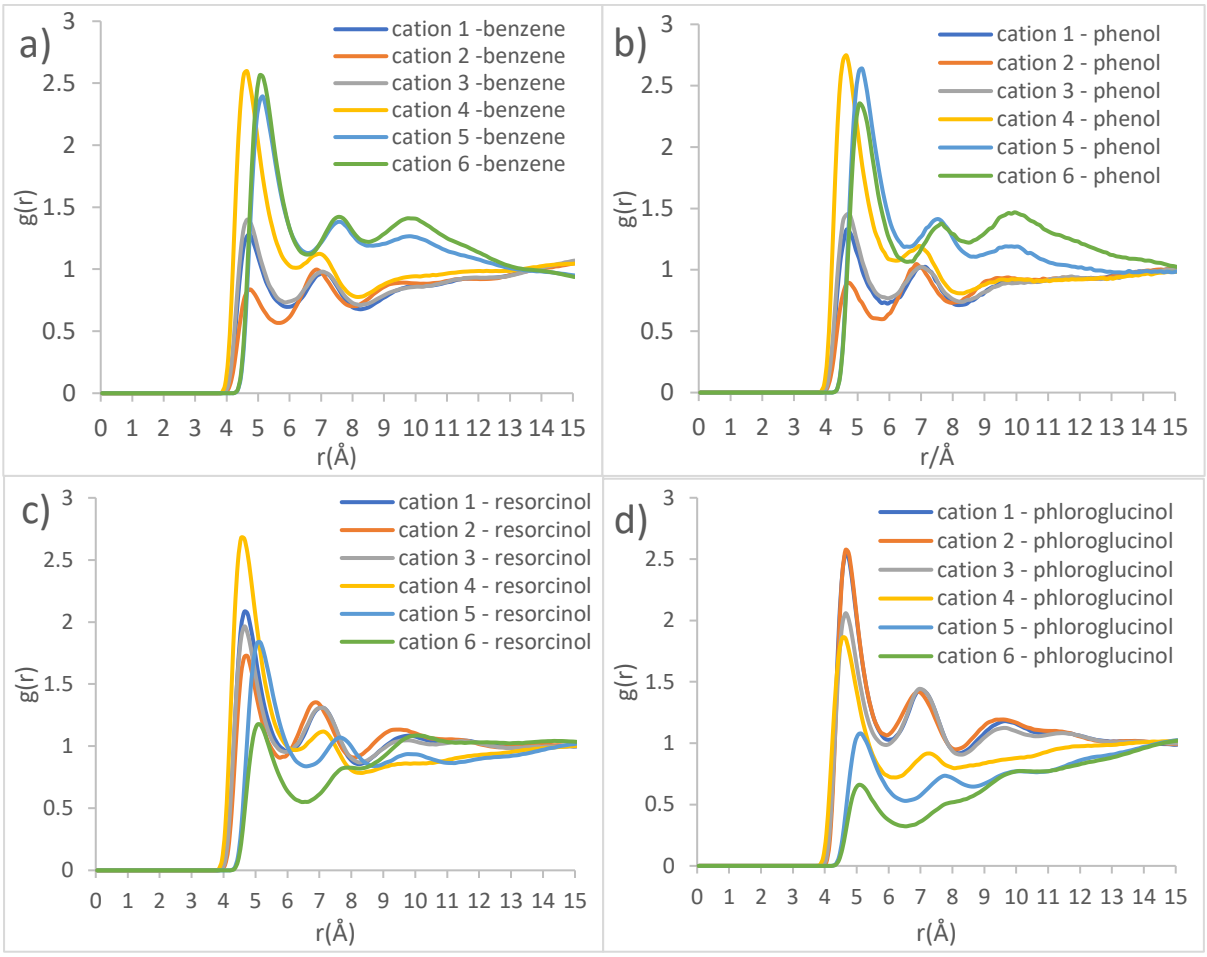

Figure 3.17. Site-site RDFs of IL templates and various precursors a) benzene, b) phenol, c) resorcinol, and d) phloroglucinol, respectively.

According to the RDF analyses, involving more hydroxyl moieties in the precursor favours the interaction with the amphiphilic part of template, leaving the hydrophobic part as potential pore structures. To confirm this, the structures of ternary mixtures containing a single ion pair were optimised by DFT calculations to manifest the dominant configurations within the dynamic systems. As shown in Figure 3.18, reference distances between terminal carbon (C10) and the projection point of precursor geometric centre onto the alkyl chain were estimated based on Table 3.5 to show the degree of dispersion. A clear trend is found that the precursors were dispersed further from the terminal carbon of alkyl chain as the hydroxyl groups increase, resulting in an increase in the reference distance from benzene to phloroglucinol. Benzene and phenol have the least distance with C5-C7, C2-C5 of the alkyl

chain, respectively. Resorcinol is distributed around C1 and C2, and phloroglucinol around N atom linked to the methyl side group of the cation. This result coincides well with the strongest pair spatial correlations in CG MD simulations.

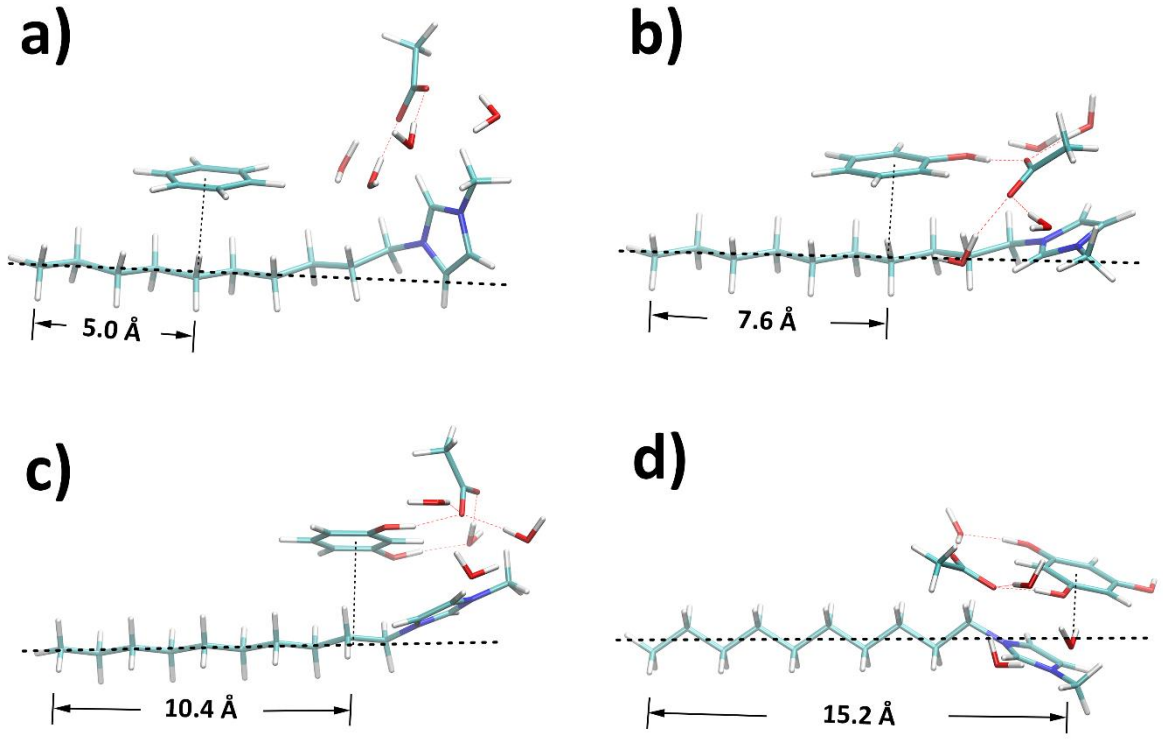

Figure 3.18. Structures optimised by DFT for ternary mixtures containing a) benzene, b) phenol, c) resorcinol, and d) phloroglucinol, respectively.

Moreover, the closer proximity of the phenolic compound and the Imidazolidine ring appears to have the effect on straightening out the cation causing the angle of the alkyl chain to approach 180°. This has an additional consequence of causing a closer to parallel orientation between the phenolic and imidazolium ring structures, which will likely induce dispersive interactions between the rings. The phenolic compound resides closer to the cation, which would be expected with the stronger interaction between the two molecules. A potential explanation is that the additional hydroxyl groups induce a stronger phenolic-ionic interaction thus disrupt the interactions between the anion and cation, allowing the phenolic compounds to occupy the space. This would also explain the weaker ionic-ionic and water-ionic found with more hydroxyl groups present.

Table 3.5. Molecular geometry parameters for each phenolic compound in relation to the cation.

Ternary mixtures containing various precursors	d1 (Å) (end chain to centre of phenolic compound ring)	d2 (Å) (nearest chain carbon to centre of phenolic compound ring)
benzene	6.15	3.52
phenol	8.36	3.51
resorcinol	10.91	3.39
phloroglucinol	15.55	3.13

Experimental evidence was acquired by 2D NOESY NMR spectroscopy. Protons close to each other in space (with a distance less than 3.5 Å) are likely to show stable cross peaks in the 2D spectra. A NOESY experiment for ternary mixture containing benzene was performed with deuterated oxide as internal reference due to the formation of lyotropic gels. From Figure 3.19, the protons on benzene (7.0 ppm) only show cross peaks with H atoms linked to C3-C9 in the alkyl chain (broad peak from 0.9 to 1.0 ppm), therefore benzene is mostly distributed near the alkyl chain. As aforementioned, benzene barely interacts with [C_{10}MIM][OAc] and water so non-H-bonding interactions such as the Van der Waal force and hydrophobic interaction play major roles in the distribution of benzene. H atoms on phenol (6.5, 6.3, and 6.1 ppm) also present weak cross peaks with methyl group linked to the imidazolium ring, which infers that a small proportion of phenol remains in the aqueous phase. The cross peaks between protons on resorcinol (6.2, 5.8, and 5.7 ppm) and the imidazolium ring (6.7 and 6.6 ppm) confirm that some resorcinol molecules have started to disperse into the aqueous phase. When the hydroxyl groups are tripled, cross peaks resulting from the interactions between phloroglucinol (5.0 ppm) and the aqueous phase (mainly water at 6.0 ppm and acetate at 1.1 ppm) become more evident due to their strong interaction with the hydrophilic aqueous phase. Moreover, the peak for water shifts to high field with a growing number of hydroxyl group, from 5.5 ppm in the case of phenol to 6.0 ppm in the case of phloroglucinol, which can be attributed to the growing H-bonding interactions between precursor and water.

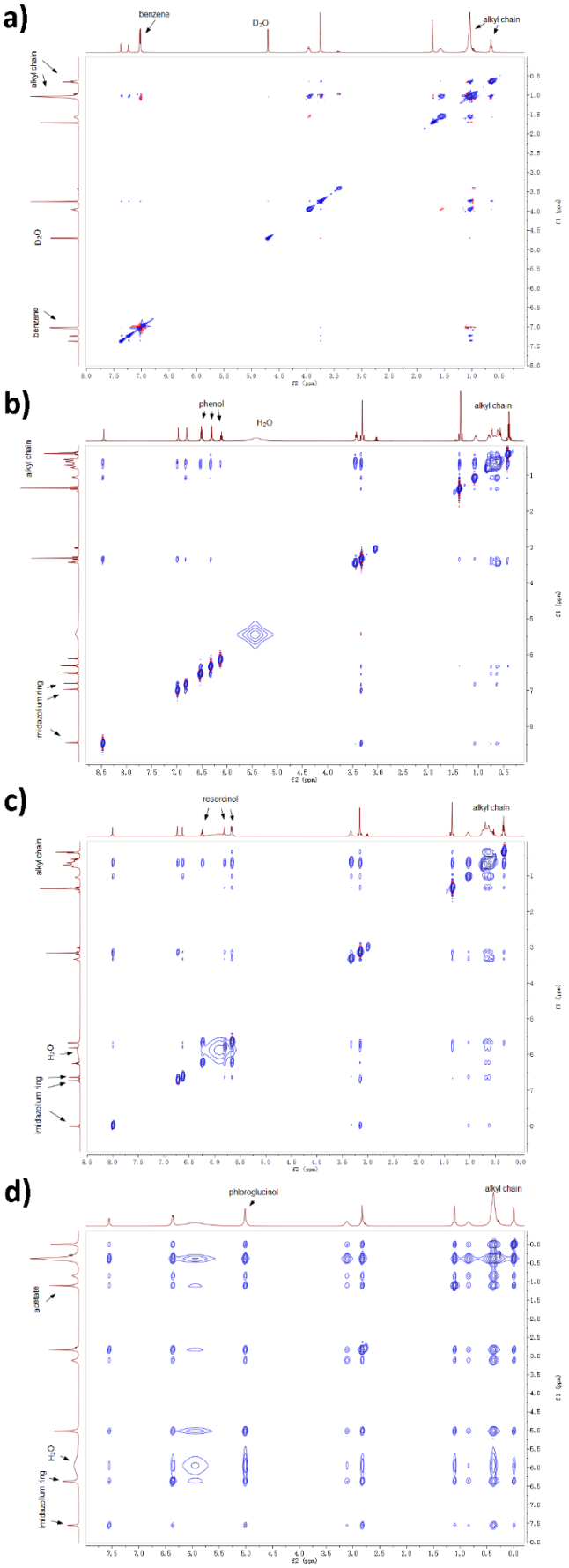

Figure 3.19. 2D NOESY NMR experiments for ternary mixtures containing a) benzene, b) phenol, c) resorcinol, and d) phloroglucinol, respectively.

The results above also provide explanations on why phenolic compounds with different hydroxyl groups present different extraction efficiencies during extraction from waste water by employing imidazolium based ILs[73–75]. The extraction percentage for phenol generally exceeds 90%, while that for resorcinol is smaller than 60%.[73] Phenol resides mostly in the hydrophobic phase of the IL cation, but its H-bonding ability *via* -OH results in a small ratio of phenol remaining in the aqueous phase. Resorcinol, due to the doubled hydroxyl groups, is observed mostly near the C1 atom of the IL alkyl chain thus has a poorer extraction efficiency.

Furthermore, template-precursor spatial correlations may also influence the morphological evolution of IL templates by influencing the competition between the hydrophobic attraction and hydrophilic ionic repulsion interactions, which determines the bending or curvature energy and the preferred packing geometries of amphiphiles.[68] At around 18 wt% of water, [C_{10}MIM][OAc]/water binary mixture shows a hexagonal columnar phase. When phenol or benzene is added, the precursors enrich the hydrophobic phase by a space-occupying effect due to their spatial preference to the IL alkyl chains, leading to much stronger hydrophobic attraction interactions. The morphology of $[C_{10}MIM]^+$ cations has transformed into lamellar bilayer array, which tends to appear at more reduced water contents, *i.e.* the reduced hydrophilic or ionic repulsion interactions. Phloroglucinol and resorcinol tend to strongly correlate with the aqueous phase thus could enrich the hydrophilic phase by a space-occupying effect and cause stronger hydrophilic ionic repulsion interactions. Consequently, spherical clusters are observed at 33.8 wt% of water for a ternary mixture containing resorcinol, and at 25.0 wt% for their phloroglucinol counterpart (Table 3.1), where the binary mixtures based on Figure 3.3a still remain in the hexagonal phase.

3.3.6. Proposed synthesis routes for nanomaterials and applications

This chapter systematically investigated the morphological evolutions of ILs as the recyclable template and the spatial correlation between IL templates and precursors; the use of recyclable IL templates delivers increasing sustainability to the preparation process of nanomaterials by potentially lowering economic cost. The findings from this chapter provide significant guidance on seeking promising synthetic routes of tailored porous nanomaterials aimed for specific applications.

Based on the difference in spatial distribution, the selection of precursors could lead to diverse nanostructures for various applications (Table 3.6). For example, the correlation

preference of phenol to hydrophobic phase of IL templates enables them for preparing 0-D carbon nanospheres, 1-D nanowires, and 2-D nanoplates/nanosheets when the morphologies of the IL templates are spherical, columnar, and lamellar, respectively. Resorcinol and phloroglucinol preferentially reside in the hydrophilic aqueous phase, leaving the hydrophobic alkyl chain phase to generate pores after removal of the IL templates. Therefore, they could be promising candidates for hollow spheres or porous materials, ordered mesoporous polymer/carbon materials when spherical, hexagonal columnar micelle clusters form, especially when using phloroglucinol as a precursor.

Table 3.6. Potential applications for nanomaterial preparation based on the results from this chapter.

Precursor	Water content[a] (wt%)	Morphologies of $[C_{10}MIM][OAc]$ templates	Potential nanomaterials	Representative down-stream applications
phenol	50 - 90	spherical	Carbon nanoparticles/nanosphere	Catalysis, oxygen reduction reactions
	30 - 45	hexagonal columnar	Carbon nanowires/fibres	Energy storage, electrocatalysis
	18 - 25	lamellar bilayer	Nanoplates, nanosheets	Photocatalysis, energy storage
resorcinol	> 34	spherical	Hollow spheres, porous carbons/polymers	Water treatment, heterogeneous catalysis
	18 - 25	hexagonal columnar	Ordered mesoporous polymer/carbon	Energy storage, drug delivery, catalysis
phloroglucinol	> 25	spherical	Hollow spheres, porous carbons/polymers	Separation, water treatment, catalysis
	< 18	hexagonal columnar	Ordered mesoporous polymer/carbon	Biosensor, energy storage, drug delivery

[a] means relative water content: $m(H_2O)/(m(H_2O) + m(ILs))$, excluding the precursor

However, the influence of cross-linkers on the self-assembly needs to be stressed. Phenolic precursors are expected to be cross-linked suitably after the self-assembly process to obtain a stable polymer structure. But commonly used cross-linkers such as formaldehyde, glyoxal and glyoxylic acid, may introduce hydroxyl groups into mixture, which can potentially affect both the template morphologies and precursor-template spatial correlations. Different precursor/template mixing ratios and chain lengths of IL cations may also lead to different results. These could be further investigated in the future by performing CG MD simulations, which in this chapter presented great reliability as confirmed by the experimental results. Nevertheless, the current version of Martini models typically underestimates the stacking distance of ring structures, resulting in lower densities than found as experimental values.[32,35,76,77] Therefore, CG MD simulations might be more competent to emphasise the mesoscopic self-assembly behaviour rather than quantifying statistic properties such as density and atomistic interaction energies.

3.4. Conclusions

The self-assembly process in a soft-templating synthesis of nano-structured polymers and carbon materials was systematically investigated, where long-chain imidazolium based ILs were employed as recyclable templates. The two crucial factors that determine the eventual structure of nanomaterials were highlighted particularly as 1) the morphology of IL templates and 2) the precursor-template spatial correlations.

The morphologies of amphiphilic IL templates are not only tuneable through the adjustment of water content in mixture but also by the selection of the precursors. With the increase of water content in the mixture, the morphology of IL templates undergoes smectic lamellar bilayer, hexagonal columnar and spherical structures. At the same mixing ratio, introducing more hydroxyl groups to the material precursor also changes the morphology of IL templates, such as from a lamellar bilayer to a hexagonal columnar phase. The rationale of both approaches lies in adjusting the H-bonding probability of IL templates in the mixture.

Material precursors with different hydroxyl moieties lead to different precursor-template spatial correlations. More hydroxyl groups in the polymer precursor could increase the H-bonding ability and disperse precursors from a hydrophobic phase to a hydrophilic phase.

This chapter presents a theoretical basis on the mechanism of soft-templating synthesis with amphiphilic ILs as recyclable templates and gives insight into how to design coveted nanomaterials for targeting applications. Consequently, special attention is expected to be paid to the precise manipulation of templates into desired morphologies by adjusting mixing ratios and the rational selection of material precursors based on template-precursor spatial correlations. The results from this chapter could guide the preparation of MCs by employing IL templates in the later chapter.

3.5. References

1 Y. Meng, D. Gu, F. Zhang, Y. Shi, L. Cheng, D. Feng, Z. Wu, Z. Chen, Y. Wan, A. Stein and D. Zhao, *Chem. Mater.*, 2006, **18**, 4447–4464.

2 D. Saha, R. Zacharia and A. K. Naskar, in *Polymer Precursor-Derived Carbon*, 2014, vol. 1173, pp. 61–83.

3 J. M. Vicent-Luna, J. M. Romero-Enrique, S. Calero and J. A. Anta, *J. Phys. Chem. B*, 2017, **121**, 8348–8358.

4 R. Vanyúr, L. Biczók and Z. Miskolczy, *Colloids Surfaces A Physicochem. Eng. Asp.*, 2007, **299**, 256–261.

5 Y. Zhao, S. Gao, J. Wang and J. Tang, *J. Phys. Chem. B*, 2008, **112**, 2031–2039.

6 J. N. A. Canongia Lopes and A. A. H. Pádua, *J. Phys. Chem. B*, 2006, **110**, 3330–3335.

7 I. Goodchild, L. Collier, S. L. Millar, I. Prokeš, J. C. D. Lord, C. P. Butts, J. Bowers, J. R. P. Webster and R. K. Heenan, *J. Colloid Interface Sci.*, 2007, **307**, 455–468.

8 H. Kaper and B. Smarsly, in *Zeitschrift fur Physikalische Chemie*, De Gruyter, 2006, vol. 220, pp. 1455–1471.

9 E. A. Crespo, N. Schaeffer, J. A. P. Coutinho and G. Perez-Sanchez, *J. Colloid Interface Sci.*, 2020, **574**, 324–336.

10 K. Dong, X. Liu, H. Dong, X. Zhang and S. Zhang, *Chem. Rev.*, 2017, 117, 6636–6695.

11 M. A. Firestone, P. G. Rickert, S. Seifert and M. L. Dietz, *Inorganica Chim. Acta*, 2004, **357**, 3991–3998.

12 K. Goloviznina, J. N. Canongia Lopes, M. Costa Gomes and A. A. H. Pádua, *J. Chem. Theory Comput.*, 2019, **15**, 5858–5871.

13 B. Doherty, X. Zhong and O. Acevedo, *J. Phys. Chem. B*, 2018, **122**, 2962–2974.

14 J. N. Canongia Lopes and A. A. H. Pádua, *Theor. Chem. Acc.*, 2012, 131, 1–11.

15 B. L. Bhargava, R. Devane, M. L. Klein and S. Balasubramanian, *Soft Matter*, 2007, **3**, 1395–1400.

16 C. Merlet, M. Salanne and B. Rotenberg, *J. Phys. Chem. C*, 2012, **116**, 7687–7693.

17 D. Sun and J. Zhou, *AIChE J.*, 2013, **59**, 2630–2639.

18 A. Moradzadeh, M. H. Motevaselian, S. Y. Mashayak and N. R. Aluru, *J. Chem. Theory Comput.*, 2018, **14**, 3252–3261.

19 H. A. Karimi-Varzaneh, F. Müller-Plathe, S. Balasubramanian and P. Carbone, *Phys. Chem. Chem. Phys.*, 2010, **12**, 4714–4724.

20 B. L. Bhargava and M. L. Klein, *Mol. Phys.*, 2009, **107**, 393–401.

21 Y. Wang, S. Feng and G. A. Voth, *J. Chem. Theory Comput.*, 2009, **5**, 1091–1098.

22 Y. Wang, S. Izvekov, T. Yan and G. A. Voth, *J. Phys. Chem. B*, 2006, **110**, 3564–3575.

23 Y. Wang, W. Jiang, T. Yan and G. A. Voth, *Acc. Chem. Res.*, 2007, **40**, 1193–1199.

24 Y. Wang and G. A. Voth, *J. Am. Chem. Soc.*, 2005, **127**, 12192–12193.

25 D. Roy and M. Maroncelli, *J. Phys. Chem. B*, 2010, **114**, 12629–12631.

26 D. Roy, N. Patel, S. Conte and M. Maroncelli, *J. Phys. Chem. B*, 2010, **114**, 8410–8424.

27 C. Merlet, M. Salanne, B. Rotenberg and P. A. Madden, *J. Phys. Chem. C*, 2011, **115**, 16613–16618.

28 Y. L. Wang, B. Li, S. Sarman, F. Mocci, Z. Y. Lu, J. Yuan, A. Laaksonen and M. D. Fayer, *Chem. Rev.*, 2020, 120, 5798–5877.

29 D. Bedrov, J. P. Piquemal, O. Borodin, A. D. Mackerell, B. Roux and C. Schröder, *Chem. Rev.*, 2019, 7940–7995.

30 B. L. Bhargava, Y. Yasaka and M. L. Klein, *Chem. Commun.*, 2011, **47**, 6228–6241.

31 M. Salanne, *Phys. Chem. Chem. Phys.*, 2015, **17**, 14270–14279.

32 S. J. Marrink, H. J. Risselada, S. Yefimov, D. P. Tieleman and A. H. De Vries, *J. Phys. Chem. B*, 2007, **111**, 7812–7824.

33 G. Huet, M. Araya-Farias, R. Alayoubi, S. Laclef, B. Bouvier, I. Gosselin, C. Cézard, R. Roulard, M. Courty, C. Hadad, E. Husson, C. Sarazin and A. Nguyen Van Nhien, *Green Chem.*, 2020, **22**, 2935–2946.

34 D. H. De Jong, G. Singh, W. F. D. Bennett, C. Arnarez, T. A. Wassenaar, L. V. Schäfer, X. Periole, D. P. Tieleman and S. J. Marrink, *J. Chem. Theory Comput.*, 2013, **9**, 687–697.

35 R. Alessandri, J. J. Uusitalo, A. H. de Vries, R. W. A. Havenith and S. J. Marrink, *J.*

Am. Chem. Soc., 2017, **139**, 3697–3705.

36 L. Martinez, R. Andrade, E. G. Birgin and J. M. Martínez, *J. Comput. Chem.*, 2009, **30**, 2157–2164.

37 G. J. Martyna, D. J. Tobias and M. L. Klein, *J. Chem. Phys.*, 1994, **101**, 4177–4189.

38 S. Nose, *Mol. Phys.*, 2002, **100**, 191–198.

39 W. G. Hoover, *Canonical dynamics: Equilibrium phase-space distributions*, 1985, vol. 31.

40 S. Plimpton, *J. Comput. Phys.*, 1995, **117**, 1–19.

41 W. Humphrey, A. Dalke and K. Schulten, *J. Mol. Graph.*, 1996, **14**, 33–38.

42 D. J. Frisch, M. J.; Trucks, G. W.; Schlegel, H. B.; Scuseria, G. E.; Robb, M. A.; Cheeseman, J. R.; Scalmani, G.; Barone, V.; Petersson, G. A.; Nakatsuji, H.; Li, X.; Caricato, M.; Marenich, A. V.; Bloino, J.; Janesko, B. G.; Gomperts, R.; Mennucci, B.; Hratch, *Gaussian Inc., Wallingford CT*, 2016.

43 T. Lu and F. Chen, *J. Comput. Chem.*, 2012, **33**, 580–592.

44 S. Emamian, T. Lu, H. Kruse and H. Emamian, *J. Comput. Chem.*, 2019, **40**, 2868–2881.

45 H. Yang, X. Cui, Y. Deng and F. Shi, *J. Mater. Chem.*, 2012, **22**, 21852–21856.

46 B. Nagy, E. Geissler and K. László, *Microporous Mesoporous Mater.*, 2020, **294**, 1–10.

47 J. Xia, J. Di, H. Li, H. Xu, H. Li and S. Guo, *Appl. Catal. B Environ.*, 2016, **181**, 260–269.

48 Z. L. Xie and D. S. Su, *Eur. J. Inorg. Chem.*, 2015, **2015**, 1137–1147.

49 X. Kang, X. Sun and B. Han, *Adv. Mater.*, 2016, **28**, 1011–1030.

50 M. Zhen, J. Yu and S. Dai, *Adv. Mater.*, 2010, 22, 261–285.

51 Q. Yang, Z. Zhang, X. G. Sun, Y. S. Hu, H. Xing and S. Dai, *Chem. Soc. Rev.*, 2018, **47**, 2020–2064.

52 B. G. Trewyn, C. M. Whitman and V. S. Y. Lin, *Nano Lett.*, 2004, **4**, 2139–2143.

53 Z. Chen, T. L. Greaves, R. A. Caruso and C. J. Drummond, *J. Mater. Chem.*, 2012, **22**, 10069–10076.

54 I. Kilpeläinen, H. Xie, A. King, M. Granstrom, S. Heikkinen and D. S. Argyropoulos, *J. Agric. Food Chem.*, 2007, **55**, 9142–9148.

55 B. G. Janesko, *Phys. Chem. Chem. Phys.*, 2011, **13**, 11393–11401.

56 R. P. Swatloski, S. K. Spear, J. D. Holbrey and R. D. Rogers, *J. Am. Chem. Soc.*, 2002, **124**, 4974–4975.

57 Y. Zhang, H. He, K. Dong, M. Fan and S. Zhang, *RSC Adv.*, 2017, **7**, 12670–12681.

58 A. Casas, J. Palomar, M. V. Alonso, M. Oliet, S. Omar and F. Rodriguez, *Ind. Crops Prod.*, 2012, **37**, 155–163.

59 J. Zhang, B. Dong, L. Zheng, N. Li and X. Li, *J. Colloid Interface Sci.*, 2008, **321**, 159–165.

60 N. Goujon, M. Forsyth, L. F. Dumée, G. Bryant and N. Byrne, *Phys. Chem. Chem. Phys.*, 2015, **17**, 23059–23068.

61 I. Goodchild, L. Collier, S. L. Millar, I. Prokeš, J. C. D. Lord, C. P. Butts, J. Bowers, J. R. P. Webster and R. K. Heenan, *J. Colloid Interface Sci.*, 2007, **307**, 455–468.

62 P. A. Heiney, in *Handbook of Liquid Crystals*, Wiley-VCH Verlag GmbH & Co. KGaA, Weinheim, Germany, 2014, pp. 1–47.

63 J. Grolik, Ł. Dudek and J. Eilmes, *Tetrahedron Lett.*, 2012, **53**, 5127–5130.

64 J. Kirres, K. Schmitt, I. Wurzbach, F. Giesselmann, S. Ludwigs, M. Ringenberg, A. Ruff, A. Baro and S. Laschat, *Org. Chem. Front.*, 2017, **4**, 790–803.

65 T. Inoue, B. Dong and L. Q. Zheng, *J. Colloid Interface Sci.*, 2007, **307**, 578–581.

66 X. W. Li, J. Zhang, B. Dong, L. Q. Zheng and C. H. Tung, *Colloids Surfaces A Physicochem. Eng. Asp.*, 2009, **335**, 80–87.

67 A. E. Bradley, C. Hardacre, J. D. Holbrey, S. Johnston, S. E. J. McMath and M. Nieuwenhuyzen, *Chem. Mater.*, 2002, **14**, 629–635.

68 J. Israelachvili, *Intermolecular and Surface Forces*, Academic Press, Burlington, MA, 2011, vol. 3rd ed.

69 P. A. Hunt, C. R. Ashworth and R. P. Matthews, *Chem. Soc. Rev.*, 2015, **44**, 1257–1288.

70 C. Liang, Z. Li and S. Dai, *Angew. Chemie Int. Ed.*, 2008, 47, 3696–3717.

71 D. Saha, R. Zacharia and A. K. Naskar, in *Polymer Precursor-Derived Carbon*, 2014, vol. 1173, pp. 61–83.

72 M. V. Fedotova and S. E. Kruchinin, *J. Mol. Liq.*, 2011, **164**, 201–206.

73 O. G. Sas, I. Domínguez, B. González and Á. Domínguez, *J. Environ. Manage.*, 2018, **228**, 475–482.

74 A. H. Turner, E. L. Byrne, T. Pereira and J. D. Holbrey, *Phys. Chem. Chem. Phys.*, 2020, **22**, 10219–10226.

75 E. J. González, I. Díaz, M. Gonzalez-Miquel, M. Rodríguez and A. Sueiras, *Sep. Purif. Technol.*, 2018, **201**, 214–222.

76 X. Periole and S.-J. Marrink, in *Biomolecular Simulations*, Humana Press, Totowa, NJ, 2013, pp. 533–565.

77 C. A. López, A. J. Rzepiela, A. H. de Vries, L. Dijkhuizen, P. H. Hünenberger and S. J. Marrink, *J. Chem. Theory Comput.*, 2009, **5**, 3195–3210.

Chapter 4

Soft-templating synthesis of mesoporous carbons for supercapacitors: the role of cross-linking

4.1. Introduction

As described in *Chapter 1*, the proposed method to prepare MCs by employing ILs as the recyclable template is comprised of four crucial steps: 1) the self-assembly of IL templates and carbon precursors, 2) the cross-linking of carbon precursors, 3) the extraction/recycling of IL template, and 4) the calcination of cross-linked carbon precursors. This chapter is built on the self-assembly mechanism of soft-template synthesis by employing IL templates, as elaborated in *Chapter 3*. Upon understanding the fundamentals on how to control the morphologies of IL templates and how to choose the suitable carbon precursors, this chapter introduces the study on the next step: the cross-linking of carbon precursors. The overall aim of this chapter is to seek out a suitable cross-linker that can bridge the carbon precursors properly to form a continuous matrix and generate a highly ordered mesopore structure after template removal.

Since the first successful attempt to prepare ordered MCs by soft-template technique, formaldehyde has been ubiquitous for the cross-linking/polycondensation of precursor monomers with the resulting pore size highly tuneable.[1–7] However, due to the toxicity of formaldehyde, effort has been directed to seek more eco-friendly substitutes. Ghimbeu *et al.*[8] first employed a plant-derived cross-linker, glyoxylic acid to replace the carcinogen formaldehyde for the soft-template synthesis of ordered MCs. Glyoxylic acid played a bi-functional role in the synthesis, the cross-linker and catalyst, thanks to the existence of both aldehyde and carboxylic acid groups. Therefore, no extra catalysts were employed for the cross-linking with glyoxylic acid cross-linker such as strong acid (HCl) and base (NaOH), which are normally used with formaldehyde cross-linker. Resulting MCs in their work exhibited high porosity with a large surface area and pore volume up to 800 m^2/g and 1 cm^3/g, respectively, and the pore size were tuneable from 0.6 to 7 nm. Moussa *et al.*[9] employed glyoxylic acid cross-linker to synthesise nitrogen-doped MCs for application in supercapacitors from phloroglucinol monomer mixed with guanine as the N source. The porosity, mesoporous morphology could be tuned by applying different preparation procedures such as phase separation, stirring and evaporation approaches, and also by adjusting the amounts of template and cross-linker. In order to improve the synthesis efficiency, Sopronyi *et al.*[10] proposed the photopolymerisation for the cross-linking reaction instead of traditional thermopolymerisation occurring at high temperature. With the newly proposed light-assisted evaporation induced self-assembly process, the cross-linking of monomer precursors can be achieved at room temperature in no more than 1 h, as opposed to

the traditional thermopolymerisation at around 80 °C for at least 12 h. Laser irradiation (UV or IR laser irradiation) not only significantly improved the cross-linking of monomer precursors with glyoxylic acid cross-linker, but also induced a better tailored mesoporous structure and graphitic structure in the resulting carbon materials. Similarly, Axente *et al.*[11] prepared thin MC films from phloroglucinol-glyoxylic acid resin by applying matrix-assisted pulsed laser evaporation (MAPLE) to the cryogenic carbon precursors, in place of the thermopolymerisation process of carbon precursors. The surface features, mesopore morphologies, and coating thickness of derived MC films are tuneable by adjusting the laser fluence, the number of applied laser pulses, or choosing different solvents. Beside of the preparation of MCs, glyoxylic acid was also reported feasible for the synthesis of other materials such as polymer and carbon spheres, where the particle size can be controlled between 500 nm and 10 μm.[12]

Glyoxal is another promising alternative to formaldehyde due to its low toxicity and cost. Initially glyoxal was employed to substitute formaldehyde for the synthesis of wood adhesives from phenolic monomers.[13] However, the soft-template preparation of MCs in nature is a "controlled cross-linking" of monomer precursors in a confined area, the hydrophiphilic phase of the micelles formed by the soft template. Inspired by the synthesis of adhesive with glyoxal cross-linker, Mayes *et al.*[14] reported for the first time the use of glyoxal as the cross-linker to prepare MCs from phloroglucinol monomer; the resulting MC product showed a well-defined mesopore (with pore size of 7.5 nm) and exhibited a superior performance than resorcinol-formaldehyde MC in capacitive deionisation experiments for brackish water treatment. It was suggested that glyoxal is a slower reacting aldehyde than formaldehyde by stabilising the intermediate structures during cross-linking. Herou *et al.*[15] employed glyoxal cross-linker to prepare ordered MCs by employing lignin as a renewable carbon resource in place of phloroglucinol monomer gradually. When the percentage of lignin in phloroglucinol was lower than 50 wt%, a well-ordered 2*D* hexagonal (*p6m*) mesoporous network was obtained, and the resulting MC showed a volumetric capacitance of 90 F/cm^3 in 6 M KOH electrolyte when employed as the supercapacitor electrodes. Their work also indicated that glyoxylic acid could result in an interrupted mesoporous structure, a different porous architecture from the glyoxal cross-linker.

Moving forward from the prevailing cross-linker formaldehyde to its greener substitutes, glyoxylic acid and glyoxal, there is lack of systematic study on how different cross-linkers could influence the resulting pore architectures of MCs and the consequential electrochemical

performance when the MCs are used as the working electrodes of supercapacitors for energy storage. Moreover, each cross-linker has distinct molecular structures due to the presence of different organic groups; this may result in different residual surface functionalities on the MCs. The surface groups together with pore architecture could significantly affect the electrochemical performance of resulting MCs. However, it also remains unclear the potential influence of cross-linker on the surface functionalities of carbon materials. To reveal this thoroughly, this chapter will prepare MCs through the same procedure by comparing the three different cross-linkers mentioned above with a special focus on the porous architecture properties and surface functionalities of MCs. The results in this chapter also shed a light on how cross-linking reactions lead to different electrochemical performance and provide insight into how to choose a suitable cross-linker when using amphiphilic IL templates in the following chapter.

4.2. Methodology

4.2.1. Preparation of MCs with various cross-linkers

The preparation process applied an evaporation-induced self-assembly (EISA) technique. Phloroglucinol monomer that preferentially resides in the hydrophiphilic phase was selected as the carbon precursor. Rather than directly employing amphiphilic ILs as the template, block copolymer Pluronic F127 (poly(ethylene oxide)$_{106}$-poly(propylene oxide)$_{70}$-poly(ethylene oxide)$_{106}$, $EO_{106}PO_{70}EO_{106}$), a well-established soft template for the preparation of MCs, was employed to achieve the goal of analysing the role of cross-linking. By doing this, the potential interference from IL templates themselves could be avoided as the feasibility of employing IL templates to prepare highly ordered MCs remains unclear yet thus a failure practice may be associated with the cross-linking or the use of IL templates. For a typical run, 0.82 g of phloroglucinol and 1.71 g of Pluronic F127 were dissolved in 40 mL of absolute ethanol in sequence. This is a widely used mass ratio between carbon precursor and template (around 1:2) to achieve the formation of ordered mesoporous structures.[8,15–17] After stirring for 30 min, the cross-linking reagent was added into above solution, which was then stirred vigorously at room-temperature for at least 2 h. The solution was poured into a smooth glass petri dish with a diameter of 12 cm and placed at 30 °C to allow ethanol to evaporate sufficiently. This process took around 24 h until most ethanol was evaporated, yielding a homogenous viscous mixture, which was sequentially placed at 85 °C in a convection oven and cured for 24 h. After the cross-linking reaction, the homogeneous transparent film was removed from petri dish, chopped into chunks, transferred into a quartz boat, and calcinated

at 800 °C for 1 h with a heating rate of 1 °C/min under N_2 flow (100 mL/min). The product was cooled down naturally to room temperature under N_2 atmosphere. Resulting carbon materials were labelled as Gx, Fx, and GAx, respectively. G, F, and GA correspond to the three different cross-linkers, namely glyoxal (40 wt% aq.), formaldehyde (37 wt% aq.), and glyoxylic acid monohydrate, with the letter x donating the molar ratio of cross-linker/precursor (C/P ratio).

4.2.2. Preparation of IL triethylammonium bis(tetrafluoromethylsulfonyl)amide

The IL electrolyte triethylammonium bis(tetrafluoromethylsulfonyl)amide ($[N_{2220}][NTf_2]$) was synthesised by using a metathesis reaction.[18] The first step is an exothermic acid-base reaction. Triethylamine (0.5 mol, Sigma-Aldrich) was added into a 500 mL three-neck flask, which was connected to a reflux condenser and immersed in an ice bath, then HCl (37 wt%, aq., 0.5 mol) was added dropwise under vigorous stirring. After the completion of adding HCl, the mixture was stirred under room temperature for 2 h. The second step is a metathesis reaction for anion exchange. The mixture was diluted with deionised water (500 mL), followed by the addition of lithium bis(tetrafluoromethylsulfonyl)amide ($Li[NTf_2]$, 0.51 mol). Slightly excess of $Li[NTf_2]$ was used to guarantee a complete replacement of chloride anion. The mixture was stirred for another 2 h and two phases was obtained. The mixture was mixed with chloroform (100 mL) then introduced into a separating funnel, where the aqueous phase was dumped. The chloroform phase was further washed by water several times until no precipitation formed in the aqueous phase with $AgNO_3$ test. Then the chloroform was removed by rotavapor, and the product was further dried under the vacuum oven until no moisture was detected in NMR spectra. The resulting IL $[N_{2220}][NTf_2]$ was place and stored in the glovebox ready for use.

4.2.3. Characterisation

Surface area and porosity analysis: BET surface area and pore volume for samples were measured by N_2 adsorption-desorption isotherms at 77 K under a TriStar II 3020 analyser. Pore size distribution was calculated by Barrett-Joyner-Halenda (BJH) method.

Morphology analysis: Pore morphologies of resulting MCs were studied by using scanning electron microscopy (SEM) with FEI Quanta 250 FEG scanning electron microscope, and transmission electron microscopy (TEM) with TALOS F200X G2 microscope; high-angle annular dark-field (HAADF) imaging technique was used where possible to obtain scanning transmission electron microscopy (STEM) images.

Surface functionality analysis: The organic groups on the surface of MCs were measured by IR on a PerkinElmer Spectrum 100 FT-IR Spectrometer equipped with a universal ATR sampling accessory. X-ray photoelectron spectroscopy (XPS) as a more precise technique was performed with the Thermo Scientific™ ESCALAB™ QXi X-ray Photoelectron Spectrometer to provide detailed analysis on surface functionalities. Each XPS spectrum was obtained by averaging at least 4 random independent measurements.

Graphitisation degree analysis: The graphitisation degree of all resulting MCs was measured by Raman spectroscopy on a WITec Alpha 300 Raman microscope equipped with a 532 nm laser (10 mW laser power). All spectra were averaged from at least 3 random independent accumulations (50 s accumulation time for each).

4.2.4. Electrochemical performance analysis

The electrochemical performance of resulting MCs was tested as electrode materials in a symmetric two-electrode Swagelok cell device (Figure 4.1). 6 M KOH solution was chosen as representative aqueous electrolyte, while $[N_{2220}][NTf_2]$/acetonitrile (weight fraction of ACN: 0.5) solution was chosen as representative organic electrolyte. Each electrode pellet consisting of 90% of MCs, 5% of PTFE binder, and 5% of multi-walled carbon nanotubes (MWCNT) as conductive material, was pressed for 5 min at 2 tons to obtain a homogeneous thin free-stand pellet (10 mg in weight, 13 mm in diameter, ~120 µm in thickness). The two electrode pellets were separated by a GF/F glass microfiber filter (Whattman®, 15 mm in diameter, 420 µm in thickness) soaked with electrolyte. With 6 M KOH electrolyte, the cell assembly and test were achieved at ambience environment with a potential window of 1.2 V. 500 cycles of initial running at 5.0 A/g were performed prior analysis to effectively improve KOH electrolyte wetting all the pores. With $[N_{2220}][NTf_2]$/ACN electrolyte, the battery cell was assembled and tested in a glovebox (water content: < 0.3 ppm, oxygen content: < 0.1 ppm) with a potential window of 2.5 V. No initial cycles were performed prior to the analysis.

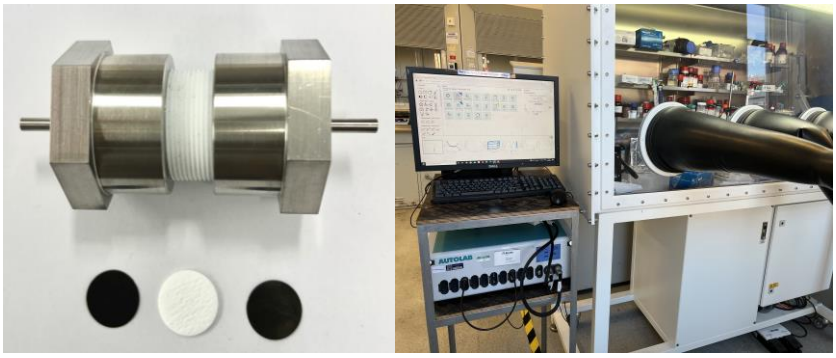

Figure 4.1. Electrochemical characterisation setup: Swagelok cell (left) and potentiostat with glovebox (right).

The gravimetric specific capacitance (C_s, F/g) was calculated from the galvanostatic charge-discharge curve:

$$C_s = 4C_{cell} = \frac{4\,\mathrm{I} \times \Delta t}{\mathrm{m} \times V} \quad \text{(Equation 4.1)}$$

The energy density (E, Wh/kg) and power density (P, W/kg) were obtained by using

$$E = \frac{1}{2}\mathrm{C}_{cell}V^2 \times \frac{1}{3600} \times 1000 \quad \text{(Equation 4.2)}$$

$$P = \frac{E}{\Delta t} \times 3600 \quad \text{(Equation 4.3)}$$

Where Δt (s), I (A), m (g), and V (V) represent the discharge time, discharge current, total mass of active materials on both electrodes, and the potential window applied.

4.3. Results and Discussion

4.3.1. Pore architecture analysis

Figure 4.2 shows the N_2 physisorption isotherms (a) and pore size distribution (b) for all resulting carbons. The Type IV isotherms with obvious hysteresis loops in Figure 4.2a indicate the dominant presence of mesopores in all resulting carbon materials except GA1.25, which exhibited a reversible Type I isotherm, typical isotherm for microporous materials.[19] GA1 exhibited the largest adsorption quantity with dominating pores of 8.7 nm; this indicates GA1 has the largest pore volume, followed by sample G1 and F2 with dominating pore size of 6.1 and 8.6 nm, respectively. A diminished effect was found in the adsorption quantity when the ratio of cross-linkers increased with either glyoxal or glyoxylic acid. It seems that more cross-linking agents added can induce a smaller porosity at the same condition. Moreover, for carbon samples with dominating mesopores (*i.e.,* excluding GA1.25), the adsorption quantity at lower relative pressure seems to be related to the cross-linker type. Glyoxal-resultant MCs showed higher adsorption quantities at low relative pressure, followed by glyoxylic acid-resultant MCs and formaldehyde-resultant MC, which may suggest that the cross-linker type influences the microporosity. Given that increasing cross-linker ratios led to a decreased total adsorption quantity, the ratio of cross-linker/precursor may influence the mesoporosity. During soft-templating synthesis, the mesopore structures are usually determined by the templates as depicted in Figure 1.3 in *Chapter 1*. Such difference in adsorption quantity at low relative pressure is likely associated with the unique chemical

structures of these three cross-linkers and particularly with the linkages formed amongst carbon precursors after cross-linking reaction. As shown in Figure 4.3, formaldehyde and glyoxylic acid as the cross-linker bridge two phloroglucinol molecules with one -C- linkage, however the carboxylic acid group in the latter could occupy the space and generate more micropores after calcination. Glyoxal has two aldehyde groups and two possible linkage types; compared with -C- linkage the longer -C-C- linkage or the presence of the other aldehyde group may increase the distance between two aromatic rings, leading to a slightly higher micropore volume after calcination.

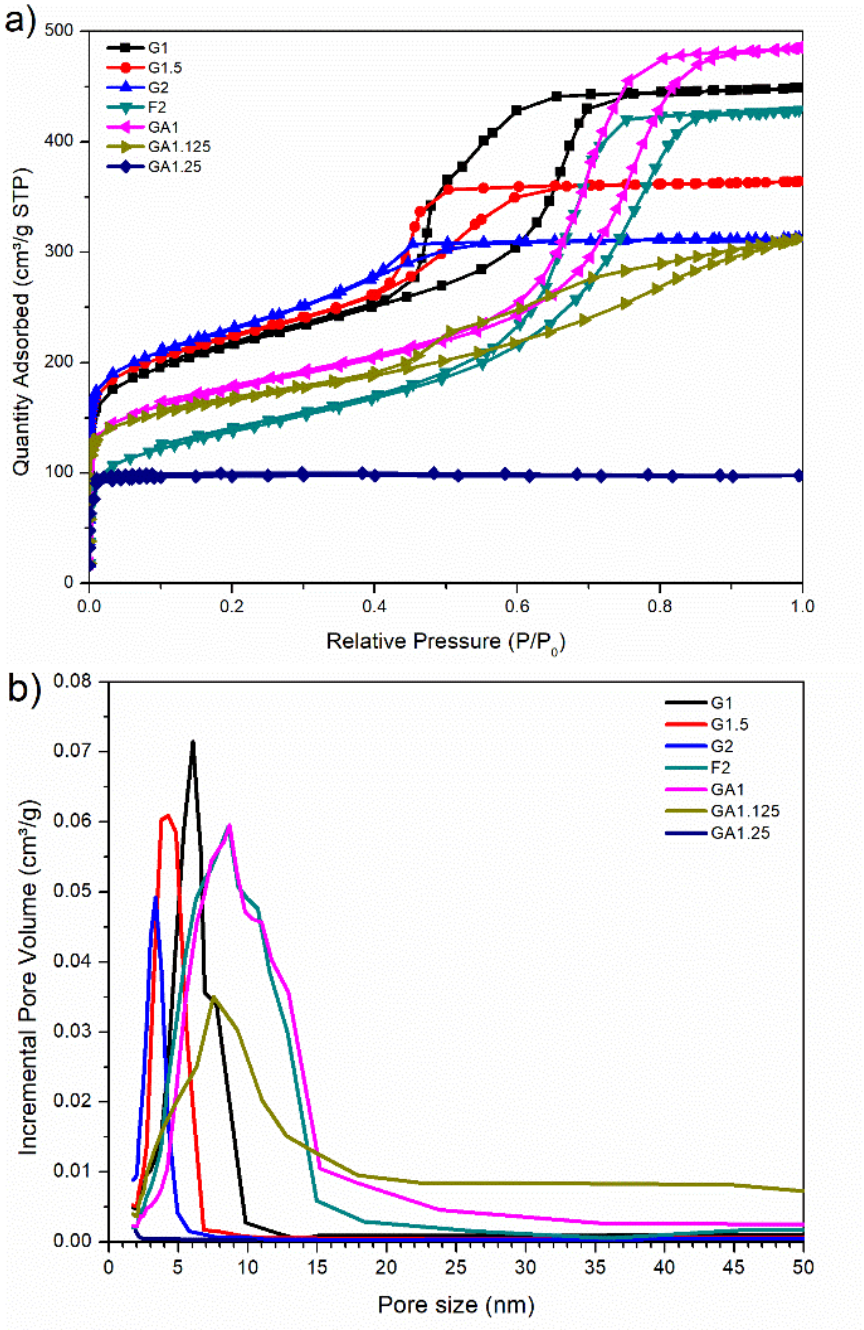

Figure 4.2. MCs synthesised with various cross-linkers: a) N_2 physisorption isotherms, and b) BJH pore size distributions.

Figure 4.2b shows another notable decreasing trend in the dominating pore size of MCs as the C/P ratio increased. For glyoxal-resultant MCs, the dominating pore size decreased from 6.1 nm for G1 to 3.3 nm for G2, whilst the value dropped from 8.7 nm for GA1 to 7.5 nm for GA1.125 prepared by employing glyoxylic acid cross-linker. Comparing the three different cross-linkers, pore size distributions for glyoxal-resultant MCs are much narrower than their counterparts, indicating that the pores generated with glyoxal cross-linker are more uniform and well-regulated compared with formaldehyde and glyoxylic acid.

Table 4.1 summarises the pore textual properties of resulting MCs. Glyoxal-resultant MCs showed an overall richer porosity than those prepared with formaldehyde and glyoxylic acid, evidenced by the larger surface area and pore volume. As the C/P ratio increased, the total surface area rose from 753.4 to 820.7 m^2/g, whilst the total pore volume declined from 0.69 to 0.48 cm^3/g. Notably, the mesopore rate dropped from 78% to 58 %, and there is also a diminishing trend in both the mesopore surface area (from 436.3 to 400.0 m^2/g) and mesopore volume (from 0.54 to 0.28 cm^3/g). When employing formaldehyde as the cross-linker, there was no homogenous film formed after being cured for 24 h at lower cross-linker/precursor mixing ratios than 2. This is probably because that formaldehyde has only one aldehyde group; lower C/P ratio only led to a deficient cross-linking reaction in the absence of catalyst, yielding a highly viscous matrix (*i.e.* adhesive) on the petri dish. As the mixing ratio reached 2, the corresponding product F2 showed the highest mesopore rate of 91%, with a total BET surface area and pore volume of 478.5 m^2/g and 0.66 cm^3/g, respectively. Glyoxylic acid as the cross-linking agent also provides only one aldehyde group per molecule but the carboxylic acid group can serve as catalyst to facilitate the cross-linking process. Therefore, lower C/P ratio with glyoxylic acid yielded polymer films. Sample GA1 exhibited a total BET surface area and pore volume of 621.7 m^2/g and 0.75 cm^3/g. However, the porosity became worse with more glyoxylic acid added evidenced by the drastically decreasing pore volume to 0.15 cm^3/g for sample GA1.25. Moreover, there was barely mesopores measured when the C/P ratio exceeded 1.25, where the mesopore rate dropped to 7%. Such rapid deterioration in the porosity is likely associated with the catalytic ability of glyoxylic acid, which might be too strong under such circumstance. Over-cross-linked precursor could be detached from the hydrophilic segment of templates, destroying the well organised ordered mesophase formed by the templates and monomer precursors.[20] At the same C/P ratio, GA1 exhibited larger total pore volume and mesopore volume than sample G1, which corresponds well with higher N_2 adsorption quantity in Figure 4.2a. The presence

of two aldehyde groups in glyoxal may have stabilised the violent cross-linking reaction of monomer precursors, whilst the carboxylic acid group in glyoxylic acid may have fasten the process and resulted in an overly cross-linked precursor matrix thus more disordered interstitial pore structures were formed after calcination.

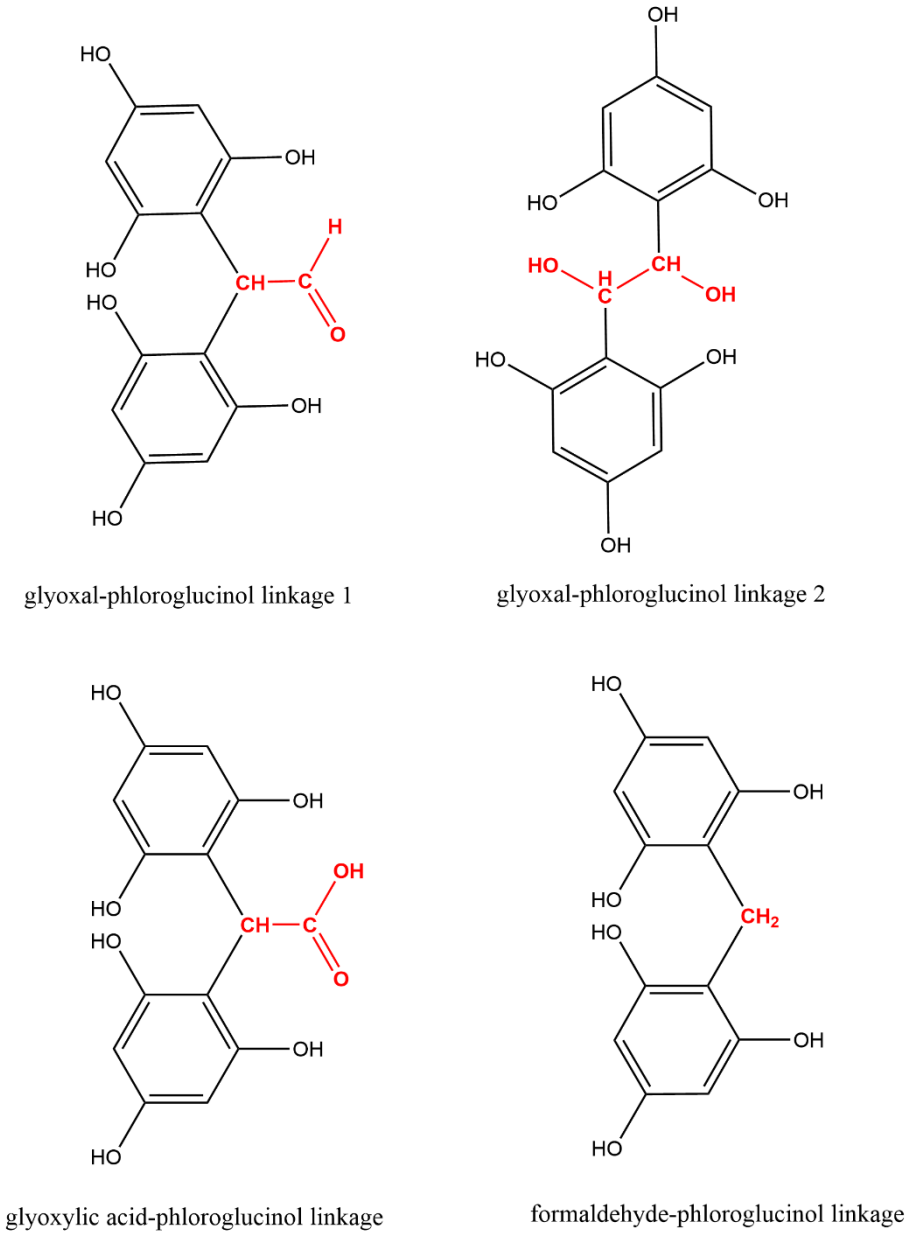

Figure 4.3. Linkages between various cross-linkers and phloroglucinol.

Table 4.1. Textural properties of resulting samples.

Samples	Pore textural property						
	S_{BET} (m^2/g)	S_{meso} (m^2/g)	V_{total} (cm^3/g)	V_{meso} (cm^3/g)	V_{meso}/V_{tot}	Dominating pore size (nm)	Pore uniformity
F2	478.5	367.2	0.66	0.60	91%	8.6	disordered
G1	753.4	436.3	0.69	0.54	78%	6.1	ordered hexagonal
G1.5	793.8	423.8	0.56	0.38	68%	4.3	ordered hexagonal
G2	820.7	400.0	0.48	0.28	58%	3.3	ordered hexagonal
GA1	621.7	348.7	0.75	0.62	83%	8.7	less ordered
GA1.125	597.5	245.6	0.48	0.32	67%	7.5	less ordered
GA1.25	393	5.7	0.15	0.01	7%	-	microporous

The representative SEM images of MC samples prepared with various cross-linkers are shown in Figure 4.4. Glyoxal-resultant MCs, at the C/P ratio ranging from 1 to 2, showed highly ordered honeycomb-like hexagonal mesoporous structures with a long periodicity (Figure 4.4a-c). Formaldehyde as cross-linker at a C/P ratio of 2 led to a randomly disordered mesopore structures (Figure 4.4d). Although the number of aldehyde groups in cross-linker used to prepare sample F2 is the same with that for G1, the pore structures were highly disordered, as opposed to the well-regulated hexagonal mesopores for G1. The difference in pore morphology with the same amount of aldehyde groups also could be stemmed from the higher reactivity of formaldehyde than glyoxal.[14] The two aldehyde groups in glyoxal are bridged together with C-C bond, which may also deliver a lower aldehyde diffusion in the mixture and possibly the lower-degree cross-linking. As shown in Figure 4.4e, sample GA1 exhibited a worm-like cylindrical mesopore channels, which were less ordered than those in sample G1. Though glyoxal provides double number of aldehyde group compared with glyoxylic acid, the presence of carboxylic acid group in the latter catalysed the cross-linking reaction which destabilised the well organised mesophase formed after the self-assembly process. As the amount of glyoxylic acid increased with C/P ratio from 1 to 1.25, the uniformity of mesopores got poorer (Figure 4.4f) rapidly even no obvious mesopores were observable anymore (Figure 4.4g).

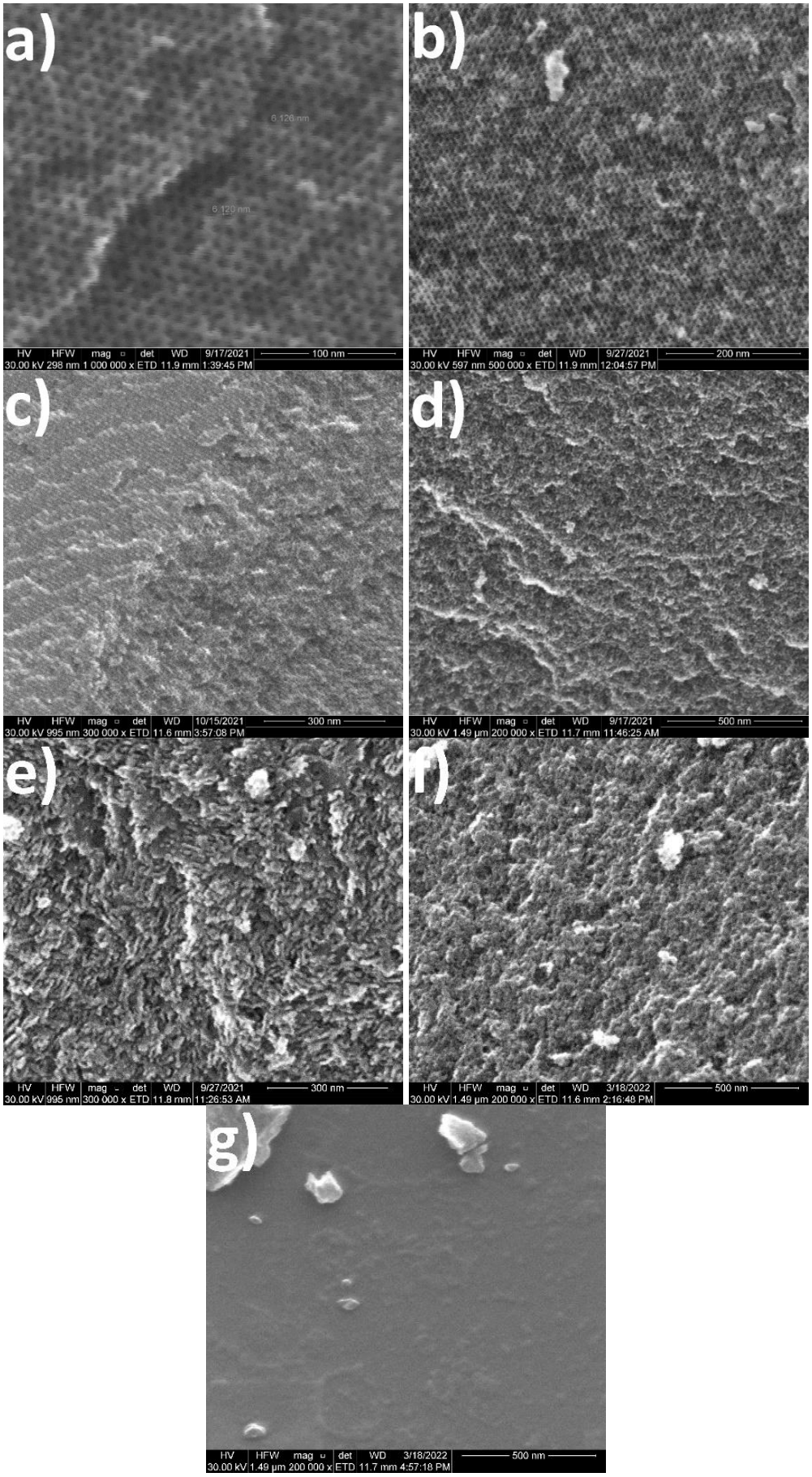

Figure 4.4. SEM images of MC samples: a-g) G1, G1.5, G2, F2, GA1, GA1.125, and GA1.25, respectively.

Figure 4.5 shows the typical TEM images of all MC samples prepared by employing different cross-linkers. The well-organised highly ordered mesopore channels were only observable in glyoxal-resultant MCs (Figure 4.5a-c), which coincides well with the SEM images. Sample F2 with formaldehyde cross-linker does not show any periodicity in the meso-structures (Figure 4.5d), which are random interstitials formed by polymer clusters. When using glyoxylic acid as the cross-linker, sample GA1 exhibited a distorted worm-like mesopore channels but the periodicity was still evident (Figure 4.5e). As the C/P ratio increases, sample GA1.125 almost lost its periodicity in mesopore channels (Figure 4.5f), displaying a disordered meso-structures. At a higher C/P ratio of 1.25, only micropores were noticeable for sample GA1.25 (Figure 4.5g) due to the strong catalytic ability of glyoxylic acid. In comparison of these three cross-linkers, at the same C/P ratio of 1, only glyoxal cross-linker yielded mesopores with well organised uniformity, whilst formaldehyde failed to sufficiently cross-link the monomer precursors to produce a 3*D* homogeneous polymer and glyoxylic acid induced the monomer precursors slightly over-cross-linked.

The periodicity of ordered mesopore channels was measured by using the STEM HAADF intensity line profile. As shown in Figure 4.6, the distance between two neighbouring peaks in the line profiles means one period, which consists of both the pore channel and pore wall. Sample G1 (Figure 4.6a and b) shows a periodicity of 10.5 nm with a pore size and pore wall of 6.1 and 4.4 nm, respectively. As the C/P ratio increased to 1.5, the periodicity decreased to 8.7 nm, where the pore size shrunk to 4.3 nm (Figure 4.6c and d). Sample G2 showed a much smaller periodicity of 8.2 nm with a narrower pore diameter of 3.3 nm (Figure 4.6e and f). The pore diameters measured here correspond exactly to the dominating pore sizes from N_2 physisorption analysis. The decline in the mesopore diameter could be induced by the increasingly stronger cross-linking degree of monomer precursors at higher C/P mixing ratios. As shown in Figure 4.6g and h, the periodicity for sample GA1 with a less ordered pore structure was 12.5 nm, which is larger compared with other ordered samples. The measured dominating pore diameter from STEM was 5.4 nm, which is smaller than the value measured by N_2 physisorption analysis. This is mainly because STEM failed to consider the distortion of pore channels and the possible discontinuity of pore walls as both pore channel and wall are three dimensional.

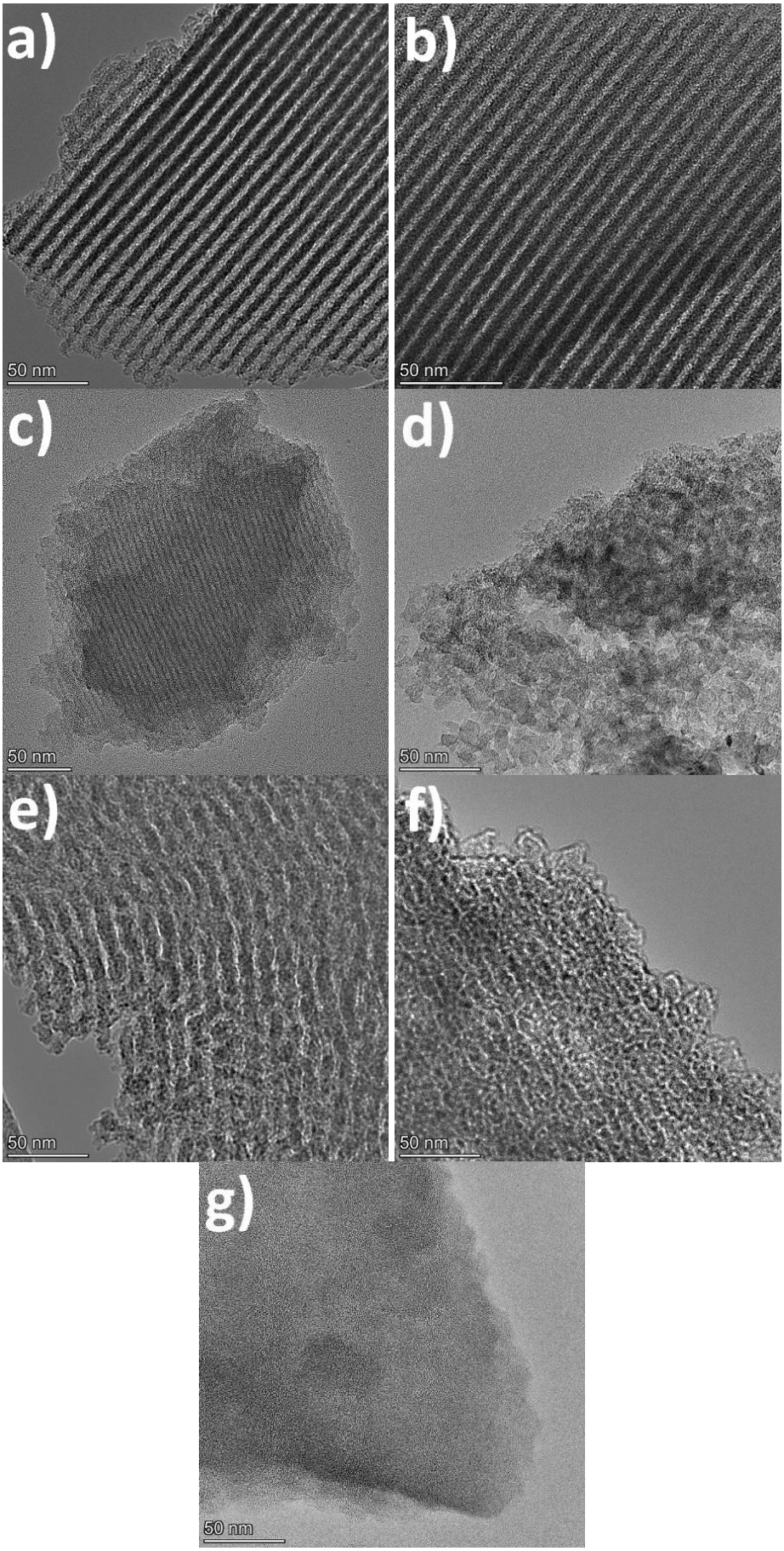

Figure 4.5. TEM images of MC samples: a-g) G1, G1.5, G2, F2, GA1, GA1.125, and GA1.25, respectively.

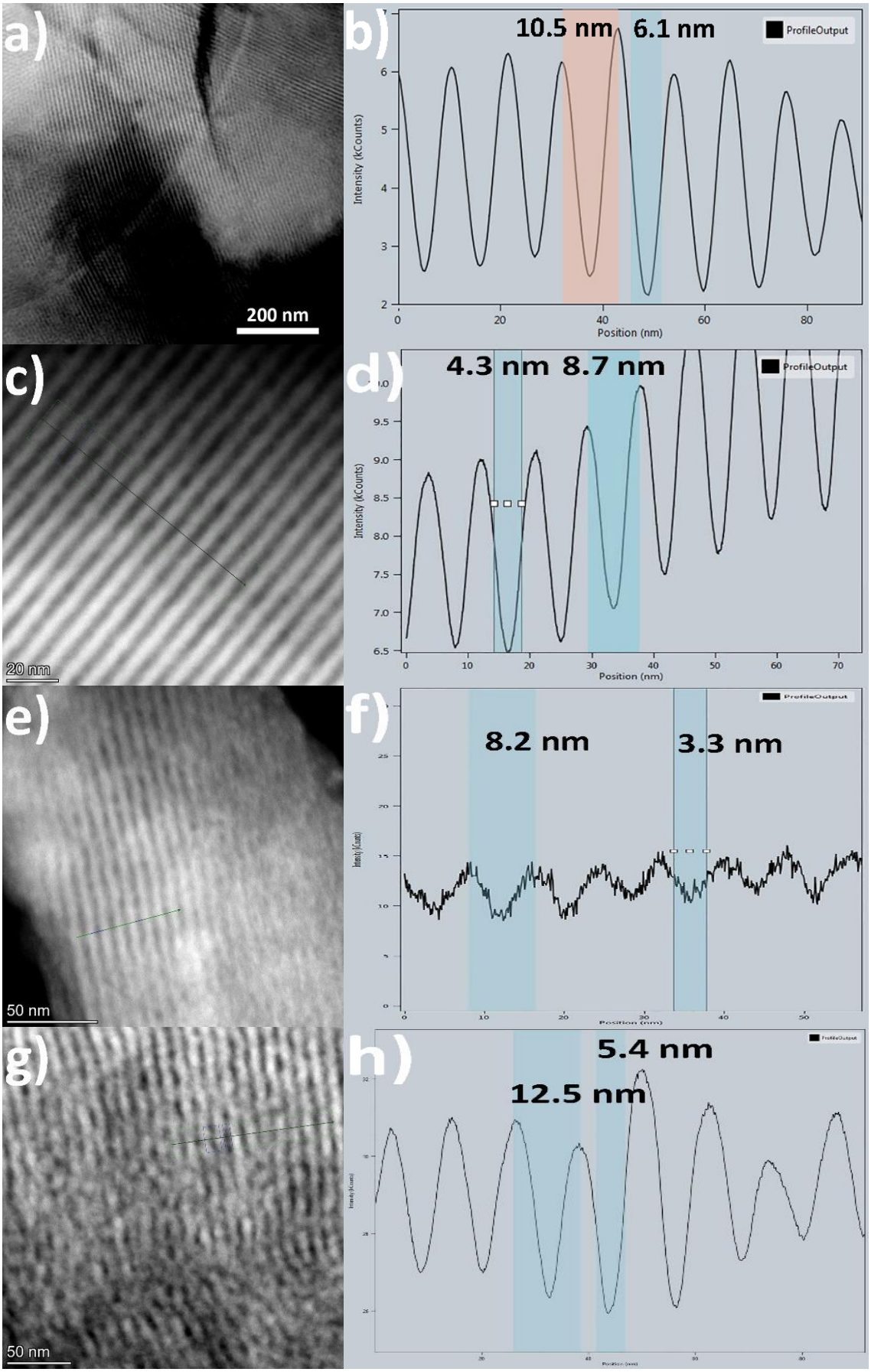

Figure 4.6. HAADF STEM image and line profile of processed HAADF intensity for ordered mesoporous samples: a, b) G1, c, d) G1.5, e, f) G2, and g, h) GA1, respectively.

4.3.2. Surface functionality analysis

Considering that the three cross-linking agents have different molecular structures, such dissimilarity could lead to different residual functionalities on the surface of MC samples. When the resulting MCs are used as working electrodes, surface functionalities may bring about pseudocapacitive behaviour. XPS was performed to investigate the functionalities and results are shown in Figure 4.7. All MCs possess dominating C element over 93% and small amounts of O element (Figure 4.7a). The deconvolution of C1s peaks (Figure 4.7b-h) indicates that the major oxygen-containing functionalities are -C-O, -C=O, and -COO, respectively. The detailed contents of each element and surface groups are summarised in Table 4.2.

With glyoxal cross-linker, the increasing of C/P ratio led to a steady growth in -C-O content from 23.3% (in sample G1) to 26.1% (in sample G2), whilst the content of -C=O group showed an overall reducing trend. This is mainly originated from the cleavage of -C=O bond during the addition of glyoxal to aromatic monomer precursors, consequently a new -C-O bond will form after the addition reaction. With the same amount of aldehyde groups used for the cross-linking, double moles of formaldehyde resulted in a higher -C-O content (24.8%) and lower -C=O content (7.5%) in the resulting carbon F2 compared with the values (23.3% and 8.2%) for sample G1. As the two aldehyde groups are bonded together by C-C bond in glyoxal, double amount of formaldehyde favours the diffusion of aldehyde groups in the mixture and induces a higher reactivity than glyoxal. Therefore, the aldehyde group of formaldehyde has more probability to participate in the cross-linking than those of glyoxal, which causes the cleavage of more -C=O bonds and the formation of more -C-O bonds. In comparison of sample G1 and GA1, the latter showed a slightly higher -COO content (6.2%) than sample G1 (5.6%); this is mainly a result of the existence of the inherent carboxyl group in glyoxylic acid. Though glyoxal possesses the double amount of aldehyde groups than glyoxylic acid, the presence of -COOH catalysed more aldehyde groups engaging in the cross-linking reaction,[8,10] evidenced by the higher -C-O content in sample GA1 (27.3%).

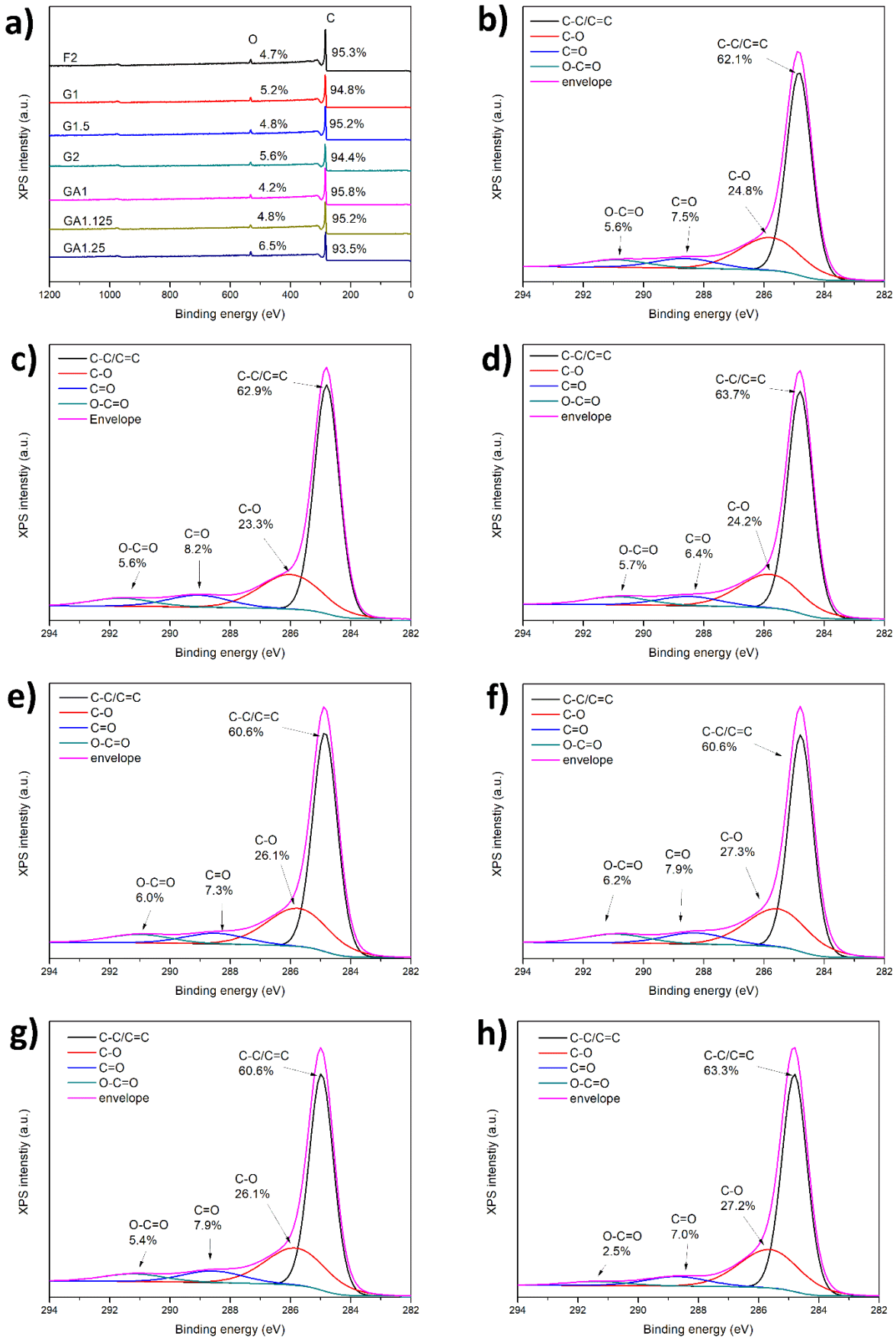

Figure 4.7. Summary of wide-scan XPS spectra (a) and deconvolution of C 1s peaks for MCs (b-h): F2, G1, G1.5, G2, GA1, GA1.125, and GA1.25, respectively.

Table 4.2. Summary of XPS analysis on resulting MC samples with various cross-linkers after carbonisation.

Samples	Overall O content	Overall C content	Different C bonds			
			C-C/C=C	C-O	C=O	O-C=O
F2	4.7%	95.3%	62.1%	24.8%	7.5%	5.6%
G1	5.2%	94.8%	62.9%	23.3%	8.2%	5.6%
G1.5	4.8%	95.2%	63.7%	24.2%	6.4%	5.7%
G2	5.6%	94.4%	60.6%	26.1%	7.3%	6.0%
GA1	4.2%	95.8%	60.6%	27.3%	7.9%	6.2%
GA1.125	4.8%	95.2%	60.6%	26.1%	7.9%	5.4%
GA1.25	6.5%	93.5%	63.3%	27.2%	7.0%	2.5%

The surface functionality was also measured by IR. Figure 4.8a shows IR results for MCs prepared with glyoxal cross-linker. The band observed at around 1560 and 1020 cm^{-1} are characteristics of -C=O and -C-O groups, respectively.[21] As the C/P ratio increases from 1 to 2, the peak for -C-O group gets higher whilst that for -C=O group shows a converse trend, getting lower; this trend keeps consistent with the content changes of both groups from XPS study. When glyoxylic acid was employed as cross-linker, the -C-O peak for sample GA1 appears higher than that for sample G1 (Figure 4.8b), which coincides well with the higher -C-O content for sample GA1 (27.3%) than the value for G1 (23.3%). Double moles of formaldehyde give the same amount of aldehyde group as glyoxal, but the peak for -C-O group became lower than those in sample G1 due to the higher reactivity of formaldehyde.

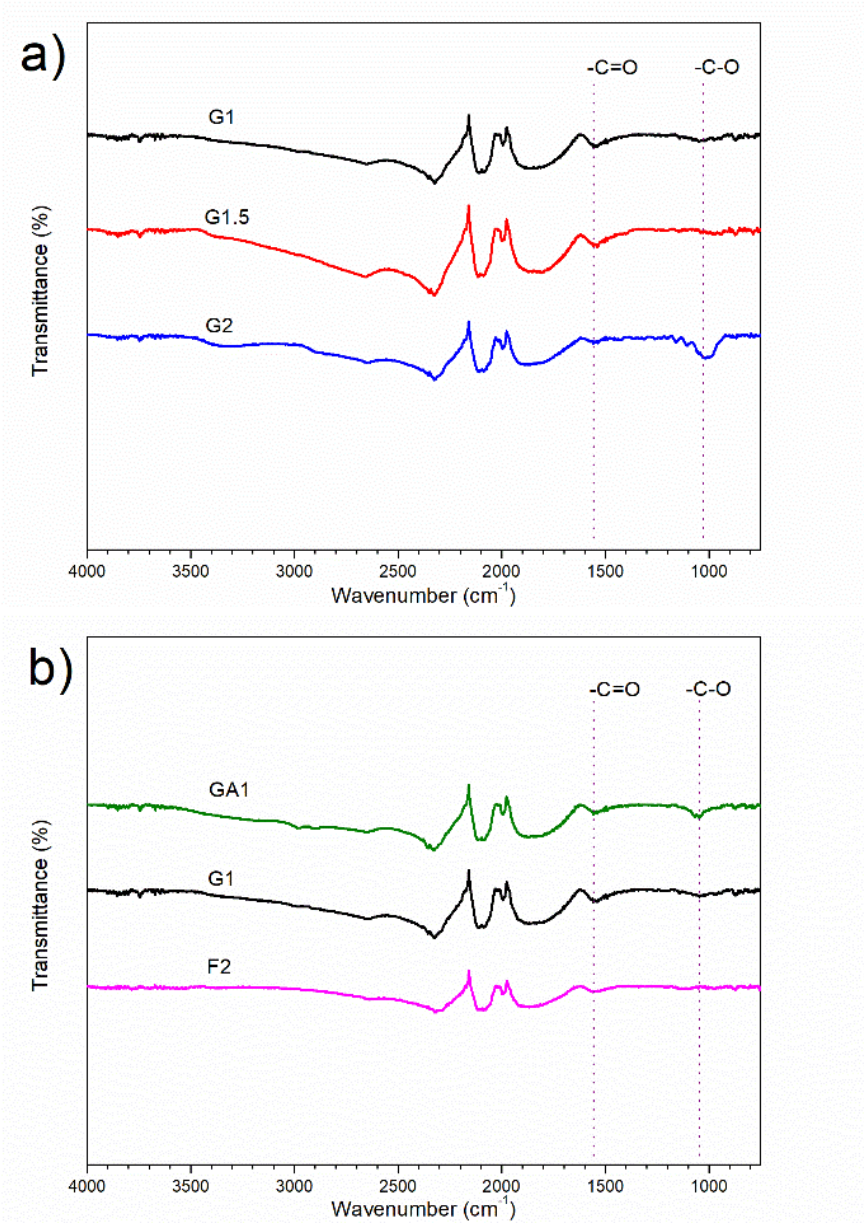

Figure 4.8. IR spectra: a) resulting MCs with glyoxal cross-linker, and b) comparison of MCs with different cross-linkers.

4.3.3. Graphitisation degree analysis

Independently of the porosity, pore size, and surface functionalities of MC materials, the graphitisation degree can be universally used to tailor the potential-dependent capacitance when MCs are employed as electrode materials.[22] Raman spectroscopy was performed to study the graphitisation degree of all MCs prepared by various cross-linkers. As shown in Figure 4.9a, only two bands were detected, *D* band at around 1350 cm^{-1} and *G* band at around 1590 cm^{-1}. *D* band is usually observed in defected graphite lattice due to structural distortion, while *G* band is induced by the presence of graphitic structures.[23,24] The strong *D* peak (I_D/I_G ≈ 1) and the absence of *2D* band (at around 2700 cm^{-1}) indicate the lack of local graphene-

like structures in all resulting MCs prepared by employing various cross-linkers. Although graphite crystalline structures are observable (Figure 4.9b) in all MCs and some samples possess periodic well-organised pore channels in mesoscale (typical glyoxal-resultant MCs), this does not change the fact that all as-made MCs are still amorphous carbon materials in nature. Overall, there is no significant difference in their graphitisation degree as they were prepared under the same calcination condition (800 °C for 1h).

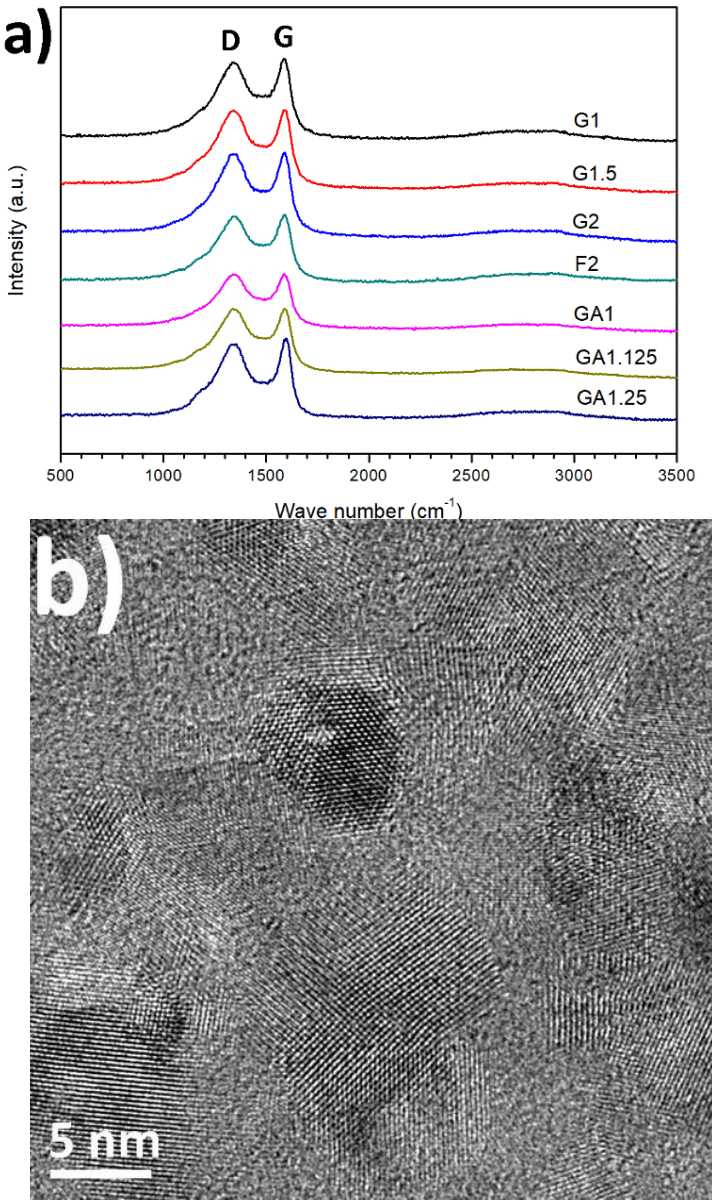

Figure 4.9. a) Raman spectra of resulting MC samples, and b) representative TEM image of random graphite crystalline structures in sample F2.

4.3.4. Electrochemical performance analysis

Cyclic voltammetry (CV) test was carried out in 6 M KOH aqueous electrolyte for all the resulting MCs at different scan rates: 5, 10, 20, 50, 100, 200, and 500 mV/s. At a lower scan

rate of 5 mV/s (Figure 4.10a), cells with MCs working electrodes, except GA1.25, displayed symmetric nearly rectangular-like curves; this suggests the highly resersible charge-discharge response, a typical behaviour of electric double-layer capacitor (EDLC). The CV curve for cell with GA1.25 working electrodes is triangular rather than rectangular. The poor charge-discharge response can be attributed to its small pore volume of 0.15 cm^3/g, consequently there are quite limited pore structures for the ionic transport and subsequent ion adsorption/desorption on the pore surface. Furthermore, cells with glyoxal-resultant MCs showed significantly larger charging/discharging currents than their counterparts prepared with glyoxylic acid and formaldehyde cross-linkers. In particular, sample G1.5 as the active material of electrodes yielded the highest charging/discharging currents. Therefore, the capacitances for glyoxal-resultant MCs are expected larger than the others at lower scan rate. Th highly ordered mesoporous channels may have favoured the fast ionic transport in pores. In CV at 50 mV/s (Figure 4.10b), the CV curves for all cells except that with GA1.25 electrodes, are more rectangular shaped, which is the ideal efficient EDLC behaviour with excellent charge-discharge kinetics. At a higher scan rate of 500 mV/s (Figure 4.10c), rectangular shaped CV curves are generally remained for all cells except that with GA1.25 electrodes, which still showed a triangular shape due to its small porosity. Noticeably, there was a slow response in the charge-discharge process of all EDLC cells. Under such circumstance, the ionic transport in mesopores may be not rapid enough to match the high scan rates, therefore the formation of electric double layers in the pores was delayed to some extent. Such delay in cells with glyoxal-resultant MC working electrodes was more evident. This is highly likely caused by the existence of the dominating highly regulated mesopore channels, the length of which usually reaches a few micrometers (Figure 4.11). Compared with shorter mesopore channels, longer mesopore length can result in a slower mass transfer, higher electrochemical resistance, poor cycling performance, and lower rate. During charging/discharging, it takes longer time for the ionic transport and subsequent adsorption/desorption of solvated K^+ and OH^- ions on the deeper pore surface owing to the long penetration depth. When employing glyoxylic acid or formaldehyde as the cross-linker, resulting mesopores are either disordered or interrupted. The mesopore structures are better interconnected than those glyoxal-resultant highly ordered mesopore channels. Obviously, the well interconnected pores decreased the penetration depth for electrolyte ions and offered a better in-pore diffusivity, which have provided a higher chance for the ions to get access to the deeper pore surface rapidly and form the electric double layers at higher scan rates. Concomitantly, a better electrochemical performance with higher capacitance was achieved.

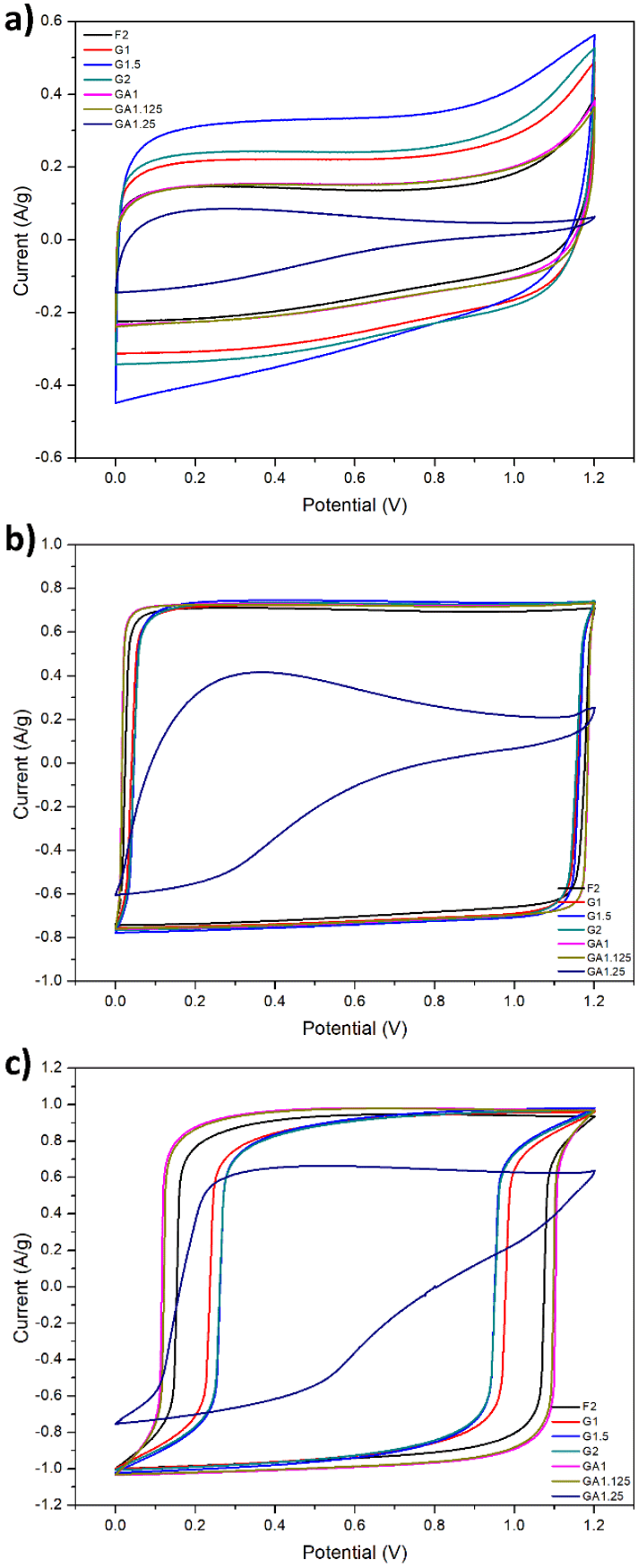

Figure 4.10. Cyclic voltammetry (CV test) in 6 M KOH electrolyte for MC samples prepared by various cross-linkers at different scan rates: a) 5 mV/s, b) 50 mV/s, and c) 500 mV/s, respectively.

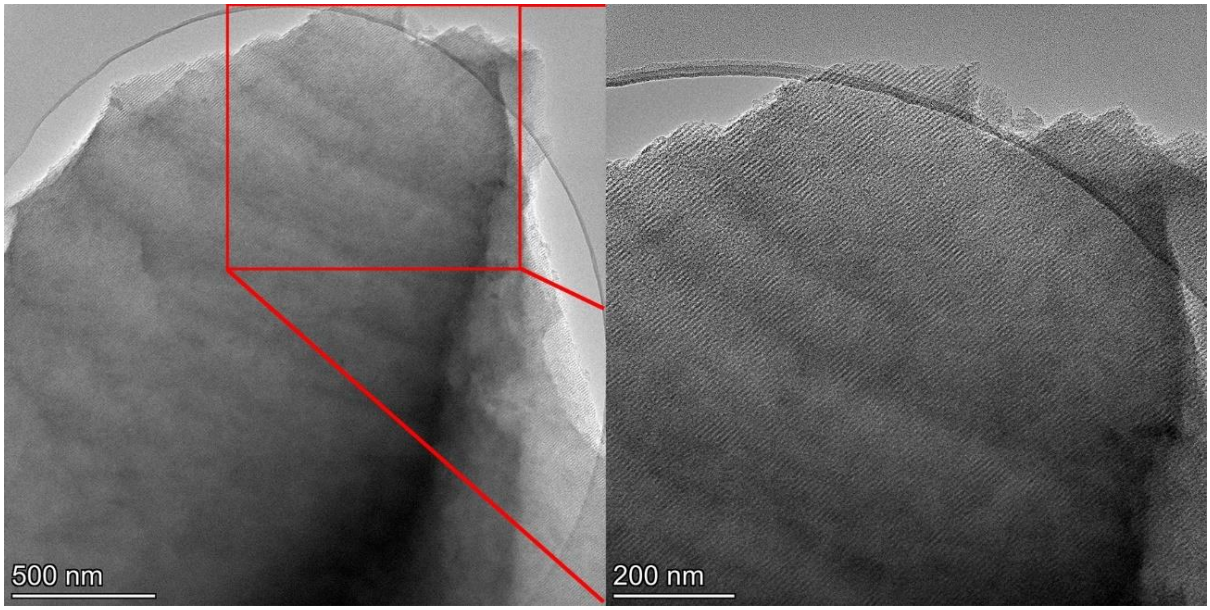

Figure 4.11. Representative TEM image of glyoxal-resultant MC with long mesopore channels in micrometres.

Consistent with the CV tests, cells with MCs working electrodes showed a symmetric triangular galvanostatic charge-discharge profile with fairly linear slope (Figure 4.12a); this is typical feature of EDLCs. At a lower current density of 0.5 A/g, MC samples prepared with glyoxal cross-linker showed longer charge-discharge time in KOH aqueous electrolyte, especially sample G1.5. Figure 4.12b summarises the gravimetric specific capacitance of resulting MCs at various current densities. Starting from 0.1 A/g, glyoxal-resultant MC electrodes exhibited higher capacitances than other samples, with the values of 153.5 F/g (for sample G1.5), 149.3 F/g (for sample G2) and 143.1 F/g (for sample G1), respectively. At a higher current density over 10 A/g, GA1 and GA1.125 showed larger capacitance ranging from 93.3 to 101.7 F/g; this could be resulted from their faster charge-discharge response at higher scan rate/current density. As expected, sample GA1.25 exhibited lowest capacitance throughout different current densities. Moussa *et al.*[9] reported N-doped MCs for supercapacitor by employing glyoxylic acid as the cross-linker, and the maximum achieved capacitance in aqueous H_2SO_4 electrolyte was 97 F/g. This value is much lower than that for glyoxylic acid-resultant sample GA1 (146.7 F/g) prepared in this work without N-doping. When employing glyoxal as the cross-linker, ordered MC sample prepared by Herou and coworkers[15] from entirely phloroglucinol monomer precursor showed a gravimetric capacitance around 75 F/g in the symmetric Swagelok cell, no more than half of the value for our glyoxal-resultant MC sample G1.5 (153.5 F/g). This is likely because that the mesopores of phloroglucinol-derived MC in their work were too big with a diameter of 7.3 nm to match the transport of solvated electrolyte ions (K^+ and OH^-) even though the surface area and pore

volume of their sample are quite comparable with sample G1.5. With the same electrolyte, larger pore size than electrolyte ions can decrease the capacitance considerably.[25] By replacing phloroglucinol precursor with 50 wt% of lignin, the gravimetric capacitance increased to around 100 F/g, nevertheless the value is still lower than our data. Sample F2 has a large pore volume of 0.66 cm^3/g and biggest mesopore rate of 93%, the capacitance was almost the smallest expect GA1.25. This is possibly because that the dominating mesopores in F2 are way too random and disordered compared with the noticeable ordered mesopore channels in MC samples prepared by glyoxal and glyoxylic acid. Furthermore, as the current density increases, there is an evident diminishing effect on the gravimetric specific capacitance for all cells with MCs working electrodes. The specific capacitances for glyoxal-resultant MCs dropped drastically with the values nearly halved at 20 A/g compared with the initial values at 0.1 A/g. This indicates that all EDLCs with MCs electrodes have a relatively limited rate capability, due to the long ordered mesopore channels. At higher scan rates or current densities, the mass transfer in longer mesopore channels is much slower thus leads to the slower charge-discharge kinetics.[26]

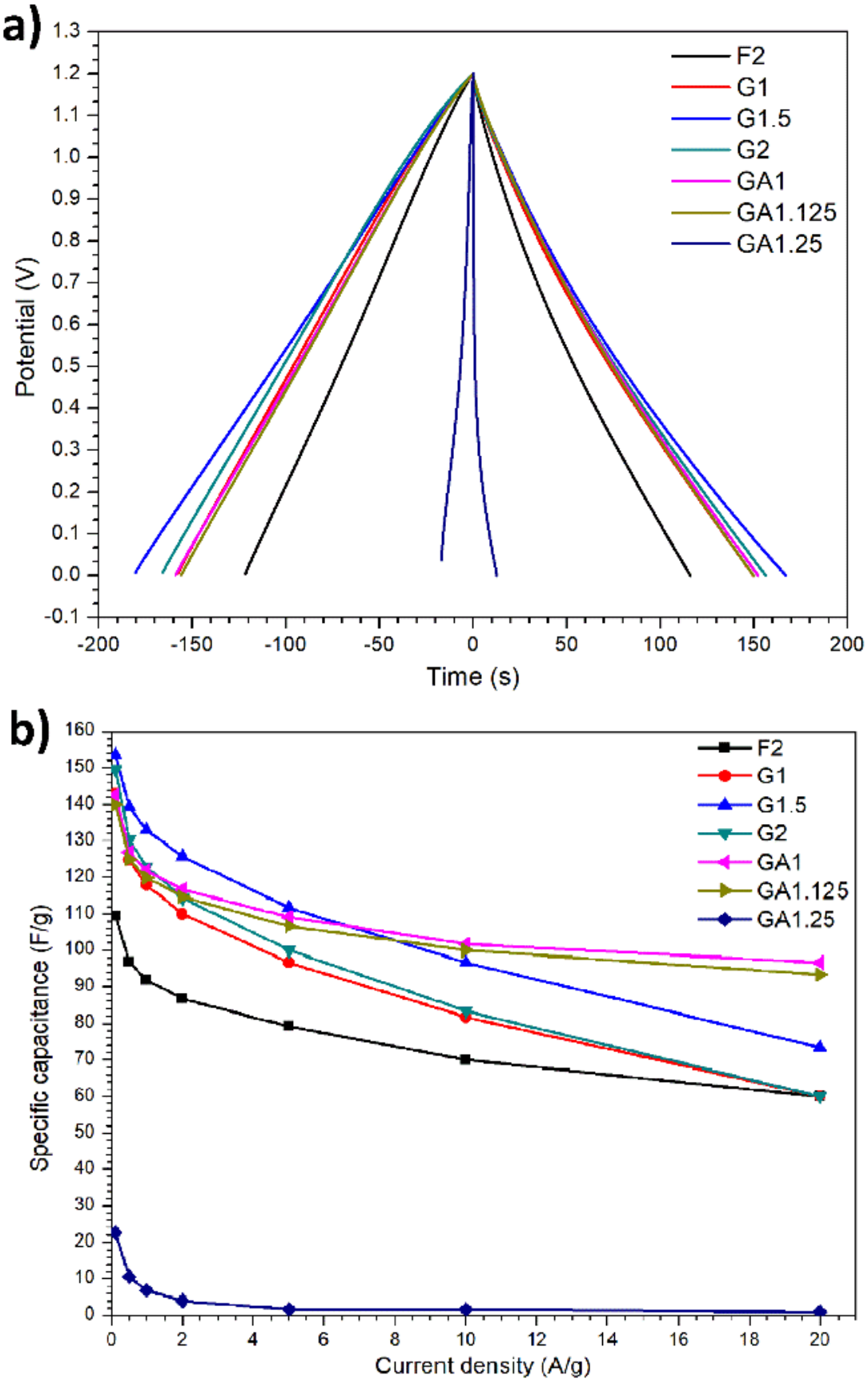

Figure 4.12. a) Galvanostatic charge/discharge at 0.5 A/g and b) gravimetric specific capacitance for MCs prepared by employing three different cross-linkers.

IL electrolyte was also used to test the electrochemical performance of all resulting MCs. IL electrolytes can provide wider operating voltage windows and larger energy density than aqueous electrolytes due to their excellent physicochemical properties such as high chemical stability, negligible volatility.[27,28] Notably, protic ILs have a better ionic conductivity than aprotic ILs due to the existence of the labile proton on the protonated organic cation. Here, $[N_{2220}][NTf_2]$/acetonitrile (weight fraction of ACN: 0.5) was used as representative electrolyte. Mixing with organic mediators such as acetonitrile and hydroquinone, could significantly decrease the viscosity of the IL electrolytes and enhance the charge transfer and ionic conductivity.[18,29] With the addition of ACN to $[N_{2220}][NTf_2]$ at a weight fraction of 0.5, the electrolyte features a higher fluidity than pure $[N_{2220}][NTf_2]$ electrolyte because of a lower viscosity and higher mobility, and delivers a maximum conductivity.[18]

Figure 4.13a shows the CV test for cells in IL $[N_{2220}][NTf_2]$/ACN electrolyte with resulting MCs working electrodes prepared with different cross-linkers. Similar with the CV test in aqueous 6 M KOH electrolyte, the nearly rectangular shaped profiles indicate excellent reversible EDLC behaviour. Cells with glyoxal-resultant MC electrodes also displayed higher charging/discharging currents in IL electrolyte compared with their counterparts prepared with formaldehyde and glyoxylic acid cross-linkers. This is highly related to the dominating presence of ordered mesopore channels. Notably, sample G1.5 still displayed the highest charging/discharging current in $[N_{2220}][NTf_2]$/ACN electrolyte, whilst sample GA1.25 displayed the lowest due to its small porosity. Besides, for cells with glyoxal-resultant MC electrodes, there is a slight increase in capacitance at higher voltage over 2.0 V. Acetonitrile is quite stable up to 2.5 V and its oxidation normally occurs above 2.7 V.[18] However, the efficiency of cells in $[N_{2220}][NTf_2]$ electrolyte is quite temperature-dependant, the increase in capacitance might be attributed to the slow decomposition of acetonitrile under the effect of polarisation at higher voltages. Brandt *et al.*[30] reported the stable cycling behaviour (over 30,000 cycles) of activated carbon-based supercapacitors in protic $[N_{2220}][NTf_2]$ electrolyte, which also displayed pseudocapacitive behaviour thanks to the presence of water in $[N_{2220}][NTf_2]$ electrolyte and the surface groups on activated carbon electrodes. However, when mixed with acetonitrile in $[N_{2220}][NTf_2]$, no obvious reversible pseudocapacitive behaviour was detected in our study although MCs possess O content on the surface ranging from 4.2% to 6.5%. Figure 4.13b summarised the gravimetric specific capacitance of MCs in IL electrolyte at various current densities. Consistent with the CV test, glyoxal-resultant MC samples showed larger capacitances, with a highest value of 57.5 F/g at 0.1 A/g. The

capacitance dropped nearly half of the initial value at higher current density of 20 A/g, suggesting a relatively poorer rate capability than MCs prepared with formaldehyde or glyoxylic acid. Sample GA1.25 barely showed capacitance due to the lack of rich porosity. In neat IL $[N_{2220}][NTf_2]$ electrolyte, Timperman *et al.*[18] reported a gravimetric capacitance of 125 F/g and 144 F/g with activated carbon working electrodes when the potential window was 2 V and 3 V respectively. When mixed with acetonitrile (weight fraction 0.5) in $[N_{2220}][NTf_2]$ electrolyte, the capacitance slightly rose to 128 F/g with a potential window of 2 V. The higher values reported from their work are mainly associated with the activated carbon electrodes, which exhibited a BET surface area of 1,500 m^2/g hence a higher potential for charge accumulation on the pore surface. Similarly, Sathyamoorthi *et al.*[29] reported the use activated carbon working electrodes (with a surface area of 965.3 m^2/g) in the $[N_{2220}][NTf_2]$ electrolyte; the specific capacitance and energy density were enhanced from 42 F/g and 18.4 Wh/kg in neat $[N_{2220}][NTf_2]$ electrolyte to 72 F/g and 31.2 Wh/kg in $[N_{2220}][NTf_2]$ mixed with 0.3 M hydroquinone as the mediator.

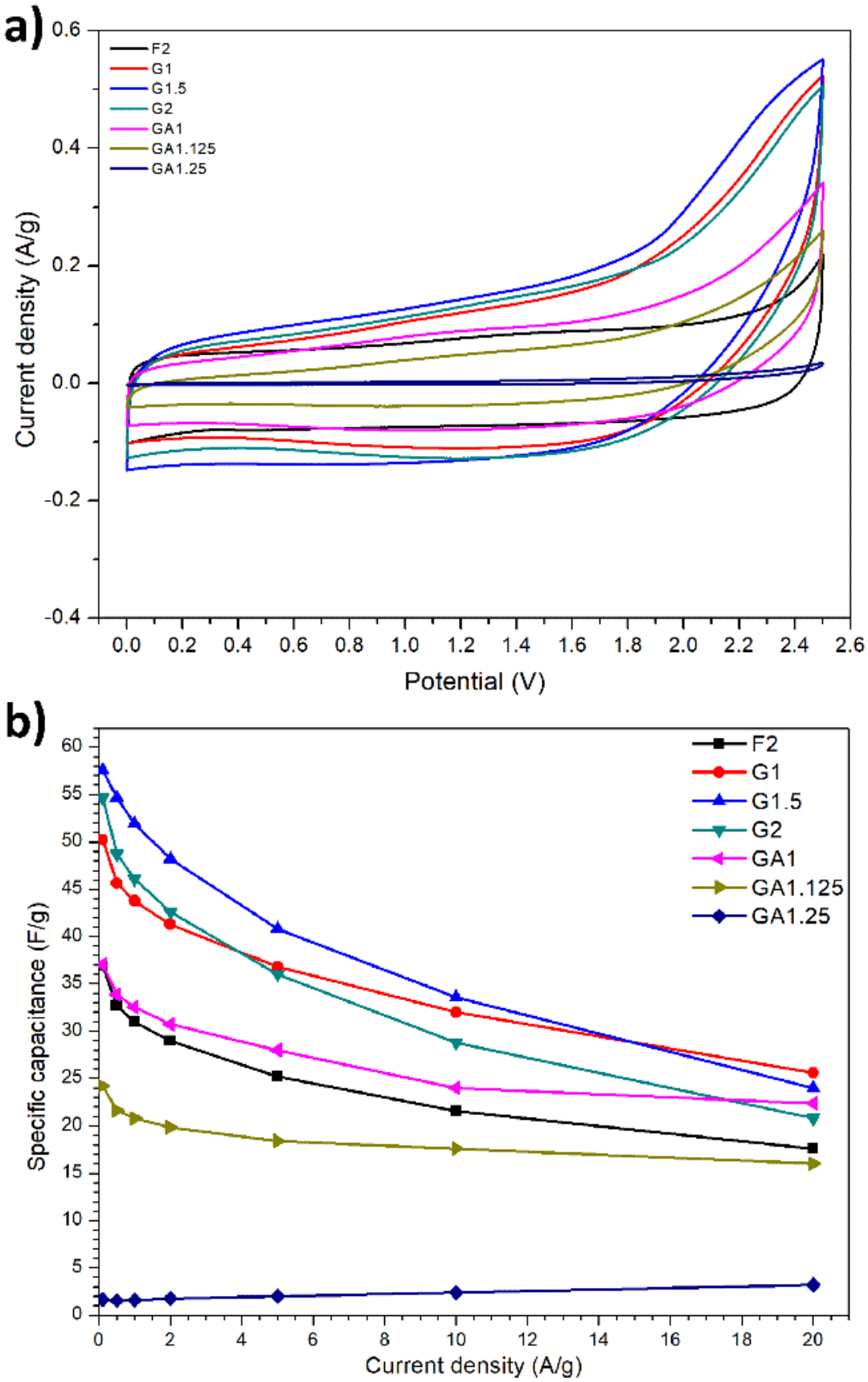

Figure 4.13. a) Cyclic voltammetry (CV test) at 5 mV/s in $[N_{2220}][NTf_2]$/ACN electrolyte and b) gravimetric specific capacitance for MC samples prepared by various cross-linkers.

Pore size close to the solvated electrolyte ion size is expected to deliver a maximum double-layer capacitance, which suggests that with the same mesopore channel both larger and smaller ion sizes could significantly decrease the capacitance.[25] For all the three glyoxal-resultant MCs with ordered mesopore channels, G1, G1.5, and G2 with an increasing C/P ratio possess a decreasing mesopore size of 6.1, 4.3, and 3.3 nm, respectively. The dominating mesopores in G1 are bigger than that in G1.5. Therefore, electrolyte ions (*i.e.* solvated K^+, OH^-, $[N_{2220}]^+$, and $[NTf_2]^-$) may match relatively better with the mesopore channels of sample G1.5 than those of G1. Amongst the four ions, the largest ion $[NTf_2]^-$ has a dynamic diameter in the longest dimension of 0.79 nm for the neat ion and 2.24 nm when solvated in acetronitrile.[31] The smaller mesopores of sample G2 seem to be more promising than G1.5 to match the ions of both electrolytes, therefore the smaller capacitance for G2 could be resulted from its relatively smaller pore volume of 0.48 cm^3/g than G1.5 (0.56 cm^3/g). Additionally, sample G1.5 has a larger mesopore rate of 68% than G2 (58%), which may also contribute to a higher potential for ion adsorption and deliver a higher capacitance. Upon balancing the pores to match electrolyte ions and pore volume for charge accumulation, sample G1.5 exhibits an intermediate mesopore size and pore volume compared with other two counterparts, thus yielded a relatively higher capacitance in both aqueous and IL electrolytes.

For ordered MCs with same pore size, different graphitisation degree or heteroatoms in MCs can lead to a significant difference in capacitance. Lin *et al.*[32] fabricated a nitrogen-doped ordered mesoporous few-layer carbon for supercapacitor, which exhibited a capacitance as high as 855 F/g in aqueous electrolyte, drastically higher than most ordinary ordered MC and mesopore few-layer carbon without doping. In comparison of the three MCs, namely ordinary templated ordered MC, mesopore few-layer carbon, and nitrogen-doped ordered mesoporous few-layer carbon, they possess similar porosity and pore size. Therefore, such huge difference in capacitance is mainly derived from: 1) higher graphitisation degree that significantly improved the electroconductivity, and 2) high content of heteroatom, which further improved the conductivity, enhanced the affinity to the electrolyte, and provided pseudocapacitance. In this work, the graphitisation degree and surface functionalities on MCs prepared by employing different cross-linkers are relatively comparable. Therefore, the difference in electrochemical performance of various MCs is mainly derived from the dissimilarity of the pore architectures.

Figure 4.14 compares the electrochemical performance of the same MC sample G1.5 in two different electrolytes, 6 M KOH aqueous solution and $[N_{2220}][NTf_2]$/ACN organic electrolyte. At a scan rate of 50 mV/s (Figure 4.14a), cells with G1.5 working electrodes exhibited excellent charging/discharging kinetics in both electrolytes, evidenced by the symmetric rectangular-shaped CV profiles. KOH electrolyte delivered a larger charging/discharging current than $[N_{2220}][NTf_2]$/ACN electrolyte, while the latter electrolyte displayed a much wider working potential window. As shown in Figure 4.14b, the discharge time for $[N_{2220}][NTf_2]$/ACN electrolyte at 0.5 A/g was 137 s, compared with 167 s for KOH electrolyte. Higher working potential window of $[N_{2220}][NTf_2]$/ACN electrolyte did not result in a longer charge/discharge time. The efficiency was expressed by the ratio of discharge time t_d to charge time t_c ($\eta = t_d/t_c$). Cell with G1.5 working electrodes showed a better reversibility with a higher efficiency of 92.8% in KOH electrolyte than that in $[N_{2220}][NTf_2]$/ACN electrolyte (84.0%). The higher efficiency of KOH electrolyte could possibly benefit from the smaller solvated ion sizes and higher mobility of K^+ and OH^- in the same mesopore channel, compared with larger organic $[N_{2220}]^+$ and $[NTf_2]^-$ ions. Sample G1.5 could form electric double-layer much rapid in KOH electrolyte. As observed on the Nyquist plots (Figure 4.14c), sample G1.5 showed typical EDLC behaviour in both electrolytes with a profile composed of a semi-circle, a 45° slope regime, and nearly vertical line at high, intermediate, and low frequencies.[33] The bulk electrolyte resistance of 6M KOH aqueous solution (0.20 Ω) was much smaller than $[N_{2220}][NTf_2]$/ACN electrolyte (0.62 Ω). KOH electrolyte also delivered an internal resistance of 0.96 Ω, which includes the electrolyte resistance, the electrode resistance, the current collector-electrode contact resistance, charge transfer resistance, and so forth. While the value of internal resistance for $[N_{2220}][NTf_2]$/ACN electrolyte was 2.10 Ω, which may provide an explanation for the slower ionic transport. The in-pores diffusivity, characterised by the 45° slope at intermediate frequencies, is quite comparable for both electrolytes, but that with KOH electrolyte is slightly better with an overall faster occurrence of knee-point. Moreover, KOH electrolyte also showed a much better dominant capacitive behaviour than $[N_{2220}][NTf_2]$/ACN electrolyte, evidenced by the shorter nearly-vertical line at low frequencies. As a consequence of the smaller resistance of KOH electrolyte, sample G1.5 exhibited a much higher specific capacitance (153.5 F/g at 0.1 A/g dropped to 73.3 F/g at 20 A/g) than in $[N_{2220}][NTf_2]$/ACN electrolyte (57.5 F/g at 0.1 A/g dropped to 24.0 F/g at 20 A/g) (Figure 4.14d). However, conversely, the energy density yielded from KOH electrolyte was much smaller than $[N_{2220}][NTf_2]$/ACN electrolyte with the value of 12.5 Wh/kg compared with 7.7 Wh/kg for

the former (Figure 4.14e). This is mainly derived from the much wider working potential window of $[N_{2220}][NTf_2]$/ACN electrolyte.

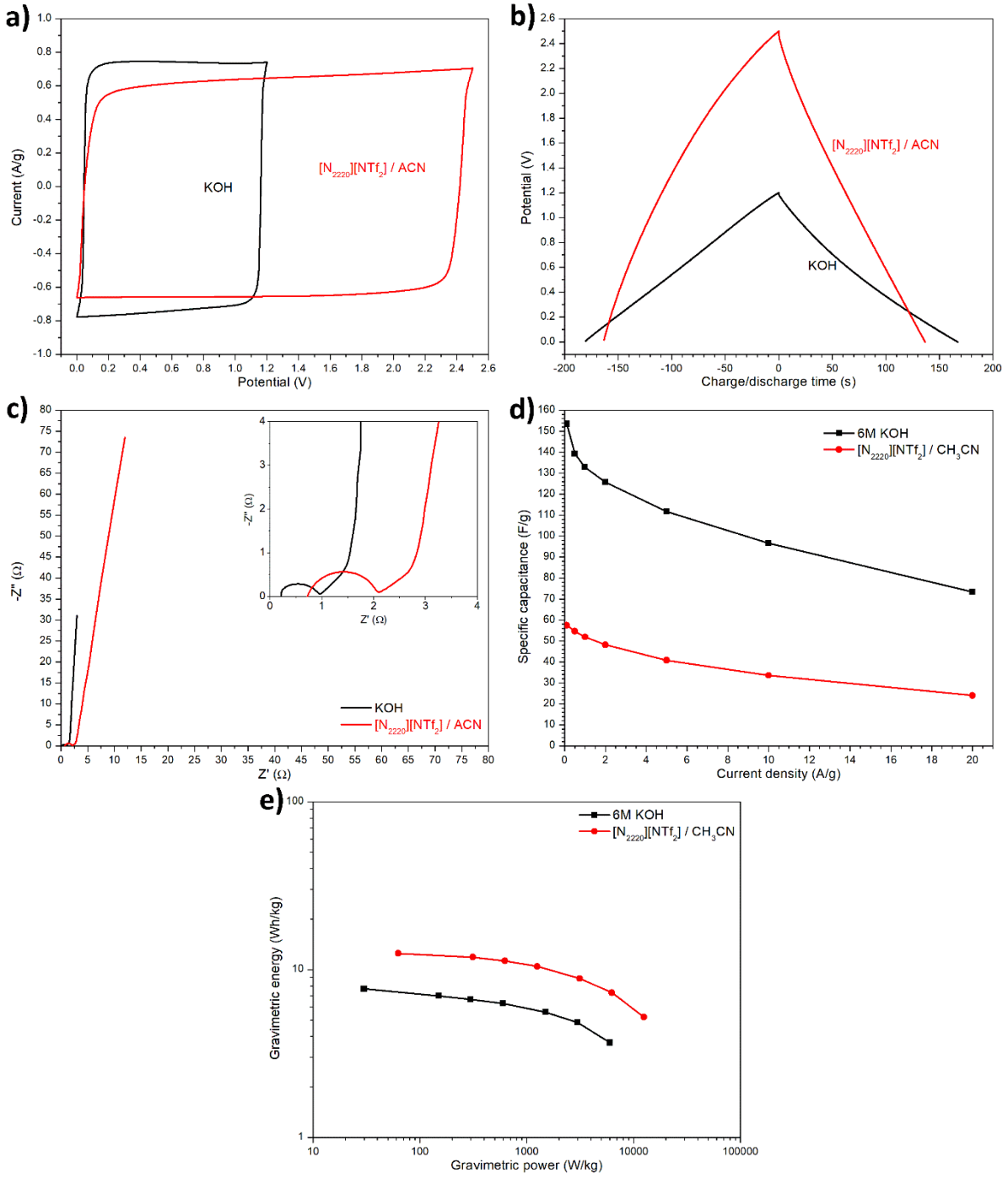

Figure 4.14. Comparison of the same sample G1.5 in two different electrolytes: a) CV test at 50 mV/s, b) galvanostatic charge/discharge at 0.5 A/g, c) Nyquist plot, d) gravimetric specific capacitance, and e) energy density, respectively.

To further improve the capacitance and energy density of ordered MCs, future effort can be directed towards 1) enhancing the graphitisation degree, 2) doping with heteroatoms such as nitrogen, sulphur, and phosphor, 3) improving the interconnectivity of mesopores, and 4) modification of surface functionalities. Template-synthesised MCs are incompletely

graphitised and belong to amorphous carbon in nature. Adjusting the degree of graphitisation by thermal treatment can enhance their conductivity and electrochemical doping thus improve the supercapacitor performance with a higher capacitance.[22,32] During templating synthesis, laser-irradiation-assisted evaporation induced self-assembly process generated a better graphitic structure on the resulting carbon material when the glyoxylic acid was employed as the cross-linker.[10] Such technique could also be introduced in combination with the use of glyoxal cross-linker, which can easily yield highly ordered mesoporous structures according to this study. Heteroatom-doping on carbon materials has multi-fold effects: 1) increasing the interfacial capacitance by extending the quantum capacitance and providing pseudocapacitance, and improving the affinity with electrolyte.[32,34] Creating smaller accessible pores on the mesopore walls to connect neighbouring mesopores will drastically improve the porosity for charge accumulation, especially pores close to with the solvated electrolyte ions. Smaller pores than the solvated electrolyte ions can also improve the capacitance due to the distortion of solvation shells which makes the ion centre closer to the electrode.[35] Moreover, the interconnectivity of adjacent mesopores would be significantly improved to decrease the penetration depth. This could be achieved by employing further activation after initial carbonisation with greener activation agents/porogens (*e.g.* CO_2 or steam). However, this additional step will lead to new problems such as an increased cost, higher carbon footprint, and reduced carbon yield.

4.4. Conclusions

The role of different cross-linkers on the pore architecture and surface functionality of resulting MCs was studied. Glyoxal favours the formation of highly ordered well-organised hexagonal mesopores with pore size easily tuneable from 3.3 and 6.1 nm thus proves to be a promising alternative cross-linker to replace formaldehyde. As the cross-linker/precursor ratio increased from 1 to 2, the surface area of glyoxal-resultant MCs rose from 753.4 to 820.7 m^2/g, whilst the pore volume decreased from 0.69 to 0.48 cm^3/g, respectively. Glyoxylic acid and formaldehyde resulted in interrupted even entirely disordered mesopore structures due to the formation of over-cross-linked precursors that destabilised the ordered mesophase generated from the self-assembly. With the improvement of calculation capability of supercomputers in the future, such study on the role of cross-linking in the pore architectures of templating synthesised MCs could be possibly carried out by performing multi-scale modelling combined with the existing experimental results, especially to reveal the influence of the presence of cross-linkers on the self-assembly and how the formation of

over-cross-linked precursor destabilises the well-organised mesophase during self-assembly. It will be also quite interesting to employ computational modelling to directly achieve the prediction of pore architectures, such as mesopore diameters and topologies.

Different cross-linkers at various mixing ratios influence the surface functionalities of resulting MCs. For the same cross-linker, a larger C/P ratio led to a higher content of -C-O group and a lower content of -C=O group. At the same mixing ratio, glyoxylic acid resulted in a higher -C-O content than glyoxal. With the same amount of aldehyde groups, formaldehyde yielded a lower -C-O content than glyoxal due to the higher reactivity of formaldehyde.

When employed as the working electrodes for symmetric supercapacitors, glyoxal-resultant MCs thanks to the existence of dominating highly ordered mesopore channels exhibited higher specific capacitance of 153.5 F/g in 6M KOH aqueous electrolyte and 57.5 F/g in IL $[N_{2220}][NTf_2]$/ACN electrolyte, respectively. MCs prepared with glyoxylic acid and formaldehyde showed a relatively lower capacitance because of their disordered or interrupted mesopore structures. Although KOH electrolyte yielded a higher capacitance with the same working electrode than $[N_{2220}][NTf_2]$/ACN electrolyte, the energy density was lower with a value of 7.7 Wh/kg compared with 12.5 Wh/kg achieved with IL electrolyte. Further optimisation of the preparation method can be applied in the future to allow both capacitance and energy density improved significantly.

4.5. References

1 B. Nagy, E. Geissler and K. László, *Microporous Mesoporous Mater.*, 2020, **294**, 1–10.

2 S. A. Al-Muhtaseb and J. A. Ritter, *Adv. Mater.*, 2003, 15, 101–114.

3 P. Zhang, L. Wang, S. Yang, J. A. Schott, X. Liu, S. M. Mahurin, C. Huang, Y. Zhang, P. F. Fulvio, M. F. Chisholm and S. Dai, *Nat. Commun.*, 2017, **8**, 1–10.

4 Y. Meng, D. Gu, F. Zhang, Y. Shi, H. Yang, Z. Li, C. Yu, B. Tu and D. Zhao, *Angew. Chemie - Int. Ed.*, 2005, **44**, 7053–7059.

5 C. Liang, K. Hong, G. A. Guiochon, J. W. Mays and S. Dai, *Angew. Chemie - Int. Ed.*, 2004, **43**, 5785–5789.

6 Y. Meng, D. Gu, F. Zhang, Y. Shi, L. Cheng, D. Feng, Z. Wu, Z. Chen, Y. Wan, A. Stein and D. Zhao, *Chem. Mater.*, 2006, **18**, 4447–4464.

7 C. Liang, Z. Li and S. Dai, *Angew. Chemie Int. Ed.*, 2008, 47, 3696–3717.

8 C. Matei Ghimbeu, L. Vidal, L. Delmotte, J. M. Le Meins and C. Vix-Guterl, *Green Chem.*, 2014, **16**, 3079–3088.

9 G. Moussa, S. Hajjar-Garreau, P.-L. Taberna, P. Simon and C. Matei Ghimbeu, *J. Carbon Res.*, 2018, **4**, 1–17.

10 M. Sopronyi, F. Sima, C. Vaulot, L. Delmotte, A. Bahouka and C. M. Ghimbeu, *Sci. Rep.*, 2016, **6**, 1–13.

11 E. Axente, M. Sopronyi, C. Matei Ghimbeu, C. Nita, A. Airoudj, G. Schrodj and F. Sima, *Carbon N. Y.*, 2017, **122**, 484–495.

12 A. Maetz, L. Delmotte, G. Moussa, J. Dentzer, S. Knopf and C. M. Ghimbeu, *Green Chem.*, 2017, **19**, 2266–2274.

13 H. Younesi-Kordkheili, *J. Adhes.*, 2019, **95**, 1075–1087.

14 R. T. Mayes, C. Tsouris, J. O. Kiggans, S. M. Mahurin, D. W. Depaoli and S. Dai, *J. Mater. Chem.*, 2010, **20**, 8674–8678.

15 S. Herou, M. C. Ribadeneyra, R. Madhu, V. Araullo-Peters, A. Jensen, P. Schlee and M. Titirici, *Green Chem.*, 2019, **21**, 550–559.

16 D. Saha, K. E. Warren and A. K. Naskar, *Carbon N. Y.*, 2014, **71**, 47–57.

17 C. Tsouris, R. Mayes, J. Kiggans, K. Sharma, S. Yiacoumi, D. Depaoli and S. Dai,

Environ. Sci. Technol., 2011, **45**, 10243–10249.

18 L. Timperman, P. Skowron, A. Boisset, H. Galiano, D. Lemordant, E. Frackowiak, F. Béguin and M. Anouti, *Phys. Chem. Chem. Phys.*, 2012, **14**, 8199–8207.

19 M. Thommes, K. Kaneko, A. V. Neimark, J. P. Olivier, F. Rodriguez-Reinoso, J. Rouquerol and K. S. W. Sing, *Pure Appl. Chem.*, 2015, **87**, 1051–1069.

20 D. Saha, R. Zacharia and A. K. Naskar, in *Polymer Precursor-Derived Carbon*, 2014, vol. 1173, pp. 61–83.

21 H. N. Tran, F. C. Huang, C. K. Lee and H. P. Chao, *Green Process. Synth.*, 2017, **6**, 565–576.

22 D. Weingarth, M. Zeiger, N. Jäckel, M. Aslan, G. Feng and V. Presser, *Adv. Energy Mater.*, 2014, **4**, 1–13.

23 A. C. Ferrari, J. C. Meyer, V. Scardaci, C. Casiraghi, M. Lazzeri, F. Mauri, S. Piscanec, D. Jiang, K. S. Novoselov, S. Roth and A. K. Geim, *Phys. Rev. Lett.*, 2006, **97**, 1–4.

24 Y. Song, J. Liu, K. Sun and W. Xu, *RSC Adv.*, 2017, **7**, 48324–48332.

25 C. Largeot, C. Portet, J. Chmiola, P. L. Taberna, Y. Gogotsi and P. Simon, *J. Am. Chem. Soc.*, 2008, **130**, 2730–2731.

26 B.-J. Lee, H.-Y. Park, D.-S. Yang, T.-H. Kang, S. Hwang and J.-S. Yu, *J. Electrochem. Soc.*, 2019, **166**, A5244–A5251.

27 S. Shahzad, A. Shah, E. Kowsari, F. J. Iftikhar, A. Nawab, B. Piro, M. S. Akhter, U. A. Rana and Y. Zou, *Glob. Challenges*, 2019, **3**, 1–17.

28 L. Yu and G. Z. Chen, *Front. Chem.*, 2019, **7**, 1–15.

29 S. Sathyamoorthi, V. Suryanarayanan and D. Velayutham, *J. Power Sources*, 2015, **274**, 1135–1139.

30 A. Brandt, J. Pires, M. Anouti and A. Balducci, *Electrochim. Acta*, 2013, **108**, 226–231.

31 R. Lin, P. Huang, J. Ségalini, C. Largeot, P. L. Taberna, J. Chmiola, Y. Gogotsi and P. Simon, *Electrochim. Acta*, 2009, **54**, 7025–7032.

32 T. Lin, I. W. Chen, F. Liu, C. Yang, H. Bi, F. Xu and F. Huang, *Science*, 2015, **350**, 1508–1513.

33 B. A. Mei, O. Munteshari, J. Lau, B. Dunn and L. Pilon, *J. Phys. Chem. C*, 2018, **122**,

194–206.

34 L. L. Zhang, X. Zhao, H. Ji, M. D. Stoller, L. Lai, S. Murali, S. McDonnell, B. Cleveger, R. M. Wallace and R. S. Ruoff, *Energy Environ. Sci.*, 2012, **5**, 9618–9625.

35 J. Chmiola, G. Yushin, Y. Gogotsi, C. Portet, P. Simon and P. L. Taberna, *Science*, 2006, **313**, 1760–1763.

Chapter 5.

Preparation of MCs by employing IL templates

5.1. Introduction

This chapter is built on the work of earlier chapters. *Chapter 3* investigated the self-assembly mechanism of the use of IL templates to prepare mesoporous carbons (MCs); the findings provided insight into key effective ways to manipulate the morphologies of ILs and select suitable carbon precursors during templating synthesis. The subsequent *Chapter 4* studied the role of cross-linking in the pore architecture, surface functionality, and electrochemical performance of resulting MCs. With the findings from both chapters, *Chapter 5* explores the practical preparation of MCs for energy storage by employing amphiphilic ILs as the recyclable template.

As mentioned in *Chapter 1*, the use of IL templates to fabricate MCs remains at an initial stage. In earlier publications, ILs mainly functioned as sacrificial precursors for carbon matrix and the dopped heteroatoms thereof such as nitrogen and boron.[1–9] Additional templates or porogens were usually employed for generating pore structures, such as mesoporous silica SBA-15[10–13], silica nanoparticles[14–16], block copolymers Pluronic F127[17], and eutectic salt[18]. Some publications pointed out the role of ILs as co-template in templating synthesis to assist a main templating agent either hard-template tetraethyl orthosilicate (TEOS) or soft-template block copolymer.[17,19] However, the role of ILs as the co-template in those studies was pretty limited. Only a few of publications employed ILs as a main even the only templating agent,[20–22] which are summarised in *Chapter 1* in detail. Overall, these explorations failed to generate highly ordered mesopores due to not only the use of less amphiphilic ILs as templates that are unable to form long range ordered mesostructures but the lack of fundamental understanding on the self-assembly mechanism by employing IL templates. *Chapter 3* and *Chapter 4* have bridged certain knowledge gap between the fundamental understanding and the practical preparation of MCs by employing ILs as the recyclable template. Therefore, this chapter puts into practice to explore the use of amphiphilic IL templates to fabricate highly ordered MCs. In this chapter, not only the use of amphiphilic ILs as sole template was studied, but also preparing MCs under the assist of a well-established non-recyclable block copolymer as co-template was explored. Some key factors including the length of cationic alkyl chain, anion of IL templates, IL template extraction, and the percentage of block copolymer in IL/block copolymer co-templating mixtures were investigated systematically with a special focus on the porosity, pore morphology, surface functionality, and electrochemical performance of resulting MC materials.

5.2. Methodology

5.2.1. Synthesis of ILs

IL 1-decyl-3-methylimidazolium acetate, [C_{10}MIM][OAc], proves to be feasible to form hexagonal cylindrical mesophase in the presence of carbon precursor in *Chapter 3* thus become a candidate template for the practical preparation. 1-octadecyl-3-methylimidazolium acetate, [C_{18}MIM][OAc], with a long cationic alkyl chain than [C_{10}MIM][OAc], hence stronger amphiphilicity, is chosen to study the effect of the length of cationic chain of IL template on the templating synthesis of MCs. A methyl sulphate-based IL [C_{18}MIM][$MeSO_4$] is chosen as representative to investigate the role of IL anions on the templating synthesis.

1) Preparation of 1-decyl-3-methylimidazolium acetate, [C_{10}MIM][OAc]

The preparation of [C_{10}MIM][OAc] follows a typical two-step process: the alkylation of 1-methylimidazole with 1-bromodecane and a metathesis reaction for anion exchange from bromide to acetate. Detailed procedures were described in *Chapter 3*.

2) Preparation of 1-octadecyl-3-methylimidazolium acetate, [C_{18}MIM][OAc]

Similar with the synthesis of [C_{10}MIM][OAc], a two-step process was applied to prepare [C_{18}MIM][OAc]: the alkylation of 1-methylimidazole with 1-bromooctadecane and a metathesis reaction for anion exchange from bromide to acetate.

In a typical procedure, 1-methylimidazole (0.6 mol, 99%, Sigma-Aldrich) and 1-bromooctadecane (0.6 mol, ≥97%, Sigma-Aldrich) were dissolved in acetone (300 mL, ≥99.8%, Fisher Scientific). The flask was connected to a Schlenk line with flowing N_2 gas (100 mL/min) and refluxed at 85 °C using an oil bath for 15 h. The liquid mixture was cooled to room temperature until getting fully crystallised. The solid product was washed with ethyl acetate then the solvent was removed by rotavapor. The product was further dried overnight in a vacuum oven at 50 °C. [C_{18}MIM]Br was obtained as white solid (yield: >99%).

For the metathesis reaction, [C_{18}MIM]Br (241.3 g) was first dissolved with potassium acetate (KOAc, 57.5 g, ≥99%, Sigma-Aldrich) in absolute ethanol (500 mL, ≥99.8%, Fisher Scientific). Slight excess of KOAc was necessary to guarantee the displacement of bromide. The mixture was stirred at ambient temperature overnight. The insoluble KBr was separated out of the solution by filtration then the remaining ethanol in the filtrate was removed by rotavapor. The product was dissolved in acetone to precipitate the rest of KBr and excessive KOAc. [C_{18}MIM][OAc] can also precipitate at lower temperature, so slightly warmer acetone

(around 30 °C) was used as solvent, rather than cold acetone and cooling in the refrigerator. The insoluble potassium salts were filtered out and the remaining acetone in the filtrate was removed by rotavapor. The product was further dried overnight in a vacuum oven at 50 °C. [C_{18}MIM][OAc] was obtained as beige solid (yield: 80%).

3) Preparation of 1-actadecyl-3-methylimidazolium methyl sulphate, [C_{18}MIM][$MeSO_4$]

The synthesis of [C_{18}MIM][$MeSO_4$] followed a two-step procedure different from the preparation of [C_{18}MIM][OAc]. Step one involved the deprotonation of imidazole followed by alkylation of imidazolium salt[23], whilst step 2 converted 1-octadecylimidazole into 1-actadecyl-3-methylimidazolium methyl sulphate by the addition of dimethyl sulphate.[24,25]

In a typical procedure, NaOMe (0.2 mol, 25 wt% in methanol) and imidazole (0.2 mol) were dissolved in 100 mL of acetonitrile then stirred at 85 °C for 2 h in a 1000 mL three-neck flask connected to a Schlenk line. 1-bromooctadecane (0.2 mol, ≥97%, Sigma-Aldrich) was added into above mixture, which reacted at 85 °C under reflux with N_2 flow (100 mL/min) for 24 h, yielding beige solid precipitate in the bottom of the flask. The solvent was removed by rotavapor, then chloroform (200 mL) was added to dissolve the beige solid product. After removing insoluble NaBr precipitate, H_2O (100 mL) was added into filtrate, forming two phases. The aqueous phase was dumped whilst the remaining chloroform solution was transferred into a flask. The solvent chloroform was removed by rotavapor, and the solid product was further dried overnight in a vacuum oven at 50 °C. 1-octadecylimidazole was obtained as beige waxy solid product (yield: >99%).

For step two, 1-octadecylimidazole (0.2 mol) was first dissolved in toluene (500 mL) at room temperature, then dimethyl sulphate (0.2 mol) was added drop wise (flow rate *ca.* 0.5 drops/sec) whilst stirring in ice bath. After 1 h, the mixture was further stirred at room temperature for another 1 h and oily solid product (meltable over 30 °C) was formed thereafter in the flask. Toluene was removed by using rotavapor at room temperature. The resulting product was washed with ethyl acetate (200 mL) for three times, then dried overnight in a vacuum oven at 50 °C. [C_{18}MIM][$MeSO_4$] was obtained as light yellowish powder (yield: >99%).

4) Preparation of IL electrolyte triethylammonium bis(tetrafluoromethylsulfonyl)amide, [N_{2220}][NTf_2]

IL triethylammonium bis(tetrafluoromethylsulfonyl)amide/acetonitrile, [N_{2220}][NTf_2]/ACN (weight fraction of ACN: 0.5), is chosen as a representative electrolyte, which provided

higher energy density than aqueous 6M KOH electrolyte in *Chapter 4*. The detailed synthesis procedures of $[N_{2220}][NTf_2]$ are described in *Chapter 4*.

5.2.2. Preparation of MCs with IL templates

An evaporation-induced self-assembly (EISA) technique was applied when employing amphiphilic ILs as the template to prepare MCs. After the self-assembly process, the cross-linking of carbon precursor monomers and the extraction of IL templates took place in sequence, followed by the calcination to form carbon materials (Figure 5.1). Phloroglucinol-glyoxal-polymer, a preliminary aromatic polymer model for lignin, was chosen as the carbon precursor. According to *Chapter 3*, phenolic polymers with phloroglucinol monomer are more suitable carbon precursors because their monomer phloroglucinol preferentially resides in the hydrophiphilic phase of IL micelles thereby leaving the hydrophobic phase to generate pore structures. Furthermore, the successful use of phloroglucinol-glyoxal-polymer as carbon precursor will potentially guide the pretreatment process of natural lignin polymer for the preparation of MCs in the future. As for the cross-linking agent, *Chapter 4* proves glyoxal to be more promising that favours the formation of ordered mesopore channels with pore diameter tuneable and delivers higher capacitance for energy storage.

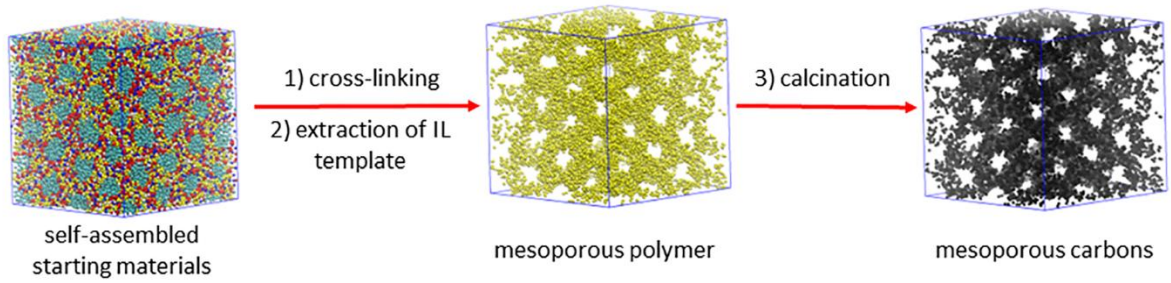

Figure 5.1. Scheme for the fabrication of mesoporous carbon materials by employing IL templates.

For a typical run, 0.82 g of phloroglucinol and 1.84 g of $[C_{10}MIM][OAc]$ were dissolved in 40 mL of absolute ethanol. After stirring for 30 min, 1.42 g of glyoxal (40 wt% aq.) was added dropwise into above solution, which was further stirred vigorously at room-temperature for at least 2 h. The solution was poured into a clean glass petri dish and placed at 30 °C to allow solvent to evaporate sufficiently. This process took over 24 h until most of the solvent was evaporated. Part of the solvent, mainly water from glyoxal solution, was trapped in the mixture to form a well-organised mesostructure. The molar ratio of glyoxal : phloroglucinol : IL : water in the remaining mixture approached around 1.5:1:1:4, at which the mixture is expected to self-assemble into a well-organised mesophase. The mass ratio

between precursor monomer and template around 1:2 was widely used in earlier publications to achieve the ordered mesopore structures.[26–29] The molar ratio of cross-linker glyoxal/precursor (C/P ratio) was kept constant at 1.5:1 in favour of the formation of highly ordered mesopore channels, and a higher capacitance of MCs was obtained when used as supercapacitor electrodes according to *Chapter 4*. After solvent evaporation, a homogenous viscous mixture was obtained, which was sequentially cross-linked at 85 °C for 24 h. The cross-linked homogeneous film was removed from petri dish, chopped into chunks, and transferred into a thimble of Soxhlet extractor for the extraction of ILs, *i.e.*, the template recycling process. The polymer film was extracted with methanol for 72 h. The product was dried completely in a 50 °C vacuum oven, transferred into a quartz boat, and calcinated at 800 °C for 1 h with a heating rate of 1 °C/min under inert environment (N_2 gas with a flow rate of 100 mL/min). The product was cooled down naturally to room temperature then N_2 gas was switched off. Extraction solvent methanol was removed by rotavapor to yield IL templates, which was further dried overnight in a 50 °C vacuum oven.

Another two IL templates with longer cationic alkyl chains hence stronger amphiphilicity, [C_{18}MIM][OAc] and [C_{18}MIM][$MeSO_4$], were also employed for the preparation of MCs. Block copolymer Pluronic F127 (poly(ethylene oxide)$_{106}$-poly(propylene oxide)$_{70}$-poly(ethylene oxide)$_{106}$, $EO_{106}PO_{70}EO_{106}$), was added together with the IL template to assist the formation of IL micelles during the self-assembly process. ILs can co-assemble with block copolymers by hydrophobic interactions between the cationic alkyl chain and the poly(propylene oxide) segment; the cationic alkyl chains reside inside the hydrophobic core formed by PO segments with the positively charged imidazolium rings exposed at the micellar core-corona interface.[30–32] The mass ratio between phloroglucinol and templating agent was still kept constant around 1:2 whilst the rest of procedures remained the same. The resulting carbon products were labelled as n%OAc or n%$MeSO_4$, where n% indicates the percentage of IL template in the total templating agents. For carbon samples prepared by the same procedure but excluding the extraction process of IL templates were labelled as n%OAc-E.

5.2.3. Characterisation

Nuclear magnetic resonance (NMR) spectroscopy. The synthesised ILs and recycled IL templates were characterised by ^{1}H NMR spectroscopy. Chloroform-d and dimethyl sulfoxide-d6 (DMSO-d6) were used as solvent and the internal reference, respectively. Proton spectra were recorded on Bruker Avance III 400 MHz NMR spectrometer.

Porosity analysis: Adsorption test of methylene blue aqueous solution was carried out for the semi-quantitative estimation of porosities of porous carbons.[33] BET surface area and pore volume for samples were measured quantitatively by N_2 physisorption isotherms at 77 K with an ASAP 2420 analyser. Pore size distribution was calculated by Barrett-Joyner-Halenda (BJH) method. Compared with the N_2 physisorption isotherm, methylene blue adsorption test is quicker and more straightforward to screen highly porous carbons from barely porous ones.

Morphology analysis: Morphologies of resulting MCs were studied by performing scanning electron microscopy (SEM), transmission electron microscopy (TEM) and scanning transmission electron microscopy (STEM) with a FEI Quanta 250 FEG scanning electron microscope, TALOS F200X G2 microscope without and with high-angle annular dark-field (HAADF) imaging technique, respectively.

Surface functionality analysis: The organic groups on the surface of MCs were measured by X-ray photoelectron spectroscopy (XPS) with a Thermo Scientific™ ESCALAB™ QXi X-ray Photoelectron Spectrometer. Each spectrum was averaged by at least 4 random independent measurements.

Graphitisation degree analysis: Raman spectra were recorded on a WITec Alpha 300 Raman microscope equipped with a 532 nm laser (10 mW laser power). Each sample was measured by at least 3 random independent accumulations with a 50 s accumulation time.

5.2.4. Electrochemical performance

The test procedure remains the same as described in *Chapter 4*. The resulting MCs were employed as electrode working materials for supercapacitors. Their electrochemical performance was tested in a symmetric two-electrode Swagelok-type full cell with IL electrolyte. The mixing mass ratio in each electrode pellet was 90:5:5 for working material, PTFE binder, and multi-walled carbon nanotubes (MWCNT) conductive material, respectively. Absolute ethanol was used to blend electrode materials into a slurry which was further pressed into a homogeneous thin free-stand pellet at 2 tons for 5 min. The obtained electrode pellet was dried completely in a 50 ℃ vacuum oven for at least 12 h and measured around 10 mg in weight, 13 mm in diameter, and 120 μm in thickness. The battery cell was assembled and tested in a glovebox (O_2 content: < 0.1 ppm, H_2O content: < 0.5 ppm). A GF/F glass microfiber separator (Whattman®, 15 mm in diameter, 420 μm in thickness) soaked with IL electrolyte was used to separate two symmetric electrode pellets.

The gravimetric specific capacitance (C_s, F/g) was calculated from the galvanostatic charge-discharge curve by using discharge time:

$$C_s = 4C_{cell} = \frac{4\,\mathrm{I} \times \Delta t}{\mathrm{m} \times V} \quad \text{(Equation 5.1)}$$

The specific energy density (E, Wh/kg) and power density (P, W/kg) were calculated by using equations:

$$E = \frac{1}{2}\mathrm{C}_{cell}V^2 \times \frac{1}{3600} \times 1000 \quad \text{(Equation 5.2)}$$

$$P = \frac{E}{\Delta t} \times 3600 \quad \text{(Equation 5.3)}$$

where Δt (s), I (A), m (g), and V (V) represent the discharge time, discharge current, total mass of active working materials on both electrodes, and operating potential window applied.

5.3. Results and Discussion

5.3.1. Determination of cross-linker/precursor mixing ratio

Long-chain ILs were chosen as the soft template not only because of their amphiphilicity but also their excellent recyclability.[20,22,34–36] According to *Chapter 4*, ordered mesopores can be obtained with glyoxal cross-linker with a wide C/P ratio between 1 and 2. However, it remains unclear if the precursor was cross-linked sufficiently to generate a stable polymer framework as the IL templates need to be extracted for recycling. The recycled IL templates are expected to contain impurities as little as possible, even no impurity under the best circumstance.

NMR spectroscopy was performed to all recycled IL templates after being extracted for 72 h. At a lower C/P ratio of 1, polymer fragments were detected in the extracted IL, as well as moisture (Figure 5.2a). Under this circumstance, polymer monomers were not cross-linked sufficiently, therefore some polymer fractions were dissolved in methanol during the extraction. As the C/P ratio exceeded 1.5, no peaks for polymer fragments were detected (Figure 5.2b and c) and the recycled ILs showed excellent structural intactness after the extraction. This suggests a sufficient cross-linking of precursor monomers and the reusability of recycle ILs once being dried entirely. Overall, the impurity study on the recycled IL templates provides a second perspective to elucidate the use of C/P ratio 1.5:1.

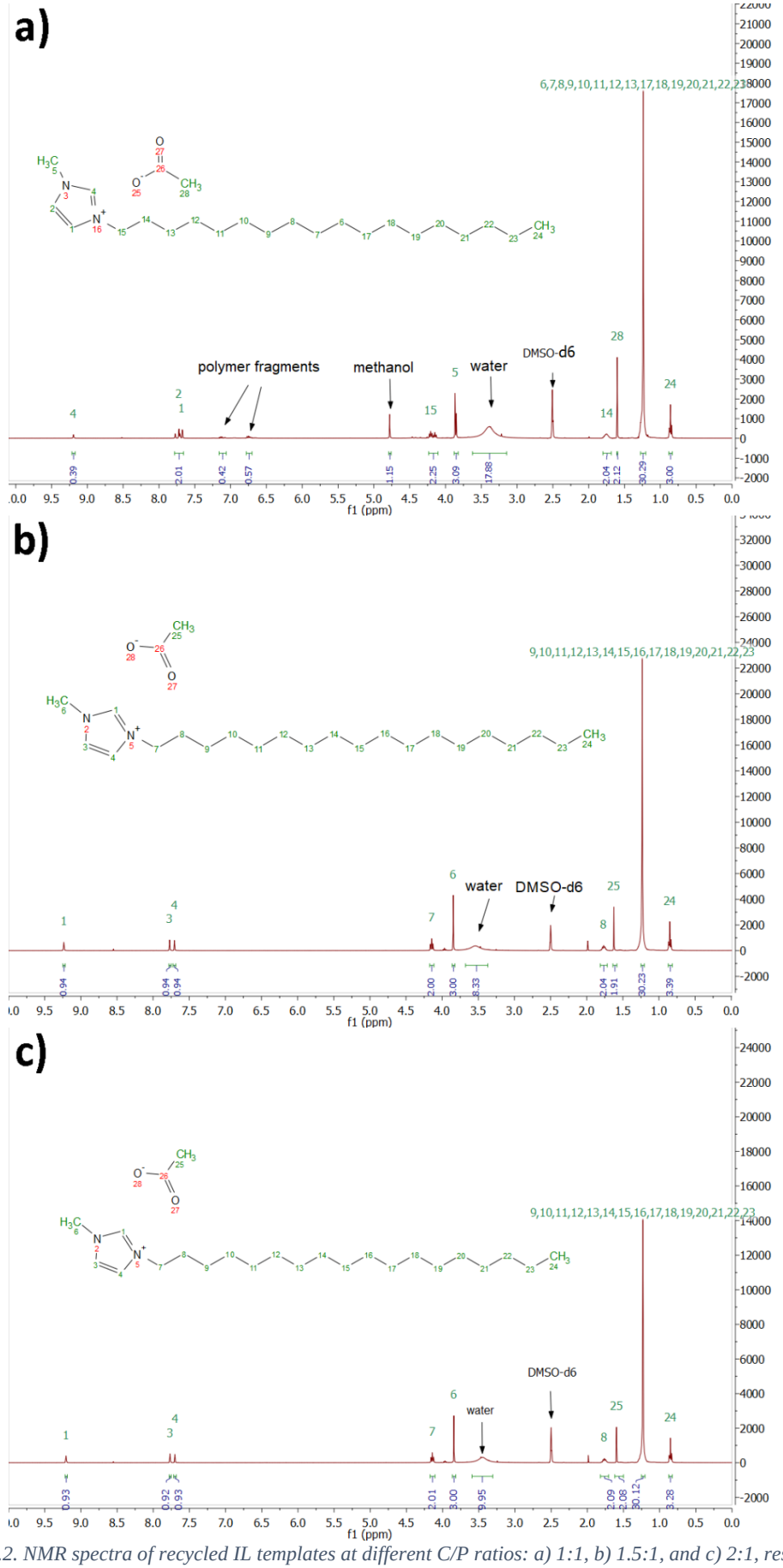

Figure 5.2. NMR spectra of recycled IL templates at different C/P ratios: a) 1:1, b) 1.5:1, and c) 2:1, respectively.

5.3.2. The role of the length of IL cationic alkyl chain

As shown in Table 5.1, carbon material prepared by employing [C_{10}MIM][OAc] template exhibited a BET surface area and pore volume of 224.8 m^2/g and 0.094 cm^3/g. The majority pore structures are micropores, evidenced by the large micropore surface area of 193.3 m^2/g and low mesopore rate of 19.2%. TEM image (Figure 5.3a) indicates the presence of dominating micropores and the lack of evident mesopores. There are two possible reasons for the absence of highly ordered mesopores: 1) the diameter of IL micelles was not large enough for the formation of mesopore structures, and 2) the ordered meso-structures were destroyed after the self-assembly process. The yield of recycled ILs reached 68.2% and 86.0% for [C_{10}MIM][OAc] and [C_{18}MIM][OAc] template respectively. The loss in IL templates mainly resulted from the batch process for recycling, such as those sticking on the wall of the flask used for rotovap and vacuum drying.

Table 5.1. Pore textural property of MCs prepared by using IL templates with different cationic length.

Template	Pore textural property				
	S_{BET} (m^2/g)	S_{micro}(m^2/g)	V_{total} (cm^3/g)	V_{meso}/V_{tot}	Methylene blue adsorption test (mL/0.1g)
[C_{10}MIM][OAc]	224.8	193.3	0.094	19.2%	0.1
[C_{18}MIM][OAc]	273.4	250.8	0.112	12.5%	0.1

As the number of carbon atoms in cationic alkyl chain increased from 10 to 18, resulting carbon exhibited a slightly elevated porosity with a larger surface area and pore volume of 273.4 m^2/g and 0.112 cm^3/g, respectively. The pores were still dominated by the micropores with a micropore surface area of 250.8 m^2/g. Similar with sample prepared with [C_{10}MIM][OAc] template, only random disordered micropores were observed in carbon prepared with [C_{18}MIM][OAc] template (Figure 5.3b). Overall, the porosity still remained relatively low although longer alkyl chain was used. Pore shrinkage during the calcination may result in the formation of micropores, but the pores are still expected to be uniform and ordered as the mixture after EISA process is homogeneous.[37] Furthermore, longer cationic alkyl chain also failed to significantly enrich the porosity of resulting carbon. This leads to a higher possibility that the mesostructures may have been destroyed after cross-linking.

The cross-linker glyoxal proves to be able to stabilise rather than destabilising the cross-linking.[38] Therefore, it could be IL templates themselves that destroyed the uniform

mesophase form after the self-assembly process. ILs are ubiquitously used green solvents and catalysts. There is a highly possibility that IL templates catalysed the cross-linking reaction and destroyed the ordered mesophase by excessively crosslinking polymer precursors and detaching them from IL templates.

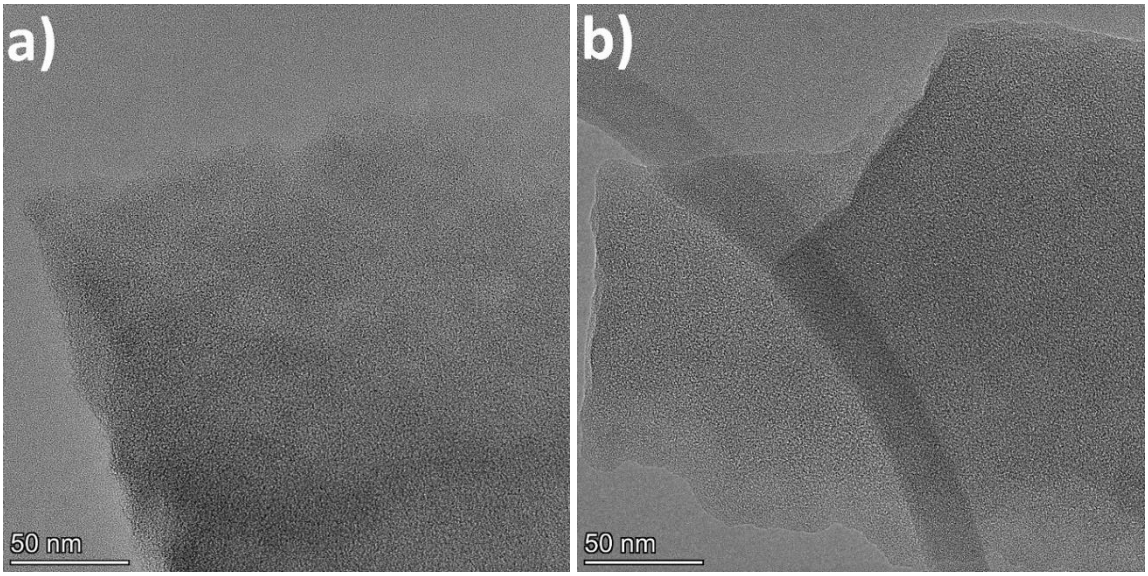

Figure 5.3. TEM images of carbon materials prepared with IL templates: a) [C_{10}MIM][OAc] and b) [C_{18}MIM][OAc].

5.3.3. Blending block copolymer as a co-template

As shown in Figure 5.3, employing solely IL templates for the preparation of MCs resulted in relatively low porosity with dominating random micropores rather than mesopores likely due to the catalytic ability of IL templates. It might be a practical strategy to blend IL templates with the well-established block copolymer template to gradually increase their percentage to replace block copolymers. ILs can co-assemble with block copolymers by hydrophobic interactions between the cationic alkyl chain and the poly(propylene oxide) segment.[30–32] Thus they can able to function compatibly as soft templates and the maximum percentage of ILs in total soft templates to yield highly ordered mesopores can also be used as a criterion to compare the catalytic ability of different IL templates.

5.3.3.1. Pore architecture

Figure 5.4a shows the N_2 physisorption isotherms of resulting MCs prepared by employing IL [C_{18}MIM][OAc] template with the assistance of Pluronic F127 co-template. MC samples prepared with lower percentages of [C_{18}MIM][OAc] template (sample 0%OAc, 5%OAc, and 10%OAc) showed obvious hysteresis loops at intermediate pressure (lower than saturation pressure P_0). They are characteristic Type IVa isotherms resulting from unrestricted monolayer-multilayer adsorption followed by pore condensation.[39] Such adsorption

behaviour usually occurs in regular cylindrical mesopores, suggesting that the pores are highly ordered in MCs prepared by employing [C_{18}MIM][OAc] template with a percentage below 10%. At a higher percentage, sample 20%OAc showed a nearly reversible isotherm though the hysteresis behaviour is still noticeable evidenced by the tiny hysteresis loop. Overall, the hysteresis loop became smaller with the increasing percentage of [C_{18}MIM][OAc] in the total templates, which also implies a shrinking in the mesopore. Sample 50%OAc and 100%OAc showed completely reversible Type I isotherms as typically observed for microporous materials.[39] Therefore, the dominating pores of resulting MCs reduced from mesoporous to microporous at higher [C_{18}MIM][OAc] contents in total templates. Notably, there is a diminishing in the total adsorption quantity with the increasing percentage of [C_{18}MIM][OAc] template, indicating a steady decline in the porosity. As shown in Figure 5.4b, sample 0%OAc, 5%OAc, and 10%OAc exhibited a narrow pore size distribution in mesopore around 4 nm. Then the peak of dominating pores, as analysed from N_2 physisorption isotherms, shifted to microporous below 2 nm at a [C_{18}MIM][OAc] content higher than 20%.

Table 5.2 summarises the pore textual properties of MCs prepared by employing [C_{18}MIM][OAc] template with an increasing content from 0 to 100 wt%. In line with N_2 physisorption isotherms, the resulting MCs exhibited a decreasing adsorption capability for methylene blue solution from 6.0 to 0.1 mL/0.1 g. Sample 0%OAc prepared solely with Pluronic F127 template showed a surface area and total pore volume of 793.8 m^2/g and 0.56 cm^3/g with a dominating pore size of 4.3 nm. By contrast, sample 100%OAc prepared solely with [C_{18}MIM][OAc] template showed a low porosity with the surface area and pore volume steadily declining to 273.6 m^2/g and 0.11 cm^3/g. The same is true of the mesopore rate. The decreasing porosity is seemingly originated from the increasing percentage of [C_{18}MIM][OAc] in the total templates. The more [C_{18}MIM][OAc] template used to prepare MCs, the higher cross-linking degree of polymer precursor can be achieved due to the bifunctional role of ILs, both soft template and catalyst. Consequently, there is a higher probability for the cross-linked precursors being detached from IL template, thereby destroying the well-organised mesostructure and yielding a more deteriorated porosity.

Moreover, the rate of IL recovery is dependent on the amount of IL templates used for the templating synthesis and major loss came from the process loss during recycling steps, such as rotovap. The yield of recycled [C_{18}MIM][OAc] was measured as 46.8%, 49.2%, 52.7%, 65.8%, and 86.0% respectively, when 5%, 10%, 20%, 50%, and 100% of [C_{18}MIM][OAc]

template was used to replace block copolymer template. The rate of IL recovery is likely to increase if continuous process for the production can be developed in the future as the procedure to prepare MCs on lab scale is restricted into batch process.

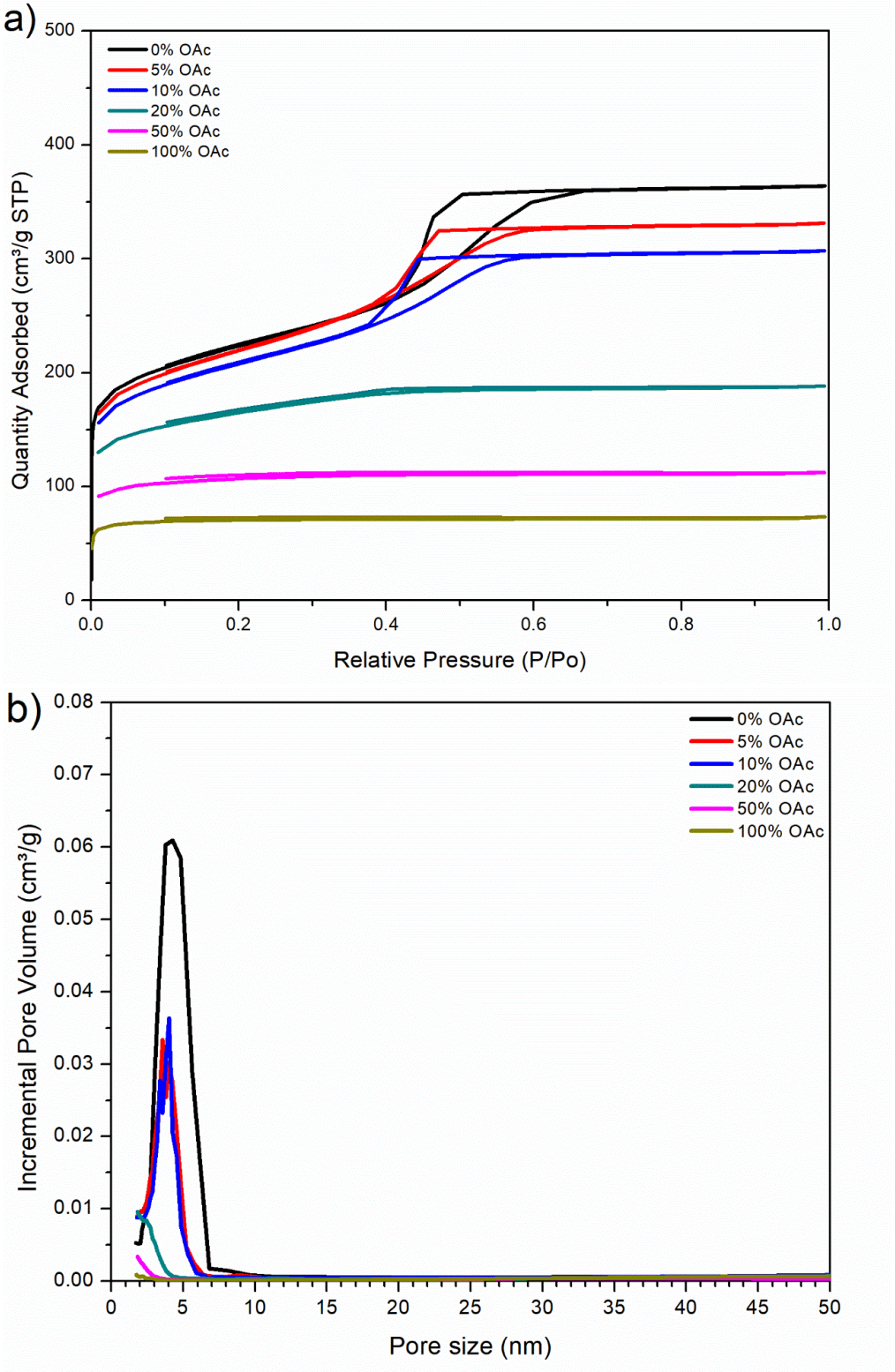

Figure 5.4. MCs synthesised by employing [C_{18}MIM][OAc] template at various contents: a) N_2 physisorption isotherms, and b) BJH pore size distributions.

Table 5.2. Textural properties of resulting MCs by employing IL templates.

Samples	Pore textural property					
	S_{BET} (m^2/g)	V_{total} (cm^3/g)	V_{meso}/V_{tot}	Mean pore size (nm)	Methylene blue adsorption test (mL/0.1g)	Porosity
G1.5 (0%)	793.8	0.56	68%	4.3	6.0	hexagonal
5% OAc	730.0	0.48	69%	3.8	3.1	High, hexagonal
10% OAc	687.8	0.44	68%	4.0	0.5	disordered
20% OAc	532.2	0.24	41%	-	0.2	low
50% OAc	330.5	0.16	16%	-	0.1	Very low
100% OAc	273.6	0.11	-	-	0.1	Very low
5% $MeSO_4$	823.7	0.48	68%	3.8	4	High, hexagonal
10% $MeSO_4$	823.0	0.40	64%	3.0	1	hexagonal
20% $MeSO_4$	770.5	0.31	49%	-	0.3	low
100% $MeSO_4$	581.9	0.22	3%	-	0.1	Very low
5% OAc - E	652.4	0.35	63%	3.2	0.4	Higher, hexagonal
10% OAc - E	654.2	0.32	54%	2.9	0.3	disordered
20% OAc - E	465.4	0.21	20%	-	0.2	low
50% OAc - E	28.2	0.013	-	-	0.1	Extremely low
100% OAc - E	3.3	0.006	-	-	0.1	Extremely low

Figure 5.5 and Figure 5.6 show the representative SEM and TEM images of resulting MCs. Similar with sample 0%OAc prepared solely with Pluronic F127 template, sample 5%OAc also exhibited a hexagonal cylindrical mesopore structure with long-range periodicity (Figure 5.5b and Figure 5.6b). At a percentage of $[C_{18}MIM][OAc]$ in the total templates over 10%, well-regulated mesopores were barely observable. Sample 10%OAc showed a random disordered mesopore structure (Figure 5.5c and Figure 5.6c). At 20% of $[C_{18}MIM][OAc]$ template, mesopores were less noticeable whilst micropores became more evident (Figure 5.5d and Figure 5.6d). As the percentage of $[C_{18}MIM][OAc]$ exceeded 50%, no mesopores were observed any more except dominating micropores, wherein the microporous interstitials were mainly originated from the stacking of polymer clusters during cross-linking (Figure 5.5e and f, Figure 5.6e and f). Overall, pore morphological study of resulting samples consists well with the pore size distribution from N_2 physisorption test.

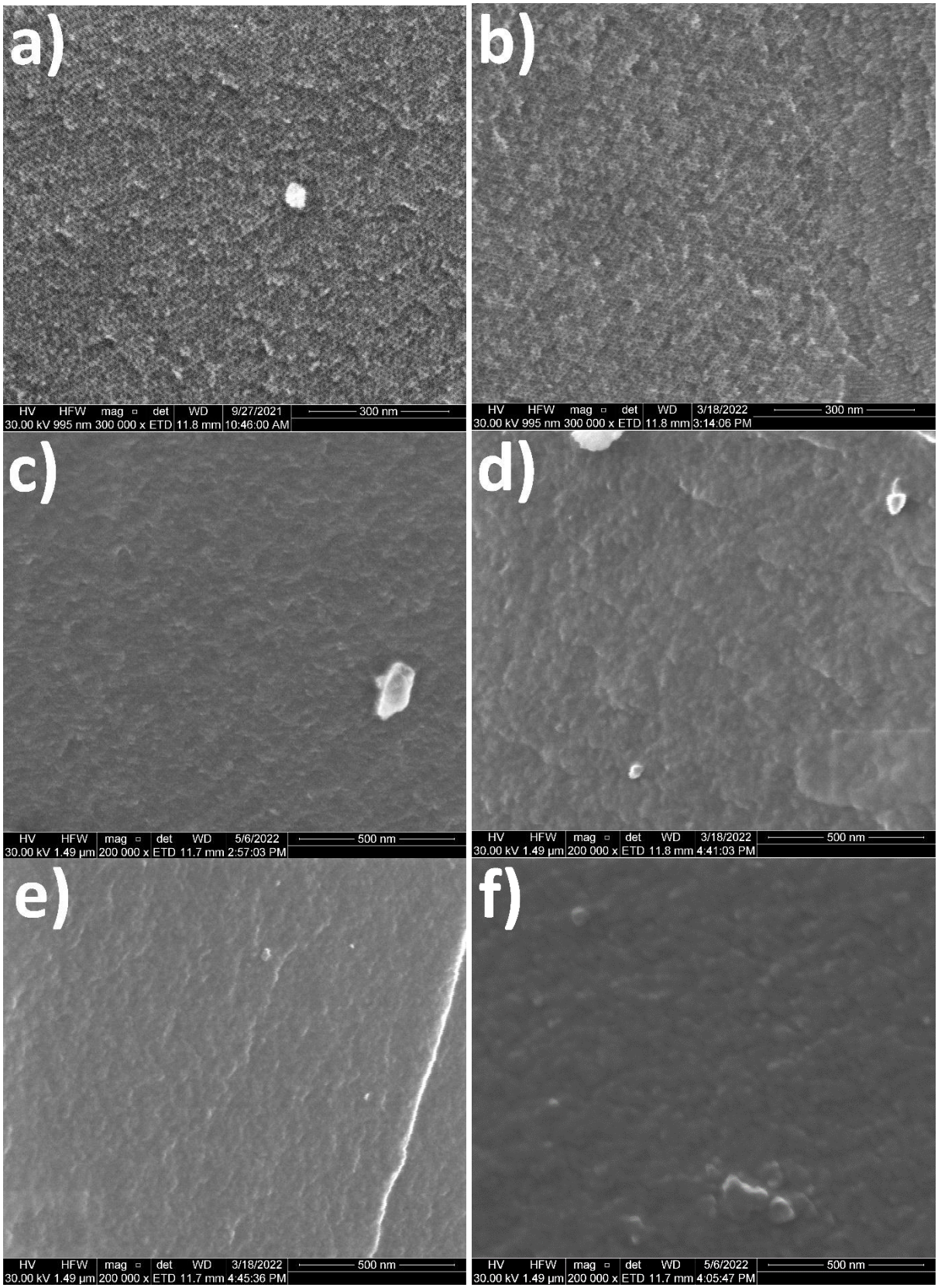

Figure 5.5. SEM images of samples prepared by [C_{18}MIM][OAc] template at increasing percentage: a) 0%OAc (G1.5), b) 5%OAc, c) 10%OAc, d) 20%OAc, e)50%OAc, and f) 100%OAc, respectively.

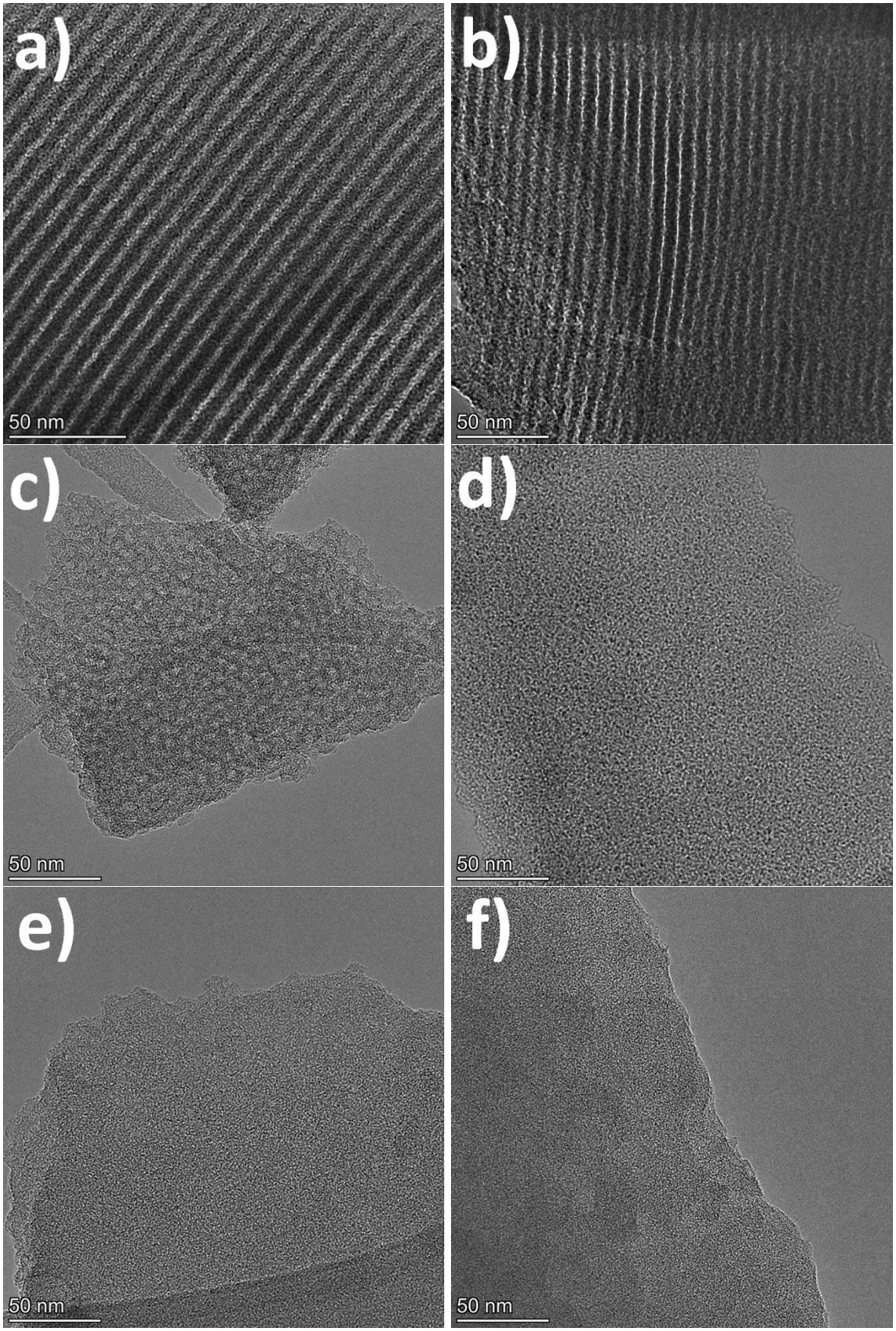

Figure 5.6. TEM images of samples prepared by [C_{18}MIM][OAc] template at increasing percentage: a) 0%OAc (G1.5), b) 5%OAc, c) 10%OAc, d) 20%OAc, e)50%OAc, and f) 100%OAc, respectively.

5.3.3.2. Surface functionality and graphitisation

XPS spectroscopy was performed to investigate the effect of the percentage of [C_{18}MIM][OAc] in total templates on the surface environment of resulting MCs. As shown in Figure 5.7, all samples comprised of dominating carbon element and a small proportion of oxygen element. There are two nitrogen atoms in the imidazolium ring of IL cation, but no nitrogen element was detected; this suggests the excellent recyclability of imidazolium-based IL templates. Noticeably, with the increase of [C_{18}MIM][OAc] content in total templates, there was an overall growth in oxygen content rising from 4.8 to 7.3 at%, conversely that for carbon declined from 95.2 to 92.7 at%.

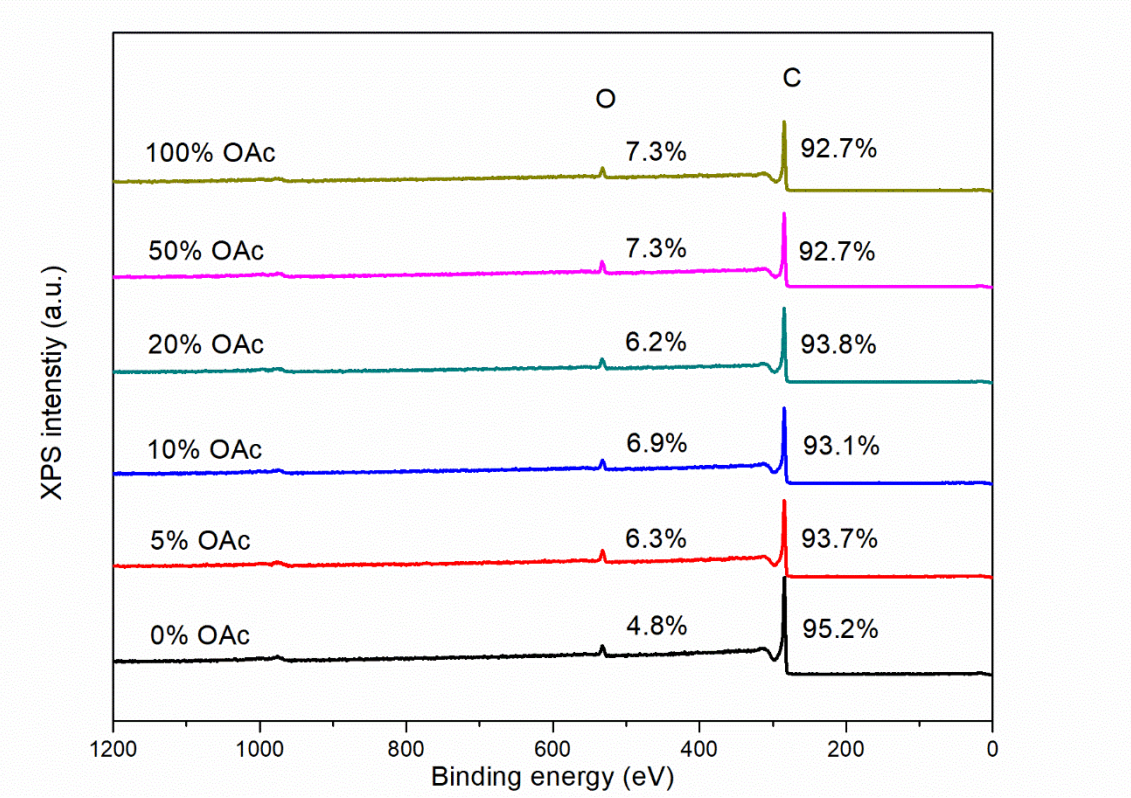

Figure 5.7. Summary of wide-scan of XPS spectra for MCs prepared by employing [C_{18}MIM][OAc] template.

Figure 5.8 shows the Raman spectra of resulting MCs to investigate their graphitisation degree that can be a universal tool to tailor potential-dependent capacitance of supercapacitors for energy storage.[40] All resulting MC samples, regardless of the [C_{18}MIM][OAc] content, showed two evident peaks at around 1350 cm^{-1} (*D* band) and 1590 cm^{-1} (*G* band), respectively. For carbon materials, *D* band is usually generated by the defected graphite lattice or structural distortion, while *G* band is typically detected for graphitic structures.[41,42] The strong *D* band with similar height with *G* band and the absence of sharp

2D band (around 2700 cm^{-1}) indicate the lack of local graphene-like structures hence the amorphous nature of all MCs prepared by employing [C_{18}MIM][OAc] template.

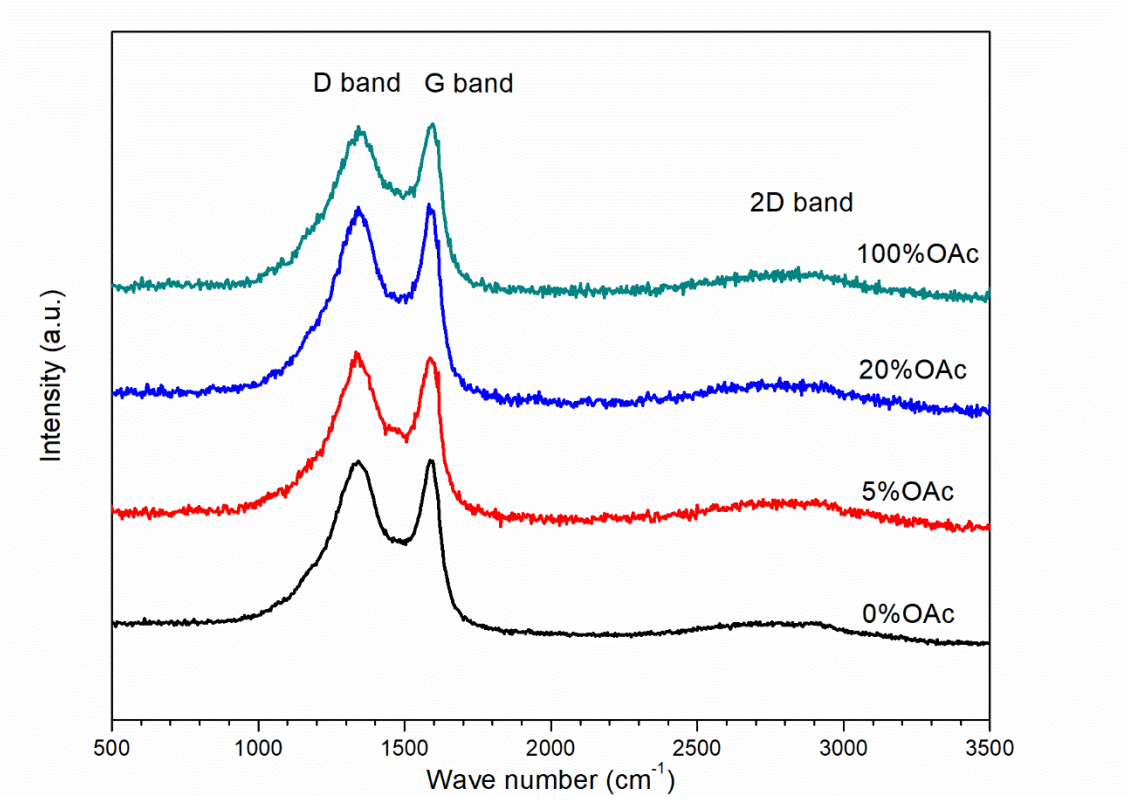

Figure 5.8. Raman spectra for MCs prepared by employing [C_{18}MIM][OAc] template at increasing percentage.

5.3.4. The role of the extraction process of the IL template

5.3.4.1. Pore architecture

The influence of extraction process of IL template on pore architecture was investigated. As shown in Figure 5.9a, MCs prepared by excluding the extraction of [C_{18}MIM][OAc] template showed a declining N_2 adsorption quantity as the percentage of [C_{18}MIM][OAc] increased, which is similar with MCs prepared with IL extraction. MC samples 0%OAc-E, 5%OAc-E, and 10%OAc-E showed obvious hysteresis loops, characteristics of typical Type IVa isotherms.[39] Besides, the hysteresis loops became smaller, implying a diminishing mesopore diameter. Sample 20%OAc-E exhibited a Type I isotherm, characteristic of microporous material, as opposed to Type IVa isotherm for sample 20%OAc. Sample 50%OAc-E and 100%OAc-E showed extremely small adsorption quantities hence porosities. Overall, the lack of an IL extraction process before calcination has led to a smaller pore size with the same amount of [C_{18}MIM][OAc] template. Figure 5.9b shows the corresponding pore size distribution of n%OAc-Es. Only 5%OAc-E and 10%OAc-E exhibited narrow peaks at mesopore range, just like their counterparts (5%OAc and 10%OAc) with the extraction

process of the IL template. In line with the reducing hysteresis loops as the amount of [C_{18}MIM][OAc] increased, the peak of dominating pores also shifted to smaller range, from mesopore to micropore.

The surface area and pore volume of resulting MCs are much lower than their counterparts prepared under the same condition but including IL extractions (Table 5.2). For example, sample 5%OAc-E exhibited a BET surface area and pore volume of 652.4 m^2/g and 0.35 cm^3/g, which are much lower than the values for sample 5%OAc (730.0 m^2/g and 0.48 cm^3/g). For the successful templating synthesis of MCs, a zero to minimal char yield of the template is crucial.[37] As mentioned earlier in the introduction, imidazolium based ILs are widely used as carbon and nitrogen precursors. For those MC samples prepared by excluding IL extraction process, the residual char yielded from the pyrolysis of IL templates may partly even completely block the pores, especially the carbonisation of hydrophobic cationic alkyl chains that are expected to generate pore structures. Under such circumstance, the pore structures of resulting carbons mainly stemmed from the pyrolysis of co-template Pluronic F127, which barely yields residual carbon.[37] Therefore, the extraction of IL template is significantly important not only by improving the sustainability of IL templates but also in favour of the generation of pore structures.

Figure 5.10 and Figure 5.11 show the morphologies of MCs prepared by excluding the IL extraction process. Similar with their counterparts prepared by including IL extraction process, low percentage of [C_{18}MIM][OAc] templates yielded highly ordered hexagonal mesopore structure, as seen in sample 5%OAc-E (Figure 5.10b and Figure 5.11b). Sample 10%OAc-E exhibited a disordered mesopore structure, just like sample 10%OAc. As the content of [C_{18}MIM][OAc] in the total templates reached 20%, dominating micropores were observed in the resulting carbon (Figure 5.10c and Figure 5.11c). Sample 50%OAc-E and 100%OAc-E exhibited random micropores due to their extremely low porosity. The pore morphological study agrees well with the N_2 physisorption test.

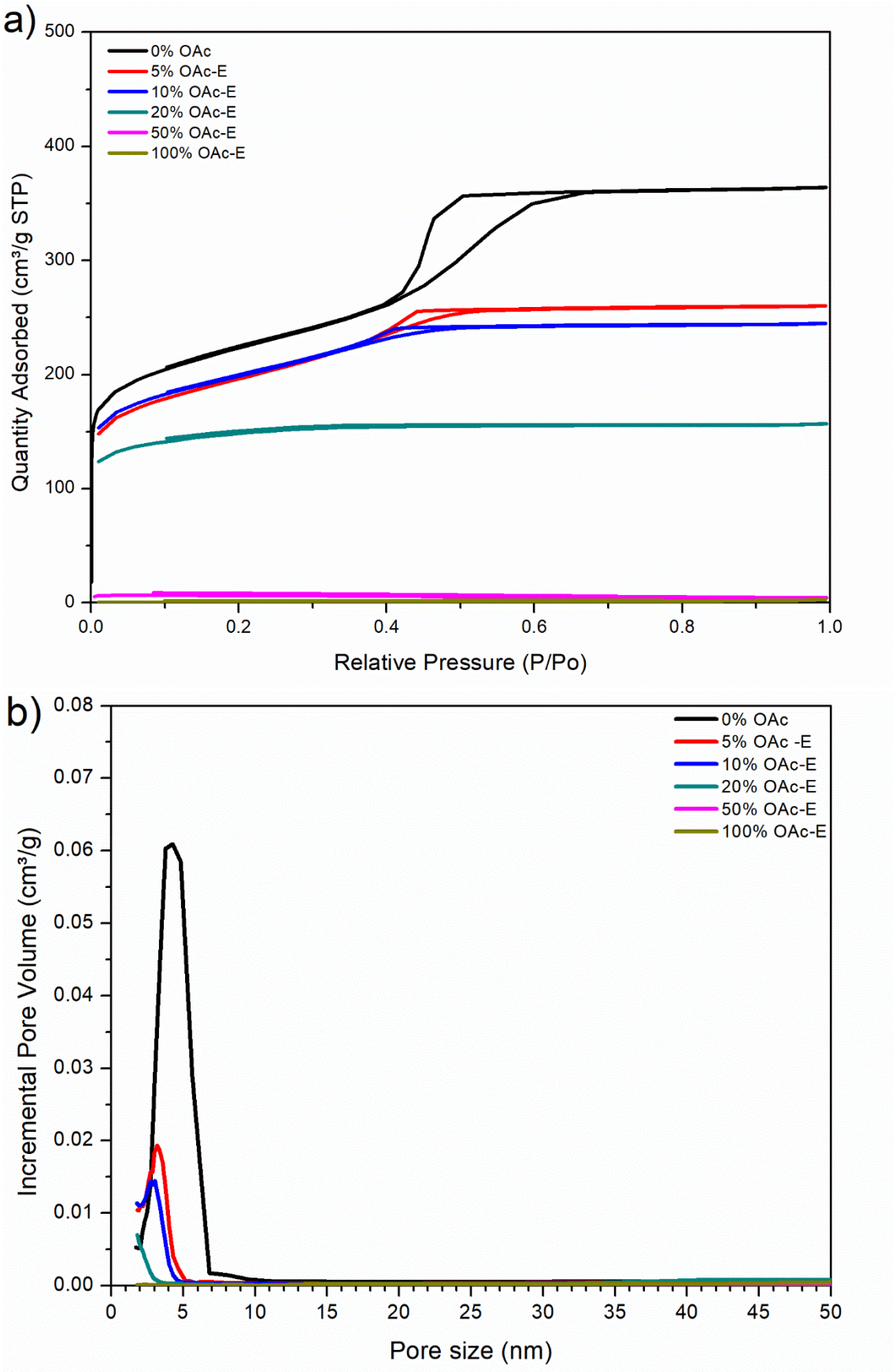

Figure 5.9. MCs synthesised by employing [C_{18}MIM][OAc] template excluding template extraction: a) N_2 physisorption isotherms, and b) BJH pore size distributions.

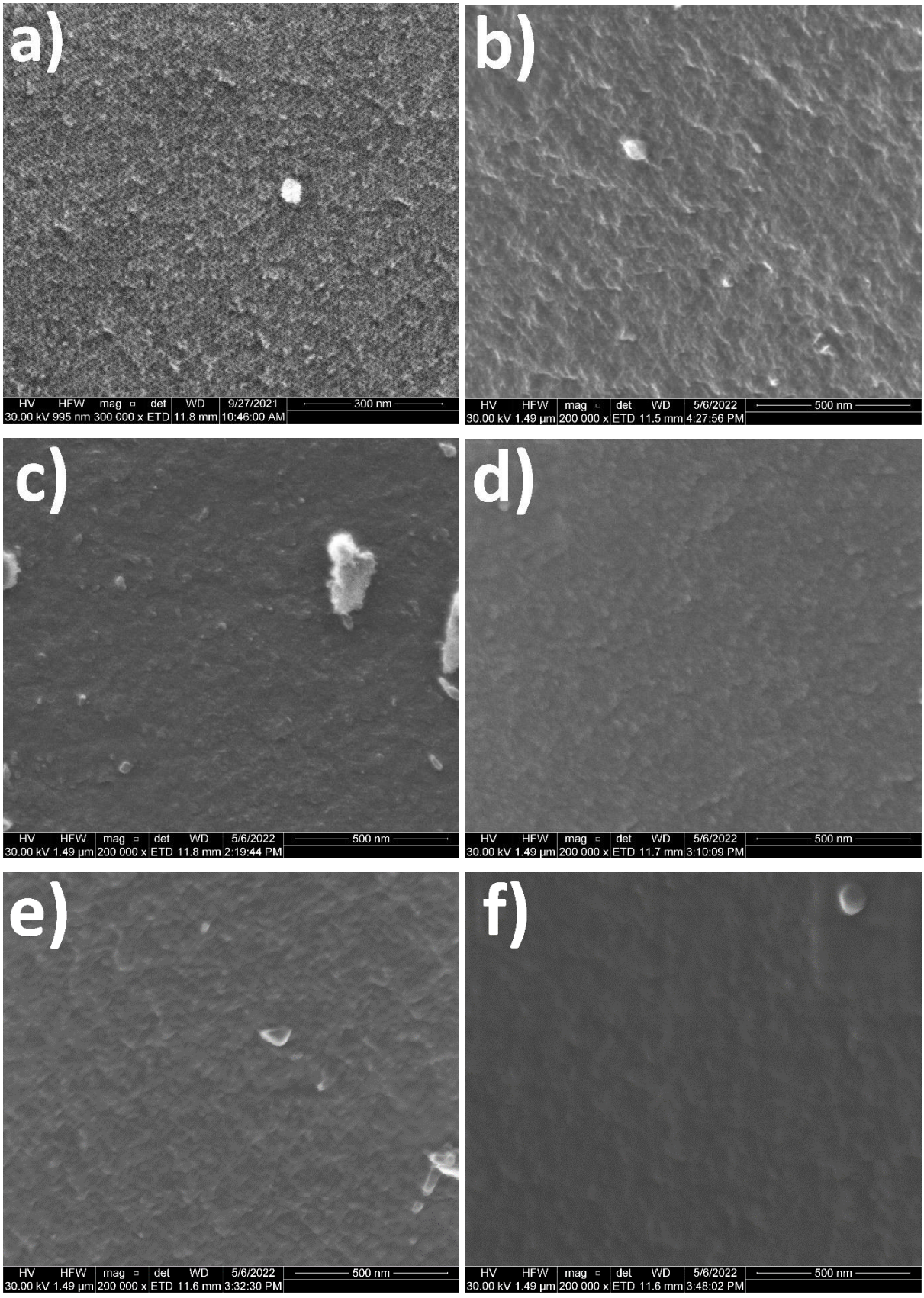

Figure 5.10. SEM images of samples prepared by [C_{18}MIM][OAc] template excluding template extraction: a) 0%OAc (G1.5), b) 5%OAc-E, c) 10%OAc-E, d) 20%OAc-E, e)50%OAc-E, and f) 100%OAc-E, respectively.

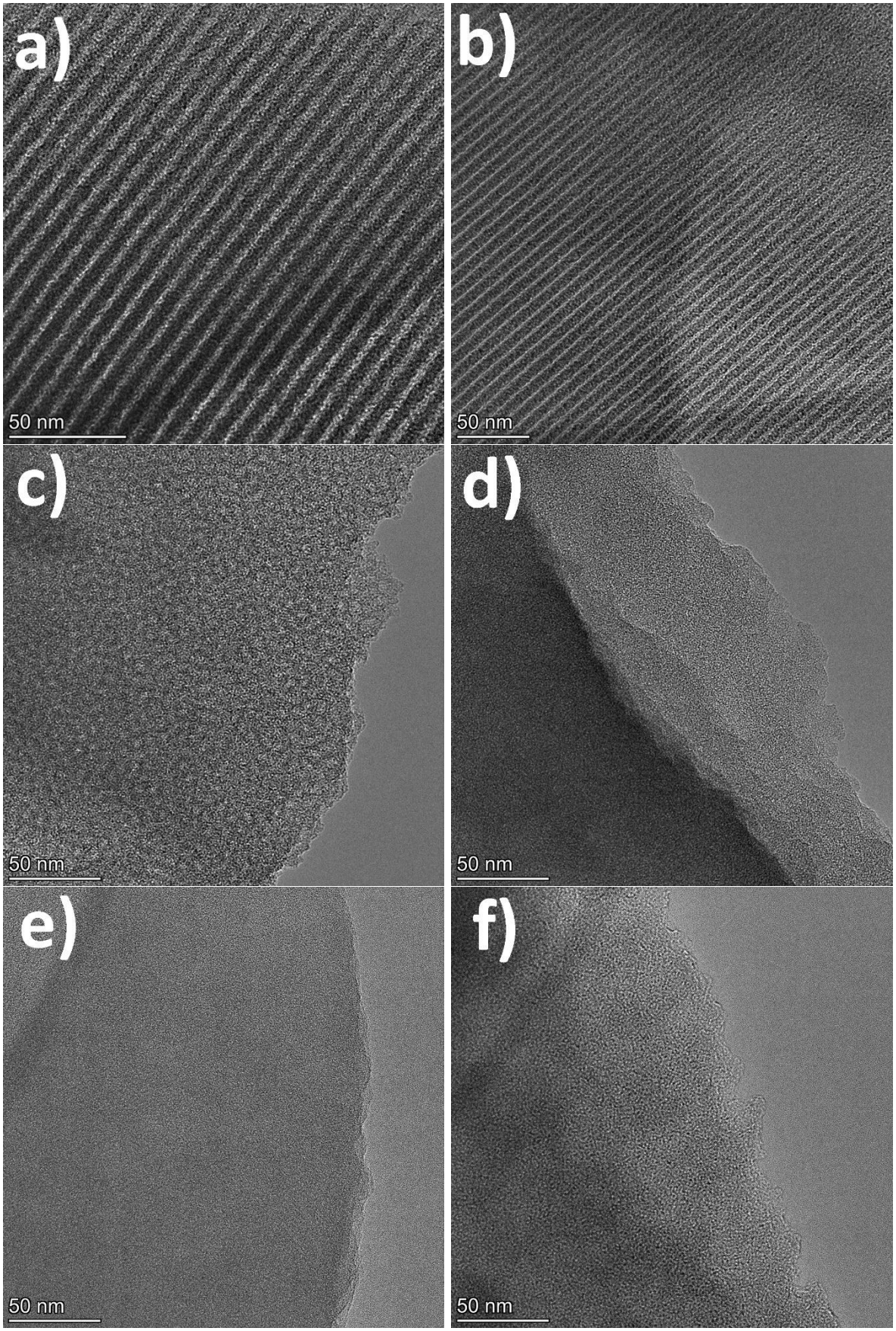

Figure 5.11. TEM images of samples prepared by [C_{18}MIM][OAc] template excluding template extraction: a) 0%OAc (G1.5), b) 5%OAc-E, c) 10%OAc-E, d) 20%OAc-E, e)50%OAc-E, and f) 100%OAc-E, respectively.

5.3.4.2. Surface functionalities

There are two inherent nitrogen atoms on the hydrophilic imidazolium ring of [C_{18}MIM][OAc] template; this could introduce N-doping to the resulting MCs. As shown in Figure 5.12, nitrogen content showed an increasing trend from 0.2 to 1.9 at% when the amount of [C_{18}MIM][OAc] template increased from 5% to 100%. Besides, a steady increase was also found in oxygen content, reaching 7.2% at 100% of [C_{18}MIM][OAc]. The growth in oxygen content stemmed mainly from the pyrolysis of acetate anion that possesses two oxygen atoms. Conversely, carbon content decreased to 90.9 at% for sample 100%OAc-E.

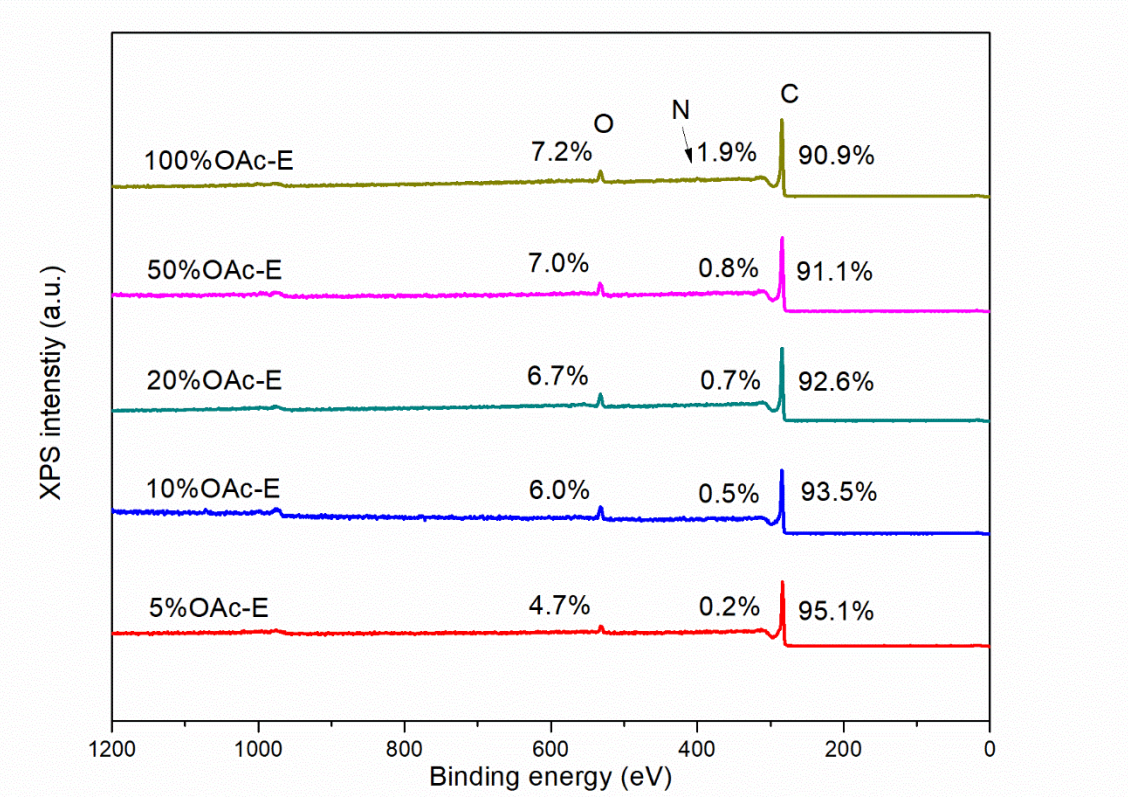

Figure 5.12. Summary of wide-scan of XPS spectra for MCs prepared by [C_{18}MIM][OAc] template excluding template extraction.

5.3.5. The role of anion of IL template

5.3.5.1. Pore architecture

[C_{18}MIM][$MeSO_4$] was employed as the template to study the effect of IL anions. N_2 physisorption isotherms of resulting MCs are shown in Figure 5.13a. In line with employing [C_{18}MIM][OAc] template, the increasing content of methyl sulphate-based IL template also resulted in a decrease in the total adsorption quantity hence the porosity. At lower percentages of [C_{18}MIM][$MeSO_4$], MC samples 0%$MeSO_4$, 5%$MeSO_4$, and 10%$MeSO_4$ exhibited typical Type IVa isotherms with obvious hysteresis loops at intermediate

pressure.[39] The shrinking hysteresis loops implied a steady decline in the diameter of regular cylindrical mesopore channels. At a higher percentage of 20%, the hysteresis loops are hardly seen and resulting sample 20%$MeSO_4$ exhibited a nearly Type IVb isotherm, as opposed to Type IVa isotherm for sample 20%OAc. This suggests smaller mesopores in sample 20%$MeSO_4$ than those in sample 20%OAc. As the percentage of [C_{18}MIM][$MeSO_4$] template continued increasing, sample 100%$MeSO_4$ displayed a reversible Type I isotherm, indicating the dominating micropores.[39] As shown in Figure 5.13b, the narrow peaks suggest that [C_{18}MIM][$MeSO_4$] template yielded quite uniform pores. The peak gradually shifted from mesopore to micropore range with the increasing [C_{18}MIM][$MeSO_4$] percentage; this coincides well with the shrinking hysteresis loops. The dominating pore size were measured as 4.3, 3.8, 3.0, 2.7 nm for MC 0%$MeSO_4$, 5%$MeSO_4$, 10%$MeSO_4$, and 20%$MeSO_4$, respectively. No peaks were detected in mesopore for 100%$MeSO_4$ due to its dominating micropores.

The pore textual properties of all resulting MCs are summarised in Table 5.2. As the [C_{18}MIM][$MeSO_4$] content in the total templates increased, the BET surface area first increased from 793.8 m^2/g (for 0%$MeSO_4$ synthesised by solely employing Pluronic F127) to 823.7 m^2/g (for 5%$MeSO_4$), then declined steadily to 581.9 m^2/g (for 100%$MeSO_4$). Whilst the total pore volume showed an ever decreasing from 0.56 cm^3/g with 68% of mesopores (for 0%$MeSO_4$) to 0.22 cm^3/g with only 3% of mesopores (for 100%$MeSO_4$). Therefore, amphiphilic [C_{18}MIM][$MeSO_4$] template also played a bifunctional role, both template and catalyst, in the synthesis of MCs just like its acetate-based counterpart.

Figure 5.14 and Figure 5.15 show the morphologies of MCs prepared by employing [C_{18}MIM][$MeSO_4$] template. At lower percentage, both sample 5%$MeSO_4$ and 10%$MeSO_4$ exhibited well-organised hexagonal mesoporous structures. As the percentage of [C_{18}MIM][$MeSO_4$] increased to 20 wt%, ordered mesopores were barely observable except dominating disordered mesopores (Figure 5.14d and Figure 5.15d). The catalytic ability of [C_{18}MIM][$MeSO_4$] template could have already overly cross-linked the polymer precursors thus destabilised the well-regulated mesophase formed by [C_{18}MIM][$MeSO_4$] themselves. At 100%, dominating micropores were more evident and no mesopores were detected (Figure 5.14e and Figure 5.15e). Again, due to the collapse of well-organised mesophase, the micropores mainly originated from the interstitials of over-cross-linked polymer clusters.

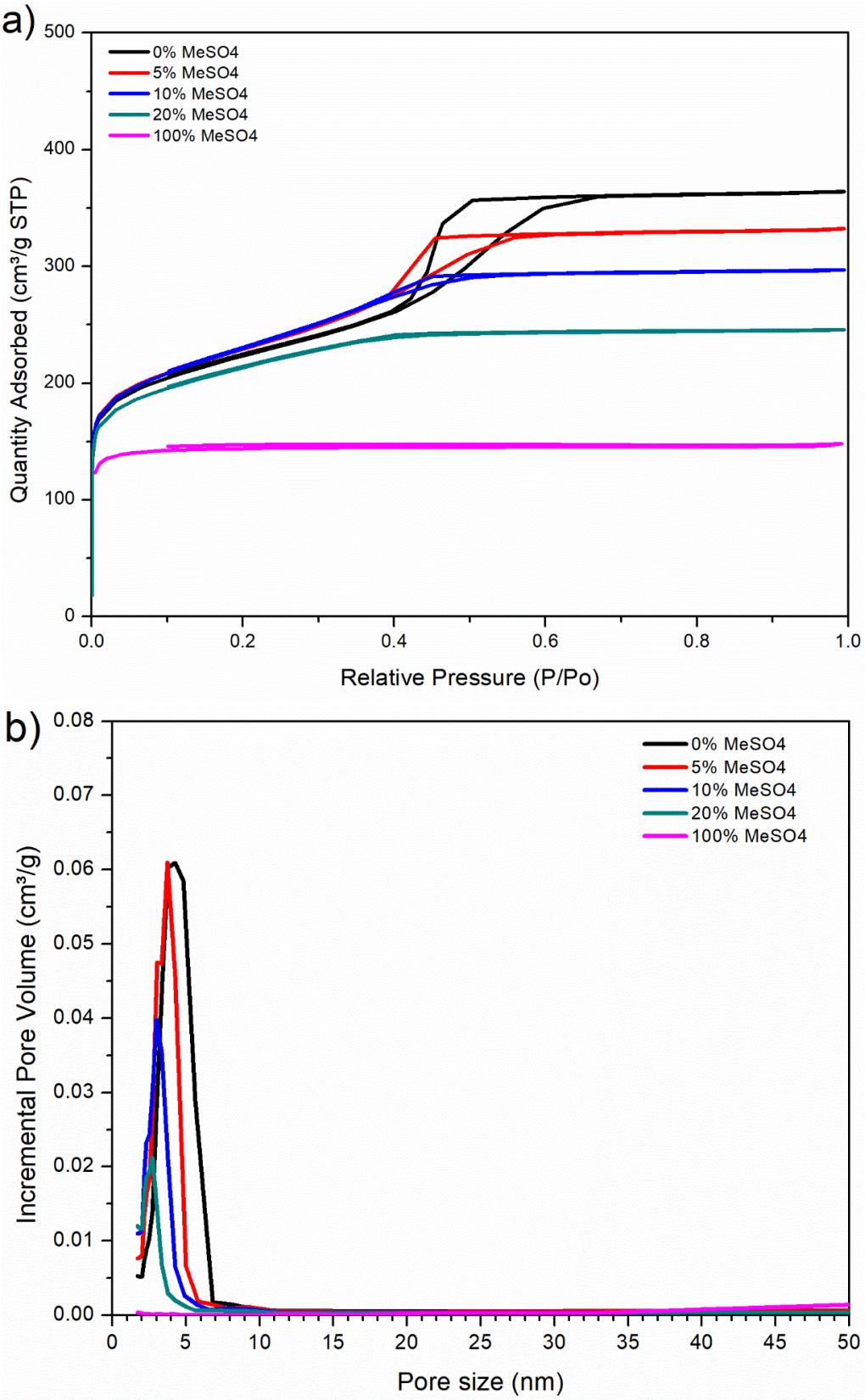

Figure 5.13. MCs synthesised by employing [C_{18}MIM][$MeSO_4$] template at various contents: a) N_2 physisorption isotherms, and b) BJH pore size distributions.

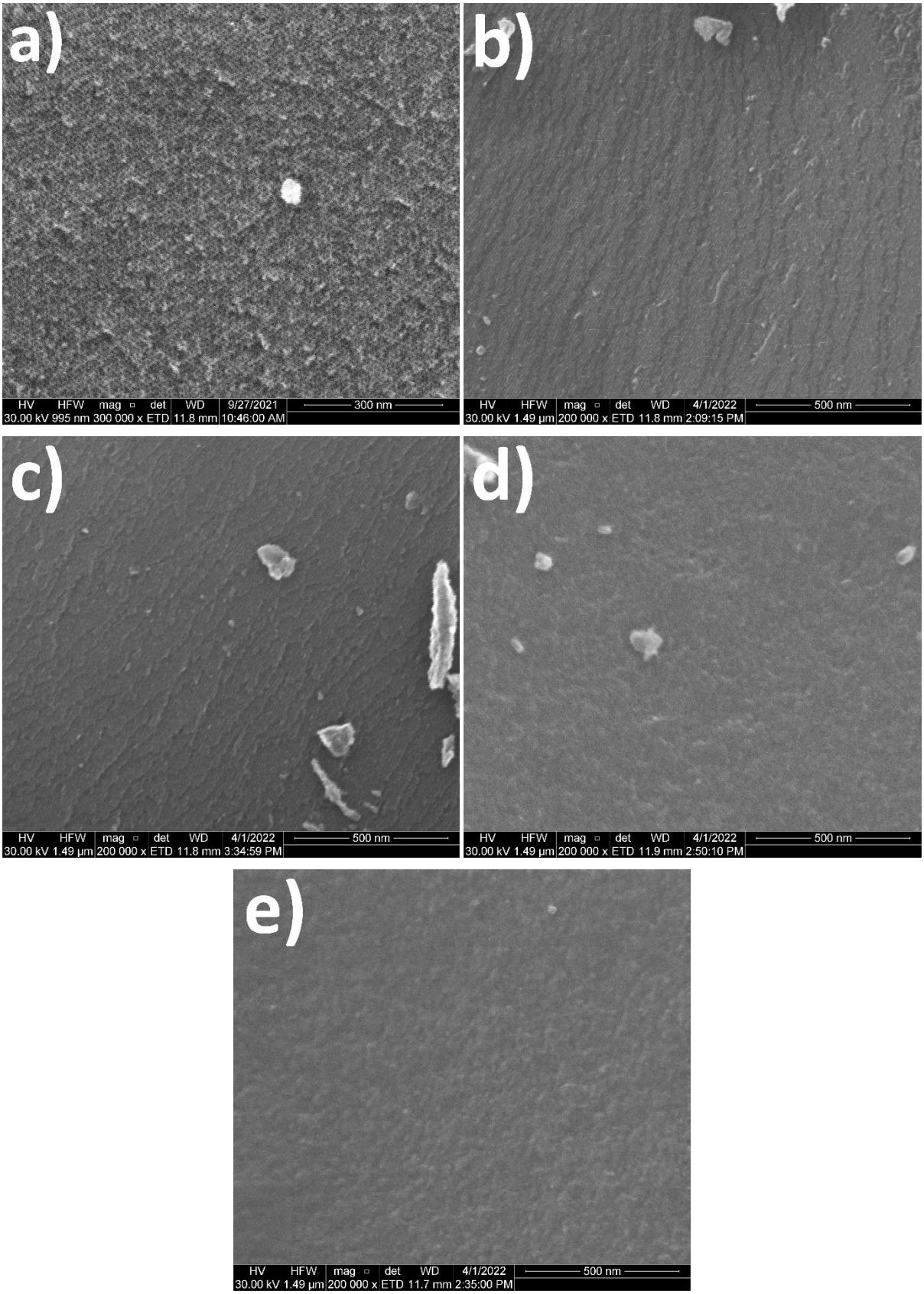

Figure 5.14. SEM images of samples prepared by [C_{18}MIM][$MeSO_4$] template at increasing percentage: a) 0%$MeSO_4$ (G1.5), b) 5%$MeSO_4$, c) 10%$MeSO_4$, d) 20%$MeSO_4$, and e) 100%$MeSO_4$, respectively.

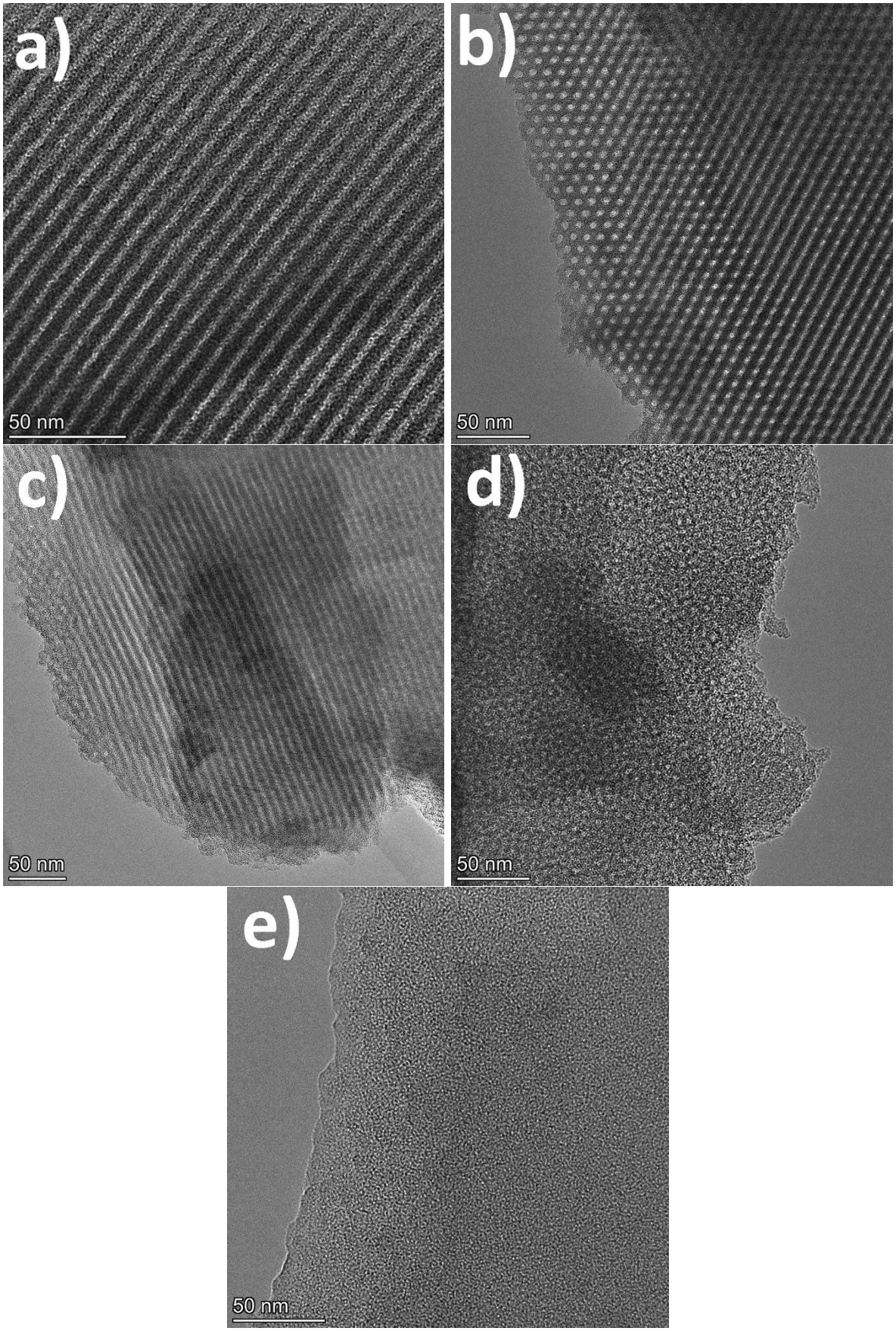

Figure 5.15. TEM images of samples prepared by [C_{18}MIM][$MeSO_4$] template at increasing percentage: a) 0%$MeSO_4$ (G1.5), b) 5%$MeSO_4$, c) 10%$MeSO_4$, d) 20%$MeSO_4$, and e) 100%$MeSO_4$, respectively.

5.3.5.2. Reusability of [C_{18}MIM][$MeSO_4$] template

The recyclability of [C_{18}MIM][$MeSO_4$] template was also investigated, with purity of recycled [C_{18}MIM][$MeSO_4$] detected by ^{1}H NMR. As shown in Figure 5.16, [C_{18}MIM][$MeSO_4$] showed an overall high structural intactness after extraction. The only detectable impurities were moisture and the extraction solvent methanol, which can be thoroughly removed by further drying. The structural consistency of the [C_{18}MIM][$MeSO_4$] before and after extraction proves its excellent sustainability as the soft template. Moreover, the yield of recycled [C_{18}MIM][$MeSO_4$] template was measured as 39.4%, 44.5%, 50.1%, and 74.3% respectively, when 5%, 10%, 20%, and 100% of [C_{18}MIM][$MeSO_4$] template was used to replace block copolymer template. Again, the rate of IL recovery is also dependent on the initial amount of [C_{18}MIM][$MeSO_4$] template used for the preparation, due to the loss in the batch process of the recycling steps.

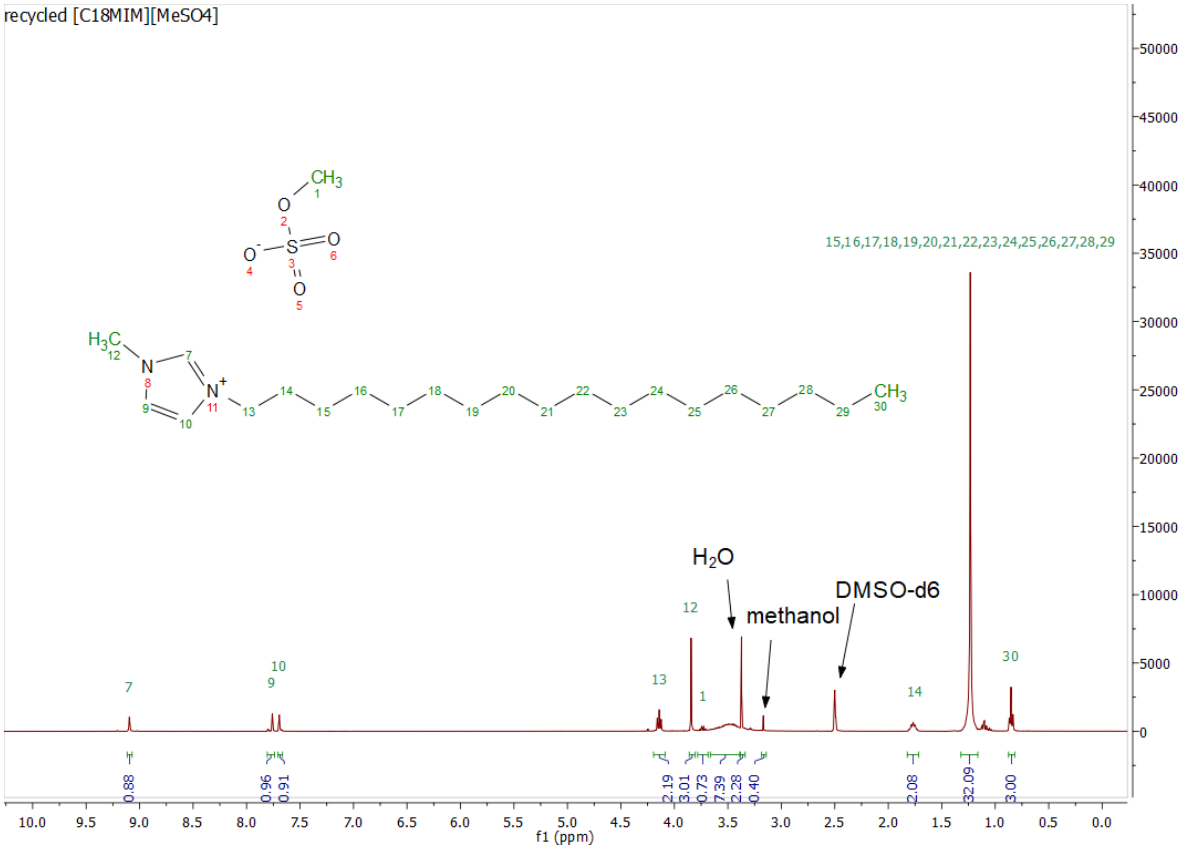

Figure 5.16. Representative NMR spectrum of recycled [C_{18}MIM][$MeSO_4$] template at a C/P ratio of 1.5:1.

5.3.5.3. Surface functionalities

Figure 5.17 shows the XPS spectra of MCs prepared by employing [C_{18}MIM][$MeSO_4$] template. After being extracted with methanol for 72 h, there were no nitrogen and sulphur element detected on the surface of resulting MCs. The overall contents of oxygen and carbon

showed a similar trend with those MCs prepared by employing [C_{18}MIM][OAc] template. The O content increased from 4.8 to 6.8 at%, as opposed to the value for C atom declining from 95.2 to 93.2 at% when the amount of [C_{18}MIM][$MeSO_4$] increased from 0 to 100%.

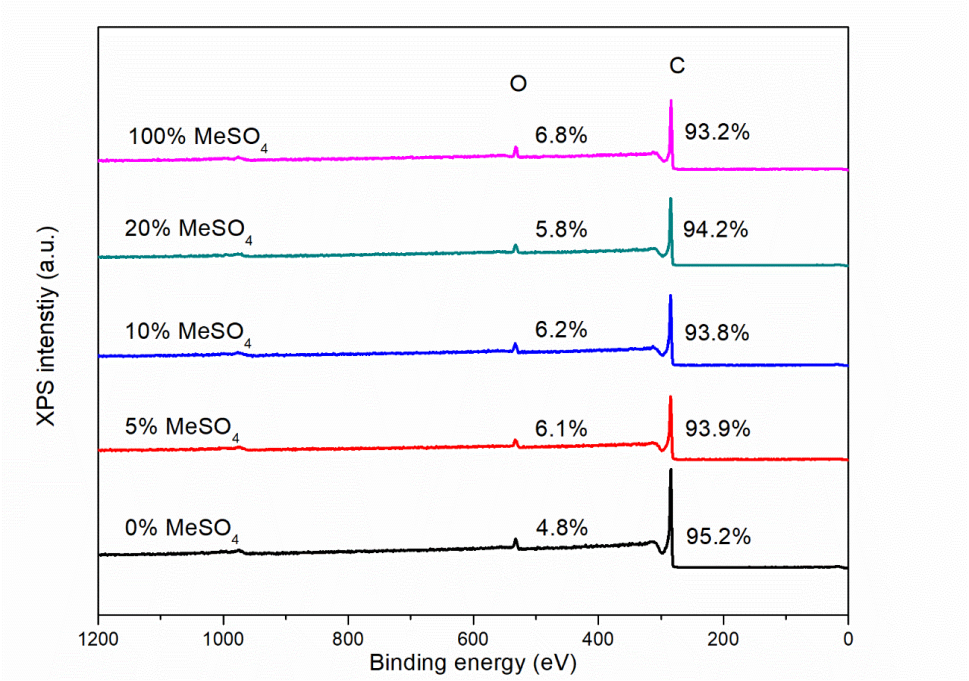

Figure 5.17. Summary of wide-scan of XPS spectra for MCs prepared by employing [C_{18}MIM][$MeSO_4$] template.

5.3.5.4. Comparison of IL anions in templating and IL extraction process

In comparison with [C_{18}MIM][OAc] template, [C_{18}MIM][$MeSO_4$] seemingly has a weaker catalytic ability for the cross-linking reaction; MCs prepared by employing [C_{18}MIM][$MeSO_4$] template showed an overall larger surface area and pore volume than those by employing [C_{18}MIM][OAc] at the same percentage. The difference in porosity suggests that IL anion plays a more pronounced role in the cross-linking of polymer monomers and porosity. Nagy *et al.*[22] employed [C_2MIM]$^+$ based ILs with three different anions (namely methyl sulphate, ethyl sulphate, and acetate) as templates and metal-free catalyst to synthesise polymer aerogels from resorcinol-formaldehyde resin. In aqueous solutions, it was found feasible to employ ILs with [$MeSO_4$]$^-$ and [$EtSO_4$]$^-$ anions to produce porous aerogels with 3*D* networks but not with [OAc]$^-$, whereby only precipitates formed.

With the same IL cation, acetate anion showed a stronger H-bonding interaction with aromatic polymers such as lignin than methyl sulphate anion.[43] Acetate anion based ILs have a slightly better H-bond basicity than those with methyl sulphate, thereby delivering a stronger H-bonding catalytic ability then inducing a higher degree of cross-linking reaction that eventually has deteriorated the porosity of resulting samples.

Zhao *et al.*[17] reported the preparation of nitrogen-doped MCs by employing IL 1-ethyl-3-imidazolium dicyanamide ([C_2MIM][DCA]) and block copolymer Pluronic F127 as templates. The resulting MCs exhibited BET surface areas and pore volumes of 413.8-607.3 m^2/g and 0.25-0.46 cm^3/g when the mass ratio of [C_2MIM][DCA] ranged from 0 to 0.5. Imidazolium based ILs are generally amphiphilic when the alkyl side chain exceeds 6 carbon atoms[44–47], though microphase separation may occur with shorter alkyl chains.[48] Therefore, in Zhao's work, the IL [C_2MIM][DCA] does not have obvious amphiphilicity thus mainly acted as N precursor. By burning ILs off, their attempt failed to take advantage of the excellent recyclability of IL templates. Moreover, the addition of higher amount of [C_2MIM][DCA] also resulted in a collapse of the ordered mesostructures, for which a plausible explanation was given that [C_2MIM][DCA] hampered the co-assembly process with block copolymer. According to our study, the collapse of ordered mesostructures at higher amounts of IL templates is more reasonably originated from the catalytic ability of IL themselves, whereby precursor monomers were overly cross-linked then detached from the co-assembled templates.

Indeed, such catalytic effect of imidazolium-based ILs on polycondensation has been widely reported, especially in the synthesis of phenolic polymers from phenol and formaldehyde, where hydrophilic anions with stronger hydrogen accepting ability were likely to exhibit stronger effect than hydrophobic anions with weaker hydrogen accepting ability.[49–52] Meanwhile, imidazolium-based ILs were also employed as the template to prepare carbon aerogels.[21] To simply illustrate the catalytic effect of IL anions, four $[C_{10}MIM]^+$ cation-based ILs with different anions were employed to prepare carbon aerogels from resorcinol-formaldehyde-polymer with a control sample without IL template. Although carbon aerogels are not highly ordered mesopores, such practice could still manifest the catalytic effect of ILs on cross-linking process in an indirect manner. Experimental procedures followed the same as Yang *et al.*'s work[21] and IL templates remained at 10 wt% in the IL template/precursor mixtures. As shown in Figure 5.18, samples with IL templates showed higher N_2 adsorption quantities than the control sample without using IL template and the four anions resulted in the N_2 adsorption quantities of carbon aerogels in the order of $[NTf_2]^- > Br^- > [OTf]^- > [OAc]^-$, with a total BJH pore volume in the order of 0.29 > 0.11 > 0.02 > 0.01 cm^3/g, respectively; this may indicate that the four anions have a catalytic ability in a reverse order. Notably, the order of catalytic ability of the four anions is also in good agreement with their H-bonding ability, confirming that the H-bonding catalytic ability played a major role in the templating preparation of MCs with [C_{18}MIM][OAc] and [C_{18}MIM][$MeSO_4$] templates. Therefore, at

the same mixing ratio, methyl sulphate anion-based IL gave rise to a slightly higher porosity and better pore morphologies due to a weaker catalytic ability.

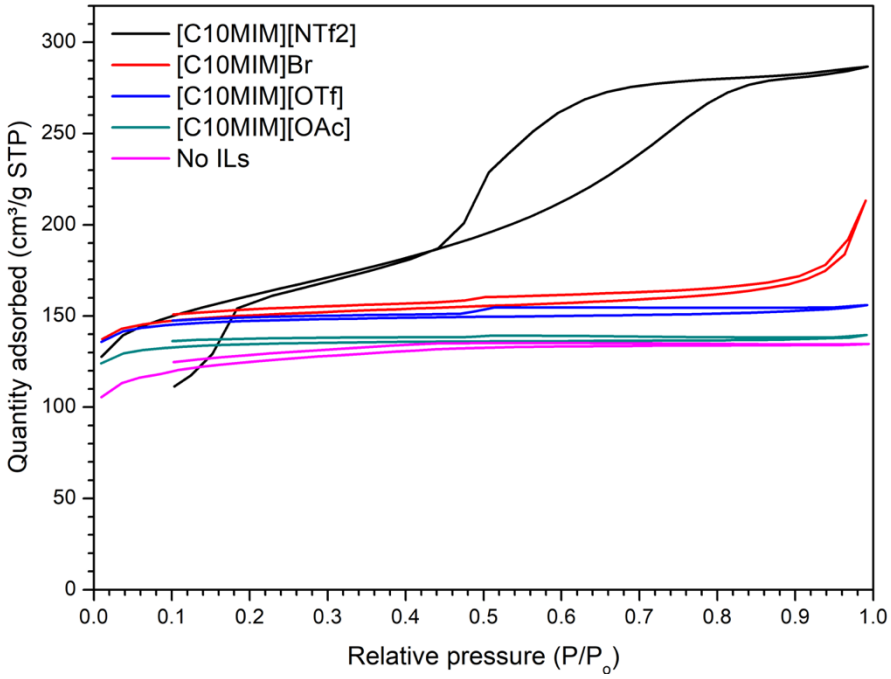

Figure 5.18. N_2 physisorption isotherms for resorcinol-glyoxal-polymer-resultant carbon aerogels with different ILs templates.

Different anions of IL templates and including/excluding IL extraction process not only influenced the resulting porosity but also induced a different pore morphology. Figure 5.19 shows the HAADF STEM and TEM images of MCs prepared by employing 5% and 10% of IL templates. At 5% of IL template, all the three MC samples (5%OAc, 5%OAc-E, and 5%$MeSO_4$) showed well-ordered honey-comb-like hexagonal mesopore channels (*p6mm*). However, at 10% of IL templates, such well-organised mesopore structures only retained in sample 10%$MeSO_4$ whilst acetate anion-derived MCs, regardless of including or excluding the IL extraction process, yielded disordered mesoporous structures due to its stronger catalytic ability than methyl sulphate anion-based IL.

The graphitisation degree was also compared by Raman spectra (Figure 5.20). In line with sample 5%OAc, sample 5%OAc-E and 5%$MeSO_4$ also showed two evident peaks, *D* band at around 1350 cm^{-1} and *G* band at round 1590 cm^{-1}. The strong *D* peak ($I_D/I_G \approx 1$) and the absence of 2*D* peak suggested the lack of local graphene-like structures and the amorphous nature of all MC samples. Obviously, IL extraction process and different anions are unable to significantly alter the graphitisation degree of resulting carbons as the carbonisation condition remained the same with a same carbonisation temperature and heating profile.

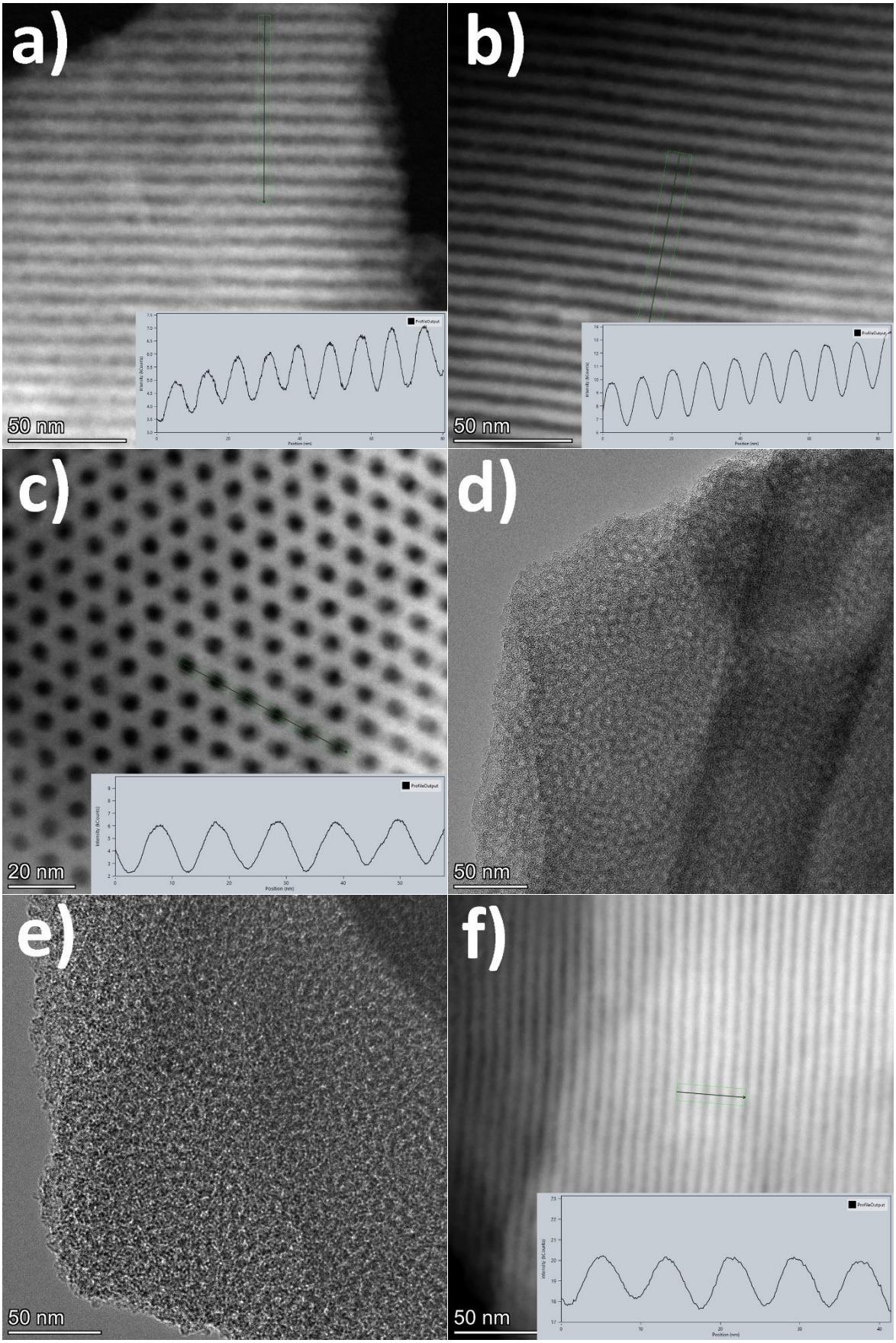

Figure 5.19. HAADF STEM/TEM images of MCs prepared at 5% of IL template: a) 5%OAc, b) 5%OAc-E, c) 5%$MeSO_4$, and 10% of IL template: d) 10%OAc, e) 10%OAc-E, f) 10%$MeSO_4$.

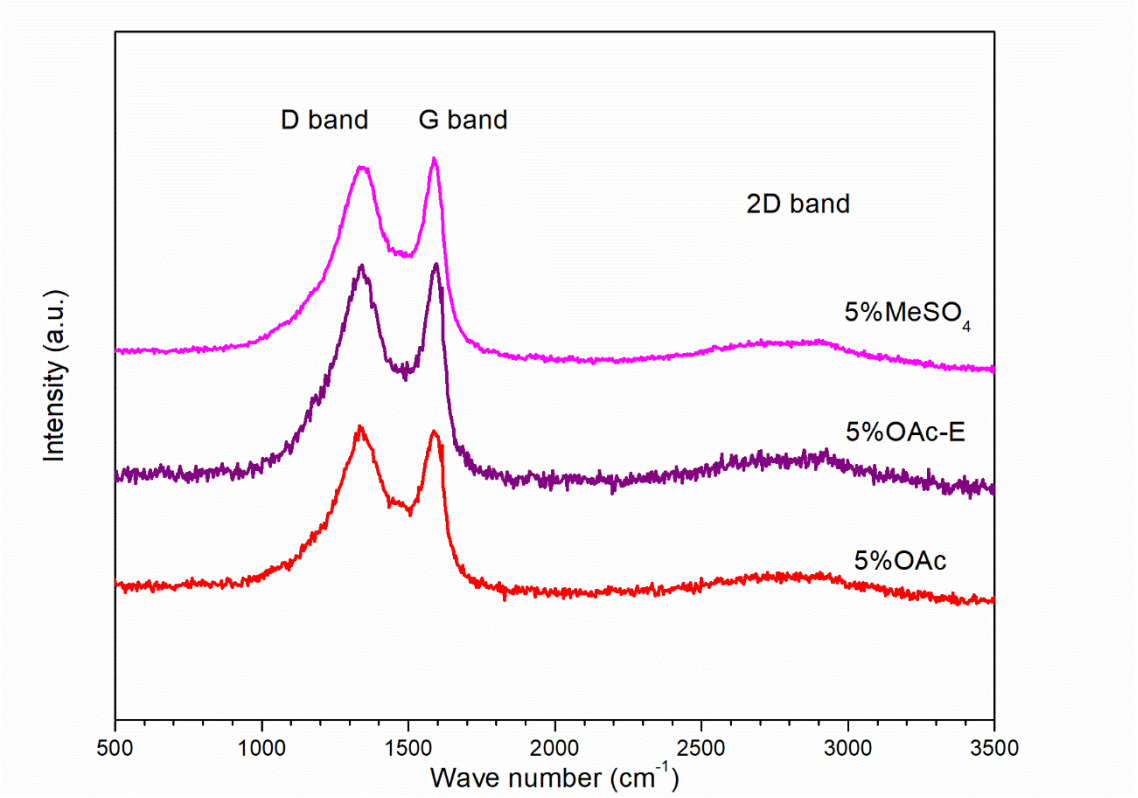

Figure 5.20. Raman spectra of MCs prepared by employing 5% of IL templates.

5.3.6. Electrochemical performance

5.3.6.1. MCs prepared employing [C_{18}MIM][OAc] template

The electrochemical performance of resulting MCs prepared by employing different contents of [C_{18}MIM][OAc] template was investigated in a Swagelok cell as electrode materials. The electrolyte was protic IL [N_{2220}][NTf_2] blended with acetonitrile (a weight fraction of 0.5) as organic mediator; the electrolyte can deliver a maximum conductivity due to an enhanced fluidity/mobility, lower viscosity, higher charge transfer ability, and ionic conductivity than pure [N_{2220}][NTf_2] electrolyte.[53,54] Cyclic voltammetry (CV) test was first carried at different scan rates: 5, 10, 20, 50, 100, 200, and 500 mV/s, respectively. As shown in

Figure 5.21a, at a low scan rate of 5 mV/s, all cells showed nearly rectangular shaped curves, especially those with MC electrodes prepared with lower contents of [C_{18}MIM][OAc] template. The rectangular shaped CV curves indicate typical behaviour of electric double-layer capacitor (EDLC). 5%OAc-based cell also exhibited a high charging/discharging current, next to that with 0%OAc that was prepared by solely employing Pluronic F127 template. The high charging/discharging current of 5%OAc electrode could be associated with the presence of highly ordered mesopore channels and large porosity, where the surface area and pore volume reached 730.0 m^2/g and 0.48 cm^3/g respectively. Cells with MC

electrodes prepared by employing higher contents of [C_{18}MIM][OAc] template showed quite small charging/discharging current probably because of the lack of highly ordered mesopores and the reducing porosity. Moreover, a slight increase in the capacitance was observed at higher voltage over 2.0 V. As discussed in *Chapter 4*, this was resulted from the slow decomposition of acetonitrile mediator under the polarisation effect at high voltage considering that the oxidation of acetonitrile usually takes place above 2.7 V.[53]

When the scan rate increased to 50 mV/s, 5%OAc electrode showed a more rectangular shaped profile (Figure 5.21b), indicating an ideal EDLC behaviour and highly reversible charge-discharge kinetics. The charging/discharging current for 5%OAc electrode was slightly lower than 0%OAc electrode due to a slightly smaller porosity. Cell with 10%OAc electrode still showed a slight oxidation peak at higher voltage over 2 V. The charging/discharging current for MC electrodes prepared by employing [C_{18}MIM][OAc] with a content over 20%, remained relatively small though the rectangular shaped CV curves were noticeable.

At a high scan rate of 500 mV/s (Figure 5.21c), rectangular shaped CV curved remained for all electrodes. In line with sample 0%OAc, electrode 5%OAc showed a slow response in the charging/discharging whilst that for the rest MC electrodes were much faster. Such delay in response for sample 5%OAc can be associated with the long mesopore channels, within which the ionic transport and the formation of electric double layers are not rapid enough at high scan rates. Too long mesopore channels were reported to cause a slow mass transfer, high electrochemical resistance, poor cycling performance, and low rate capability.[55] Due to the disordered nature of pore structures, samples prepared with higher content of [C_{18}MIM][OAc] (sample 10%OAc, 20%OAc, 50%OAc, and 100%OAc) have a better interconnectivity between neighbouring pores hence a better in-pore diffusivity. By contrast, it took longer time for the solvated $[N_{2220}]^+$ and $[NTf_2]^-$ ions to penetrate into the deeper pores then accumulate on the surface of pore channels in sample 5%OAc. Despite of this, sample 5%OAc still exhibited a higher charging/discharging current at high scan rate than the rest samples thanks to its higher porosity. Moreover, pseudocapacitive behaviour could happen for porous carbon-based supercapacitors with [N_{2220}][NTf_2] electrolyte for the presence of moisture in electrolyte and oxygen-containing surface groups on carbon electrodes.[56] In this work, no obvious pseudocapacitance was measured for MCs prepared by employing [C_{18}MIM][OAc] template.

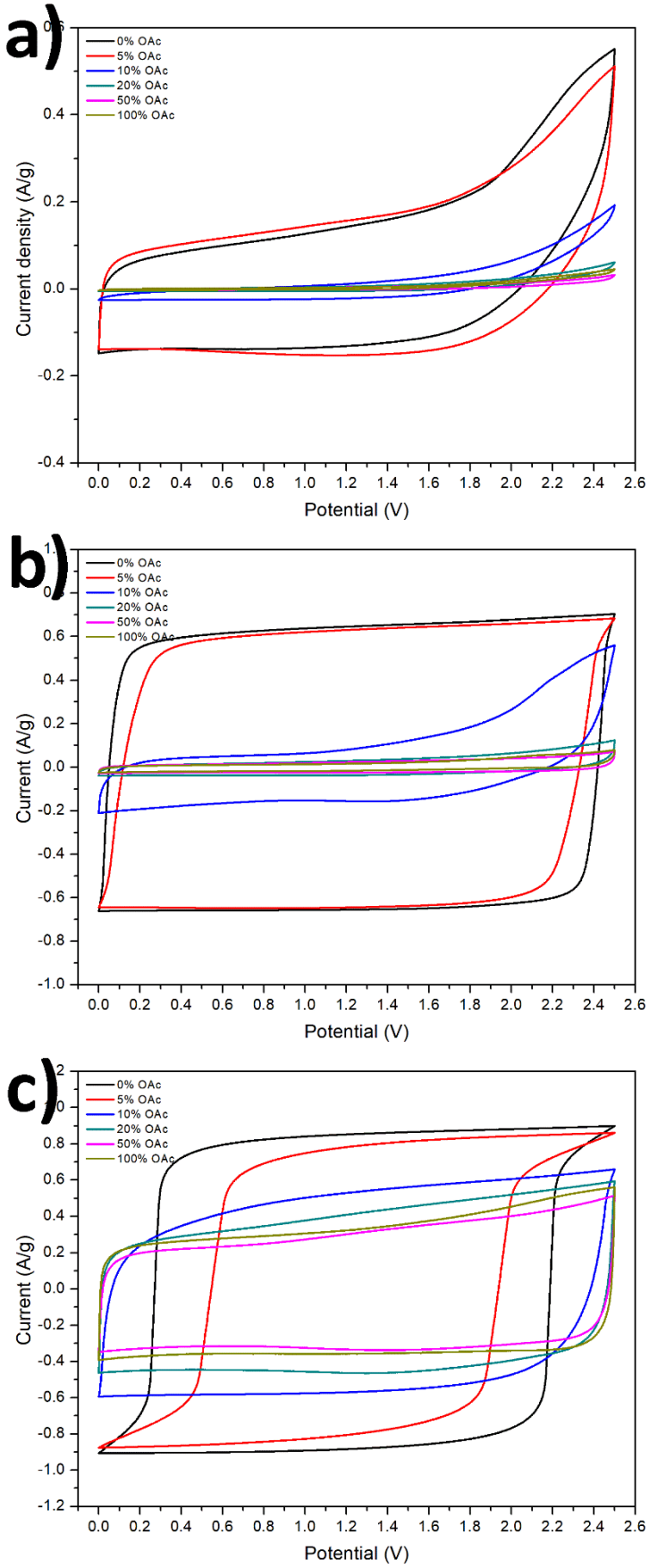

Figure 5.21. Cyclic voltammetry (CV) test for MC samples prepared by [C_{18}MIM][OAc] template at different scan rates: a) 5 mV/s, b) 50 mV/s, and c) 500 mV/s, respectively.

Consistent with the CV test, all MC electrodes showed symmetric triangular galvanostatic charge-discharge profiles (Figure 5.22a); the linear slope conforms with the typical feature of EDLCs. At a low current density of 0.5 A/g, samples prepared by lower content of [C_{18}MIM][OAc] such as 5%OAc showed longer charge/discharge time in [N_{2220}][NTf_2] electrolyte. As the percentage of [C_{18}MIM][OAc] in the total templates increased, the charge/discharge time dropped substantially. As shown in Figure 5.22b and c, electrode 5%OAc exhibited larger capacitance and higher energy density throughout different current densities with the largest values of 55.4 F/g and 12.0 Wh/kg at 0.1 A/g. This mainly originated from the higher surface area and pore volume of sample 5%OAc. When the percentage of [C_{18}MIM][OAc] in the total templates increased, the total pore volume and surface area declined steadily. In addition to the disappear of ordered mesopore structures, the specific capacitance of MCs showed a drastic decrease with a value of 1.5 F/g only for sample 100%OAc at 0.1 A/g. Despite the content of oxygen on sample surface appeared an overall growth from 4.8 to 7.3 at%, it did not significantly alleviate the decline in the specific capacitance. On the other hand, this implies that the pore architectures play a more important role than the surface functionalities in the electrochemical performance. Overall, it is feasible to use amphiphilic IL [C_{18}MIM][OAc] as the recyclable template to prepare MC materials for energy storage, however the eventual electrochemical performance of resulting MCs is hugely subject to the percentage of [C_{18}MIM][OAc] in total templates. The strong catalytic ability of [C_{18}MIM][OAc] template plays a recalcitrant role in the pore architectures of the resulting MCs thus worsening their electrochemical performance when employed as supercapacitor electrodes.

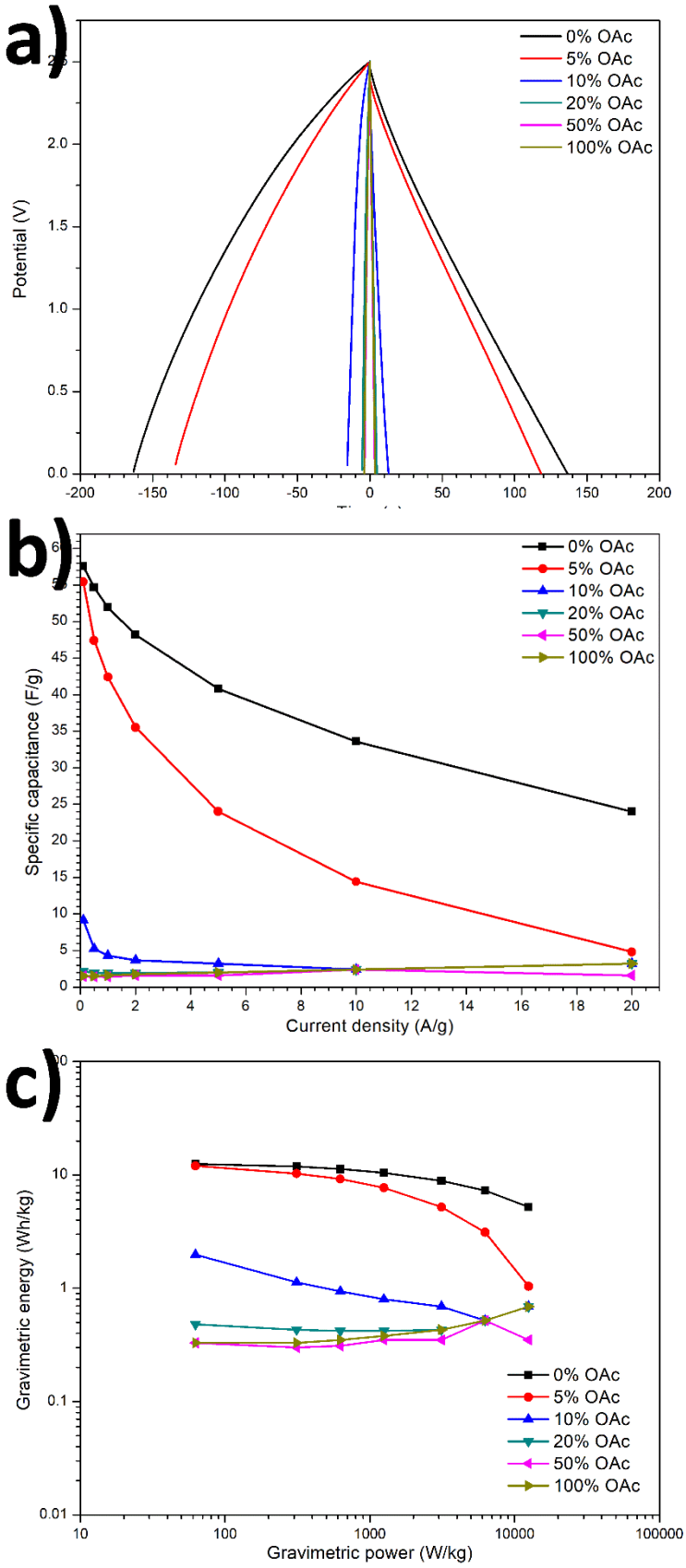

Figure 5.22. a) Galvanostatic charge/discharge at 0.5 A/g, b) gravimetric specific capacitance, and c) energy density vs power density for MCs prepared by employing [C_{18}MIM][OAc] template.

5.3.6.2. The role of IL extraction process

The role of IL template extraction in the electrochemical performance was investigated. As shown in Figure 5.23a, with the same amount of [C_{18}MIM][OAc] template, electrode 5%OAc-E prepared by excluding the extraction process, showed a discharge time of 49.5 s at a current density of 0.5 A/g, which was less than half the value of its counterpart 5%OAc (118.5 s) prepared with IL extraction. This is mainly because 5%OAc-E has a lower porosity with a pore volume of 0.35 cm^3/g than the latter with a pore volume of 0.48 cm^3/g. The N-doping in 5%OAc-E did not significantly offset the loss in the capacitance due to the decreased porosity. Figure 5.23b shows the capacitance of MC samples prepared by excluding IL extraction process. At a low percentage of [C_{18}MIM][OAc], sample 5%OAc-E exhibited a higher capacitance throughout different current densities with the maximum value reaching 29.2 F/g at 0.1 A/g. MCs prepared by employing [C_{18}MIM][OAc] higher than 10% showed low capacitance below 6.0 F/g. Despite the content of doped N atoms increased steadily with the increasing percentage of [C_{18}MIM][OAc] template, the drastically declined porosity played a major role in impairing their electrochemical performance. Overall, the capacitance showed a similar declining trend as the current density increased, and the value was smaller than their counterparts prepared with IL extraction process due to a reduced porosity by the exclusion of IL extraction. Therefore, the extraction process to recycle IL template is essential as it not only improves the sustainability of IL templates but also enhances the electrochemical performance by increases the porosity.

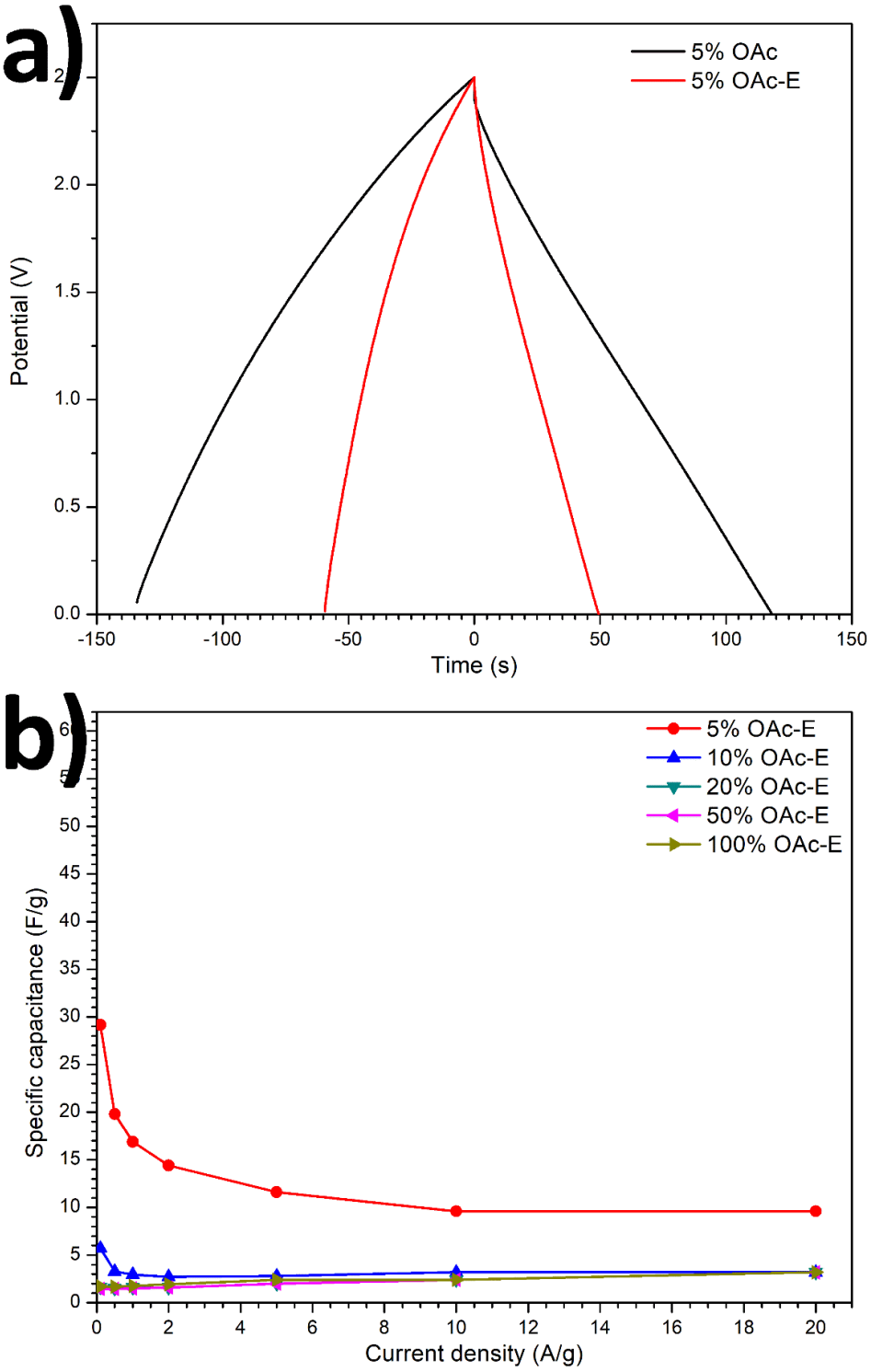

Figure 5.23. a) Galvanostatic charge/discharge test for 5%OAc and 5%OAc-E at 0.5 A/g, and b) gravimetric specific capacitance of MCs prepared by employing [C_{18}MIM][OAc] template but excluding the template removal process.

5.3.6.3. The role of IL anions

The electrochemical performance of resulting MCs prepared by employing [C_{18}MIM][$MeSO_4$] template was studied to investigate the role of different anions of IL templates. Figure 5.24 shows the CV tests for cells with corresponding MC electrodes. At a

low scan rate of 5 mV/s (Figure 5.24a), MC electrodes showed nearly rectangular shaped CVs, indicating the typical reversible charge/discharge response of EDLC behaviour. A slight increase in the capacitance was also found at high voltage over 2 V, evidenced by the oxidative peak originating from the slow decomposition of acetonitrile. MC 100%$MeSO_4$ prepared by 100% of [C_{18}MIM][$MeSO_4$] template barely showed charging/discharging behaviour because of the small porosity (with a total pore volume of 0.22 cm^3/g). At an intermediate scan rate of 50 mV/s (Figure 5.24b), all MC especially sample 5%$MeSO_4$ and 10%$MeSO_4$ showed more rectangular shaped CV profiles, characteristics of ideal EDLCs. As the percentage of [C_{18}MIM][$MeSO_4$] in the total templates increased, there was an overall diminishing effect on the charging/discharging current. Notably, the charging/discharging current for electrode 5%$MeSO_4$ was slightly higher than that of 0%$MeSO_4$ prepared by solely employing Pluronic F127 template; this suggests a slightly improved capacitance when 5% of [C_{18}MIM][$MeSO_4$] template was employed. Compared with 10%$MeSO_4$ electrode, the charging/discharging current for 20%$MeSO_4$ electrode declined so drastically. According to the morphological study, well-regulated ordered mesopore channels remained in sample 10%$MeSO_4$, as opposed to the disordered mesopores in sample 20%$MeSO_4$. Therefore, the drastic drop in charging/discharging current could be mainly attributed to the loss of ordered mesopore channels. At a high scan rate of 500 mV/s (Figure 5.24c), rectangular shaped CV profiles were remained for all MC electrodes. A slow response in the charging/discharging was also observed for MC electrodes with highly ordered mesopore channels, such as sample 5%$MeSO_4$ and 10%$MeSO_4$. Again, as discussed early, such delayed response mainly stemmed from the presence of long ordered mesopore channels that resulted in a slower the ionic transport thus delays in the formation of electric double layers under faster scan rates. No delay in charging/discharging was found for sample 20%$MeSO_4$. Higher amount of [C_{18}MIM][$MeSO_4$] template incurred deterioration in the order of pore structures hence a better interconnectivity between neighbouring pores. Consequently, sample 20%$MeSO_4$ and 100%$MeSO_4$ were expected to have a better in-pore diffusivity and it took shorter time for the solvated $[N_{2220}]^+$ and $[NTf_2]^-$ ions to accumulate on the pore surface thanks to the reduced penetration depth. There was no obvious pseudocapacitive bahaviour observed for MCs prepared by [C_{18}MIM][$MeSO_4$] template either, in spite of the presence of oxygen-containing surface functionalities with O content ranging from 4.8 to 6.8 at%.

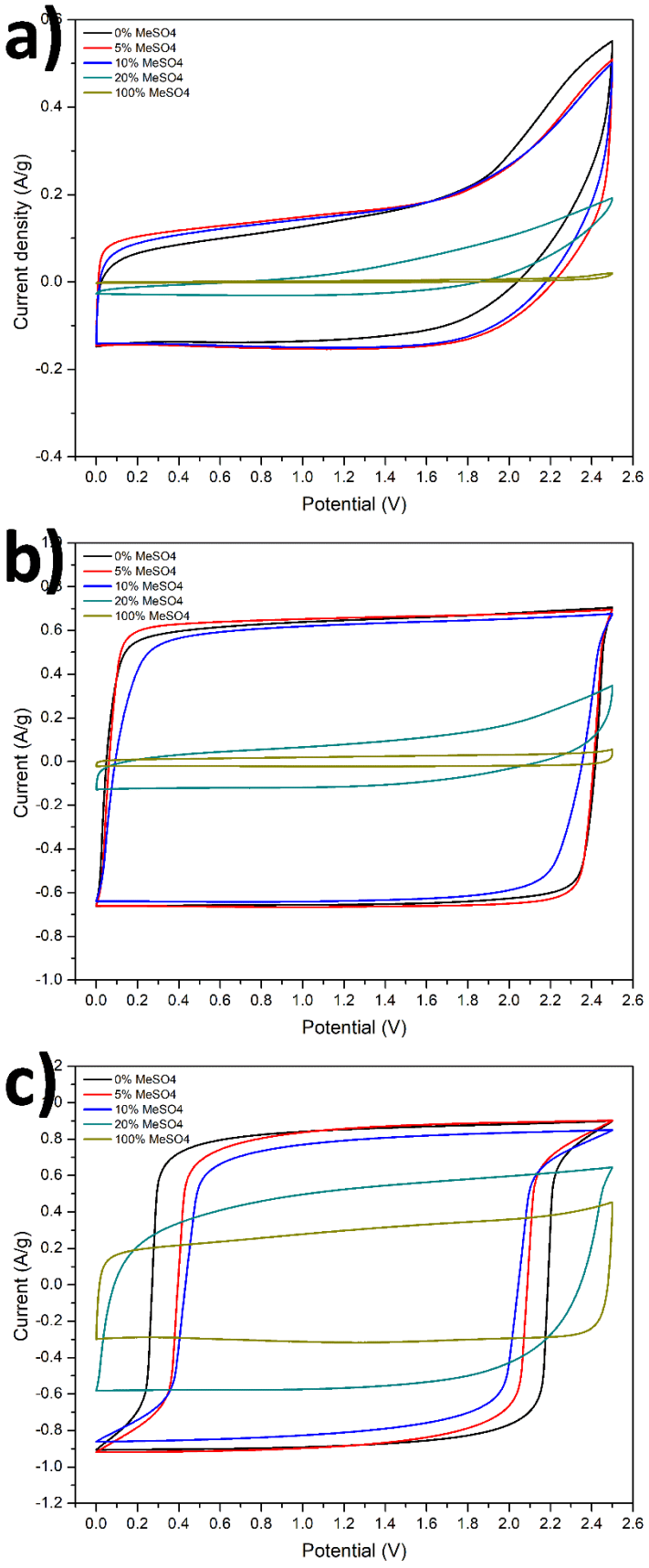

Figure 5.24. Cyclic voltammetry (CV) test for MC samples prepared by [C_{18}MIM][$MeSO_4$] template at different scan rates: a) 5 mV/s, b) 50 mV/s, and c) 500 mV/s, respectively.

Figure 5.25a shows the galvanostatic charge/discharge test at 0.5 A/g for MCs prepared by employing [C_{18}MIM][$MeSO_4$] template. The symmetrical triangular shaped galvanostatic charge-discharge curves with linear slops confirmed the characteristic EDLC behaviour. Thanks to the presence of highly ordered mesopore channels, electrodes 5%$MeSO_4$ and 10%$MeSO_4$, exhibited a long discharging time of 141.3 and 114.4 s, implying a better capacitive behaviour. As the percentage of [C_{18}MIM][$MeSO_4$] in the total templates increased to 20%, the discharge time for sample 20%$MeSO_4$ dropped drastically to only 7.6 s. Electrode 20%$MeSO_4$ exhibited a surface area and pore volume of 770.5 m^2/g and 0.31 cm^3/g. Therefore, such drastically decreased capacitance probably originated from the loss of ordered mesopore channels. When 100% of [C_{18}MIM][$MeSO_4$] template was used, resulting MC showed a discharge time of 3.8 s only. Furthermore, the discharge time (141.3 s) for sample 5%$MeSO_4$ is notably longer than that of sample 0%$MeSO_4$ (136.7 s), in line with the higher charging/discharging current from the CV test. Sample 0%$MeSO_4$ has a larger pore volume of 0.56 cm^3/g than that for sample 5%$MeSO_4$ (0.48 cm^3/g), but sample 5%$MeSO_4$ possesses a larger surface area of 823.7 m^2/g and smaller mesopore diameter of 3.8 nm than the former sample (793.8 m^2/g, 4.3 nm). For the same solvated electrolyte ions, pores with diameter close to the ions are expected to deliver a maximum double-layer capacitance.[57] The mesopore diameter for sample 5%$MeSO_4$ matched better with the solvated electrolyte ions, amongst which the largest ion $[NTf_2]^-$ has a dynamic diameter in the longest dimension of 2.24 nm when solvated in acetronitrile.[58] Therefore, sample 5%$MeSO_4$ showed an overall higher capacitance than sample 0%$MeSO_4$ (Figure 5.25b); the value hit 60.9 F/g at 0.1 A/g then dropped to 22.4 F/g at 20 A/g. As the percentage of [C_{18}MIM][$MeSO_4$] in the total templates increased to 100%, resulting sample exhibited lowest capacitance below 2 F/g throughout different current densities. Consistent with the specific capacitance, sample 5%$MeSO_4$ also showed a higher gravimetric energy density of 13.2 Wh/kg than sample 0%$MeSO_4$ with the value of 12.5 Wh/kg (Figure 5.25c).

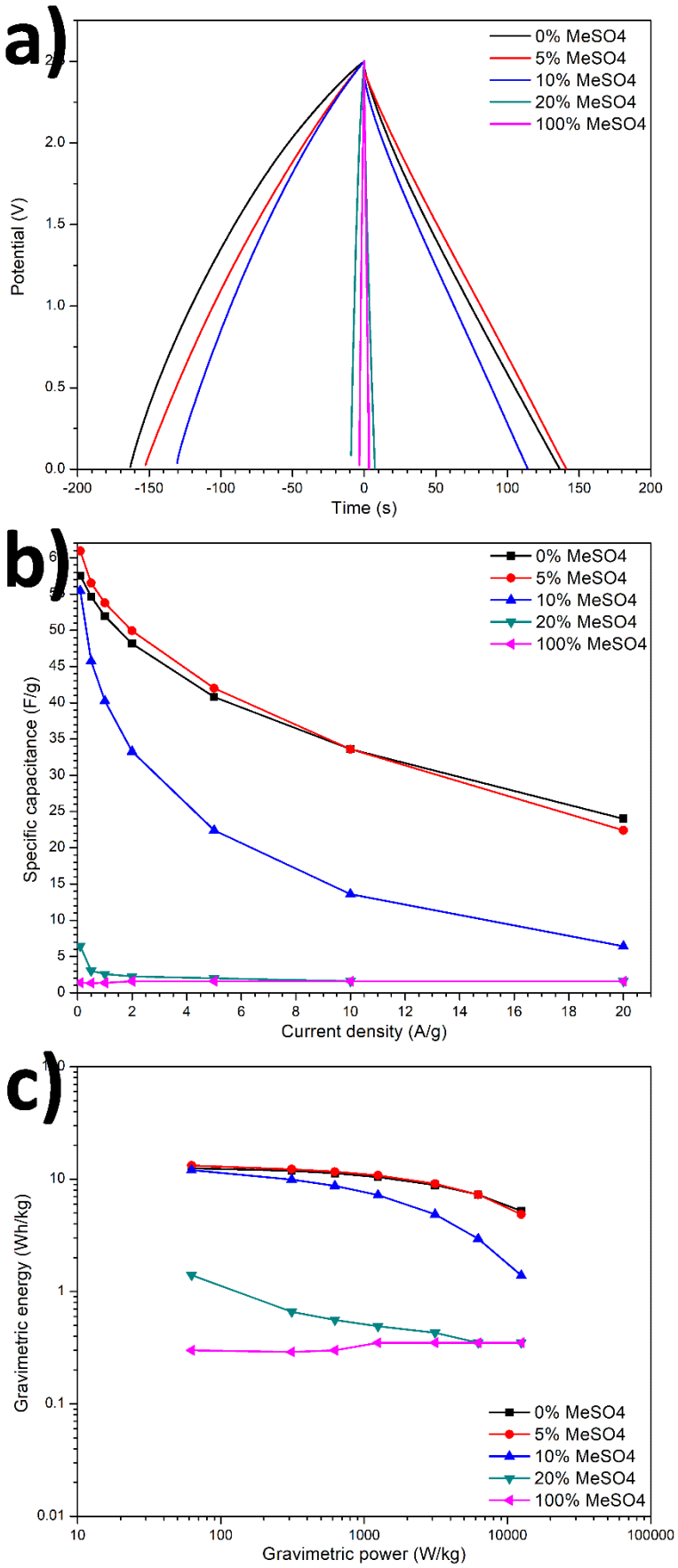

Figure 5.25. a) Galvanostatic charge/discharge at 0.5 A/g, b) gravimetric specific capacitance, and c) energy density vs power density for MCs prepared by employing [C_{18}MIM][$MeSO_4$] template.

In comparison of the two different IL templates, namely [C_{18}MIM][OAc] and [C_{18}MIM][$MeSO_4$], methyl sulphate-based IL template seemingly yielded a richer porosity than acetate-based counterpart at the same percentage of IL templates employed for MC preparation (Table 5.2). As shown in Figure 5.26a, at the same scan rate of 50 mV/s, MC samples prepared by employing IL templates less than 10% showed rectangular shaped CV curves and characteristic ideal EDLC behaviour. The charging/discharging currents were quite comparable when 5% of IL templates was employed; methyl sulphate anion-based IL resulted in a relatively higher charging/discharging current than acetate-based IL template. This is mainly because that methyl sulphate anion gave rise to a larger surface area of 823.7 m^2/g than acetate anion (730.0 m^2/g) thus a higher potential for ion adsorption/desorption during charging/discharging. With 10% of IL templates, acetate-based IL template exhibited a much lower charging/discharging current than methyl sulphate-based counterpart, though 10%OAc exhibited a larger pore volume of 0.44 cm^3/g and surface oxygen content of 6.9 at% than sample 10%$MeSO_4$ (0.40cm^3/g and 6.2 at%). Figure 5.26b shows the galvanostatic charge-discharge test at a current density of 0.5 A/g. Consistent with CV test, sample 5%$MeSO_4$ displayed a longest discharge time of 141.3 s, followed by sample 0%ILs (136.7 s) prepared by solely employing Pluronic F127 template and sample 5%OAc (118.5 s). As the IL percentage reached 10%, sample 10%OAc exhibited a significantly smaller discharge time (only 13.0 s), whilst that for sample 10%$MeSO_4$ remained 114.4 s. Figure 5.26c shows the gravimetric specific capacitance of MCs prepared by employing two different IL templates. Sample 5%$MeSO_4$ exhibited the largest value of 60.9 F/g at 0.1 A/g, followed by sample 0%ILs (57.5 F/g) and 5%OAc (55.4 F/g). The capacitance for sample 10%OAc was smaller than 10 F/g, whilst that for sample 10%$MeSO_4$ was much higher reaching 55.5 F/g at 0.1 A/g; this value is quite comparable with that for sample 0%ILs. According to the pore morphology study, highly ordered mesopore channels with a diameter of 3.0 nm were remained in sample 10%$MeSO_4$ whilst only disordered mesopores with a mean pore size of 4.0 nm were observed for sample 10%OAc. Therefore, the substantial deterioration in the electrochemical performance for sample 10%OAc was mainly caused by the loss of well-regulated mesopore channels and larger pore size. Furthermore, the comparable capacitance values between sample 10%$MeSO_4$ and sample 0%ILs may also suggest that replacing the block copolymer template with 10% of [C_{18}MIM][$MeSO_4$] to prepare MCs will not significantly decrease their capacitance at lower current densities.

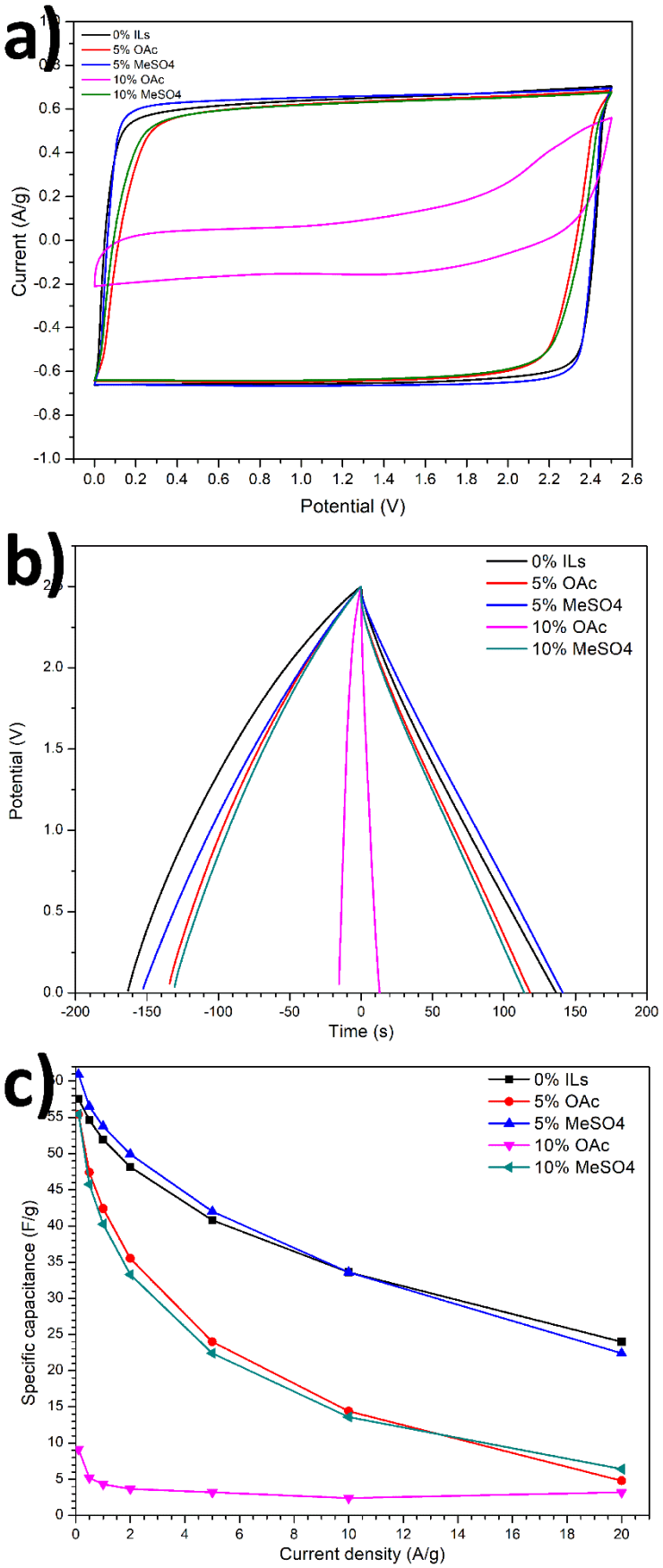

Figure 5.26. Comparison of MCs prepared by different IL templates: a) CV at the scan rate of 50 mV/s, b) galvanostatic charge/discharge at the current density of 0.5 A/g, and c) gravimetric specific capacitance.

Overall, the anion of IL templates played a crucial role in the electrochemical performance of resulting MC electrodes by influencing the pore architecture; anions with less catalytic ability favoured the formation of well-organised mesopores and eventually delivered a better electrochemical performance. During the preparation of highly ordered MCs, seeking or designing IL templates with excellent amphiphilicity but much weaker catalytic ability is required to further increase the percentage of recyclable IL template to substitute non-recyclable block copolymer template.

5.4. Conclusions

The use of amphiphilic imidazolium based ILs as recyclable templates to substitute non-recyclable block copolymer template was studied to prepare MC materials for energy storage. Phenolic polymer, a preliminary lignin model, was employed as carbon precursor with phloroglucinol monomer cross-linked sufficiently by glyoxal. After templating, IL templates showed excellent structural intactness hence reusability. Four factors that influenced the pore architecture of resulting MCs were identified as 1) the length of cationic alkyl chain of IL templates, 2) the percentage of ILs in the IL/block copolymer co-templating mixtures, 3) IL template extraction process, and 4) the anion of IL templates.

Increasing the length of IL cationic alkyl chain can slightly elevated the porosity of resulting carbon materials. From [C_{10}MIM][OAc] to [C_{18}MIM][OAc], the BET surface area and pore volume of resulting carbon materials increased from 224.8 m^2/g and 0.094 cm^3/g to 273.4 m^2/g and 0.112 cm^3/g with dominating pores remaining as microporous though.

When block copolymer Pluronic F127 was employing to assist the self-assembly of IL templates, there was an overall diminishing effect on the porosity and mesopore rate of resulting MCs as the percentage of ILs increases in the total templates. This can be attributed to the bifunctional role of IL templates, both soft template and catalyst. The strong catalytic ability of IL templates will overly cross-link precursor monomers and detach precursors from ordered templates, thereby worsening the porosity of resulting MCs. Methyl sulphate anion-based ILs has a weaker catalytic ability than acetate anion-based ILs thus can result in a slightly higher porosity at the same mixing ratio. With [C_{18}MIM][OAc] template, well-regulated mesopore channels only remained when the percentage of [C_{18}MIM][OAc] was below 5%; resulting MC showed a BET surface area and pore volume of 730.0 m^2/g and 0.48 cm^3/g with pore diameter of 3.8 nm. Higher percentages of IL template led to disordered mesopores at 10% and micropores at over 20%. With [C_{18}MIM][$MeSO_4$] template, ordered

mesopore channels remained when the percentage of [C_{18}MIM][$MeSO_4$] was no more than 10%, with mesopore diameter shrinking from 3.8 nm at 5% to 3.0 nm at 10%. As the percentage of [C_{18}MIM][$MeSO_4$] increased, the total pore volume exhibited an ever-decreasing trend with the value dropping from 0.56 cm^3/g (at 0%) to 0.22 cm^3/g (100%), whilst surface area showed a growth first with a value up to 823.7 m^2/g then declined to 581.9 m^2/g.

The extraction process of the IL templates before calcination are crucial to not only ensure the reusability of IL templates but also enrich the pore structures. Carbon materials prepared by excluding the IL extraction process showed an overall reduced porosity than those prepared by including IL extraction. The residual char yielded from the pyrolysis of IL templates themselves can partly even completely block the pores, especially the carbonisation of hydrophobic cationic alkyl chains that are expected to generate pore structures.

The surface oxygen content of resulting MCs showed an overall increasing trend as the percentage of IL templates increased, regardless of IL anion species and including/excluding the extraction process of IL template. Besides, there is no significant difference in the graphitisation degree of all resulting MCs due to the use of same carbonisation process.

When the resulting MCs were employed as electrode materials for energy storage, all samples showed characteristic EDLC behaviour, but their electrochemical performance is highly subject to the percentage of ILs in the total templates. With [C_{18}MIM][OAc] template, the specific capacitance of resulting MCs decreased as the percentage of [C_{18}MIM][OAc] increased; the value dropped from 57.5 F/g for sample 0%ILs to 55.4 F/g for sample 5%OAc and only 1.5 F/g for sample 100%OAc at a current density of 0.1 A/g. By excluding the IL extraction process, the specific capacitance decreased drastically due to a reduced porosity compared with those prepared by including IL extraction process. With [C_{18}MIM][$MeSO_4$] template, the specific capacitance of resulting MCs first showed an increase then a decline as the percentage of [C_{18}MIM][$MeSO_4$] increased. At 5% of [C_{18}MIM][$MeSO_4$], there was an overall elevated electrochemical performance with the capacitance increasing from 57.5 F/g for sample 0%ILs to 60.9 F/g for sample 5%$MeSO_4$ at 0.1 A/g. As the percentage of [C_{18}MIM][$MeSO_4$] exceeded 10%, the capacitance showed a decreasing trend with a value of 1.4 F/g only for sample 100%$MeSO_4$ at 0.1 A/g. The value of 55.5 F/g for sample 10%$MeSO_4$ still remained comparable with that for sample 0%ILs prepared by solely employing Pluronic F127 template. Therefore, it will not significantly decrease the

capacitance at low current densities by replacing non-recyclable block copolymer with 10% of $[C_{18}MIM][MeSO_4]$ during the preparation of MCs.

Overall, IL templates themselves play a crucial role in pore architecture, surface functionality, and electrochemical performance of resulting MC electrodes. To further increase the percentage of recyclable IL template to substitute non-recyclable block copolymer template during the preparation of highly ordered MCs, future effort can be directed into the careful selection and design of ILs with excellent amphiphilicity but much weaker catalytic ability.

5.5. References

1 Y. Su, H. Wang, J. Zhao, M. H. Rummeli, Y. Gao, Y. B. Jiang, L. Zhang and G. Zou, *Electrochim. Acta*, 2018, **280**, 258–265.

2 Y. She, Z. Lu, M. Ni, L. Li and M. K. H. Leung, *ACS Appl. Mater. Interfaces*, 2015, **7**, 7214–7221.

3 N. Ranjbar Sahraie, J. P. Paraknowitsch, C. Göbel, A. Thomas and P. Strasser, *J. Am. Chem. Soc.*, 2014, **136**, 14486–14497.

4 B. Karimi, H. Behzadnia and H. Vali, *ChemCatChem*, 2014, **6**, 745–748.

5 S. Zhang, M. S. Miran, A. Ikoma, K. Dokko and M. Watanabe, *J. Am. Chem. Soc.*, 2014, **136**, 1690–1693.

6 A. Chen, Y. Yu, H. Lv, Y. Wang, S. Shen, Y. Hu, B. Li, Y. Zhang and J. Zhang, *J. Mater. Chem. A*, 2013, **1**, 1045–1047.

7 B. J. P. Paraknowitsch, J. Zhang, D. Su, A. Thomas and M. Antonietti, *Adv. Mater.*, 2010, **22**, 87–92.

8 X. Wang and S. Dai, *Angew. Chemie*, 2010, **122**, 6814–6818.

9 J. S. Lee, X. Wang, H. Luo, G. A. Baker and S. Dai, *J. Am. Chem. Soc.*, 2009, **131**, 4596–4597.

10 B. Karimi, H. Behzadnia, M. Rafiee and H. Vali, *Chem. Commun.*, 2012, **48**, 2776–2778.

11 B. Qiu, C. Pan, W. Qian, Y. Peng, L. Qiu and F. Yan, *J. Mater. Chem. A*, 2013, **1**, 6373–6378.

12 B. Haghighi, B. Karimi, M. Tavahodi and H. Behzadneia, *Mater. Sci. Eng. C*, 2015, **52**, 219–224.

13 M. Rafiee, B. Karimi and H. Shirmohammadi, *Electrocatalysis*, 2018, **9**, 632–639.

14 W. Yang, T. P. Fellinger and M. Antonietti, *J. Am. Chem. Soc.*, 2011, **133**, 206–209.

15 F. Hasché, T. P. Fellinger, M. Oezaslan, J. P. Paraknowitsch, M. Antonietti and P. Strasser, *ChemCatChem*, 2012, **4**, 479–483.

16 B. E. Wilson, S. He, K. Buffington, S. Rudisill, W. H. Smyrl and A. Stein, *J. Power Sources*, 2015, **298**, 193–202.

17 X. Zhao, S. Li, H. Cheng, J. Schmidt and A. Thomas, *ACS Appl. Mater. Interfaces*, 2018, **10**, 3912–3920.

18 N. Fechler, T. P. Fellinger and M. Antonietti, *Adv. Mater.*, 2013, **25**, 75–79.

19 A. Chen, Y. Li, L. Liu, Y. Yu, K. Xia, Y. Wang and S. Li, *Appl. Surf. Sci.*, 2017, **393**, 151–158.

20 Z. L. Xie, R. J. White, J. Weber, A. Taubert and M. M. Titirici, *J. Mater. Chem.*, 2011, **21**, 7434–7442.

21 H. Yang, X. Cui, Y. Deng and F. Shi, *J. Mater. Chem.*, 2012, **22**, 21852–21856.

22 B. Nagy, E. Geissler and K. László, *Microporous Mesoporous Mater.*, 2020, **294**, 1–10.

23 S. Livi, J. F. Gérard and J. Duchet-Rumeau, *Chem. Commun.*, 2011, **47**, 3589–3591.

24 J. Gräsvik, J. P. Hallett, T. Q. To and T. Welton, *Chem. Commun.*, 2014, **50**, 7258–7261.

25 H. Shekaari and E. Armanfar, *Fluid Phase Equilib.*, 2011, **303**, 120–125.

26 C. Matei Ghimbeu, L. Vidal, L. Delmotte, J. M. Le Meins and C. Vix-Guterl, *Green Chem.*, 2014, **16**, 3079–3088.

27 D. Saha, K. E. Warren and A. K. Naskar, *Carbon N. Y.*, 2014, **71**, 47–57.

28 C. Tsouris, R. Mayes, J. Kiggans, K. Sharma, S. Yiacoumi, D. Depaoli and S. Dai, *Environ. Sci. Technol.*, 2011, **45**, 10243–10249.

29 S. Herou, M. C. Ribadeneyra, R. Madhu, V. Araullo-Peters, A. Jensen, P. Schlee and M. Titirici, *Green Chem.*, 2019, **21**, 550–559.

30 L. Zheng, C. Guo, J. Wang, X. Liang, S. Chen, M. Junhe, B. Yang, Y. Jiang and H. Liu, *J. Phys. Chem. B*, 2007, **111**, 1327–1333.

31 P. K. Singh, M. Kumbhakar, R. Ganguly, V. K. Aswal, H. Pal and S. Nath, *J. Phys. Chem. B*, 2010, **114**, 3818–3826.

32 J. S. Nambam and J. Philip, *J. Phys. Chem. B*, 2012, **116**, 1499–1507.

33 J. J. Kipling and R. B. Wilson, *J. Appl. Chem.*, 1960, **10**, 109–113.

34 M. aki Murakami, Y. Kaneko and J. ichi Kadokawa, *Carbohydr. Polym.*, 2007, **69**, 378–381.

35 P. Snedden, A. I. Cooper, K. Scott and N. Winterton, *Macromolecules*, 2003, **36**, 4549–4556.

36 K. Matsumoto and T. Endo, *Macromolecules*, 2008, **41**, 6981–6986.

37 D. Saha, R. Zacharia and A. K. Naskar, in *Polymer Precursor-Derived Carbon*, 2014, vol. 1173, pp. 61–83.

38 R. T. Mayes, C. Tsouris, J. O. Kiggans, S. M. Mahurin, D. W. Depaoli and S. Dai, *J. Mater. Chem.*, 2010, **20**, 8674–8678.

39 M. Thommes, K. Kaneko, A. V. Neimark, J. P. Olivier, F. Rodriguez-Reinoso, J. Rouquerol and K. S. W. Sing, *Pure Appl. Chem.*, 2015, **87**, 1051–1069.

40 D. Weingarth, M. Zeiger, N. Jäckel, M. Aslan, G. Feng and V. Presser, *Adv. Energy Mater.*, 2014, **4**, 1–13.

41 A. C. Ferrari, J. C. Meyer, V. Scardaci, C. Casiraghi, M. Lazzeri, F. Mauri, S. Piscanec, D. Jiang, K. S. Novoselov, S. Roth and A. K. Geim, *Phys. Rev. Lett.*, 2006, **97**, 1–4.

42 Y. Song, J. Liu, K. Sun and W. Xu, *RSC Adv.*, 2017, **7**, 48324–48332.

43 Y. Zhang, H. He, K. Dong, M. Fan and S. Zhang, *RSC Adv.*, 2017, **7**, 12670–12681.

44 J. M. Vicent-Luna, J. M. Romero-Enrique, S. Calero and J. A. Anta, *J. Phys. Chem. B*, 2017, **121**, 8348–8358.

45 Y. Zhao, S. Gao, J. Wang and J. Tang, *J. Phys. Chem. B*, 2008, **112**, 2031–2039.

46 J. N. A. Canongia Lopes and A. A. H. Pádua, *J. Phys. Chem. B*, 2006, **110**, 3330–3335.

47 I. Goodchild, L. Collier, S. L. Millar, I. Prokeš, J. C. D. Lord, C. P. Butts, J. Bowers, J. R. P. Webster and R. K. Heenan, *J. Colloid Interface Sci.*, 2007, **307**, 455–468.

48 S. S. Sarangi, B. L. Bhargava and S. Balasubramanian, *Phys. Chem. Chem. Phys.*, 2009, **11**, 8745–8751.

49 T. Ogoshi, T. Onodera, T. A. Yamagishi and Y. Nakamoto, *Macromolecules*, 2008, **41**, 8533–8536.

50 H. Tang, J. Tang, S. Ding, M. Radosz and Y. Shen, *J. Polym. Sci. Part A Polym. Chem.*, 2005, **43**, 1432–1443.

51 J. Lu, F. Yan and J. Texter, *Prog. Polym. Sci.*, 2009, **34**, 431–448.

52 P. Kubisa, *Prog. Polym. Sci.*, 2009, **34**, 1333–1347.

53 L. Timperman, P. Skowron, A. Boisset, H. Galiano, D. Lemordant, E. Frackowiak, F. Béguin and M. Anouti, *Phys. Chem. Chem. Phys.*, 2012, **14**, 8199–8207.

54 S. Sathyamoorthi, V. Suryanarayanan and D. Velayutham, *J. Power Sources*, 2015, **274**, 1135–1139.

55 B.-J. Lee, H.-Y. Park, D.-S. Yang, T.-H. Kang, S. Hwang and J.-S. Yu, *J. Electrochem. Soc.*, 2019, **166**, A5244–A5251.

56 A. Brandt, J. Pires, M. Anouti and A. Balducci, *Electrochim. Acta*, 2013, **108**, 226–231.

57 C. Largeot, C. Portet, J. Chmiola, P. L. Taberna, Y. Gogotsi and P. Simon, *J. Am. Chem. Soc.*, 2008, **130**, 2730–2731.

58 R. Lin, P. Huang, J. Ségalini, C. Largeot, P. L. Taberna, J. Chmiola, Y. Gogotsi and P. Simon, *Electrochim. Acta*, 2009, **54**, 7025–7032.

Chapter 6.

Epilogue

6.1. Summary

This work aims to employ amphiphilic ionic liquids (ILs) as recyclable template to prepare ordered mesoporous carbons (MCs) for energy storage from lignin. There are four major steps in the proposed method, including: 1) the self-assembly process, 2) the cross-linking of carbon precursors, 3) extraction of IL templates, and 4) calcination.

The self-assembly mechanism indicates that the morphologies of IL templates are tuneable through the adjustment of water concentration, temperature, and the selection of different precursors. With the increasing water concentration, the morphology of IL templates undergoes lamellar bilayer, hexagonal columnar, and spherical structures. Introducing more hydroxyl groups to carbon precursor can also change the morphology of IL templates, such as from lamellar to columnar. The rationale of both approaches lies in adjusting the H-bonding probability of IL templates in the mixture. Moreover, carbon precursors with different hydroxyl moieties lead to different precursor-template spatial correlations. More hydroxyl groups in carbon precursor increase the H-bonding ability thus disperses precursors from hydrophobic to hydrophilic phase. The result presents a thorough understanding on the manipulation of the morphologies of IL templates and the selection/modification of carbon precursors, thereby guiding the preparation of MCs.

The cross-linking of carbon precursors with various cross-linkers, from formaldehyde to its two greener substitutes, glyoxal and glyoxylic acid, has significant influence on the pore architecture, surface functionality, and electrochemical performance of the resulting MCs. Glyoxal favours the formation of well-organised hexagonal mesopores with pore size tuneable between 3.3 and 6.1 nm. The surface area of glyoxal-resultant MCs inclined from 753.4 to 820.7 m^2/g as the cross-linker/precursor ratio (C/P ratio) increased from 1 to 2, whereas the pore volume decreased from 0.69 to 0.48 cm^3/g. Formaldehyde and glyoxylic acid only resulted in interrupted even entirely disordered pore structures due to the formation of overly crosslinked precursor that destabilised the ordered mesophase after self-assembly. Besides, different cross-linkers also influence the surface functionalities of resulting MCs. A larger C/P ratio will lead to a higher content of -C-O group and a lower content of -C=O group. At the same mixing ratio, glyoxylic acid can result in a higher -C-O content than glyoxal. With the same amount of aldehyde groups, formaldehyde can yield a lower -C-O content than glyoxal due to its higher reactivity. When employed as the working electrodes for symmetric supercapacitors, glyoxal-resultant MCs thanks to the dominating ordered mesopore channels exhibited higher specific capacitance of 153.5 F/g in 6M KOH aqueous

electrolyte and 57.5 F/g in IL $[N_{2220}][NTf_2]$/ACN electrolyte. Conversely, the energy density was lower in KOH electrolyte (7.7 Wh/kg) than the value of 12.5 Wh/kg in IL electrolyte. MCs prepared with formaldehyde or glyoxylic acid exhibited a relatively lower capacitance because of the disordered or interrupted mesopore structures. Overall, glyoxal proves to be a promising cross-linker by resulting in ordered mesopore channels and higher capacitance for energy storage.

Upon understanding the manipulation of template morphologies, selection of carbon precursor and cross-linker, the use of amphiphilic imidazolium-based IL templates was explored to prepare MCs for energy storage whilst assessing their recyclability. Phloroglucinol-glyoxal polymer was employed as preliminary lignin model and carbon precursor. Four factors were identified to influence the pore architecture of resulting MCs: 1) the length of cationic alkyl chain of IL templates, 2) the percentage of ILs in IL/block copolymer co-templating system, 3) the extraction of IL template, and 4) the anion of IL templates. Notably, IL templates showed excellent structural intactness after extraction.

Increasing the length of IL cationic alkyl chain from $[C_{10}MIM][OAc]$ to $[C_{18}MIM][OAc]$ can slightly elevated the porosity of resulting carbons with increased BET surface area and pore volume from 224.8 m^2/g and 0.094 cm^3/g to 273.4 m^2/g and 0.112 cm^3/g. However, the resulting pores are dominated by disordered micropores. In IL/Pluronic F127 co-templating system, there is an overall diminishing effect on the porosity and mesopore rate of resulting MCs with the increasing percentage of ILs in total templates due to the bifunctional role of ILs, both soft template and catalyst. The strong catalytic ability of IL templates will overly cross-link carbon precursor thus worsen the porosity of resulting MCs. Methyl sulphate anion-based ILs have a weaker catalytic ability than acetate anion-based ILs thus can result in a slightly higher porosity at the same mixing ratio. Well-regulated mesopore channels only remained when the percentage of $[C_{18}MIM][OAc]$ was below 5% with BET surface area, pore volume, and mesopore size of 730.0 m^2/g, 0.48 cm^3/g, and 3.8 nm, respectively. While ordered mesopores remained when the percentage of $[C_{18}MIM][MeSO_4]$ reached 10% with shrinking mesopore diameter from 3.8 nm at 5% to 3.0 nm at 10%. As the percentage of $[C_{18}MIM][MeSO_4]$ increased, the pore volume exhibited an ever-decreasing trend with the value dropping from 0.56 cm^3/g (at 0%) to 0.22 cm^3/g (at 100%), whilst the surface area showed a growth first to 823.7 m^2/g (at 5%) then declined to 581.9 m^2/g (at 100%). Higher percentages of IL template in total template can lead to disordered mesopores even dominating micropores. The extraction of IL templates before calcination are crucial to not

only ensure the reusability of IL templates but also enrich the pore structures. The residual char yielded from the pyrolysis of IL templates themselves can partly even completely block the pores, leading to a reduced porosity. Furthermore, the surface oxygen content of resulting MCs showed an overall increasing trend as the percentage of IL templates increased, with relatively comparable graphitisation degree.

When employed as electrode materials, all MCs showed characteristic EDLC behaviour. With [C_{18}MIM][OAc] template, the increasing IL percentage for the preparation of MCs resulted in a declining capacitance from 57.5 F/g at 0% to 55.4 F/g at 5% with only 1.5 F/g remaining at 100%. Excluding the extraction of IL template can drastically decrease the capacitance due to a reduced porosity. With [C_{18}MIM][$MeSO_4$] template, the capacitance of resulting MCs first showed an increase to 60.9 F/g at 5% then decreased to 1.4 F/g only at 100%. Notably, at 10% of [C_{18}MIM][$MeSO_4$] template, the capacitance value of 55.5 F/g still remained comparable with initial value at 0%ILs. Therefore, the capacitance will not significantly decrease at low current density by replacing block copolymer template with 10% of [C_{18}MIM][$MeSO_4$] during the templating preparation of MCs whilst maintaining ordered mesopore structures.

Overall, IL templates themselves, by simultaneously acting as catalyst for the cross-linking of carbon precursor, play a crucial role in the pore architecture, surface functionality, and electrochemical performance of resulting MC materials. So far, ordered mesopores can be obtained by replacing non-recyclable block copolymer template with 10% of [C_{18}MIM][$MeSO_4$] at maximum. To prepare ordered MCs by solely employing ILs as the recyclable template may require using amphiphilic ILs with much weaker catalytic ability.

6.2. Suggestions for future work

Due to the bifunctional role of amphiphilic ILs in templating synthesis of MCs, acting both as soft template and catalyst, it is still challenging to achieve the preparation of highly ordered MCs by solely employing ILs as the recyclable template. A successful practice will require the use of amphiphilic ILs with a much weaker catalytic ability. The structural diversity of ILs offers a high chance to find or design a type of unique ILs that have both excellent amphiphilicity and weak even negligible catalytic ability thus can be employed solely to fabricate ordered MCs, even ultimately from lignin rather than lignin model polymer. Based on this thesis, suggested future explorations can be carried out on the following topics:

1) Design amphiphilic IL surfactants with negligible catalytic ability for templating synthesis of ordered MCs

Some anions can deliver H-bonding catalytic ability due to their varying H-bond basicity. Therefore, to customise the structures of ILs, research can be first carried out by comparing a series of anions including but not limited to halogens, nitrate, formate, dicyanamide, tetrafluoroborate, triflate, bis(sulfonyl)imide, alkylsulfates, alkylsulfonates, phosphates and their derivatives. The structural diversity of ILs makes it possible to ultimately tailor one type of unique ILs with excellent amphiphilicity but weak/negligible catalytic ability that can be employed solely (if not, at least maximise the percentage of ILs in co-templating system) for templating synthesis of ordered MCs whilst recycling IL templates.

2) Employ lignin directly as carbon precursor for the preparation of ordered MCs by using the customised IL templates

Once a type of unique ILs is tailored feasible to be solely employed for templating synthesis of highly ordered MCs, the proposed ILs can be transferred to the use of lignin as carbon precursor rather than lignin model polymer. Even with block copolymer template, moving forward from phenolic polymer to lignin, pretreatment of lignin is always carried out before templating synthesis to obtain low-molecular-weight, small-fragment lignin as carbon precursor, rather than directly using natural lignin with recalcitrant structures. Additionally, according to this thesis, carbon precursors themselves can influence the morphology of IL templates and template-precursor spatial correlations, which eventually determine the topology of resulting MCs. Therefore, when employing ILs as the recyclable template, the pretreatment of lignin will still be crucial to obtain suitable molecular weight and functionalities that favour the self-assembly with IL templates and lead to highly ordered meospores.

3) Tailor the pore size of ordered porous carbons by employing recyclable IL templates

The catalytic ability of IL templates is mainly derived from the anions. Once a type of unique ILs is tailored feasible to be solely employed for templating synthesis of highly ordered MCs. Further research can be directed into the customisation of IL cations, especially with respect to the cationic chain length. This provides high potential to tailor the pore diameters of resulting ordered porous carbon materials. By customising the length of cationic chains, it is likely to tune the ordered pore diameter in a range from micropores to mesopores, thereby satisfying different requirements for various applications.

4) Investigate the role of cross-linkers in the self-assembly of IL-templating synthesis

The self-assembly behaviour of ternary IL systems containing IL templates, phenolic carbon precursor monomers, and solvent has been systematically investigated in this thesis by employing a combination of experimental and computational techniques. Such strategy can be extended to quaternary IL systems by further incorporating cross-linkers into the ternary systems. Commonly used cross-linkers such as formaldehyde, glyoxal, and glyoxylic acid may also influence the morphological evolution of IL templates by interfering the hydrophilic or ionic repulsion interactions and the hydrophobic attraction interactions, thereby changing the critical packing parameter of amphiphilic IL templates in mixtures. Such influence of cross-linkers on the self-assembly can be further studied by performing experiments and MD simulations as has been carried out in this thesis. The prerequisite lies in the use of reliable and compatible models for cross-linkers.

5) Decoupling the effect of cross-linkers on the reaction rate for templating synthesis of MCs by employing amphiphilic IL templates

The role of cross-linking in the soft-templating synthesis of MCs has been studied in detail by employing block copolymer as soft template. Such investigation can be carried out for templating synthesis by directly employing amphiphilic IL templates. In the presence of ILs, the cross-linking process may be slightly different from that with block copolymer templates due to the catalytic ability of ILs. Reactive MD simulations and experimental studies shall give insights into such process, which will lead to further understanding on the role of cross-linking in the templating synthesis of MCs by employing amphiphilic IL templates.

6) Clarify the catalytic effect of IL templates during templating synthesis of MCs

Amphiphilic imidazolium-based ILs seem to play a bi-functional role in the templating synthesis of MCs, both soft template and catalyst. Cations with long alkyl chains exhibit excellent amphiphilicity and factors such as acidity, polarity, and H-bonding ability may contribute to the catalytic ability for the cross-linking. Therefore, whilst designing/sampling ILs for templating synthesis of MCs, the catalytic effect can also be studied by experimental work or computational calculations especially by DFT calculations and reactive MD simulations. This will reveal the role of ILs fundamentally and guide the design and selection of promising ILs for templating synthesis of MCs.